UNIVERSITÀ DEGLI STUDI DI TRIESTE

XXVIII CICLO DEL DOTTORATO DI RICERCA IN

NANOTECNOLOGIE

The FERMI beamline system: a unique tool for investigating matter at nano-scale

Settore scientifico-disciplinare: FIS/03

DOTTORANDO
Cristian Svetina

COORDINATORE
PROF. Lucia Pasquato

SUPERVISORE DI TESI
Dr. Marco Zangrando

ANNO ACCADEMICO 2014 / 2015

The FERMI beamline system: a unique tool for investigating matter at nano-scale

Cristian Svetina

February 17, 2016

Introduction

The advent of X-ray Free Electron Lasers (FEL) has opened a new era for exploring the fundamental properties of matter. These machines are the 4th generation light sources and combine the exceptional properties of conventional lasers (ultra-short, brilliant, coherent, and transform limited pulses) and synchrotrons (short and selectable wavelengths, selectable polarizations), allowing to probe the ultra-fast dynamics of atoms and molecules in simple and complex systems at a nano-scale level. In the last decade many unsolved problems in understanding the properties in areas such as atomic, molecular, condensed matter physics, astrophysics and biology have found a solution thanks to the operating FELs. For this reason the number of FEL large scale user facilities is now growing fast all around the world.

In order to provide the required experimental conditions, the emitted FEL light has to be characterized, transported and focused inside the end-stations. This task is extremely important since the FEL radiation is generally of poor use for the experimentalists without any knowledge of its properties and without any manipulation. As a matter of fact, the FEL photon transport and diagnostic is much more challenging compared to the synchrotrons. This is because these 4th generation light sources do not emit constantly in the same configuration, like synchrotrons, but have to be tuned and optimized accordingly to the experimental needs almost before every beamtime. In addition, the photon beam has to be switched fast from one end-station to another (differently from synchrotrons, only one experiment at the time is carried on at an FEL user facility) while preserving the wave-front, the coherence, the pulse length and the brightness as well. For these reasons the FEL photon optics and diagnostics represent a brand new field of science-technology, requiring clever custom solutions and years of R&D.

The FEL photon beam is transported inside the beamlines by means of dedicated optics, and it is measured and characterized by high-tech customized diagnostics, specifically designed to be transparent and to work on-line. In this way, an immediate feedback about the FEL status is provided to the machine and experimental physicists. Finally, the radiation is focused on the samples down to few-microns spot size, providing extremely high fluence when needed.

This PhD thesis introduces and describes the Photon Analysis Delivery and REduction System (PADReS) operative at FERMI, the Italian FEL. It will be shown that the FERMI beamlines (in terms of photon diagnostics, transport and focusing) have been designed, realized and commissioned fulfilling the requirements of reliability and stability needed for a world-class user facility.

After an introduction to the FEL working principle, the FERMI facility is described both in terms of machine layout and scientific case in chapter 1.

The following three chapters are devoted to describe the PADReS photon diagnostics (chapter 2), transport (chapter 3) and focusing (chapter 4) sections. The design of the employed instrumentation/optics is explained in detail as well as the adopted technological solutions, and the expected performance.

In chapter 5 the experimental results are reported and described. The first section illustrates the achievements of the FERMI source both in nominal and in exotic configurations measured by means of the PADReS diagnostics. The second section shows the results obtained with the in-house-built Kirkpatrick-Baez Active Optics System (KAOS) focusing section, and reports the most important experiments that have taken advantage of this unique system. The last two sections describe in detail two milestone experiments: the first coherent diffraction imaging, and the first transient grating spectroscopy done at FERMI. Both these experiments combine the exceptional properties of the FEL radiation with the performance and functionality of the PADReS.

The last chapter deals with the forthcoming beamlines at FERMI: MagneDyn, devoted to magneto-dynamics studies, and TeraFERMI, working with the TeraHertz radiation. The beamlines layout, the main components and the designs as well as the expected features are described in detailed.

After the conclusions and outlooks section, a brief section (Author research) describing in detail my contribution to the FERMI, PADReS and the experiments is present, followed by the list of my publications during the PhD studies (Author Publications).

Introduzione

L’avvento dei laser ad elettroni liberi (Free Electron Laser, FEL) ha segnato l’inizio di una nuova era per lo studio delle proprietà fondamentali della materia. Queste macchine fondono le proprietà uniche dei laser convenzionali (impulsi ultra-brevi, coerenza, brillanza, radiazione al limite di Fourier) e dei sincrotroni (lunghezze d’onda corte e selezionabili, polarizzazione variabile) permettendo di sondare le dinamiche ultra-veloci che caratterizzano sistemi atomici e molecolari, semplici e complessi, su scala nanoscopica.

Durante gli ultimi dieci anni i FEL operativi hanno permesso di rispondere a molte domande irrisolte della fisica atomica, molecolare, dello stato solido, dell’astrofisica e della biologia. Per questo motivo il numero di laboratori FEL (user facilities) dedicati ai ricercatori sperimentali sta crescendo in tutto il mondo.

Per poter creare le condizioni sperimentali necessarie, la luce emessa dal FEL deve essere caratterizzata, trasportata e focalizzata all’interno delle camere sperimentali. Questo compito è di estrema importanza in quanto la non conoscenza delle proprietà della radiazione FEL e/o la non focalizzazione rendono tale luce di poca o nulla utilità per gli sperimentali. In generale, il trasporto e la diagnostica del fascio FEL è molto più difficile rispetto al caso di un sincrotrone perché l’emissione FEL, a differenza del sincrotrone, è variabile e dipende fortemente dalle richieste sperimentali. Inoltre il fascio dev’essere spostato velocemente da una camera sperimentale all’altra (in quanto, a differenza dei sincrotroni, viene fornita luce ad una sola linea alla volta) preservando le proprietà della radiazione quali il fronte d’onda, la coerenza, la durata dell’impulso e la brillanza. Per questi motivi l’ottica e la diagnostica della radiazione FEL rappresentano di fatto un nuovo filone tecnologico-scientifico che richiede soluzioni ad hoc e anni di ricerca e sviluppo.

La radiazione FEL viene trasportata all’interno delle linee di luce (beamlines) per mezzo di speciali componenti ottiche e viene caratterizzata da un sistema di diagnostica altamente tecnologico in grado di operare in modo trasparente ed in tempo reale in modo da fornire le informazioni necessarie ai fisici di macchina ed agli sperimentali. Infine, la radiazione viene fortemente focalizzata sul campione all’interno delle camere sperimentali raggiungendo dimensioni dell’ordine dei micron e fornendo altissima fluenza quando richiesto.

In questo mio lavoro di Tesi di Dottorato il sistema di diagnostica, trasporto e focalizzazione (PADReS) del FEL italiano FERMI, viene descritto dettagliatamente dimostrando che le linee di FERMI sono state progettate, realizzate e messe in funzione soddisfacendo le richieste di affidabilità e stabilità necessarie per un centro d’eccellenza di livello internazionale.

Nel capitolo 1 vi è un’introduzione al principio di funzionamento dei FEL seguito da una descrizione del laboratorio FERMI sia come schema di funzionamento che come caso scientifico.

I seguenti tre capitoli sono incentrati sulla diagnostica (capitolo 2), sul trasporto (capitolo 3) e sulla focalizzazione (capitolo 4) del fascio FEL da parte del sistema PADReS. La progettazione e lo sviluppo delle ottiche e della strumentazione vengono spiegati dettagliatamente così come le soluzioni tecnologiche adottate e le prestazioni dei sistemi.

Nella prima sezione del capitolo 5 vengono riportati e discussi i risultati sperimentali ottenuti durante la messa in funzione di FERMI (per entrambe le sorgenti in modalità classica ed esotica) per mezzo delle diagnostiche PADReS. Nella seconda parte vengono riportati i risultati ottenuti con il sistema di focalizzazione attivo KAOS riportando gli esperimenti più significativi che hanno beneficiato di tale sistema. Le ultime due sezioni descrivono dettagliatamente due esperimenti fondamentali, vere pietre miliari per la comunità scientifica, in cui sono state combinate le proprietà uniche della radiazione emessa da FERMI con le eccezionali prestazioni del sistema PADReS.

L’ultimo capitolo descrive nel dettaglio le componenti ottiche e di diagnostica così come le prestazioni delle future linee di luce di FERMI: MagneDyn, per studi di magneto-dinamica, e TeraFERMI, che utilizzerà la radiazione al TeraHertz.

Dopo le conclusioni segue una sezione nella quale viene descritta la mia attività di ricerca svolta (Author Research) con annessa la lista delle pubblicazioni (Author Publications) durante il corso di Dottorato.

Table of contents

1 Introduction to Free Electron Lasers

In this chapter an introduction to the Free Electron Laser (FEL) is given. After an overview of the working principles of the SASE and Seeded FEL schemes, the properties of the emitted radiation will be described.
In section two the FERMI FEL will be discussed both in terms of machine layout and main components. The last section will be devoted to the FERMI scientific case and the existing experimental stations.

1.1 Free electron lasers

Natural sciences benefit from the use of electromagnetic radiation to probe the phenomena of nature. From the structure of atoms and molecules to their evolution in complex systems for various energy conditions, photons have been proved to be an essential tool for exploring matter in all its form. For this reason, in the last century the number of light source facilities has increased exponentially in order to solve the open questions of science.
The advent of infrared (IR), visible (V) and near ultraviolet (NUV) LASERs (Light Amplification by Stimulated Emission of Radiation) providing high brilliance, spatial and temporal coherence and short pulses, have allowed to dig deeply into the properties of matter probing temporal scales otherwise inaccessible. Atoms and molecules oscillate around their equilibrium positions with typical periods of a few hundreds of femtosecond. This is also true for the movement of atoms during chemical reactions or phase transformations. On the other hand the advent of brilliant emission in the ultraviolet (UV), extreme ultraviolet (EUV or XUV), soft and hard x-ray ranges, where the radiation wavelength is comparable to the system's spatial scale, have allowed to perform imaging of these systems at the nano-scale as well as spectroscopy of absorbed/emitted light from the specimen. The possibility to selectively use these wavelengths (e.g., to tune the radiation wavelengths properly) has been achieved by the exploitation of synchrotron radiation, which is emitted by charged particles orbiting in a circular storage ring.
In order to fully characterize the nanoscopic systems, the temporal duration and radiation wavelength must be comparable to the process and system under investigation. Moreover, several advanced experiments need to take advantage of other important properties of light such as: transverse and longitudinal coherence, brilliance and degree of polarization.
The Free Electron Lasers (FEL) are the joining link between lasers and synchrotrons. They can deliver fully coherent high powerful femtosecond pulses scanning the UV-EUV-x-rays spectral regions. FELs features have been theoretically studied since the late 60s. In their papers Pantell, Soncini, and Puthoff [1] and Pellegrini [2] describe the distinctive properties of the stimulated scattering of the radiation of relativistic electrons moving inside an undulator. Free electron lasers have been developed over many years,

starting from the first one built at Stanford in the 70s and going to the currently operational large scale single pass x-ray FEL facilities such as FLASH [3, 4], LCLS, [5, 6] SAKURA [7] and FERMI [8, 9]. Because of the theoretical, experimental and technological advances it is now possible to have x-ray FEL facilities open to the users coming from all over the world. In the last 20 years it has been possible to begin to study matter at the atomic level with unprecedented resolution in the ultrafast timescale with a direct impact on materials and life science.

1.1.1 FEL working principles

The essential difference between a conventional laser and a free electron laser is that the former takes advantage of a gain medium (a suitable material) able to amplify the stimulated emission, while for an FEL the medium is the bunch of relativistic electrons.
The emission process starts from the synchrotron radiation mechanism where a bunch of electrons radiates energy in the form of electromagnetic waves when accelerated. When the electron bunch passes through a series of static and periodic magnetic fields (named undulators [10]) they start to oscillate transversally with consequent photon emission [11] (Figure 1, top). When this emission occurs, the radiation co-propagates with the electron bunch and couples with the transverse component of their velocity resulting in a force along the direction of propagation. This radiation-matter interaction generates an interference that leads to a density modulation within the electron bunch. Depending on their relative phase with respect to the co-propagating radiation, electrons can gain or lose energy and this creates micro-bunches on the scale of the radiation wavelength (Figure 1, bottom).

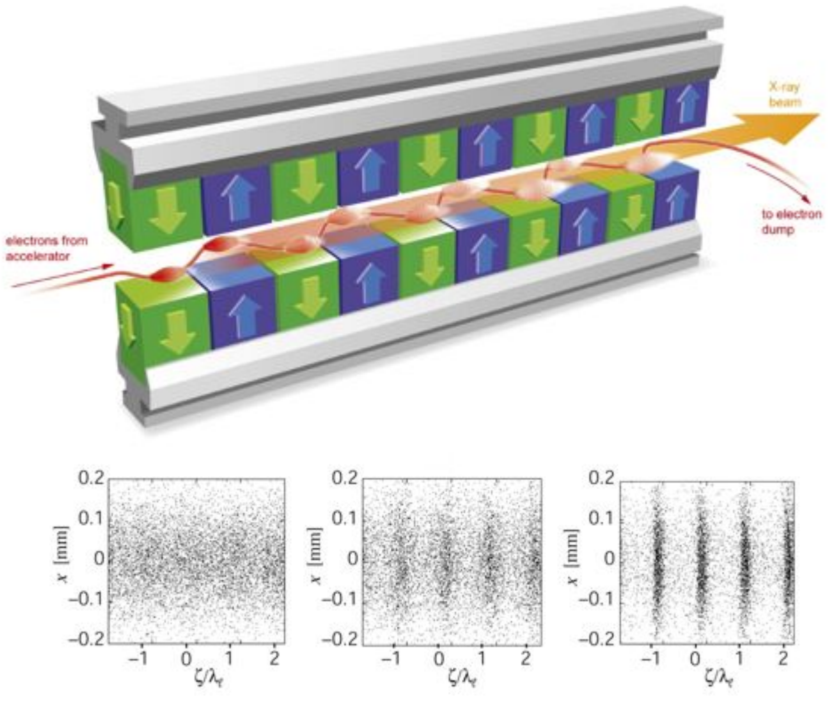

Figure 1 Top: Schematic representation of the electron bunch following a sinusoidal trajectory inside an undulator with consequence emission (Credits [12]). Bottom: Numerical simulation of micro-bunching inside an undulator (Credits [13])

The micro-bunching effect is the starting point of the FEL emission, which is an amplification of the electromagnetic wave at the expenses of the electron's energy. The net energy transfer occurs when there is the resonant condition, i.e., the electrons, moving in a sinusoidal trajectory, "slip" back in respect to the radiation (slippage), which moves forward, by one wavelength for every undulator period. The time required for an electron, with mean speed $\bar{v}_e$, to travel one undulator period (λ_u) is $t = \lambda_u / \bar{v}_e$. If λ_n is the radiation wavelength, the slippage condition is satisfied when the light travels the distance $\lambda_u + n\lambda_n$ (with n an integer number) during the same time t. Thus:

$$\lambda_n = \frac{\lambda_u}{n}\left(\frac{1 - \bar{v}_e / c}{\bar{v}_e / c}\right),$$

with c the speed of light and defining the Root-Mean-Square (RMS) undulator parameter K as a function of the undulator period λ_u, the electron charge e and mass m and a magnetic field B:

$$K = \frac{\lambda_u eB}{2\pi\, mc},$$

and expressing the electron energy in terms of the RMS of K, the Lorenz factor γ and θ the polar angle

$$\bar{v}_e = c\left(1 - \frac{1 + K^2/2}{2\gamma^2}\right),$$

the emitted radiation wavelength becomes:

$$\lambda_n = \frac{\lambda_u}{2\gamma^2 n}\left(1 + \frac{K^2}{2} + \gamma^2\theta^2\right).$$

The obtained formula is called *undulator equation* and predicts that the resonance condition occurs only at integer harmonics n of the resonant wavelength λ_u. The fundamental harmonic has n=1, the second harmonic n=2, and so on. The emitted light is amplified until the electron-radiation interaction becomes strongly non-linear and the process reaches the saturation.

As explained in detail in [14], an electron bunch with n_e electrons ($n_e >> 1$) moving inside an undulator emits a power

$$P \sim \left|\sum_{j=1}^{N} E_j e^{i\phi_j}\right|^2 = \sum_{j=1}^{N} E_j^2 + \left|\sum_{j=1}^{N}\sum_{k \neq j} E_j E_k e^{i(\phi_j + \phi_k)}\right|,$$

with E_j and ϕ_j the radiation electric field and relative phase. For a system with uncorrelated phases the second term interferes destructively, and the power of the spontaneous radiation emitter is roughly the sum of the power emitted from n_e independently emitting electrons, as it happens inside an undulator at a synchrotron. When the electrons are periodically bunched at the resonant wavelength, the phases are correlated, and the term n_e^2 dominates with an extraordinary extraction of power as it is for FEL emission. The reason why this happens is because the electron resonant interaction causes an energy modulation of the electron beam with consequent modulation of the density where electrons are in phase and radiate more power coherently. The parameter that rules this amplification process is the Pierce parameter (or FEL parameter) ρ defined as:

$$\rho = \frac{1}{\gamma_r}\left(\frac{K}{8\pi}\frac{\omega_p \lambda_u}{c}\right)^{\frac{2}{3}},$$

where $\omega_p{}^2 = \frac{4\pi e^2 n_e}{m}$ is the plasma frequency, and $\gamma_r{}^2 = \frac{\lambda_u}{2\lambda_r}\left(1+K^2\right)$ with n_e the electron number density. It can be demonstrated that the Pierce parameter determines how many undulator periods the electron bunch must travel in order to increase the emitted power by a factor *2e*. For X-ray FELs ρ is of the order of 10^{-3}-10^{-4}, and essentially measures the radiation-electron interaction efficiency.

The complete FEL process can be described by starting from the Maxwell and Lorentz equations treating it as an electromagnetic radiation amplifier where the electron beam is the active medium and the undulator the interaction region. A complete treatment of the FEL theory goes beyond this work and the full theory can be found in [15-17].

Free electron lasers can operate based on two different schemes: the oscillator configuration and the single-pass. The former is obtained by confining an electromagnetic wave inside an optical cavity making it interact multiple times with the electron bunch, which is orbiting in circles. This configuration can be found at the synchrotron FEL beamlines. In the single-pass configuration the amplification process occurs in just one passage through the undulator. The latter can be divided into two distinguished classes: the Self Amplified Spontaneous Emission (SASE) [18-22] and the seeding schemes [23-30]. In the former case the electromagnetic field is generated by a spontaneous emission of the electron bunch while in the latter case it comes from an external laser source (the seed). These two single-pass classes, discussed in the following sub-sections, are the most efficient schemes, and they are employed at the large scale facilities.

1.1.2 SASE FEL

Self Amplified Spontaneous Emission scheme takes advantage of the amplification of the electron distribution intrinsic noise. The incoherent spontaneous emission generated at the beginning of the undulator couples with the electrons that meanwhile aggregate into many micro-bunches within the bunch. The radiation emitted by every micro-bunch region interacts with the neighbor micro-bunch ahead, and this keeps going until saturation occurs. In the VUV/soft-hard x-ray regime the saturation is reached after the electrons have traveled inside many undulators making these facilities quite long (from hundreds of meter to kilometer). At the end of the SASE process a train of ultra-short spiky pulses with a noisy temporal-energy distribution (within the band of the undulator) are produced (Figure 2). This scheme is very sensitive to the electron beam properties and every energy-current variation between the shots cause strong instabilities in the emitted FEL radiation in the RMS of intensity and wavelength [31,32]. SASE scheme provides very high brilliance but the single pulses within the envelope have random intensity and duration. Nonetheless, with such scheme it is possible to reach the hard x-ray region where the seeded schemes are poorly efficient.

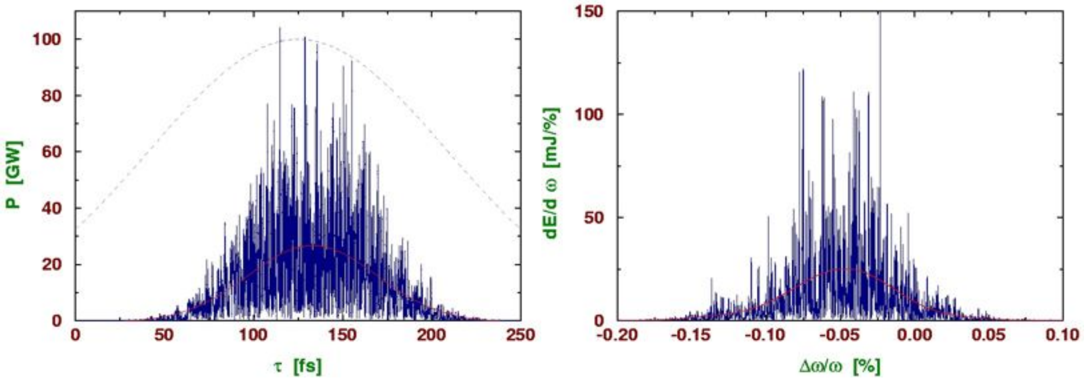

Figure 2 *Typical temporal (left) and spectral (right) structure of the radiation pulse from a SASE XFEL at a wavelength of 1 Å. The red lines correspond to averaged values. The dashed line represents the axial density profile of the electron bunch. (Credits [13])*

Up to now three large scale facilities are based on the SASE scheme: FLASH, covering the EUV-soft x-ray range, LCLS and SAKURA both covering the hard x-ray region.

1.1.3 Seeded FEL

In the seeded scheme the FEL process starts from a monochromatic laser radiation (named seed) rather than from the electron noise. In this configuration an external coherent source couples with the electron bunch at the beginning of the first undulator. The coherence and transform-limited properties (Fourier limit) of the seed are transferred to the generated FEL radiation. The external seed radiation might come from a laser, from a High Harmonic Generation (HHG) source, or from an external FEL. There are several seeding techniques that might be adopted; the most used are: direct seeding with radiation (HHG), electron beam manipulation (High Gain Harmonic Generation, HGHG, and Echo-Enabled Harmonic Generation, EEHG), and self-seeding. All of them allow increasing the longitudinal coherence length but are significantly different in their layout.

In the direct seeding an external HHG source, based on the non-linear interaction between a laser and a gas jet, irradiates the electron bunch at the same resonant wavelength of the FEL, and then the amplification occurs inside the undulator (Figure 3). The only limitation in the direct seeding process for obtaining EUV-soft/hard x-rays is the availability of suitable sources at short wavelengths with enough power.

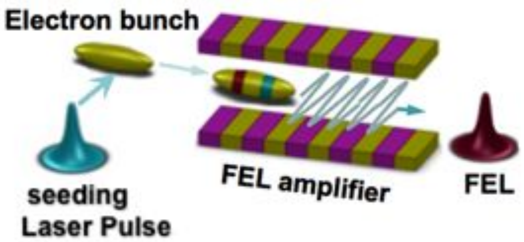

Figure 3 *Principle of the direct seeding FEL scheme. The electron bunch illuminated by the HHG source acts as an active medium. The amplification inside the undulator generates high power coherent FEL pulses.*

In the electron beam manipulation schemes the external laser induces a coherent bunching inside the electron beam when it propagates inside the first undulator, named modulator, tuned in resonance with the seed wavelength. In the HGHG scheme [33-35] the energy modulation created inside the modulator is converted in density modulation (micro-bunching) by a magnetic dispersive section, and then the amplification occurs inside a second undulator, named radiator, tuned at an harmonic of the resonant wavelength (Figure 4). In this way all the properties of the seed laser are inherited by the generated FEL radiation, such as high degree of temporal coherence, narrow bandwidths, and higher stability as compared to the SASE schemes where the FEL process starts from noise.

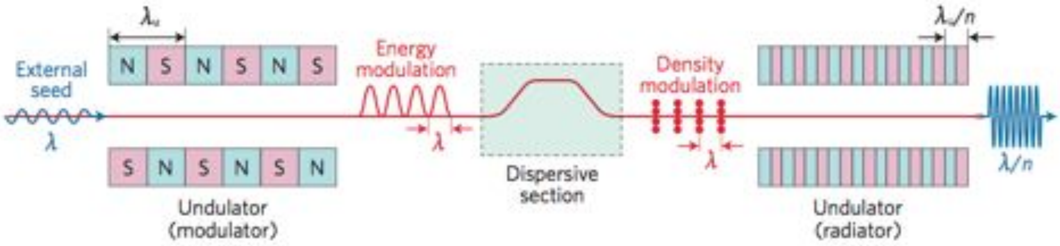

Figure 4 *Scheme for a single stage HGHG. The external laser source impinges over the high-energy electron bunch inside the modulator creating an energy modulation set at the laser resonant wavelength. A chicane modifies the electron trajectory creating a density modulation. The FEL is amplified through the radiator set a harmonic wavelength of the seed.*

An alternative electron beam manipulation scheme is the EEHG [36,37] where the density modulation at high frequencies is generated by the interaction with two seed lasers inside two modulators, both followed by two magnetic dispersive sections. Afterwards the FEL amplification occurs inside a radiator as for the HGHG scheme. With this scheme it is possible to reach very short wavelengths and some experimental results can be found in [38, 39]. One of the main difficulties with such seeding schemes is the synchronization between the seed laser and the electron bunch. Nevertheless employing powerful feedback systems and on-line diagnostics it is possible to reach an overall very high stability.

In the self-seeding scheme [40-43] the radiation generated from the SASE process is separated, monochromatized and again overlapped to the electron bunch inside an undulator like a direct seeding scheme (Figure 5). The main advantage of this configuration is the natural synchronization between the seed pulses and the electron bunches as well as the short wavelengths achievable. Recent results at LCLS have shown that this scheme is suitable for both soft and hard x-ray FEL generation [44, 45].

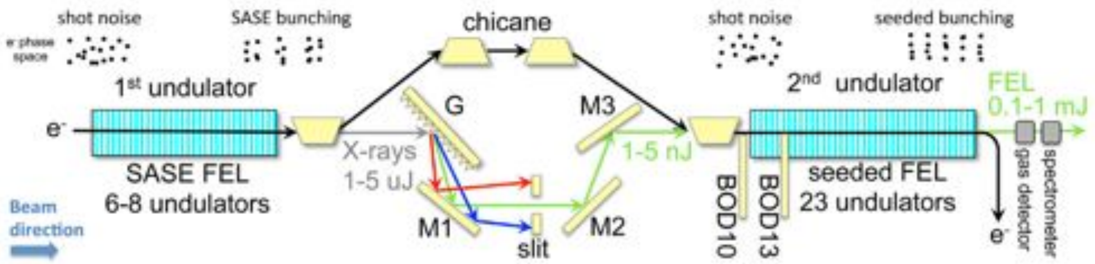

__Figure 5__ Schematic of the self seeding scheme adopted at LCLS. Shot noise from randomly distributed electrons generates 1–5 μJ of relatively wide bandwidth SASE radiation in the first chain of undulators (grey line). The seeding monochromator selects a small bandwidth (green line) while the electron chicane directs the electron bunch around the monochromator and delays its optical path. Finally, the electrons and monochromatic x rays are overlapped in the second half of the FEL (reproduced from [46])

1.2 FERMI

The FERMI (Free Electron laser Radiation for Multidisciplinary Investigations) single-pass FEL source at ELETTRA is a 4th generation light source user facility designed to supply photons in a spectral range from 100 to 1.3 nm. Taking advantage of the HGHG scheme FERMI is the first operative seeded FEL in the EUV/soft x-ray regime [47]. The machine is composed of three main parts: the linear accelerator, the undulator chains, and the photon transport. In the following, an overview of the FERMI scheme will be given (Figure 6). FERMI begins 5 meter underground inside the tunnel where the electron bunches are extracted from the photocathode gun by means of a strong UV Photo-Injector Laser (PIL). Typically the extracted charge is around 500-800 pC with an average energy of about 5 MeV. The electrons are then accelerated by a normal conduction linear accelerator (LINAC) composed of 13 Radio Frequency (RF) S-band accelerating cavities (2.998 GHz) up to energies around 1.5 GeV.

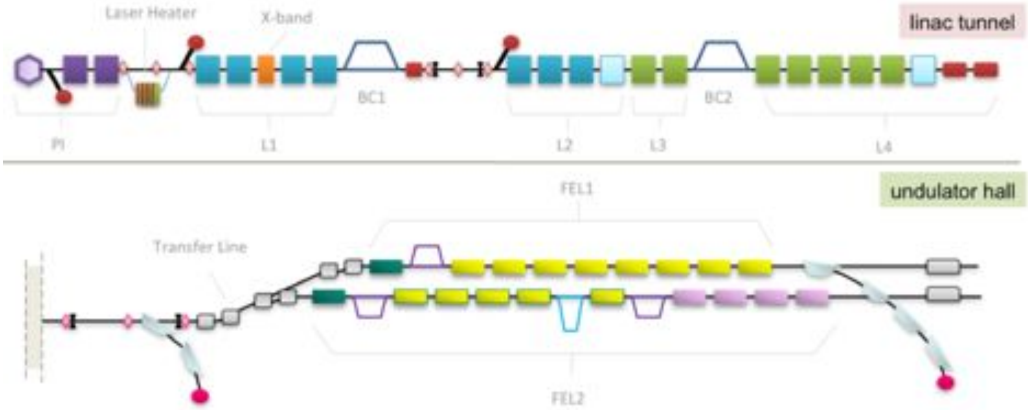

__Figure 6__ Layout of the machine FERMI FEL user facility. Top: linac tunnel where the electrons are extracted and accelerated. Bottom: Undulator Hall (UH) where the FEL radiation is generated by FEL1 or FEL2 undulator chains.

The fine tuning of the electron energy spread is obtained through the interaction with an external laser inside a short undulator called Laser Heater (LH) [48]. Between the cavities two Bunch Compressors (BC) based on magnetic chicanes allow to compress the beam by a factor of 10, reaching a peak current up to 700 A, while the X-band cavity (11.4 GHz) is used to linearize the compression. A series of diagnostics (screens, beam position monitors, spectrometers, etc.) monitor the beam quality and the pointing, while steering magnets correct the beam trajectory and solenoid magnets compensate the transverse defocusing of the electron bunch due to the Coulomb repulsion. Once accelerated the ultra relativistic electrons pass through a transfer line and feed one of the two FEL lines: the low energy FEL1 or the high energy FEL2.

FEL1 is based on the HGHG scheme and covers the low energy range from 100 nm down to 20 nm (12 eV – 65 eV). Inside the modulator the third harmonic of a Ti:sapphire seed laser (260 nm) overlaps the electron bunch creating an energy modulation. A magnetic chicane converts the energy into density modulation and the following six radiators amplify the FEL emission until saturation (Figure 7). The undulators, 2.34 m-long containing 36 periods each, are of the APPLE-II generation with permanent magnets and variable gap in order to select different harmonics of the seed laser. Since the seed laser wavelength is tunable itself, the generated FEL radiation can be tuned continuously while the polarization can be selected from linear (horizontal-vertical) to circular (left-right).

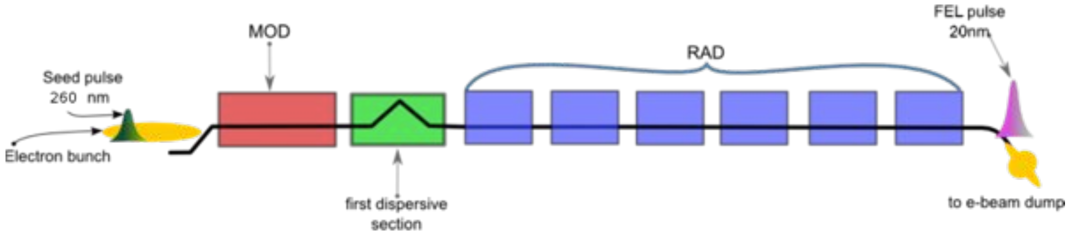

***Figure** 7 Layout of the HGHG FEL1 source. The modulator (red) is fed by the electron bunch and the UV seed laser. Afterwards, the beam passes through the dispersive section (magnetic chicane) and then is propagated inside the radiation where the FEL process occurs. At the exit of the last undulator the radiation propagates until the experimental hall while the electrons are deflected and dumped to the Main Beam Dump (MBD).*

The high-energy source FEL2 is based on the HGHG scheme too, but the FEL process is divided into two stages (Figure 8). In the first stage the external UV seed laser modulates the electrons and FEL radiation between 32-65 nm is generated, as for FEL1, but with just two radiators. Then a magnetic delay line is used to separate and delay the electrons with respect to the just-generated photons, and to recombine them again. In this way the seeding is then performed, within a second modulator, by the first-stage powerful short-wavelength FEL radiation on a fresh part of the electron beam (that had not concurred with the generation of the first stage radiation). Finally a series of six radiators amplify the FEL process up to saturation. The FEL2 undulators, 2.40 m-long with 48 periods each, have variable gap and are able to create linear and circular polarized light.

At the end of both FEL sources three bending magnets deflect the electron beam to the Main Beam Dump (MBD) section, while the FEL radiation propagates to the Experimental Hall (EH) through the Photon Analysis Delivery and REduction System

(PADReS) until the experimental end-stations. The PADReS is devoted to measure on-line and shot-to-shot the FEL properties, to transport the radiation, and to provide a focused beam for the experiments. The whole system will be described in detail in the next chapters. The FEL radiation generated with both sources has a very high degree of both spatial and temporal coherence, brilliance and short pulse duration. These properties, coupled with the narrow bandwidth, energy stability and variable polarization, make FERMI a unique source with endless possible applications. The most important will be described in the next section.

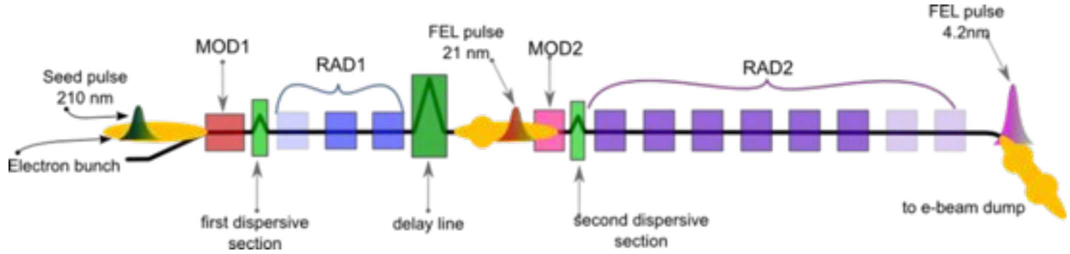

Figure 8 *Layout of the double-stage cascade FEL2 source.*

1.3 FERMI scientific case

The unique properties of the FERMI output radiation such as coherence, high brilliance, wavelength tunability, polarization, short duration and narrow bandwidth, have opened new scientific possibilities allowing to perform new classes of experiments so far impossible with the existing light sources. The high degree of coherence and the high photon flux allow to perform single shot imaging over a wide set of complex molecules and nano-structures with a great potential in life, environmental, materials and chemical sciences as well as in nanotechnology. The high peak power in the soft x-ray region triggers non-linear, multi-photon processes inaccessible with other lasers. The short time duration of the FEL pulses enables time domain experiments from probing the ultra-fast nuclear fundamental reactions as well as electronic dynamics to the evolution of complex systems can be studied with an impact on atmospheric, astrophysical and environmental physics. The possibility to change continuously the FEL wavelength coupled with the narrow bandwidths allow to scan through the absorption/emission edges of solid state materials and gases. Finally the presence of the synchronized IR laser, available for the users, in combination with the FEL allows to perform pump-probe experiments with unprecedented resolution. Four beamlines have been designed, installed and commissioned in the FERMI experimental hall: LDM [49], DiProI [50], EIS-TIMEX [51] and EIS-TIMER [52]. In the following sections the scientific case of the four FERMI beamlines will be explained together with the layout and capabilities.

1.3.1 DiProI

The advent of new generation free electron laser (FEL) sources, providing ultra-short pulses with high transverse coherence and peak brightness, has opened extraordinary opportunities for lensless Coherent Diffraction Imaging (CDI) with unprecedented spatial and temporal resolution. When an object is illuminated by a coherent radiation, the generated speckle pattern contains all morphological information necessary to retrieve the object shape, even though the phase information remains unknown. The possibility to reconstruct the real space image of a sample from a diffraction pattern was suggested by Sayre [53] and was theoretically supported by the Shannon's theorem [54]. For a long time the limitation of this technique was the lack of sufficiently bright and spatially coherent sources and the need to employ dedicated optics that reduce dramatically the resolution. At the end of the 80s the first experimental demonstration of recovering object morphology from the diffraction pattern of a non-crystalline sample was made using a laser [55].

With the advent of synchrotron facilities providing X-rays the highest resolution achieved on living systems has reached the limit of ~20 nm, imposed by radiation damage. The damage is caused mainly by chemical changes, diffusion, and local heating over timescales greater than microseconds. This resolution barrier can be overcome by using intense pulses of duration shorter than that of any process causing structural damage, like FEL pulses. Indeed, the concept of single-shot imaging can be extended to achieve atomic size resolution for the imaging of single molecules. Moreover, diffractive imaging does not require any optics and hence does not impose any technological limit to the resolution. In fact, the coherence of FEL radiation is fundamental to lensless imaging techniques such as phase contrast imaging, micro-tomography and holography. The multipurpose experimental station Diffraction and Projection Imaging (DiProI) has been designed in order to meet the requirements for static and ultra-fast dynamic CDI experiments together with the possibility to perform complementary projection imaging and nano-spectroscopy. With these techniques structural information of non-periodic samples are obtained. Even though the specimens are destroyed by the intense FEL pulse, the information contained in the diffraction pattern is preserved since the different time scale between the scattered photons and the atoms motion. The collected information on a bi-dimensional CCD detector is sufficient for the reconstruction of the object image by recovering the missing phase using a phase-retrieval computational algorithm (Figure 9). The polarization (circular or linear) of the FEL light extends the information to spin and orbital momentum, revealing features such as the orientation of magnetic domains, bonds in constituent molecules, etc.

The wavelength tunability of FERMI enables to perform Resonant Coherent Diffraction Imaging (R-CDI) of selected atomic absorption edges, adding information about the spatial distribution of the chemical constituents of the specimen. The DiProI end-station has a modular versatility that allows for different scattering experimental schemes for static and time-resolved experiments, both with fixed and free-standing objects. The station can host different experimental setups for performing experiments in transmission and/or reflection geometry using both FEL1 and FEL2 radiation and all possible pump–probe combinations using FEL and the IR laser radiation. It has also an expansion module that can be added to use two detectors positioned at different distances behind the sample to simultaneously monitor small and large scattering angles (Figure 10).

The DiProI end-station hosts also a system composed of an aerosol particle injector, combined with a Time-of-Flight (ToF) mass spectrometer devoted to the investigation of free standing nano-particulate samples. Such systems deliver particles from solution or atomic clusters of noble gases into the interaction region of the focused FEL beam.

The flying objects are hit in the interaction region by the FEL and/or the IR pump laser and the diffraction patterns are monitored by the CCD. Simultaneously, the ToF mass spectrometer provides information about the products of sample ionization. This allows to explore the dynamics of Coulomb explosions and the resolution limits that can ultimately be achieved.

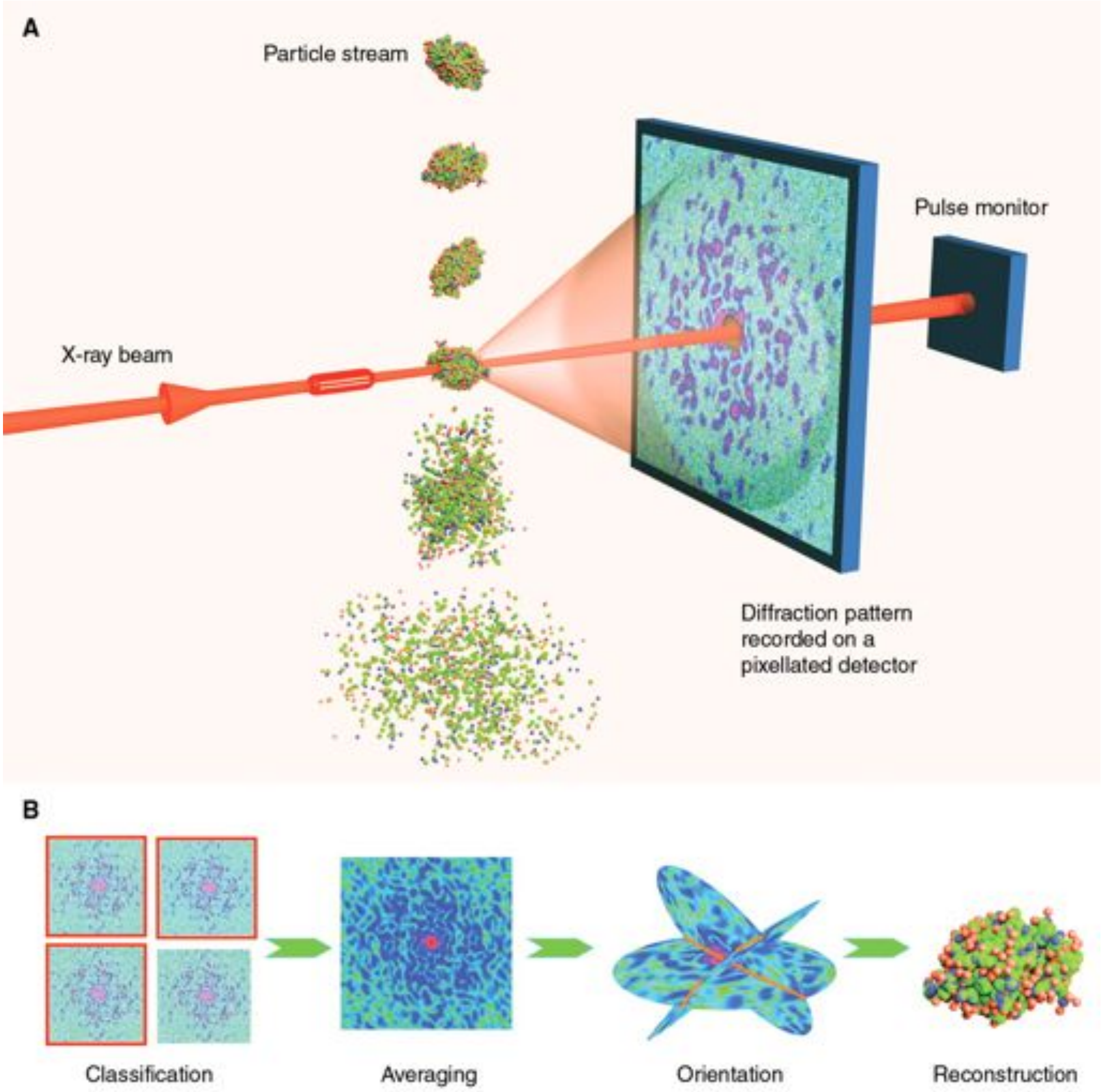

Figure 9 *Experimental set-up for atomic resolution imaging based on single pulse diffraction patterns using the FEL radiation (from https://desy.cfel.de/cid/).*

In order to achieve the focal spot needed to perform the experiments the beamline has been equipped with a custom active focusing mirror system (KAOS, described in detail in chapter 4 section 4.3) able to reach spot sizes down to 5 μm and to control the focal position as well. During the beamline commissioning (2012) DiProI has demonstrated to be able to perform single-shot CDI over static lithographic samples ([56] described in chapter 5 section 5.3). Following this first result, after opening the DiProI end-station to users, a number of successful experiments have been performed. A remarkable result, obtained by a group from CFEL (DESY), have demonstrated the conformation sequence recovery from randomized single-shot diffraction patterns of a stack of purposely fabricated structures [57].

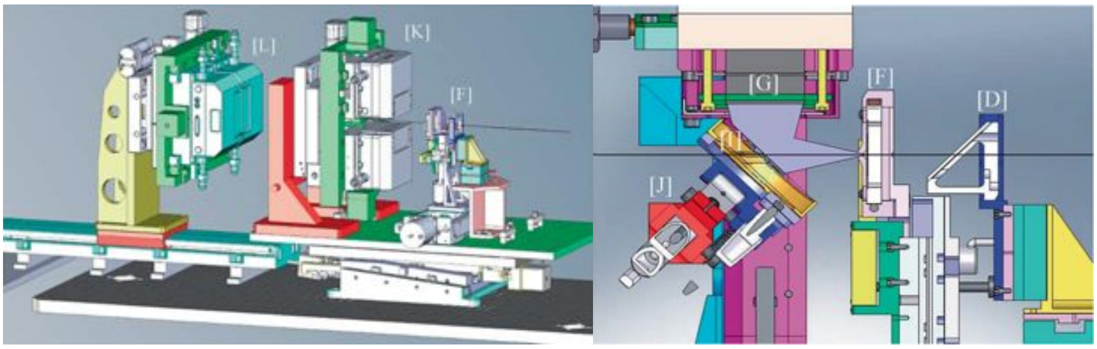

Figure 10 *Sketch of the two experimental setups at DiProI. Left: Direct acquisition set-up using two detector systems. Photons scattered from the sample F) are detected by a near K) or a far L) CCD system, depending on the deflection angle. Right: Indirect acquisition setup using a multilayer deflecting mirror. Propagating from the right, the beam passes through the apertures stage D), the sample F), and the multilayer mirror I), which deflects the diffraction image to the CCD G), letting the primary beam J) through a hole (reproduced from [50])*

In addition DiProI has made significant advancements with the advent of the variable polarization FELs in magnetism and, in particular, identifying the mechanisms of ultrafast nanoscale magnetization switching, induced by femtosecond optical laser pulses [58, 59]. Finally, thanks to the continuous implementation of new experimental schemes for exploring transient states of matter interacting with FEL pulses of variable wavelengths, intensities and pulse durations, a first step toward nonlinear wave-mixing experiments has been done. These experiments have a dedicated experimental station at the EIS-TIMER beamline (see section 1.3.3 below) [52, 60] and some simplified scheme has been employed at DiProI as well. Very recently, using a mini-delay line, it has been demonstrated for the first time the generation of a transient grating in a glass sample by hitting simultaneously the specimen at different angles with the two split FEL pulses and probing with an optical laser pulse the induced electron density modulation [61].

1.3.2 LDM

The Low Density Matter (LDM) end-station is an instrument for studying atomic, molecular and cluster physics in combination with EUV/soft-X-ray radiation. It is endowed by a state of the art Velocity Map Imaging (VMI) spectrometer that can be used for electron or ion imaging as well as for Time-of-flight (ToF) spectrometry allowing to measure the angular and kinetic energy distributions simultaneously with a 4π-collection efficiency. The instrument is described in detail in [62] and its layout as well as an example of spectrum acquired are shown in Figure 12.
Taking advantage of the unique properties of the FERMI radiation, the LDM experimental station can cover a wide set of experiments. The VMI coupled with the extremely high FEL *brightness* allows to investigate the electronic structure of nano-particles and nano-clusters. Currently there are several important open questions that have not been solved. Examples of important quantum size effects in small particles are

the highly discrete electronic density of states in metal clusters [63], the metal/nonmetal transition in divalent metals [64], the indirect/direct band-gap transition in silicon clusters [65], the general increase of the band-gap in semiconductor clusters [66] or the increase of the magnetic moment of ferromagnetic clusters [67]. For other properties like superconductivity only some evidence for related effects have been found in small particles [68]. The related spectroscopic features such as line shapes (with phonon and low energy electronic contributions) or satellite structures (strong correlations as for the “6 eV satellite” in nickel) constitute an entirely unexplored, yet interesting and important, field of research. The reason for this lack of knowledge, despite the wealth of existing photoelectron spectroscopy results concerning free clusters and nano-particles, is that the limited photon energy of standard laser systems allows studying electronic states only down to ~5 eV below the Fermi energy. This limitation prevents measuring the full valence electron structure as well as, for example, performing photon energy dependent spectroscopy across shallow core edges (resonance photoemission [69]), data that would greatly contribute to the understanding of the evolution of the electronic structure as a function of cluster size. The beam intensities available at 3rd generation synchrotron radiation facilities are still far below what is required for meaningful gas phase experiments. Size-selective spectroscopy at FERMI-LDM therefore allows measurements of unprecedented significance leading to a deeper understanding of the electronic structure of nanoscale metals and semiconductors, as well as of electron correlation effects in solids in general.

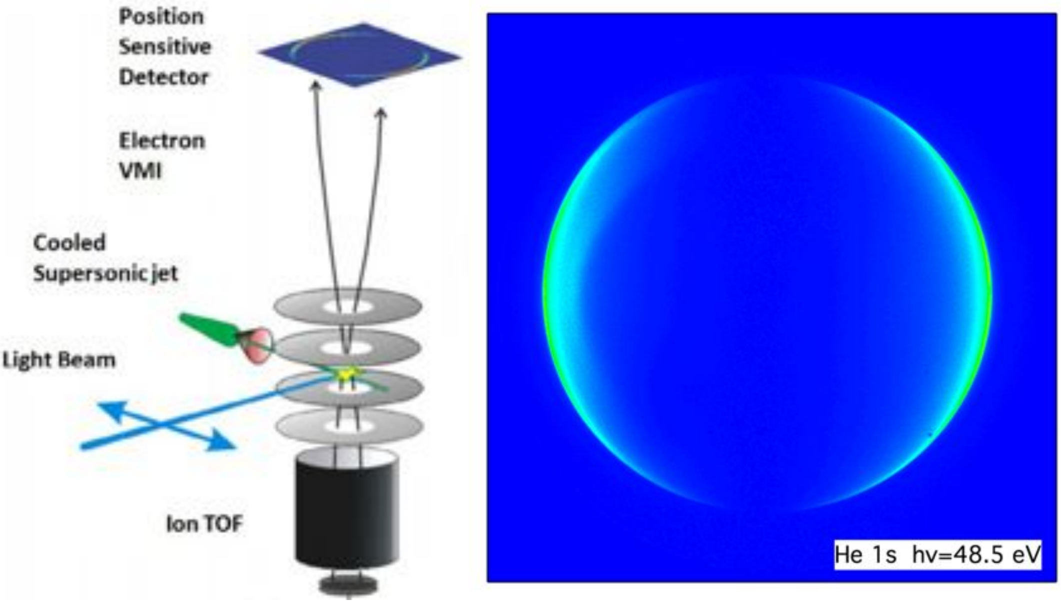

Figure 11 *Left: general scheme of the interaction chamber. Right: example of signal measured at LDM end-station with the Velocity Map Imaging (VMI).*

The FERMI’s *narrow bandwidth* and *wavelength tunability* permit to perform high resolution spectroscopy studies of atoms, ions, neutral molecules and reaction intermediates.

Non-linear optics in absorption and ionization hitherto inaccessible with lasers (particularly shallow core levels) of simple systems like Noble gases atoms (Ne, Ar, Kr and Xe) have a key role for LDM. The most relevant processes are: two-photon resonant absorption at the doubly excited states of He (to access even states), multi-

photon double ionization of He and of the other rare gases and basic non-linear interaction between atoms and strong electromagnetic fields.
Pump-probe two-colour double ultra-short pulses (IR laser and FEL) allow to measure with unprecedented resolution important processes like auto-ionization, fragmentation and conformational changes. To follow the temporal evolution of intra-molecular, photo-induced processes, femtosecond pump-probe techniques are the only means of resolving, in real time, relaxation processes and nuclear motion too.
Finally the availability of *variable polarization* opens the possibility to study dilute species of macromolecules. Employing the Circular Dichroism (i.e., dichroism involving circular polarized light), a standard method of determining protein folding, the basic structures of helix, coil and sheet can be distinguished providing structural information about free macromolecules, potentially more detailed than with UV/visible absorption circular dichroism, because the spectral range is much broader.

As for DiProI, the LDM beamline is equipped with a custom active focusing mirror system able to control the beam size at the sample: from 300 μm down to 5 μm FWHM. Depending on the experiment the focused photon beam is optimized by means of the photon diagnostics of the PADReS group (as described in chapter 4).

1.3.3 EIS-TIMER

The EIS-TIMER beamline is dedicated to TIME-Resolved spectroscopy of mesoscopic dynamics in condensed matter. The primary aim of EIS-TIMER is to exploit the full (i.e., both transverse and longitudinal) coherence of FERMI to extend coherent non-linear methods from the optical into the EUV/soft x-ray spectral domain. In this context, the main goal is to develop FEL-based four-wave-mixing (FWM) experiments [70-72], in particular those based on the transient grating (TG) approach.

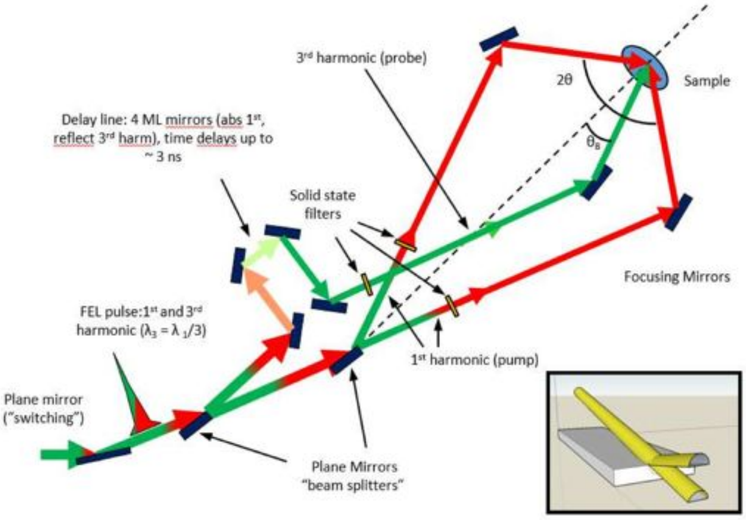

Figure 12 *Sketch of EIS-TIMER beamline layout. Insert: wave-front beam splitting of the FEL photon beam by means of a sharp edge-plane mirror.*

As these experiments rely upon the coherent interaction of three FEL pulses, the key requirement for the EIS-TIMER photon transport system is the capability to split the FEL beam into three parts, that have to be delayed and recombined at the sample at given angles (a sketch of the layout is shown in Figure 14). The idea for the basic configuration is to use both the first and third harmonics of the FEL emission: two first-harmonic pulses are sent to the sample with an inter-beam angle 2θ in time coincidence, while a third harmonic beam is time-delayed by a right angle delay line, made out of 4 multilayer (ML) coated mirrors, and then impinges on the sample at an angle $\theta_B = \sin^{-1}\left(\sin\left(\theta/3\right)\right)$ to fulfill the so-called phase matching condition. The beam splitting is achieved by a sequence of two wave-front division beam splitters [73-75], while two additional plane mirrors steer the third harmonic beam into the delay line. The focusing of the beams at the desired angles is finally provided by three independent toroidal mirrors.

Such a configuration allows to study the time evolution of density fluctuations in disordered systems performing impulsive stimulated Brillouin, Raman and Rayleigh scattering experiments in the unexplored 0.1-1 nm^{-1} wavevector (Q) range, which is expected to be of the highest relevance for the study of dynamics in disordered systems and nanostructures as shown in Figure 15.

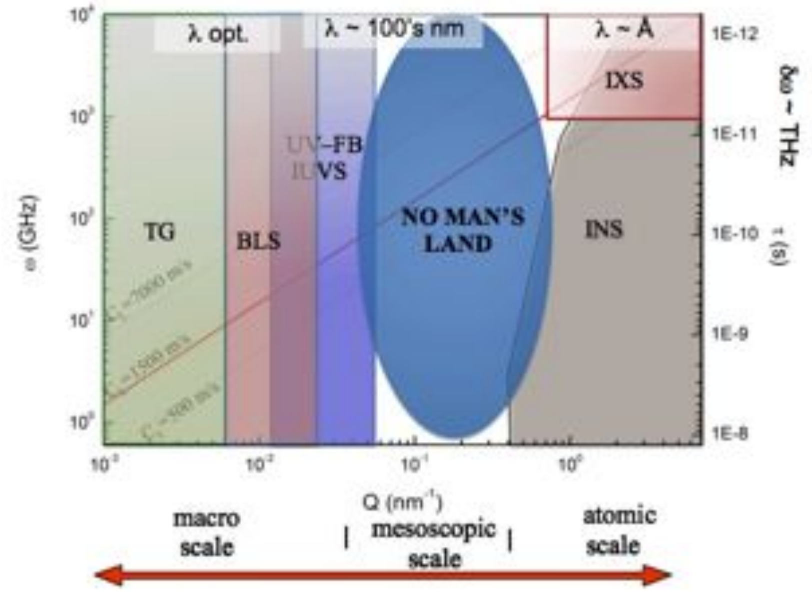

Figure 13 *Techniques from lower to higher Q-values: optical transient grating (TG), Brillouin Light and UV Scattering (BLS-VIS, BLS-UV and IUVS) and Inelastic X-rays and Neutrons Scattering (IXS, INS). (Readapted from [52])*

On the other hand, the possibility offered by FERMI and EIS-TIMER to exploit the two-color FEL emission (described in chapter 5), additional "jitter-free" optical pulses and the independent control of the relative time delays between the three pulses, will allow to carry out further FWM-based experiments, such as, e.g., coherent Raman scattering [70,76], photon echo or multi-dimensional spectroscopy [77]. These methods are currently applied in the optical regime and have demonstrated their capability to probe a large array of dynamical processes, ranging from molecular vibrations to spin waves, with energy-wavevector selectivity and ultrafast time resolution, as well as to investigate dynamical processes inaccessible to linear light-matter interactions. The EUV/soft x-ray analogues of such techniques will potentially extend the range of investigable excitations towards high-energy modes, such as valence-band excitons, and will allow for nanometric to atomic spatial resolution, as well as for atomic selectivity, through the selective exploitation of core resonances.

1.3.4 EIS-TIMEX

The EIS-TIMEX end-station is focused on ultrafast TIme-resolved studies of Matter under EXtreme and metastable conditions [51, 78]. The two main concerns at the basis of the instrumental design are the maximization of the FEL photon flux at the sample, needed to photo-excite solid specimen into extreme thermodynamic conditions [79], and the possibility to exploit a large array of pump-probe options, with sub-ps time resolution.

Condensed matter exposed to high energy density sub-ps pulses of light is rapidly driven into a non-equilibrium "exotic" regime characterized by a hot electron subsystem and an unperturbed ionic subsystem. This condition relaxes in the ps time scale as the electrons and ions thermalize leading, under certain circumstances, to a warm dense matter (WDM) phase.

Both the exotic and the WDM regimes are almost unexplored experimentally, and poorly described by available theoretical models. Experimental complexities reside in the extremely short lifetime that characterizes these phases as well as in the opacity of condensed matter to visible light. On the theoretical side, difficulties to model such transient states are ascribed to the poor control of microscopic mechanisms such as the electron-electron and electron-phonon coupling and their characteristic time scales under non-equilibrium extreme conditions of pressure and temperature. In addition, a comprehensive theoretical framework, capable of satisfactorily describing a condensed material with solid densities and strong internal correlations but average temperatures in the realm of the plasma regime, is lacking.

One of the principal aims of EIS-TIMEX is to investigate the electronic properties of both the exotic and the WDM regimes through spectroscopic techniques such as absorption and emission. The use of a laser/pump-FEL/probe approach with sub 10 fs time jitter, associated with a proper deconvolution procedure to clean out effects originated by long pulses, can guarantee the needed time resolution to monitor the collective electron dynamics after the pump absorption. A EUV FEL pump can be used to isochorically heat opaque specimen when laser pumps are not effective. EIS-TIMEX also aims at elucidating the nature of intriguing phase transitions that lead to short lived states of matter, such as the so called low density liquid (LDL) matter, which is expected to show up when covalent systems lose their local open atomic order under the action of pressure and/or temperature. Such transient local structures in condensed matter are expected to be accessible by means of an ultrafast isochoric heating.

In order to meet the former requirement, EIS-TIMEX is featured by an essential photon transport system, able to minimize intensity losses from the source to the sample and to provide a focal spot of few μm^2 with the employment of an ellipsoidal focusing mirror [80]. FEL fluences as large as 10^2 J/cm^2 can be thus achieved at the sample. Beams of such fluxes with energies in the EUV/soft x-ray range of operation for FERMI can induce efficient and homogeneous ultrafast excitations in solid samples. Figure 16 left is a picture of the EIS-TIMEX experimental chamber while on the right the main experimental setup is shown.

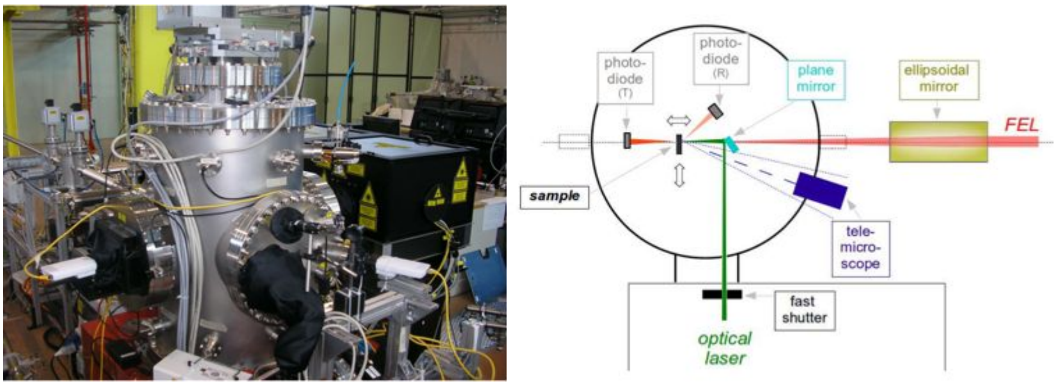

***Figure 14** Left: External view of the main EIS-TIMEX chamber. On the right one can distinguish the black box that protects the laser setup . Right: EIS-TIMEX end-station main experimental setup.*

References

[1] R.H. Pantell, Y. Soncini, and H.E. Puthoff, Stimulated Photon-Electron Scattering, IEEE Quantum Electronics 4 (1968) 905
[2] C. Pellegrini, The history of X-ray free-electron lasers, Eur. Phys. J. H, vol.37, 659-708 (2012)
[3] W. Ackermann et al. “Operation of a free-electron laser from the extreme ultraviolet to the water window”. In: Nature Photonics 1.6 (June 2007), pp. 336–342
[4] http://flash.desy.de/accelerator/
[5] P. Emma et al. “First lasing and operation of an angstrom-wavelength free-electron laser”. In: Nature Photonics 4.9 (Sept. 2010), pp. 641–647
[6] http://lcls.slac.stanford.edu
[7] T. Ishikawa et al. “A compact X-ray free-electron laser emitting in the sub- angstrom region”. In: Nature Photonics 6.8 (Aug. 2012), pp. 540–544
[8] E. Allaria et al. “Highly coherent and stable pulses from the FERMI seeded free- electron laser in the extreme ultraviolet”. In: Nature Photonics 6.10 (2012), pp. 699– 704
[9] www.elettra.trieste.it/FERMI
[10] H. Motz. “Applications of the radiation from fast electron beams”. In: Journal of Applied Physics 22.5 (1951), pp. 527–535
[11] B. W. J. McNeil and N. R. Thompson. “X-ray free-electron lasers”. In: Nature Photonics 4.12 (2010), pp. 814–821
[12] http://www.xfel.eu/overview/how_does_it_work/
[13] http://photon-science.desy.de/facilities/flash/index_eng.html
[14] B. W. J. McNeil and N. R. Thompson. “X-ray free-electron lasers”. In: Nature Photonics 4.12 (2010), pp. 814–821
[15] A. M. Kondratenko E. L. Saldin. “Generation of coherent radiation by a relativistic electron beam in an undulator”. In: Part. Accel. 10 (1980), pp. 207–216
[16] R. Bonifacio C. Pellegrini L. M. Narducci. “Collective instabilities and high-gain regime in a free electron laser”. In: Opt. Comm. 50.373 (1984)
[17] B. Murphy C. Pellegrini. “Generation of high intensity coherent radiation in the soft x-ray and VUV region”. In: Journ. OSA 259.373 (1985)
[18] S. V. Milton, et al., “Observation of self- amplified spontaneous emission and exponential growth at 530 nm”. In: Phys. Rev. Lett. 85 (2000), pp. 988–991
[19] M. Babzien, et al., “Observation of self-amplified spontaneous emission in the near-infrared and visible wavelengths”. In: Phys. Rev. E 57 (1998), pp. 6093–6100
[20] J. Andruszkow, et al., “First observation of self-amplified spontaneous emission in a free-electron laser at 109 nm wavelength”. In: Phys. Rev. Lett. 85 (2000), pp. 3825– 3829
[21] A. M. Kondratenko, et al., “Generation of coherent radiation by a relativistic electron beam in an undulator”. In: Part. Accel. 10 (1980), pp. 207–216
[22] R. Brinkmann. “The European XFEL project”. In: Proceedings of the 2006 FEL Conference. 2006

[23] R. Coisson F. De Martini. Physics of quantum electronics. Addison-Wesly Reading, 1982

[24] L. H. Yu. “Generation of intense UV radiation by subharmonically seeded single pass free electron lasers”. In: Phys. Rev. A 44.5178 (1991)

[25] A. Doyuran, et al., “Characterization of a high-gain harmonic-generation free-electron laser at saturation”. In: Phys. Rev. Lett. 86.5902 (2001)

[26] L. H. Yu, et al., “First ultraviolet high-gain harmonic-generation free-electron laser”. In: Phys. Rev. Lett 91.074801 (2003)

[27] A. Doyuran, et al., “Experimental study of a high-gain harmonic-generation free-electron laser in the ultraviolet”. In: Phys. Rev. ST Accel. Beams 7.050701 (2004)

[28] E. Allaria , et al., “Experimental characterization of nonlinear harmonic generation in planar and helical undulators”. In: Phys. Rev. Lett. 100.17 (2008), p. 174801

[29] G. De Ninno , et al., “Self-induced harmonic generation in a storage-ring Free-Electron Laser”. In: Phys. Rev. Lett. 100.10 (2008), p. 104801

[30] E. Allaria, et al., “Soft-X-Ray coherent radiation using a single-cascade Free- Electron Laser”. In: Phys. Rev. Lett. 99.1 (2007), p. 014801

[31] P. Pierini W. M. Fawley. “Shot noise startup of the 6 nm SASE FEL at the TESLA test facility”. In: Nucl. Instr. and Meth. A 375 (1996), pp. 332–335

[32] K.-J. Kim. “Three-dimensional analysis of coherent amplification and self-amplified spontaneous emission in free-electron lasers”. In: Phys. Rev. Lett. 57 (1986), pp. 1871–1874

[33] L. H. Yu. “Generation of intense UV radiation by subharmonically seeded single pass free electron lasers”. In: Phys. Rev. A 44.5178 (1991).

[34] L. H. Yu, et al., “First ultraviolet high-gain harmonic-generation free-electron laser”. In: Phys. Rev. Lett 91.074801 (2003).

[35] A. Doyuran, et al., “Experimental study of a high-gain harmonic-generation free-electron laser in the ultraviolet”. In: Phys. Rev. ST Accel. Beams 7.050701 (2004)

[36] G. Stupakov. “Using the beam-echo effect for generation of short-wavelength radiation”. In: Physical Review Letters 102.7 (2009), pp. 1–4

[37] D. Xiang and G. Stupakov. “Echo-enabled harmonic generation free electron laser”. In: Physical Review Special Topics - Accelerators and Beams 12.3 (2009), pp. 1–10

[38] Z. T. Zhao and D Wang. “Progress in the Sduv-Fel and Development of X-Ray Fels in Shanghai”. In: Proceedings of International FEL Conference, Malmo, Sweden (2010), pp. 15–19

[39] D. Xiang et al. “Demonstration of the echo-enabled harmonic generation technique for short-wavelength seeded free electron lasers”. In: Physical Review Letters 105.11 (2010), pp. 8–11

[40] J. Feldbaus et al. “Possible application of X-ray optical elements for reducing the spectral bandwidth of an X-ray SASE FEL”. In: Nuclear Instruments and Methods in Physics Research, Section A: Accelerators, Spectrometers, Detectors and Associated Equipment 393.1-3 (1997), pp. 162–166

[41] E. L. Saldin et al. “X-ray FEL with a meV bandwidth”. In: Nuclear Instruments and Methods in Physics Research, Section A: Accelerators, Spectrometers, Detectors and Associated Equipment 475.1-3 (2001), pp. 357–362

[42] G. Geloni, et al., “Self-seeded operation of the LCLS hard X-ray FEL in the long-bunch mode”. In: arXiv.org December (2010)

[43] G. Geloni, et al., “A novel self-seeding scheme for hard X-ray FELs”. In: Journal of Modern Optics 58.16 (Sept. 2011), pp. 1391–1403

[44] J. Amann et al. “Demonstration of self-seeding in a hard-X-ray free-electron laser”. In: Nature Photonics 6.10 (2012), pp. 693–698

[45] D. Ratner et al. “Experimental Demonstration of a Soft X-Ray Self-Seeded Free- Electron Laser”. In: Physical Review Letters 114.5 (2015), pp. 1–5

[46] D. Ratner, et al., “Experimental demonstration of a soft x-ray self-seeded free-electron laser". (http://www.slac.stanford.edu/pubs/slacpubs/16000/slac-pub-16214.pdf)

[47] Allaria, E., et al., “The FERMI free-electron lasers (2015) Journal of Synchrotron Radiation”, 22, pp. 485-491

[48] S. Spampinati et al. “Laser heater commissioning at an externally seeded free-electron laser”. In: Phys. Rev. ST Accel. Beams 17 (2014), p. 120705

[49] Svetina, C., et al., “The Low Density Matter (LDM) beamline at FERMI: Optical layout and first commissioning”(2015) Journal of Synchrotron Radiation, 22, pp. 538-543

[50] Pedersoli, E., et al., “Multipurpose modular experimental station for the DiProI beamline of Fermi@Elettra free electron laser” (2011) Review of Scientific Instruments, 82 (4), art. no. 043711

[51] Di Cicco, A., et al., “Probing phase transitions under extreme conditions by ultrafast techniques: Advances at the Fermi@Elettra free-electron-laser facility” (2011) Journal of Non-Crystalline Solids, 357 (14), pp. 2641-2647

[52] Masciovecchio, C., et al., ”EIS: The scattering beamline at FERMI”(2015) Journal of Synchrotron Radiation, 22, pp. 553-564
[53] D. Sayre, Acta Crystallogr. 5 (1952), p. 843
[54] C.E. Shannon, Proc. Inst. Radio Eng. 37 (1949), pp. 10–21
[55] J.N. Cederquist, J.R. Fienup, J.C. Marron, and R.G. Paxman, Opt. Lett. 13 (1988), pp. 619–621
[56] Capotondi, F., et al., Coherent imaging using seeded free-electron laser pulses with variable polarization: First results and research opportunities (2013) Review of Scientific Instruments, 84 (5), art. no. 051301
[57] C. H. Yoon, et al., "Conformation sequence recovery of a nonperiodic object from a diffraction-before-destruction experiment" *Opt. Express* **22** (2014) 8085
[58] Muller, L. et al. (2013b). Synchrotron Radiat. News, 26, 27–32
[59] Korff Schmising, et al., (2014). Phys. Rev. Lett. 112, 217203
[60] Cucini, R., Bencivenga, F., Zangrando, M. & Masciovecchio, C. (2011). Nucl. Instrum. Methods Phys. Res. A, 635, S69–S74
[61] Bencivenga, F. et al. (2015). Nature (London). 520, 205–208
[62] O’Keeffe, P., et al. (2012). Nucl. Instrum. Methods Phys. Res. B, 284, 631 69
[63] G. Wrigge, M. Astruc Hoffmann, and B.v. Issendorff, Phys.Rev. A 65, 063201 (2002)
[64] B. v.Issendorff, and O. Cheshnovsky, Annu. Rev. Phys. Chem. 56, 549–580 (2005)
[65] L. Canham, Nature 408, 411 (2000).
[66] A.D. Yoffe, Advances in Physics 42, 173 (1993).
[67] Billas, Isabelle M. L.; Chatelain, A.; de Heer, Walt A., Science, 265, 1682 (1994)
[68] Ramiro Moro, et al., Phys. Rev. Lett. 93, 086803 (2004); Science 300, 1265 (2003)
[69] C. Guillot et al., Phys. Rev. Lett. 39, 1632 (1977)
[70] Tanaka, S. & Mukamel, S. (2002). Phys. Rev. Lett. 89, 043001;
[71] Bencivenga, et al., (2013). New J. Phys. 15(12), 123023;
[72] Marcus, G., Penn, G. & Zholents, A. A. (2014). Phys. Rev. Lett. 113, 024801
[73] Bencivenga, F. & Masciovecchio, C. (2009). Nucl. Instrum. Meth. A, 606(3), 785 – 789;
[74] R., Bencivenga, F. & Masciovecchio, C. (2011). Opt. Lett. 36(7), 1032–1034.
[75] Cucini, R., et al., (2011). Nucl. Instrum. Meth. A, 635, 69
[76] Bencivenga, et al., (2014). Faraday Discuss
[77] Mukamel, S. (1995). Principles of Nonlinear Optical Spectroscopy. Oxford University Press
[78] Di Cicco, et al., (2011). vol. 8077, p. 4.
[79] Lee, R. W., et al., (2003). J. Opt. Soc. Am. B, 20(4), 770–778
[80] Svetina, C., et al., (2011). Nucl. Instrum. Meth. A, 635(1 SUPPL.), S12–S15

2 PADReS Photon Diagnostics

As for optical lasers and synchrotron sources, the emitted radiation has to be characterized, transported and focused over the sample. This task is quite straightforward for low energy photons (up to the Ultra Violet, UV range) where transmissive (lenses, beam splitters) and non-linear (crystals) optical elements can be used, and the photon beam propagates in air (no vacuum needed). On the other hand, at higher energies the radiation is absorbed within few hundreds of nanometers inside materials as well as in air. For this reason the photon beam needs to be transported inside empty pipes (with a pressure below 10^{-9} mbar) and reflected/focused by means of grazing incidence mirrors taking advantage of the total external reflection phenomenon. The photon diagnostics are different too, as the detectors should work at higher photon energies and, most of the time, in vacuum conditions. At FERMI the Photon Analysis Delivery and Reduction System (PADReS) is devoted to the measurement of the FEL properties, mostly on-line and shot-to-shot, and to deliver and focus the photon beam to the experimental end-stations. This chapter is dedicated to the photon diagnostics; all the PADReS [1-3] diagnostic instrumentation is presented and explained in detail, while the next two chapters are devoted to the optical part and the focusing of VUV/Soft x-ray radiation.

2.1 PADReS photon diagnostic layout

The whole PADReS layout is reported in Figure 1. As explained extensively in the previous chapter, FERMI is endowed with two FEL sources composed of two parallel sets of undulators used alternatively according to the user's needs. Both these lines have a dedicated front-end, in the Undulator Hall (UH), where the photon beam can be blocked by shutters and beam stoppers, defined with the Beam Defining Apertures (BDA), measured in terms of intensity with the gas based Intensity monitors (I0M), characterized in terms of beam position with the Beam Position Monitors (BPM), attenuated by means of the Gas Absorber (GA) or solid state filters, and visually seen by YAG screens. Around 45 meter from the sources, the beams reach the first part of the experimental hall (EH) named safety hutch (SH). This is a restricted-access area (for radiation safety reasons) and the two FEL lines are merged by means of plane mirrors (PM1a for FEL1 and PM2a for FEL2) working at grazing incidence angles. Inside the hutch there is another set of I0 monitors and BPMs, YAG screens, solid state filters, and photodiodes. Downward the safety hutch a single vacuum pipe transports both FELs into the EH. The first element installed afterward is the photon energy spectrometer (PRESTO) where the spectral content is measured on-line and shot-to-shot, delivering almost the whole radiation to the beamlines. Around 70 meters downstream the sources the Auto-Correlator/Delay Creator (AC/DC) is placed; it allows to split and recombine the FEL beam introducing a time delay between the pulses in order to perform pump and probe experiments providing information about the pulse length. After AC/DC the beam is delivered to the end-stations by means of a dedicated set of plane mirrors, and finally focused by dedicated focusing mirrors. A system devoted to the measurement of the transverse coherence of the FEL beam, based on the diffraction by a set of double slits, is installed along the optical path. In table 1 the naming and distances between all the PADReS diagnostic elements and the FEL1-2 sources is presented. In the following sections all the elements composing PADReS will be described.

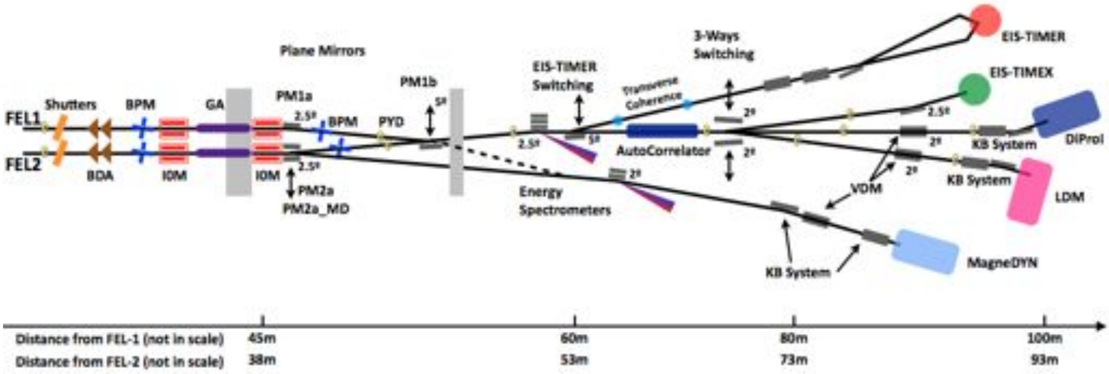

Figure 1 *Layout of the PADReS system and end-stations at FERMI. Left to right: shutters, beam defining apertures (BDA), beam position monitors (BPM), intensity monitors (I0M), gas absorber (GA), plane mirrors inside the safety hutch (PM1a, PM1b, PM2a, PM2aMD), Ce:YAG screens, Photodiode-YAG-Diagnostics (PYD). At the beginning of the experimental hall (EH) the photon energy spectrometer (PRESTO) and the Auto-Correlator Delay-Creator (AC/DC) are present, followed by the beamlines with their dedicated refocusing systems.*

Table 1 *Distances of PADReS elements from the sources (FEL1/FEL2): the elements are duplicated for the two FEL lines until the YAG$_{SH}$'s. From that point the transport system is shared by the two sources. The AC/DC is composed of eight mirrors, thus only the central point distance is reported.*

Element	d$_{FEL1}$ / m	d$_{FEL2}$ / m
YAG$_{UH}$	32.5	24.8
Shutter	33	25.3
Beam Defining Apertures (BDA)	33.4	25.7
Beam Position Monitor$_{UH}$ (BPM$_{UH}$)	33.8	26.1
Intensity Monitor$_{UH}$ (I0$_{UH}$)	35	27.3
Gas Attenuator (GA$_{Center}$)	41	33.3
Intensity Monitor$_{SH}$ (I0$_{SH}$)	46.6	38.9
Beam Position Monitor$_{SH}$ (BPM$_{SH}$)	50.6	43.5
YAG$_{SH}$	53.6	45.6
PRESTO	57.5	49.8
Auto-Correlator DelayCreator (AC/DC$_{Center}$)	71.2	63.6
YAG$_{EH}$	72.8	63.6
Double Slits$_{coherence}$	66.4	58.7
YAG$_{coherence}$	74.7	67

2.2 Beam Defining Apertures (BDA)

The BDAs are the first elements after the shutters and beam stoppers (whose duty is to simply block the photon beam when needed), and have two purposes: to define the acceptance angle of the incoming photon beam and to define the Gaussian mode getting rid of the off-axis radiation. While the former is needed to avoid diffraction at the edge of the mirrors (both transport and focusing mirrors), the latter is an experimental requirement for washing out spurious radiation with an unwanted spectral content (FEL harmonics), and to obtain a diffraction-limited spot inside the end-stations. Another application of the BDAs is to define preselected slices of the FEL beam as to sample and characterize the radiation properties in the transverse direction with the PADReS diagnostics (position vs. energy scan).

They are placed 32.5 meter and 24.8 meter (from FEL1-2) and are composed of a set of two copper trunks of pyramids (square base) with a maximal aperture of 20×20 mm^2 corresponding to an angular acceptance of 0.6 mrad for FEL1 and 0.8 mrad for FEL2 (see Figure 2). Each trunk can be moved up to 12.5 mm around the ideal axis, in order to accept the whole Gaussian mode or to give the possibility to explore off-axis emission structures.

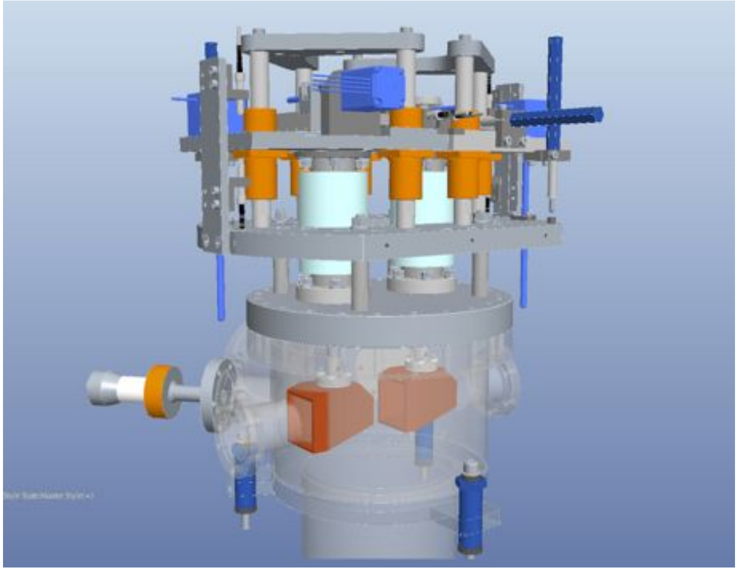

Figure 2 *Mechanical drawing of the beam defining apertures (BDA) setup. The two trunks of pyramid are clearly visible inside the vacuum chamber. Each of them is moved in the two directions perpendicular to the direction of propagation of the photon beam up to 12.5 mm. The maximum central aperture allowed by the system is 20×20* mm^2.

Due to the high fluence of the FEL light (up to 400 mJ/cm^2) the BDAs work at a grazing incidence condition: the walls of the pyramids have an angle of 30° with respect to the direction of propagation of the radiation, in order to avoid radiation damage effects. An example of the effect of the BDA to the FEL photon beam can be seen in Figure 3 where a Ce:YAG screen (see section 2.7) is used to convert the EUV radiation into visible light.

2.3 Beam Position Monitors (BPM)

Each BPM is composed of four blades, one for every direction, made of copper tilted by 20º to avoid radiation damage. The blades can be moved independently, in order to intercept the tails of the incoming photon beam and to collect the drain current generated by the photoelectric effect (see Figure 4). Each blade has a dedicated channel and the current is read with an in-house built picoammeter (named XPI). Since the FEL transverse distribution is a Gaussian, it is possible to calculate precisely the centroid by comparing the four readings.

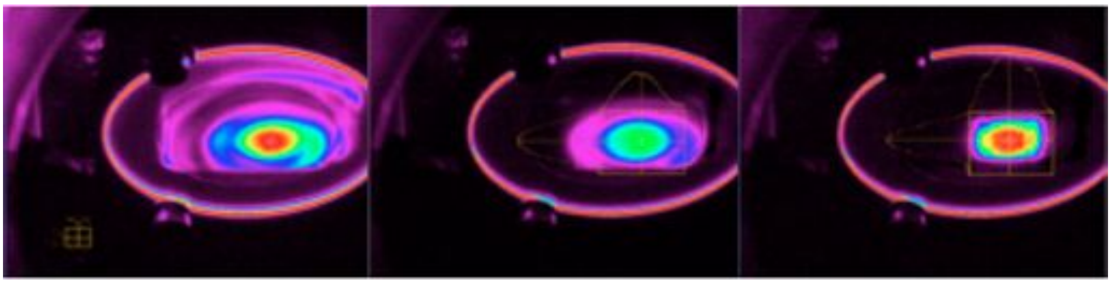

Figure 3 *Example of FEL spots as seen at the* YAG_{SH} *with various apertures of the BDA. Left, 20×20* mm^2 *gap corresponding to 750×750* μrad^2*: the full mode is delivered to the end-stations. Center, 9×8.5* mm^2 *gap corresponding to 340×320* μrad^2*: the transverse mode is well defined. Right, 5×4* mm^2 *gap corresponding to 190×150* μrad^2*: the FEL mode is limited to the central part of the Gaussian distribution.*

The spatial resolution of the detector is determined by the resolution of the XPI (10^{-6} for the picoammeter used at FERMI) and by the minimum mechanical step of the motors controlling the travel of the blades which is around 1 µm. Considering a displacement of the blades in the tails of the Gaussian distribution ($\geq 3\sigma$ from the center), the relative variation of the measured current for 1 µm movement is of the order of 3×10^{-6}, thus detectable by the XPI.

As explained in the introduction there are two BPMs for each source, separated about 17 m apart. With the contemporary reading of both detectors it is possible to determine the angular movement of the photon beam shot-to-shot with sub-µrad precision as well as the beam divergence.

2.4 Intensity Monitors (I0M)

There are several ways, invasive or not, for measuring the photon beam intensity, with various degrees of complexity and costs. At FERMI we have implemented two independent systems, one invasive (PYD, described in the next paragraph) and one non-invasive (I0M) able to characterize shot-to-shot the FEL intensity with high precision and reproducibility. Both systems have been extensively used during the machine commissioning, performing a cross check of the obtained data with different detectors, and during the experiments. Additional instruments, installed inside the experimental stations, are used once in a while to measure the intensity at the sample and estimate the beamline transmission at a given photon energy.

During the regular FEL operation the most used diagnostic are the gas based Intensity monitors (I0M). There are two of them for each source, one in the UH and the other in the SH, separated by the gas attenuator (GA), devoted to control the FEL intensity if needed. They are simple ion chambers (see Figure 5 left for a mechanical sketch)

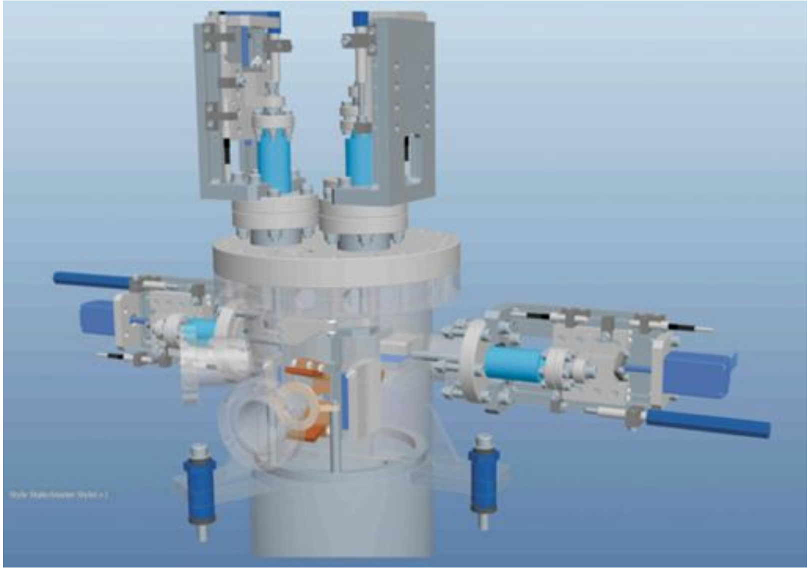

Figure 4 *Left: mechanical drawing of the BPM. The incoming beam enters the BPM vacuum chamber through the flange visible in the forefront. The tilted brown plates intercept the tails of the photon beam distribution in the four directions up, down, left, and right.*

based on the atomic photoionization of a rare gas (usually Nitrogen) at a low pressure (around 3×10^{-5} mbar), i.e., at a low particle density in order to minimize absorption of the FEL radiation. The I0Ms work in the whole FERMI energy range, are transparent, do not suffer from saturation effects and their reading is independent of the beam angular fluctuations. They have been calibrated during dedicated machine time with PYDs (previously calibrated at the BEAR beamline at Elettra synchrotron radiation facility [4, 5]), and cross checked with respect to a calibrated bolometer installed in the EH (ForTech HTS High Speed Thermal detector). The I0Ms provide the absolute number of photons per single pulse and a typical signal acquired is shown in Figure 5 right, where the FEL intensity at 21.6 nm can be seen in a time window of 5 minutes.

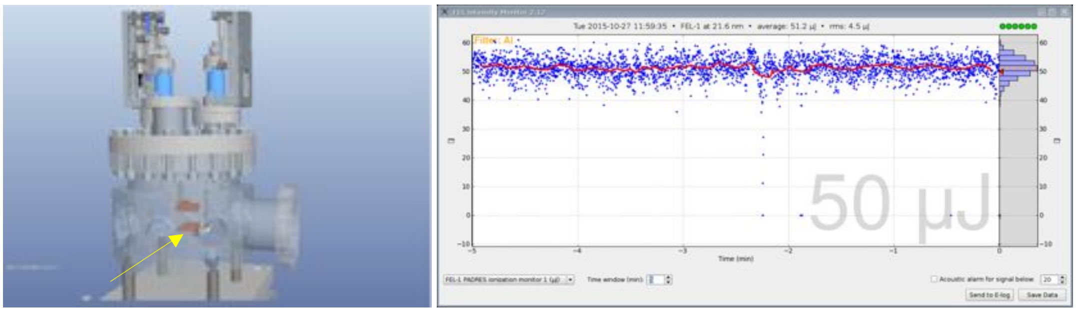

Tue 2015-10-27 11:59:35 • FEL-1 at 21.6 nm • average: 51.2 µJ • rms: 4.5 µJ

FEL-1 PADRES ionization monitor 1 (µJ)

Time window (min): 5

☐ Acoustic alarm for signal below 20

Figure 5 *Left: mechanical drawing of the I0M installed at FERMI. The arrow represents the incoming beam, and the two plates forming the ion chamber condenser are visible. Right: typical behavior of the intensity (µJ) versus time (5 minutes) as recorded by the intensity monitors through the control system at 21.6 nm of radiation wavelength (57.4 eV).*

2.5 Gas Attenuator (GA)

FERMI is able to generate extremely high brilliant pulses that can damage or even destroy the samples when focused. There are several reasons to control the FEL power delivered to the end-stations:

- Alignment and focusing purposes: the beam over the detector has to be visible but must be low enough not to damage or saturate the instrumentation/screens/sample

- Avoid radiation damage of the sample during the experiment: for some experiments the photon energy deposited (dose) over the sample has to be well below the ablation threshold in order not to compromise the specimen and consequently the experiment

- Perform scans as a function of the fluence: a wide class of experiments require to tune the FEL intensity in order to determine the behavior of the sample under study. In this case an active fine control of the photon beam intensity is required and cannot be performed by means of solid state filter with fixed attenuation.

- Filter the harmonic components: since the FEL process is based on the emission from undulator devices, the presence of harmonics is unavoidable. These photons have higher energies and might compromise the measurement (creating unwanted excitations or simply adding a spurious signal to the detectors).

- Sometimes there is the need to filter the fundamental harmonic and take advantage of some FEL harmonic component.

In order to accomplish these tasks two 5.5 m-long pipes named Gas Attenuators (GA), placed between the two I0Ms of each FEL line, can be filled up by a properly selected gas. Different gases might be used accordingly to the photon energy emitted by the machine and to the task to be accomplished. At the moment three gases are available to the users (Nitrogen, Helium, Neon) and the pressure inside the pipe can be dosed in the range 10^{-7} to 0.1 mbar. The system allows to achieve a reduction of the photon intensity up to 10^{-4} in the whole FERMI energy range. As an example of the achievable attenuations Figure 6 shows the transmission of Xe, N_2 and Kr at a pressure of 0.1 mbar as a function of the photon wavelength. By changing the gas it is possible to have full control of the attenuation over the fundamental harmonic as well as of the other harmonics.
In order to maintain an ultra high vacuum inside the pipes/chambers up/downstream the GA, two differentially-pumped sections are present [6].
While filling the GA, the reading of the second I0M (located downstream) drops as a consequence of the attenuation. The ratio between this signal and the one from the first I0M (unperturbed) gives the actual attenuation of the FEL photon beam. An example of the typical behavior of the ratio between the I0 monitors as a function of the pressure (Nitrogen) inside the GA at 32.5 nm of FEL wavelength is shown in Figure 7.

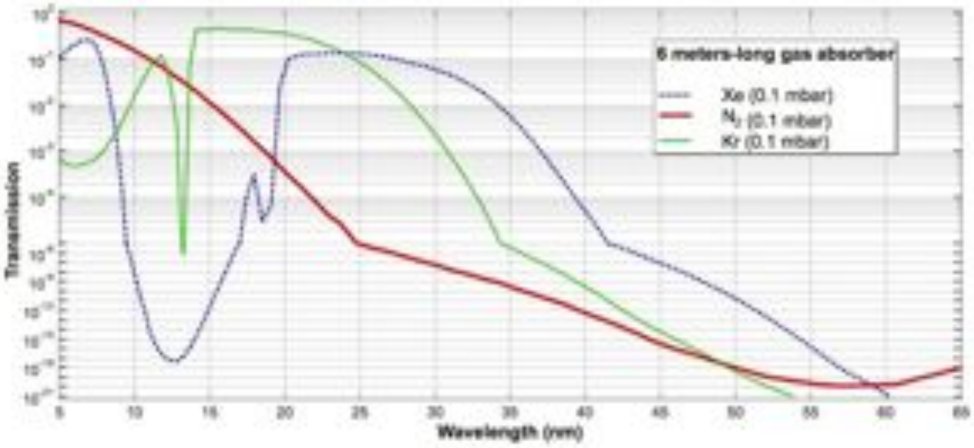

Figure 6 *Gas attenuator transmission filled with Nitrogen (red), Xenon (dotted blue) or Krypton (green) at 0.1 mbar as a function of the radiation wavelength.*

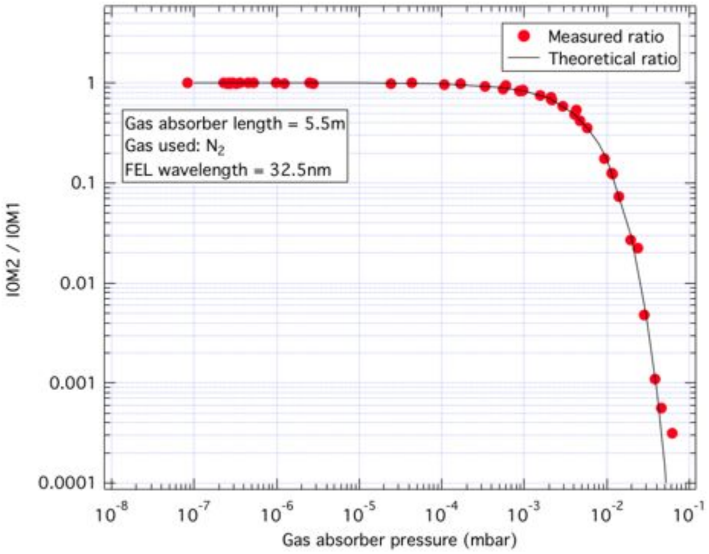

Figure 7 *Ratio of the photon beam intensities measured by the second and first I0 monitors as a function of the Nitrogen pressure inside the GA (in mbar). The data was acquired at 32.5 nm wavelength photon beam during a dedicated machine time. The theoretical values, as calculated by the CXRO toolset [7], are also reported.*

2.6 Solid State Filters

In addition to the GA several sets of solid state filters are employed along PADReS. Unlike the gas-based attenuator, where acting on the pressure inside the pipe allows to reduce the intensity continuously, the filters have a fixed attenuation factor given by the material composing the filter itself and the thickness. For FERMI we have employed several self-standing thin foils made of different materials and with different thicknesses (see table 2 for details) in order to cover as much as possible of the FERMI wavelength range for the following purposes:

- Removing the residual seed laser propagating with the FEL beam for both FELs

- Attenuate the FEL photon beam by a fixed attenuation factor
- Remove the first stage FEL emission of FEL2, which propagates together with the second one
- Remove the contamination of the unwanted harmonic content

The first set of filters is installed right before the PADReS shutter, inside the UH, for both FEL sources. The second set is inside the SH after the second BPM, and another set is present in the EH along the photon transport. In addition, the users have the possibility to install a dedicated filter inside the experimental end-station for a specific purpose. In the near future the PADReS attenuation system will be upgraded adding a set of ~50 more filters placed inside three different rotating revolver holders, in order to fulfill all the user needs. In Figure 8 right the transmission measured at the BEAR beamline (Elettra synchrotron) of the first set of Pd and Zr filters is shown.

Table 2 *List of solid state filters installed along the PADReS. Different materials (Aluminum, Zirconium, Palladium) with different thicknesses allow to attenuate the photon beam with different attenuation factors.*

Material	Thickness / nm	Location
Al Pd Zr	200 300 300	UH
Al Pd Zr	200 300 300	SH
Al	200/800	EH

2.7 Transverse Intensity Distribution

The determination of the transverse spatial distribution of the photon beam is crucial for proper optimization of the machine parameters. A misalignment of the orbit of the electron bunch inside the undulator chain causes the transverse mode of the FEL beam to have multiple spots, while a non-perfect resonant condition of the undulators causes the appearance of additional modes rather than the expected Gaussian TEM_{00}. The appearance of out-of-axis radiation and/or multiple peaks is the sign of a mis aligned machine, even though the emitted total intensity is as high as expected. In fact it has been observed that the intensity of the off-axis radiation can be non-negligible with respect to the central mode; the I0Ms collect all the radiation and do not discriminate which part of the beam is contributing. These misalignments not only affect the overall performance of the machine but also compromise the focusing properties of the mirrors at the end of the beamlines. For these reasons the transverse intensity distribution has to be observed and a set of Ce:YAG screens (25 mm-diameter, 0.5 mm-thickness, manufactured by Crytur) has been installed along the photon beam transport. They

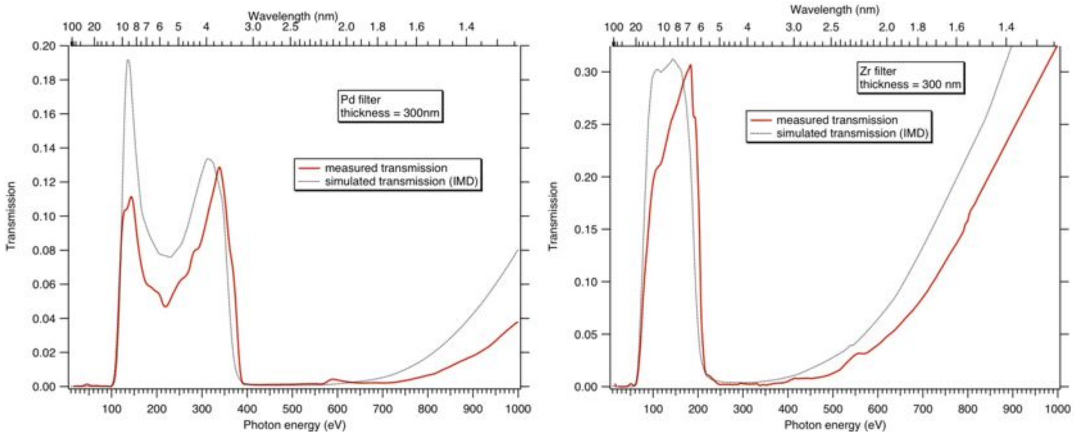

Figure 8 *Transmission of Palladium (left) and Zirconium (right) filters installed inside the UH. The red curves have been measured at the BEAR beamline (Elettra synchrotron) while the black curves are the simulated transmissions in the ideal case of a thin foil without contamination.*

convert the VUV/soft x-ray radiation into a visible signal, observed with a CCD camera, and can be inserted intercepting the FEL beam when needed. These screens are routinely used for alignment purposes and during the focusing stages inside the experimental end-stations by the PADReS team. An example of the evolution of the FEL transverse mode during the machine preparation as seen at the YAG screen in SH is shown in Figure 9.

The YAG screens have also been routinely used to measure the photon beam divergence. This can be done by looking at the spot dimension with two screens separated by a known distance and calculating the divergence from geometrical considerations. Of course this kind of measurement is invasive and is performed during the optimization phase of the machine only.

Another way to obtain a partial, but nonetheless useful, information about the transverse intensity distribution of the photon beam is the vertical projection of the spot recorded by the spectrometer PRESTO. The instrument and its features will be described in detail in the next chapter.

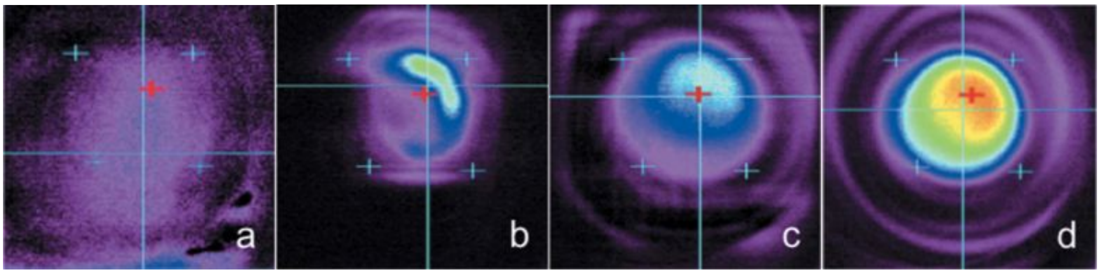

Figure 9 *Evolution of the optimization of the FEL emission process, as monitored on a YAG screen placed along PADReS (Ce:YAG in SH, around 54 m from the FEL1 source). The mode quality is clearly increasing from left to right, following a proper tuning of the machine.*

2.8 Photodiode-YAG-Detector (PYD)

Even though the purpose of the PADReS instrumentation is to work on-line, sometimes there is the need to calibrate or cross-check the instrumentation. For this reason a set of

Photodiode-YAG-Detectors (PYD) has been installed to measure the FEL intensity (invasively). The system has been built in-house and has been calibrated at the BEAR beamline (Elettra synchrotron) during a dedicated beamtime. The working principle of the PYD is shown in Figure 10-left: the FEL photon beam impinging on the YAG screen (one inch diameter) is converted into visible light (mostly green – 520 nm) and its intensity is measured with the absolutely calibrated photodiode SXUV100 from Opto Diode Corp. For the FEL1 branch the YAG screen has an Aluminum coating on top, in order to filter the residual seed laser, which might affect the intensity measurement. In Figure 10-right a picture of the PYD mounted on its holder is shown.

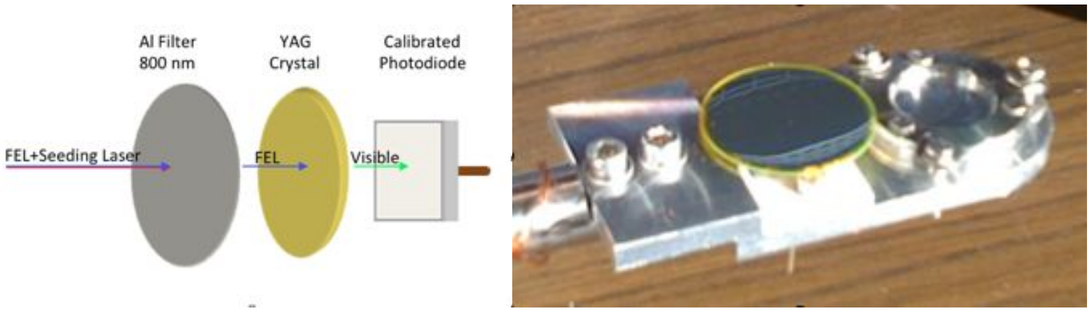

Figure 10 *Left: the working principle of the PYD. The FEL beam is filtered by an aluminum filter deposited on the YAG crystal which converts the high energy photons into visible light. The photodiode collects and measures the light and provides the absolute intensity of the incoming FEL radiation. Right: picture of the PYD installed in the holder before the installation.*

2.9 Transverse Coherence

As explained in the first chapter, the FEL emission of FERMI is based on the HGHG scheme, in which the seed laser imprints its properties onto the electron beam. Along with all the other useful properties (such as the short pulse duration, the narrow bandwidth, and the longitudinal coherence) the seed laser is expected to transfer to the FEL photon beam a high degree of transverse coherence, too. While the longitudinal coherence is important for many experiments (such as the generation of the transient grating), the transverse coherence is essential for diffraction experiments and, more in general, for imaging.

Along PADReS there is a system devoted to the measurement of the degree of transverse coherence of the FEL beam based on the Young double slits setup [8]. It is composed of a set of horizontal/vertical double slits (with different separations, from 0.8 mm up to 4 mm, and widths, from 20 µm up to 50 µm) and a YAG screen. The slits have been realized with laser-cut technique on a copper foil that is placed 64 m downstream the FEL1 last radiator exit, while the YAG is placed 8.5 m downstream the slits (Figure 11-top show a sketch of the setup).

It is of course evident that such a setup (measuring the coherence properties of the photon beam) cannot be operated online as it is invasive and, moreover, it requires long times both for the alignment and the acquisition. Nevertheless, various campaigns of measurement of the transverse coherence have been carried out at FERMI and the results have shown that the coherence factor is about 90% at 0.3σ of the Gaussian beam, and about 50% at 0.9σ, meaning that the degree of transverse coherence is very high (see Figure 11-bottom for a typical diffraction pattern recorded by the CCD camera).

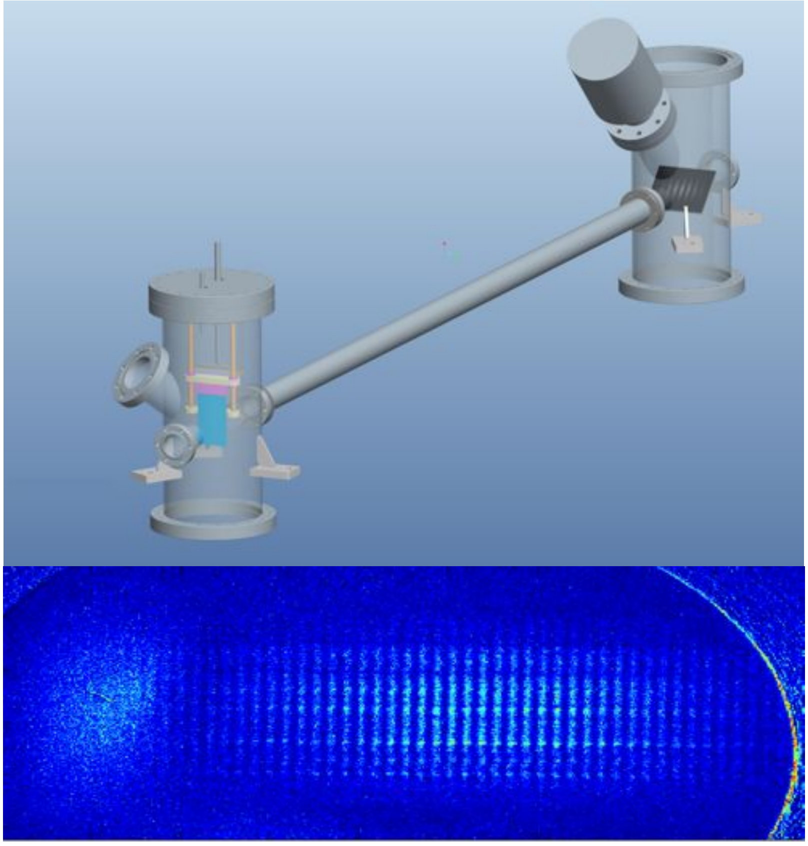

Figure 11 *Top: sketch of the transverse coherence setup. It is composed of a movable set of double slits with various separations and widths and a YAG screen coupled with a visible CCD camera. Bottom: a typical diffraction pattern of the FEL photon beam diffracted by the slits as recorded by the CCD. The measurement of the intensity of maximum and minimum areas gives the degree of coherence of the radiation.*

References

[1] M. Zangrando, et al., "The photon analysis, delivery, and reduction system at the FERMI@Elettra free electron laser user facility" (2009) Review of Scientific Instruments, 80 (11), art. no. 113110

[2] D. Cocco, et al., "The FERMI@Elettra FEL photon transport system", (2009) Proceedings of SPIE - The International Society for Optical Engineering, 7361, art. no. 736106

[3] M. Zangrando, et al., "First results from the commissioning of the FERMI@Elettra free electron laser by means of the Photon Analysis Delivery and Reduction System (PADReS)",(2011) Proceedings of SPIE - The International Society for Optical Engineering, 8078, art. no. 80780I

[4] S. Nannarone et. al., "The BEAR Beamline at Elettra", AIP Conference Proceedings, Vol. 705 - 1, pp. 450-453 (2004)

[5] https://www.elettra.trieste.it/it/lightsources/elettra/elettra-beamlines/bear/bear.html

[6] L. Rumiz, et al., "The gas attenuator vacuum system of FERMI@Elettra", Proceedings IPAC, vol. 2011, 1530 (2011)

[7] http://henke.lbl.gov/optical_constants/

[8] J.W. Goodman, Statistical Optics (Wiley-Interscience, New York, 1985)

3 PADReS: Photon transport

After the FEL emission process the radiation propagates freely with its natural divergence. The beam has to be transported and focused to the sample inside the end stations in order to perform the experiments. This is the other duty of PADReS: to deliver and focus the beam to the users. The FERMI Free Electron Laser emits in the VUV/Soft x-ray range (1.3 nm – 100 nm, or equally 12.5 eV – 955 eV) and the photon energy is too high to allow the use of standard optics, such as lenses and crystals, as for visible lasers. At energies above 6 eV the absorption coefficient of optical materials is such that the radiation is totally absorbed. As a consequence two important differences are present compared to the other energy regimes: the need for vacuum conditions and the use of alternative optical elements. Between 6 eV and 1000 eV even the air is opaque and the radiation has to be transported inside empty pipes and vacuum chambers hosting the mirrors/instrumentation. The standard pressure kept along the PADReS is usually between 10^{-9} and 10^{-10} mbar. These very low pressure condition, named Ultra High Vacuum (UHV), can be produced by using different pumping techniques depending on the initial pressure within the pipe/chamber. Starting with the pipe/chamber in air (previously mounted and isolated from the outside) the pressure is lowered down to 10^{-7}-10^{-8} mbar by turbo pumps and then ion pumps are employed to reduce the pressure down to 10^{-10}-10^{-11} mbar.

For the same reason (absorption in the medium) lenses and prisms cannot be used and have to be replaced by mirrors and diffraction gratings working at a grazing incidence configuration. When a high energy photon beam impinges on the surface of a mirror at a grazing incidence the principle of total external reflection applies and the radiation is only partially absorbed. The reflectivity is of course a function of the photon energy, the incident angle and the mirror material. In the VUV/Soft X-ray range the photon energy is high enough to require working at grazing incident angles well below 10 °s, and the mirrors need to have a coating on top of the surface, in order to enhance the reflectivity (usually Au, C, Ni are employed). If higher incident angles are required then a multilayer coating have to be used.

In the first section of the chapter a brief description of the key points of the beamline design will be given with particular attention to the preservation of the FEL radiation properties. In the second section the PADReS transport system will be explained in detail in all its components.

3.1 Beamline Design

The design of the photon beam transport system is the major task to be accomplished to fulfill the requests of FEL users, in order to perform the experiments at the end-stations. The principal function of the mirror system is to transport and focus the FEL radiation to the experimental end-stations without perturbations. Many aspects have to be taken into account such as the beam divergence, the position stability, the wave front preservation, the transverse coherence, the pulse length preservation, the energy resolution, the beam splitting, the focusing in the experimental chambers as well as the fact that multiple sources might be present, as for FERMI. In addition different scientific cases of the experimental end-stations have to be fulfilled, too. During the design phase many aspects of the VUV/Soft x-ray optics have to be taken into account in order to optimize the overall performance, of course considering the unavoidable constraints. In the following, the most relevant aspects of the beamline design will be explained in detail.

3.1.1 Reflectivity and polarization of VUV/Soft x-ray Optics

The reflectivity of a mirror can be calculated [1] starting from the generalized Fresnel equations for reflection. They are a function of the complex index of refraction $\tilde{n}$ and the angle of incidence (respect to the surface normal) α:

$$R_s = \frac{(a-\cos\alpha)^2 + b^2}{(a+\cos\alpha)^2 + b^2}$$

$$R_p = R_s \frac{(a-\sin\alpha\tan\alpha)^2 + b^2}{(a+\sin\alpha\tan\alpha)^2 + b^2}$$

where R_s is the reflectivity of the component whose E vector (electric field) is perpendicular to the plane of incidence, and R_p refers to the reflectivity of the E vector parallel to the plane of incidence, with a and b are defined as follow:

$$a^2 = \frac{1}{2}\left[\sqrt{(n^2 - k^2 - \sin^2\alpha)^2 + 4n^2k^2} + (n^2 - k^2 - \sin^2\alpha)\right]$$

$$b^2 = \frac{1}{2}\left[\sqrt{(n^2 - k^2 - \sin^2\alpha)^2 + 4n^2k^2} - (n^2 - k^2 - \sin^2\alpha)\right].$$

Here n and k are the real and imaginary part of the complex index of refraction of the material at a fixed photon energy (E) defined as:

$$\tilde{n}(E) = n(E) + ik(E)$$

For photon energies between 30 eV and 10 keV, the optical constants for most of the materials can generally be calculated from the atomic scattering factors or can be actually retrieved by measuring the reflectivity and the phase shift of *s* and *p* waves. Generally the results between theory and experimental results are in agreement but for some special cases where the coating method influences the overall reflectivity which is not our case. As an example the theoretical optical constants of the most common material used as a coating (Gold, Carbon, Nickel, Platinum and Iridium) as a function of the photon energy are shown in Figure 1.

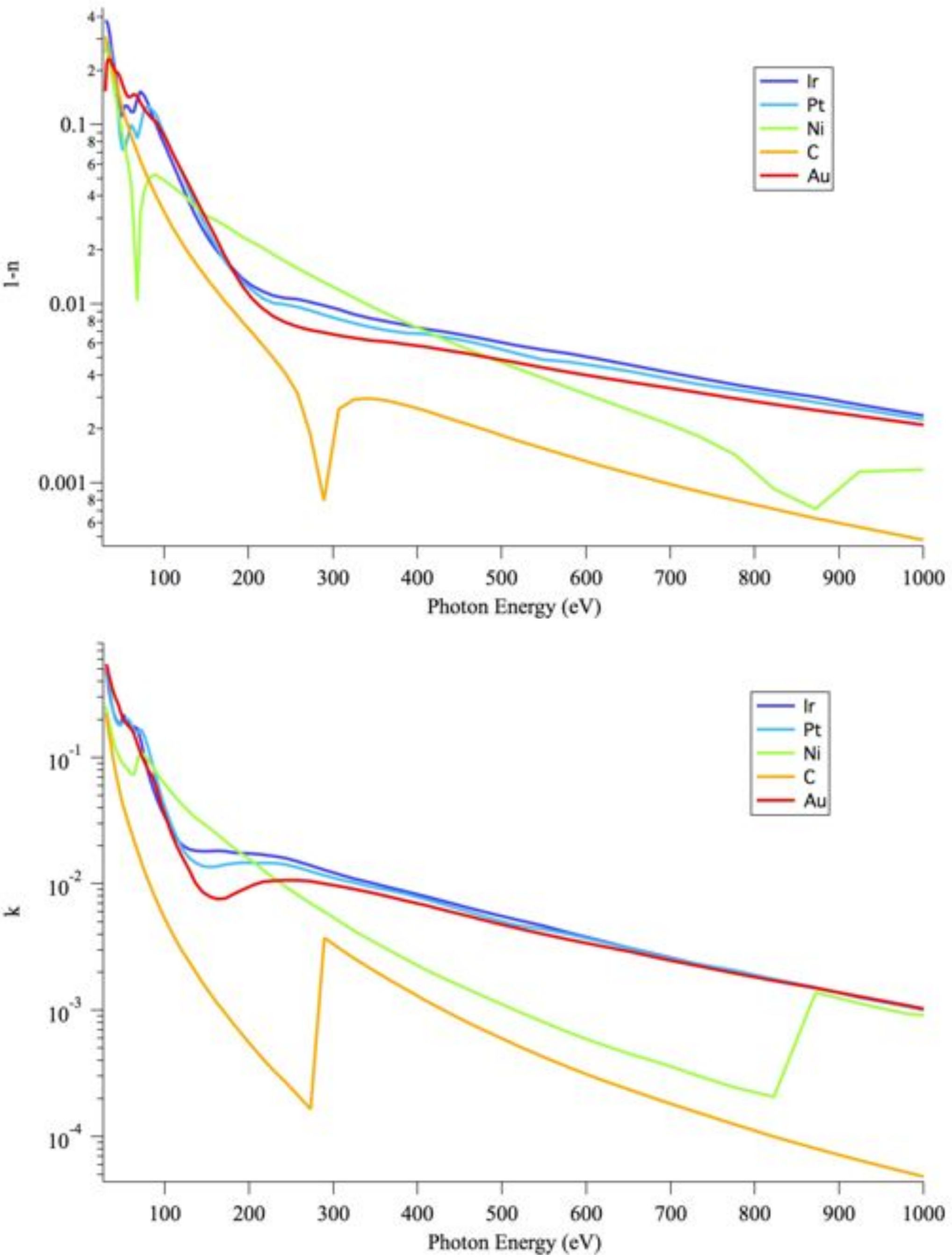

Figure 1 *Optical constants (top: real part, 1-n; bottom: imaginary part, k) as a function of the photon energy (30 eV – 1000 eV) for the most commonly used coating materials of VUV/Soft x-ray mirrors: Gold (red), Carbon (orange), Nickel (green), Platinum (azure) and Iridium (Purple) (data taken from [2]).*

From the above equations it is clear that, given the photon energy range and the material of the coating, the reflectivity is a function of the incident angle only. The more grazing the incident angle, the higher the mirror reflectivity, both for *s* and *p* components of the electric field. As an example Figure 2 shows the calculated reflectivity for a mirror with a Gold coating (30 nm thick) at various incident angles as a function of the photon energy [2]. From the Figure it can be seen that the R_s and R_p components, for grazing angles of incidence, are almost the same at high energies (above 100 eV). Near the Brewster angle (function of the index of refraction) the difference between the two components of the electric field become not negligible at low photon energies. This causes a variation in the polarization of the reflected radiation. In fact, the degree of linear polarization P is defined as:

$$P = \frac{I_s - I_p}{I_s + I_p}$$

where I_s and I_p are the intensity of the s and p components respectively. In the case of an FEL source employing APPLE-II type undulators, such as FERMI, the radiation can be emitted in linear vertical/horizontal ($P=\pm1$), circular left/right ($P=0$) and elliptical ($0<P<1$) as well. After the reflection the circular polarized radiation will be slightly elliptical so during the design phase of a beamline not only the overall transmission of the mirrors but also the change in polarization have to be taken into account.

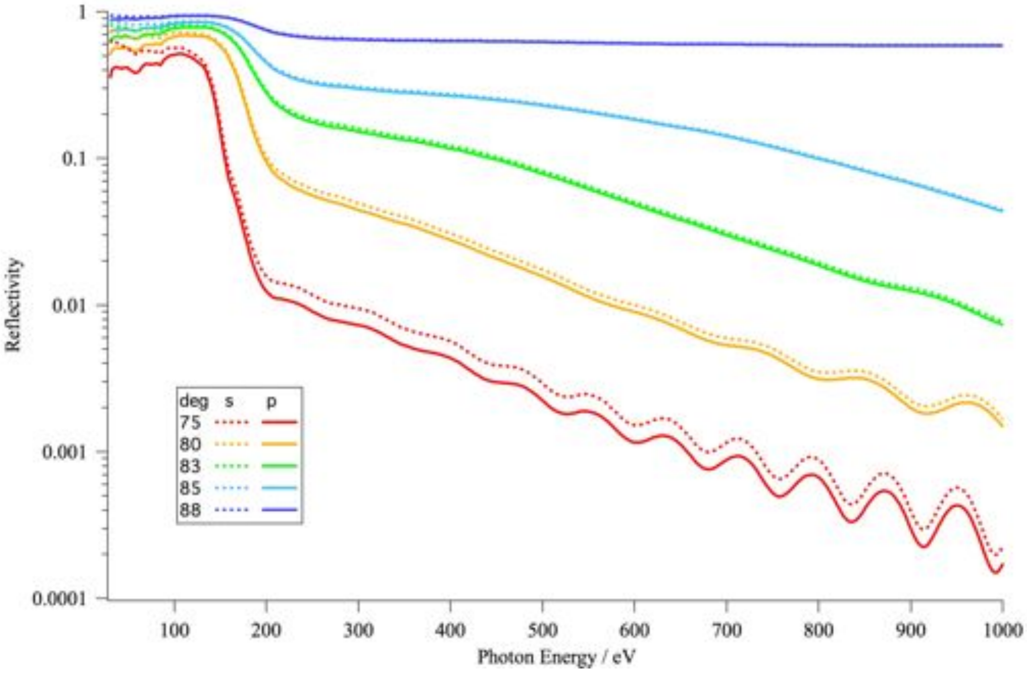

Figure 2 *Calculated reflectivity for a Gold coated mirror at various incident angles (represented with different colors) as a function of the photon energy. The dotted lines correspond to the reflectivity of the s component while the continuous line corresponds to the p component of the electric field.*

A variation Δ in the phase between the s and p components after the reflection is expected, and it can be calculated with the following formula:

$$\tan\Delta = \frac{-2b\sin\alpha\tan\alpha}{a^2 + b^2 - \sin^2\alpha\tan^2\alpha}.$$

A special case of coating is the multilayer interference coating, often called multi-layered mirror, which is composed of alternative layers of two materials with different refractive indexes. The materials have a low and high atomic number in order to maximize the difference in the electron density creating a constructive interference of the reflected radiation.

The reflection follows the Bragg's law for a periodicity d equal to the thickness of one bilayer pair:

$$m\lambda = 2d\sin\alpha.$$

Multi-layers allow achieving high reflectivity also out of the standard grazing incidence configuration, but for a very narrow bandwidth in the VUV/Soft x-ray energies, meaning that many of them should be employed in order to cover a wide energy range. Multi-layered mirrors have been successfully used for many systems such as synchrotron-FEL beamlines, delay-lines, microscopes and telescopes.

3.1.2 Mirror dimension

Ideally, mirrors and diffraction gratings should be big enough to accept the whole incoming photon beam. The portion of optical surface illuminated by the radiation is called FootPrint (FP), and its dimension (both tangentially and sagittaly) should be smaller than the mirror active optical surface in order not to cut part of the photon beam. In the case of a mirror placed at a distance r with respect to the source and working at a grazing incident angle α_{graz} (α_{graz}=90-α), the geometrical relation between the FP in the tangential direction and the incoming beam with rms divergence σ' (valid for $\alpha_{graz} >> \sigma'$) is the following:

$$FP = \frac{2r\sin\sigma'}{\sin\alpha_{graz}}.$$

For FERMI the relation between the divergence (in µrad) and the wavelength (in nm) is the following:

$$\sigma'_{\mu rad} = c\lambda_{nm},$$

where c equals 1.25 for FEL1 and 1.5 for FEL2. These values depend on the M^2 of the Gaussian beam as explained in chapter 1. Of course the spot size along the optical path depends linearly on the propagation distance of the radiation r. In the sagittal direction the FP is simply the spot size, since no projection occurs. From the FP formula it can be seen that the more grazing the incident angle, the bigger will be the FP and the longer should be the mirror. On the other hand, as seen in the previous section, optics should work at very grazing incidence angles, in order to have a very high reflectivity, but at the cost of having very long mirrors.

As an example we consider a 32.5 nm radiation linearly polarized, emitted by FEL1 source over a Gold coated mirror placed 50 m downstream of the source. In this case the divergence is expected to be 40.6 µrad meaning that the spot size before the mirror is about 2 mm sigma (or 4.7 mm FWHM). If the mirror works at 5° of grazing incidence the FP is 22.9 mm sigma with a theoretical reflectivity of about 85%. If we decrease the incident angle down to 2° the reflectivity would rise to 94% but the FP would become

58 mm sigma. If we keep decreasing the angle down to 1° the reflectivity would rise up to 97% with a FP of about 115 mm.

In the first case the whole beam (6 sigma) requires a mirror 140 mm long, the second case needs a 350 mm long mirror while in the last case the optics should be at least 690 mm long. The choice of the mirror dimension and its working angle is thus essential in order to keep the beamline transmission high, i.e., having high reflectivity without losing too many photons due to the geometrical losses (radiation lost due to the finite size of the mirrors).

Even if it seems that choosing very long mirrors is the solution, there are several problems to deal with:

- Required space inside the vacuum chamber
- Mirror quality
- Costs

The longer the mirror the bigger has to be the vacuum chamber. This leads to additional problems such as less free space in the experimental hall, bigger mechanical holders, more powerful vacuum pumping system, and of course higher costs. The mirror quality is another important issue. Manufacturers can produce extremely high-quality optical surfaces (both flat and curved) for mirrors up to a length of 500 mm. For larger dimensions the manufacturing tools used during the production generally cannot be as precise as for smaller dimensions, and the optical quality might not be guaranteed. The cost of the optics is another important point since a beamline requires several mirrors and, as explained before, the longer the mirror the harder is to produce it and, of course, the higher is the price. On the other hand short mirrors do not accept enough photons, and their edges can partly diffract the photon beam, with consequent possible degradation of the focal spot inside the vacuum chambers. Finally, the overall transport system results to be very sensitive to the positional jitter of the beam.

Generally the mirrors/gratings employed at FERMI have an active area between 20 mm and 40 mm wide, and 250 mm to 500 mm long. With these dimensions the high-energy radiation is accepted entirely by the mirrors, while a small fraction is lost at lower energies (i.e., long wavelengths with higher divergence).

3.1.3 Beamline transmission

The total transmission of a beamline at a given photon energy is the product of the reflectivity of all the employed mirrors multiplied by the overall geometrical acceptance. For this reason the number of optical elements has to be as small as possible and the working angles and mirror lengths chosen properly. Considering a set of 4 Gold coated mirrors all working at the same grazing incident angle, assuming 5°, 2°, and 1° of grazing incidence, the expected transmission of the beamline would be around 61%, 83% and 91% respectively (without geometrical losses). In the first case the mirrors would be smaller but at the cost of 30% less intensity at the sample compared to the 1° option.

3.1.4 Heatload, radiation damage and surface contamination

Mirrors and gratings are continuously irradiated with high-energy photons. This might lead to several undesired side effects such as: heatload, damage, and surface contamination. When the radiation impinges on the optics, a part of its power is absorbed by the substrate. If the time-averaged power is high enough the mirror might suffer from heatload with consequent deformation of its figure due to the expansion in the irradiated area. In this case the mirror will end up having a thermal bump with consequent degradation of the beam properties after the reflection. This can compromise the experiments that require very good focusing and high fluence at the sample.
At synchrotrons this effect is mostly present on the first mirror of a beamline, located right after the front-end, where the beam size is small and the mirror is close to the source. In these cases the optics are equipped with a cooling system able to keep the temperature of the substrate stable, avoiding the thermal bump. The time-averaged power at a FEL source is quite modest and at FERMI this effect is negligible (well below 1 W [3]) since the first mirrors are placed about 45 m downstream of the source and the beam dimension is large enough, heatload effects should not be an issue.

One of the main problems related with the very high peak brilliance is the power of a single FEL pulse in a very short temporal interval. The power hitting the optics can be very high and the absorbed energy can take many materials over their melting temperatures. Above these temperatures the radiation damage occurs with consequent ablation of the coating. For this reason the mirrors/gratings must be operated below their damage thresholds that can be calculated knowing the photon energy, the optical constants and the specific heat values of the material. Starting from the penetration depth ($d_{1/e}$) of the evanescent wave, which is tabulated and can be calculated from theory, the absorbed dose per atom (D_{atom}) at the mirror surface is give by:

$$D_{atom} = \frac{(1-R)P_d \sin\alpha_{graz}}{d_{1/e}\rho_{atom}},$$

with P_d the peak normal incidence power density, ($1-R$) the transmission to the mirrors, ρ_{atom} the number of atoms per unit volume, and α_{graz} the grazing angle of incidence. In order to stay well below the ablation threshold the coating material has to be chosen properly as well as the mirror position and incidence angle. To give an example, amorphous-Carbon (a-C) irradiated by a 25 fs FEL pulse at 32.5 nm wavelength has an ablation threshold of around 60 mJ cm^{-2} [4].
If the heatload gives rise to a thermal bump, the radiation damage is a permanent modification of the mirror's surface and, of course, must be avoided.
As for other facilities, the PADReS first mirrors are the ones that receive the higher dose being closer to the source. Nevertheless, the incident angles are such that the absorbed dose is well below (1/10) the ablation threshold.

Finally, if the vacuum is not as high as needed and/or some residual gas is present inside the pipes/chambers, the mirror's surface will be contaminated. When the radiation impinges on the mirror surrounded by residual gas, a series of carbon layers will form on top of the coating. As a consequence a general drop of reflectivity might occur and, at the carbon absorption edges, the reflectivity might drop dramatically. Several cleaning procedures have been developed during the last 30 years spanning from UV lamps to Oxygen plasma cleaning. After several years of operation at FERMI no relevant carbon contamination of the mirrors has been detected by visual inspection nor by any change of beamline transmission around the carbon absorption edges.

3.1.5 Residual errors on the mirror surface

Ideally the mirrors should have a perfect shape such as plane mirrors for transport and concave mirrors (spherical, toroidal, ellipsoidal, elliptical) for focusing. In reality, manufacturers can produce very high quality mirrors that nonetheless present some residual structures on the surface, with different spatial frequencies that cannot be removed. The presence of these irregularities has multiple effects depending on their specific spatial frequency and the working angle of the mirror, and the photon energy as well. The most commonly used statistical parameter that gives information about the surface quality is the rms value σ defined as:

$$\sigma^2 = \frac{1}{L}\int_0^L \left[z(x) - z_0\right]^2 dx\,,$$

where L is the length of the mirror, $z(x)$ is the tangential section profile, and x the tangential local coordinate (Figure 3). This quantity, applied to different spatial lengths, gives some useful information about the mirror quality.
Historically two classes of spatial frequencies have been considered, based on their characteristic scale, with very different effects on the reflected photon beam. These are:

- Short frequencies: generally called slope errors, they have a spatial range between the length of the mirror down to the millimeter scale. If they are too high these structures cause the reflected beam to have a distorted wave front and the focused spot to be aberrated. These frequencies can be measured with a profilometer (such as a Long Trace Profiler, LTP [5,6]) with very high accuracy. The effect of the slope errors can be predicted by using a geometrical approach such as ray tracing simulations. For standard VUV/Soft x-ray mirrors the amplitude of these frequencies is below 2 µrad rms (Figure 3)

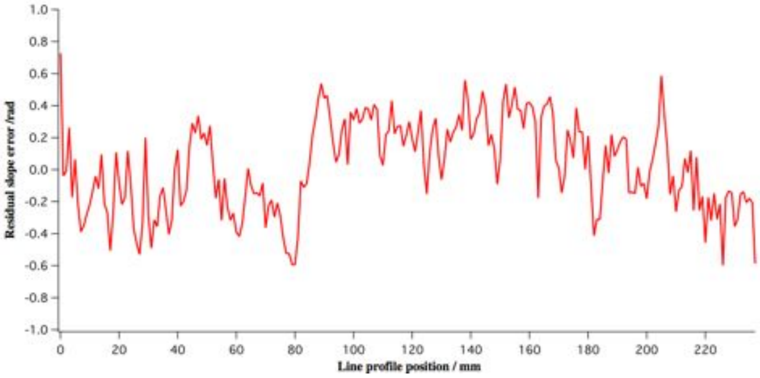

Figure 3 *Example of residual profile of a typical mirror installed at FERMI measured with the Long Trace Profiler (LTP) at the Elettra metrology laboratory.*

- High frequencies: also known as micro-roughness, they have a spatial scale below the millimeter and cause a drop in reflectivity and a blurring in the outcoming spot. This is because the radiation is randomly scattered by the surface. The mirror is considered to be smooth when the surface condition is fulfilled:

$$\lambda > 2\pi\sigma\sin\alpha .$$

The previous equation explains why a mirror with a certain rms surface micro-roughness (σ) works well at some wavelengths (λ) and/or incident angles (α) only. The shorter the radiation wavelengths (i.e., the higher the photon energy) the smaller the micro-roughness has to be in order to avoid scattering. The drop in reflectivity can be predicted by the Debye-Waller formula:

$$R_\sigma = R_0 e^{-\left(\frac{4\pi}{\lambda}\sigma\sin\alpha_{graz}\right)^2},$$

where R_0 is the reflectivity in the case of a perfectly smooth mirror. As for the previous formula, the reflectivity depends strongly on the rms surface micro-roughness or, for a given mirror, on the wavelength and the working incident angle. The micro-roughness can be measured by means of white light interferometer, possibly in combination with the Atomic Force Microscope (AFM).

Generally the mirrors employed at FERMI have a σ below 3 Å, and the drop in reflectivity due to the presence of the micro-roughness is negligible (below 0.01% at 32.5 nm with 2° of grazing incidence). Figure 4 shows results of measurements done with an AFM and a white light interferometer over a plane gold-coated mirror installed at FERMI.

The previous cases are just a guideline to surface quality, and do not necessarily take into account the actual performance of the optics. In reality there is not a clear boundary between these two classes of surface errors, and the intermediate range (called mid-frequencies) have as well important effects on the reflected beam such as diffraction. These mid-frequencies cannot be treated with simple geometrical considerations, as for the short ones, nor an analytical estimation such as for the micro-roughness. For this reason a full description of the surface quality has to be considered in order to predict accurately how well the mirror will perform under certain conditions of angle of incidence and photon energy.

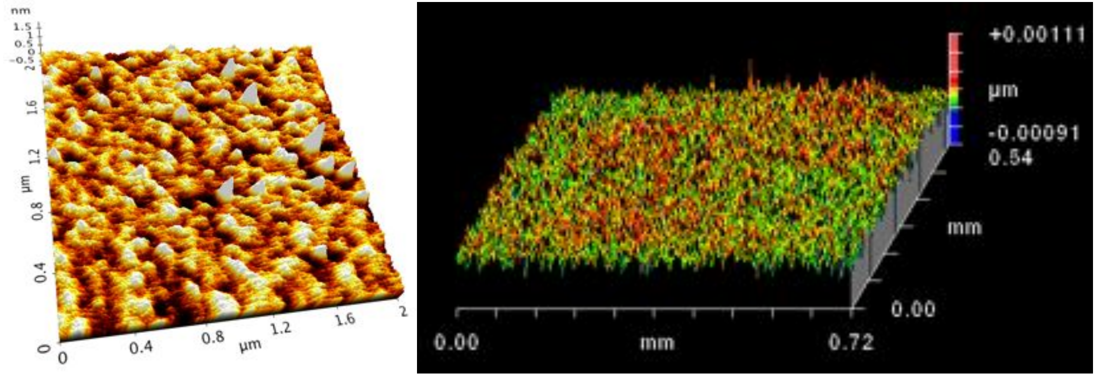

Figure 4 *Example of micro-roughness measurement with the AFM (left) and the white light interferometer (right) over a gold coated mirror. The field of view of the AFM is 2 µm while the interferometer goes up to 720 µm but at the cost of spatial resolution.*

The quantity that better represent the statistical weight of the residual frequencies over the surface is the Power Spectral Density (PSD), which is defined as the square of the Fourier transform of the surface profile per spatial frequency:

$$PSD(f) = \frac{1}{L}\left|\int_0^L z(x)e^{-ikx}dx\right|^2 .$$

Generally, the global PSD is a collection of the PSD obtained by the measurements done at different spatial scales. At low frequencies (slope errors) the PSD is obtained by averaging several profiles along the whole mirror while, at higher frequencies (micro-roughness), an ensemble average of PSD measured in different positions along the mirror is needed.

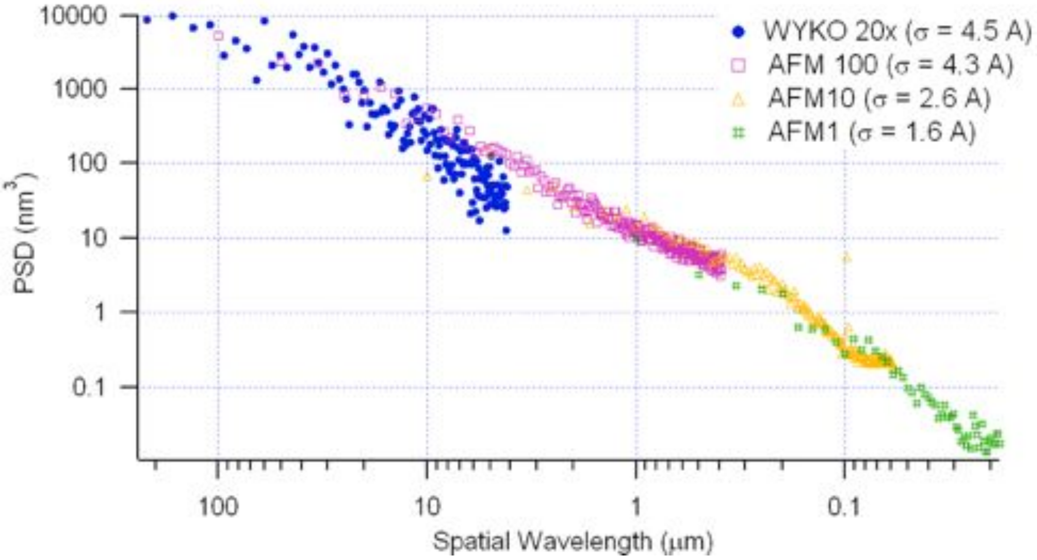

Figure 5 *Example of typical high frequency PSD of a VUV/Soft x-ray mirror. The spatial frequencies span from 200 μm down to 50 nm. It is a collection of several averaged PSD obtained with white light interferometers and Atomic Force Microscope.*

The global PSD is generally fitted with a power-law function of the form:

$$PSD(f) = \frac{K_n}{F^n},$$

being n an integer number, K_n the coefficients and F is the spatial frequency. An example of calculated PSD obtained from a collection of measurements done at different spatial scales is shown in Figure 5.

3.1.6 Wave-front preservation

After the reflection from a real mirror, the photon beam wave-front may to be altered. From a geometrical consideration it can be easily seen that when a flat wave-front is reflected by a surface that presents a step shape (of height *h*), the reflected beam results to have a degraded wave front. Analytically the Peak-to-Valley (*PtV*) distortion of the wave front impinging at an incident angle α can be estimated with the formula:

$$P_tV = h\frac{1-\cos 2\alpha}{\sin\alpha}.$$

A more complete description of the wave-front quality is given by the Strehl Ratio (SR) defined as the ratio of the intensity with and without wave-front distortion. It is related in a simple way to the rms wave-front distortion ω:

$$SR \approx e^{-(2\pi\omega)^2}.$$

The Maréchal Criterion states that for good optical systems the SR should exceed 0.8. The wave-front distortion ω is related to path length errors due to the residual surface errors by the formula

$$\sigma_{rms} = \frac{2\alpha_{graz} h_{rms}}{\lambda},$$

where h_{rms} is the rms surface height error, α_{graz} the grazing angle of incidence, and λ the wavelength of the radiation.

Even though the surface optical quality of a single mirror might be good, the beamline is generally composed of several mirrors, and the emerging beam might suffer from a wave-front degradation after multiple reflections. During the design phase it is important to consider the total number of optical elements that will be employed, and to define the tolerances on the surface quality accordingly. In the case of an optical system composed of *N* mirrors, the requirement for the surface height errors of the mirrors in order to fulfill the Maréchal Criterion is:

$$h_{rms} < \frac{\lambda}{14\sqrt{N}2\alpha_{graz}}.$$

As an example if we consider a beamline with five mirrors all working at 2° of grazing incidence, the Maréchal Criterion is satisfied if the rms surface height errors are below 0.45λ (i.e., h_{rms}<4.5 nm for a 10 nm radiation!).

3.2 Photon transport at FERMI

PADReS employs a vast set of plane mirrors devoted to transport the photon beam from the sources to the end-stations (see layout in Figure 6). After every reflection the beam changes the pointing, and the collection of these segments is usually called “beamline” that ends into the experimental station. After the Undulator Hall (UH) the photon beam propagates inside the Safety Hutch (SH) where a first set of plane mirrors is present. The first mirror of the source FEL1, named PM1a (Figure 7), is placed about 48.1 meter downstream of the last undulator while the first mirror of the FEL2 line, called PM2a, is about 41.4 meter downstream. Both mirrors work at 2.5° of grazing incidence and their purpose is to deflect the beams and merge the optical paths inside a vacuum chamber placed 6.2 meter downstream (respect to PM1a), at the end of the SH. This chamber hosts a third mirror, named PM1b, which works at 5° of grazing incidence and is inserted in the optical path when FEL1 source is operative, while it is completely removed when FEL2 is used.

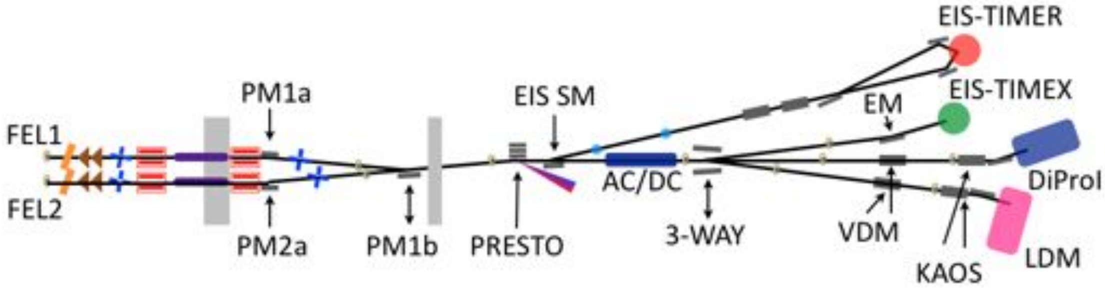

Figure 6 *Layout of the PADReS photon beam transport. From left to right: the first plane mirrors (PM1a, PM2a) deflect the two FEL lines into the PM1b vacuum chamber where the optical paths merge. After the radiation shielding wall the beam propagates through the PRESTO where the spectral content is measured on-line. Then the beam is delivered to the focusing mirror just before the experimental end-stations where the radiation is focused onto the sample under investigation.*

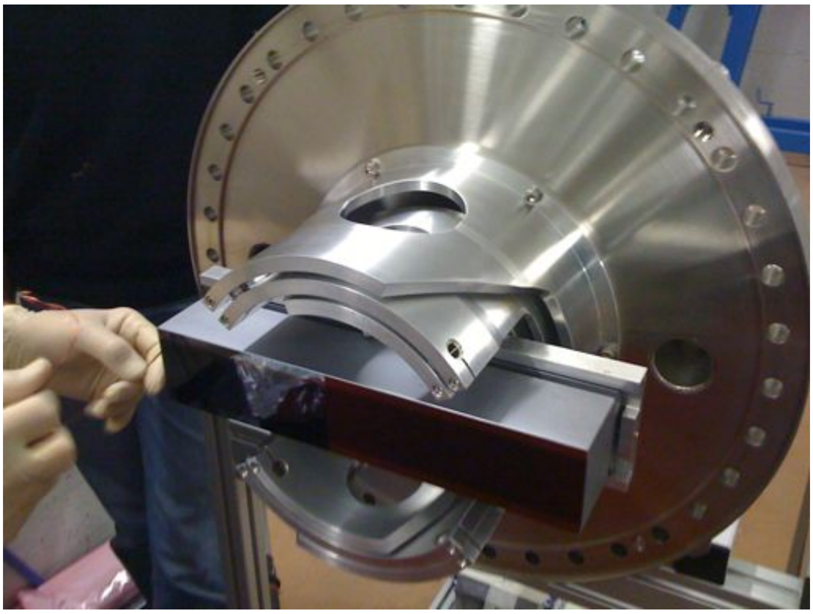

Figure *7 PM1a mounted on its holder and flange. The mirror’s active area is 20 mm wide and 400 mm long in order to accept the whole incoming photon beam.*

Outside the SH the common optical path of the two FEL sources reaches the PRESTO (Pulse Resolved Photon Energy Spectrometer: Transparent and On-line) at the beginning of the Experimental Hall (EH). This instrument is composed of a set of three diffraction Variable Line Spacing plane gratings (VLS-PG) able to fully characterize the spectral content of the FEL radiation while delivering the beam unperturbed to the end-stations. The design of this instrument as well as its performances will be described in detail in section 4.2.2. Depending on the beamline under operation the photon beam can be deflected by the EIS-Switching Mirror (EIS-SW), providing light to the EIS-TIMER beamline, or it can freely propagate until the split and delay line AC/DC (Auto Correlator/Delay-Creator) section. This instrument, composed of eight gold-coated plane mirrors, is devoted to pump and probe experiments as well as autocorrelation measurements. Its design and features will be described in section 4.2.3. About 20 meter downstream of the PRESTO, the 3-Way switching chamber (3-Way) is used to deliver the photon beam to one of the following end-stations. It is composed of two plane mirrors facing each other, both working at 2° of grazing incidence. Inserting one or the other, it is possible to deliver the beam to the LDM (Low Density Matter) or the EIS-TIMEX beamline. Finally, if none of the mirrors is inserted the beam freely propagates downstream reaching the DiProI (Diffraction and Projection Imaging) section. Both LDM and DiProI have a vertical deflecting mirror (VDM) intended to rise the beam up to the Kirkpatrick-Baez Active Optics System (KAOS), which is devoted to focus the FEL beam to the sample.

Table 1 *PADReS mirror parameters: distance from the two sources, dimensions, grazing incidence angle, coating material, substrate shape and mirror orientation respect to the EH. The AC/DC distances are referred to the central point of the instrument.*

Mirror name	d (FEL1/2) m	$w \times l$ mm	α_{Graz} deg	Coating material	Shape (Orientation)
PM1a	48.1/-	20 × 400	2.5	Graphite	Plane (H)
PM2a	-/41.4	20 × 300	2.5	Graphite/Ni	Plane (H)
PM1b	54.3/-	20 × 250	5	Graphite	Plane (H)
PRESTO	57.5/49.8	20 × 250	2.5	Graphite/Au/Ni	VLS-PG (H)
EIS-SM			2.5	Au	Plane (H)
AC/DC	71.2/63.6		2/3	Au	Plane (V)
3-WAY	77.5/69.9	25 × 480	2	Graphite/Au/Ir	Plane (H)
VDM	95.6/87.9	20 × 390	2	Au	Plane (V)
EM		40 × 400	2	Au	Ellipsoidal (H)
V-KB	95.6/87.9	40 × 400	2	Au	Active (V)
H-KB	96.1/88.5	40 × 400	2	Au	Active (H)

On the other side EIS-TIMEX employs a standard ellipsoidal mirror (EM) as a focusing optic. All the focusing mirrors have a gold coating and work at 2° of grazing incidence. The focusing sections will be described in detail in the next chapter in terms of their metrological characterization, their expected performances and their actual performances as well.

In table 1 the position, dimension, coating material, grazing working angle, shape and orientation of the employed mirrors are listed.

3.3 Pulse Resolved Energy Spectrometer: Transparent and On-line (PRESTO)

The measurement of the emission wavelength and the spectral content of the photon radiation is an essential information for both machine and experimental scientists at a FEL user facility. The knowledge of the photon beam spectral properties is needed during the machine optimization and for performing machine studies (*i.e.*, monitoring the change of the FEL output as a function of the machine parameters). The experimentalists, on the other side, need to know the photon beam spectral distribution of the source, shot to shot, to discriminate the acquired data. Consequently, the main requirement for the instrument, supposed to obtain this information, is the capability of working on-line and shot-to-shot, with minimal perturbation of the photon beam delivered to the experimental stations. In order not to perturb the radiation, only a small fraction of the incoming beam has to be used. PRESTO has been designed in order to allow the accurate measurement of the photon energy spectral distribution in the whole FERMI energy range, including the third harmonic. The most important information directly obtained by using this instrument is the energy distribution, in particular the central wavelength (peak position) and the bandwidth (FWHM) of the emitted radiation. Other useful information can also be obtained, as will be described following.

The instrument is composed of three grazing incidence flat Variable Line Spacing plane gratings (VLS-PG) that can be chosen according to the wavelength of the incoming radiation. With these three gratings PRESTO can cover the whole energy range of FERMI, from 100 nm down to 1 nm. The reflected radiation (*e.g.*, the 0th-order of diffraction) is sent to the beamlines downstream, while the diffracted part of the radiation is focused to a triggered detector acquiring the single-shot images. While other methods could be used to characterize the spectral content (for instance a Time Of Flight spectrometer - TOF), PRESTO has been considered the easiest option since the acquired data is immediately recorded and does not require further analysis, and the system is simple and reliable. In the following sections the spectrometer design, parameters and performances are described in detail.

3.3.1 Spectrometer design: VLS equations

As mentioned in the previous sections the diffractive optical elements are three VLS-PG. Despite the flat substrate, the diffracted beam is focused because of the groove density variation. In fact, the groove density increases along the tangential direction of the grating. As a consequence, different diffraction angles occur on different parts of the grating, and focusing in the tangential direction is realized. The VLS groove density can be expanded in power series

$$N(w) = D_0 + D_1 w + D_2 w^2 + D_3 w^3 + \ldots,$$

as a function of the tangential local coordinate w (centered at the grating pole), and it is expressed in lines mm^{-1} (often referred to as grooves mm^{-1}), D_0 is the central groove density equal to $N(0)$, D_1 is the linear variation, D_2 is the quadratic variation, and so on.

The optical path function F for a plane VLS grating can be expressed as a power series too, and the most important terms are [7]: F_{100} the grating equation, F_{020} the sagittal focus, F_{200} the tangential focus, and F_{300} the primary coma.

$$
\begin{aligned}
F_{100} &= mN\lambda - (\sin\alpha - \sin\beta),\\
F_{200} &= \frac{1}{2}\left[-mD_1\lambda + \left(\frac{\cos^2\alpha}{r} + \frac{\cos^2\beta}{r'}\right)\right],\\
F_{020} &= \frac{1}{r} + \frac{1}{r'},\\
F_{300} &= -\frac{1}{3}mD_2\lambda + \frac{1}{2}\left(\frac{\cos^2\alpha\sin\alpha}{r^2} + \frac{\cos^2\beta\sin\beta}{r'^2}\right).
\end{aligned}
$$

The constant incidence angle α has been chosen to be 87.5° in order to have a high efficiency at the 0^{th}-order (reflected beam to the users), and to accept more than 3σ of the incoming photon beam in most of the FERMI wavelength range.

The source distance r is assumed to be constant (57.5 m for FEL1 and 49.9 m for FEL2), considering the source waist position placed inside the last undulator. Having fixed α and r, the position of the focal point is a function of the photon wavelength only. The set of all the focal points is a curve in the dispersion plane called the focal curve, which can be calculated defining the grating coefficients and knowing α and r, by using the previous formulas.

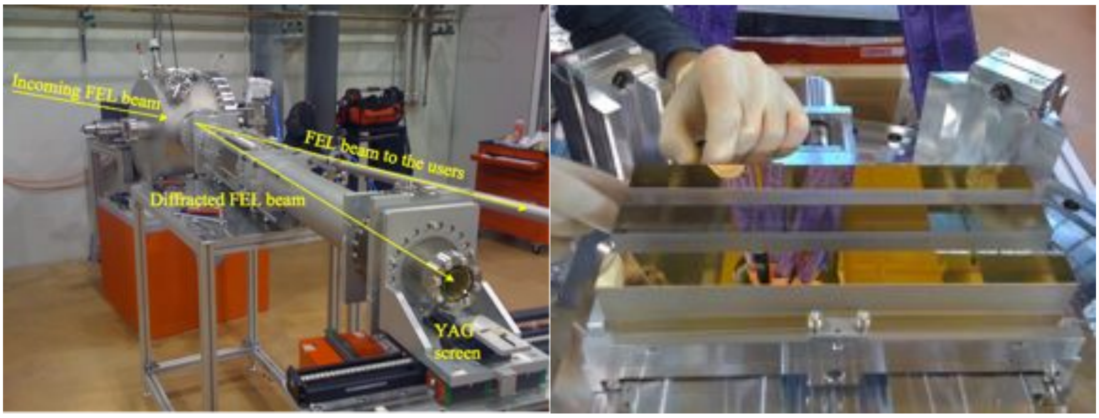

Figure 8 *Left, picture of the vacuum chamber hosting the diffraction gratings and the movable detector. Right, picture of the LE, ME and HE gratings mounted on the holder.*

In order to allow the placement of the detector at different focal points, the spectrometer has a movable exit arm capable of both radial (r') and angular (β) movements (Figure 8, left). The minimum angle of diffraction allowed by the mechanical design of the instrument is about 9.2°, while the maximum is 18.4°, giving an angular span of about 9.2°. The minimum and maximum exit arm lengths are 2550 mm and 3050 mm, for a total excursion of 500 mm. Both these movements are remotely controlled with micrometric precision. The spectral distribution is obtained by using the first, second or third diffraction order of the employed grating.

3.3.2 PRESTO parameters

The main parameters and performances of the three VLS-PG are summarized in table 2. The substrates are 250 mm-long, 25 mm-wide, and 40 mm-thick (not cooled since the deposited power is low and thermal bump does not occur). The grating patterns have been holographically ruled in the central 60 × 20 mm^2 part. The low energy grating (G1) covers the wavelength range from 24.8 nm to 100 nm (12 - 50 eV) in the first diffraction order (m=1), while the second and third orders can be used to reach 8 nm (155 eV). The medium energy grating (G2) can measure from 27.6 nm to 6.7 nm (45 - 185 eV) in the first order and, using the second and third orders, down to 2.2 nm (560 eV). The high energy grating (G3) covers the range from 12.7 nm to 3.1 nm (98 - 400 eV) in the first order of diffraction and, down to 1.03 nm (1200 eV) by using the second and third order.

Table 2 *Spectrometer gratings parameters. The low energy grating is briefly named as G1, the medium energy is called G2 while the high energy grating is G3.*

Parameter	G1	G2	G3
Wavelength (Energy) range m=1 / nm (eV)	100-24.8 (12-50)	27.6-6.7 (45-185)	12.7-3.1 (98-400)
Wavelength (Energy) range m=2 / nm (eV)	24.8-12.4 (24-100)	13.9-3.4 (89-370)	6.3-1.55 (196-800)
Energy resolution / meV	0.2-3.7	0.3-9.5	0.4-8.1
D_0 / gr mm^{-1}	500	1800	3750
D_1 / gr mm^{-2}	0.35	1.26	2.68
D_2 / gr mm^{-3}	1.7×10^{-4}	6.3×10^{-4}	1.4×10^{-3}
Groove profile	Laminar	Laminar	Laminar
Groove height / nm	12	4	8
Groove ratio (w/d)	0.60	0.65	0.65
Coating material	a-C	Au	Ni

The grating profiles have been chosen to guarantee low efficiency in the diffraction orders, *i.e.,* to the detector. In this way almost all the radiation is efficiently transported to the experimental end-stations. The gratings are mounted with parallel surfaces, one above the other, in a holder limiting the substrate distortions, preventing undesired aberrations of both the reflected and diffracted beams. The in-vacuum motorized holder allows the vertical translation, to select the gratings, and the rotation of pitch and roll, while the other movements have to be performed by acting directly on the vacuum chamber. A picture of the holder hosting the gratings is shown in Figure 8 (right).

The detection system is composed of a Ce:YAG crystal coupled with a cooled Charge Coupled Device (CCD) camera. The Ce:YAG crystal is placed in vacuum, glued on a viewport, and it converts the VUV/soft X-rays into visible light with an efficiency from 35% up to 80%, depending on the radiation wavelength. Right before the Ce:YAG a retractable Aluminum filter can be inserted in order to attenuate the beam intensity, followed by a manual valve that allows to replace the Ce:YAG crystal when needed without breaking the vacuum in the grating chamber. The CCD camera is produced by

Hamamatsu Photonics (C8800 series) and is endowed with a 1000×1000 pixels-chip with quantum efficiency from 30% up to 50% in the visible range. The detector is placed in front of the viewport (in air) and the radiation emitted by the Ce:YAG crystal is focused onto the CCD chip by a lens system. Two orthogonal translation stages permit to move the detector along the focal curves.

3.3.3 Grating efficiency

The determination of the grating profiles (groove shape, groove height, and ratio) as well as the choice of the coatings have been done by calculating the efficiency at various orders of diffraction. From the diffraction grating theory it is known that different groove profiles influence the efficiencies at various diffraction orders. Since the spectrometer is an on-line diagnostic (ideally non-invasive), the intensity of the diffracted radiation has to be as low as possible (differently from a standard monochromator), but high enough to obtain a detectable signal at the detector. In order to check the consistency of the outputs, the efficiency has been calculated with two different codes: REFLEC [8] and LUMNAB [9]. The results are in good agreement, with a negligible difference below 5 %. The results obtained by using REFLEC are shown in Figure 9. The profile better matching the requests, and available from the state of the art manufacturing techniques, has been found to be the laminar one: it gives a relative low efficiency as compared to that of a blazed shape, which on the contrary maximizes the efficiency at the first order of diffraction reducing the intensity of the zeroth order. In table 2 the groove heights and ratios for the low (G1), medium (G2) and high (G3) energy gratings are reported together with their working energies at different diffraction orders. The coatings have been chosen to be 50 nm-single layers of amorphous-carbon (a-C) for G1, gold (Au) for G2, and nickel (Ni) for G3. The expected efficiencies are well below 5%, and the photon beam transmission to the end-stations is very close to the reflectivity in the case of plane mirrors. For this reason PRESTO is able to work online without significantly disturbing the photon beam transported to the end-stations.

3.3.4 Resolving power

The grating groove density has been chosen in order to provide high resolution within the working spectral range. The resolving power has been evaluated considering the combined contribution of both the gratings and the detector. The grating contribution has been evaluated adopting the Rayleigh criterion (the minimum resolvable energy at the focus of two different energies) by performing ray-tracing simulations with Shadow code [10] taking into account the ideal and measured substrate shape, and the roughness obtained after the metrological investigation, as explained in detail in [11].

The detector spatial resolution has been simulated by considering the finite pixel size of the CCD imaged over the Ce:YAG screen by the used lens (with a field of view, FoV, of 15.4 mm). It has resulted that the latter is the main cause of the final resolution of the instrument, which ranges between $1.5\cdot10^4$ to $3\cdot10^4$. The resolving power can be

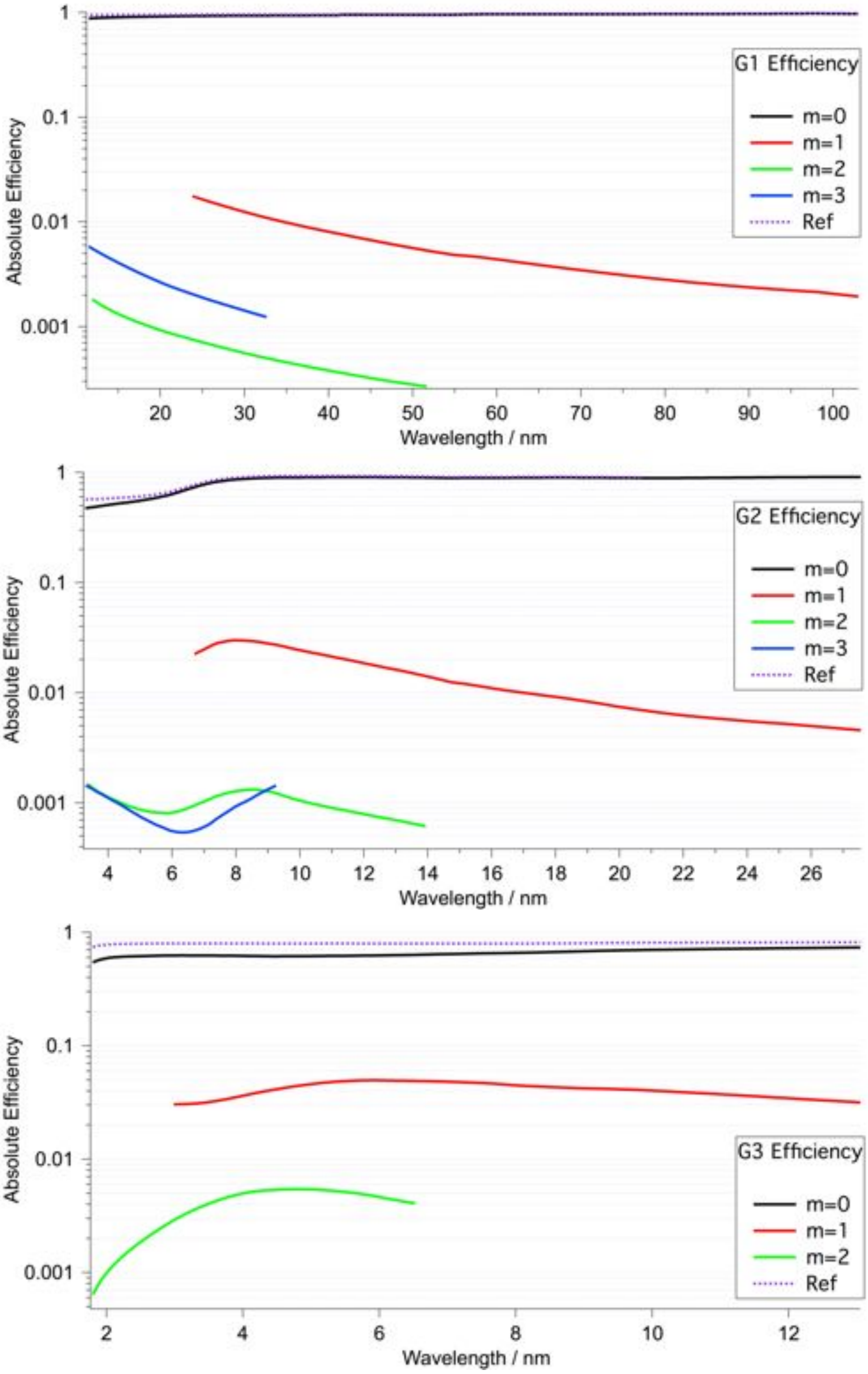

Figure 9 *Grating efficiency at the zeroth (m=0 black), first (m=1 red), second (m=2 green), and third (m=3 blue) orders of diffraction for the low (G1, up), medium (G2, centre) and high energy (G3, bottom) gratings in the whole FERMI wavelength range. The intensity used for the measurement of the spectrum is much lower than the total radiation delivered to the users (zeroth order m=0, black), which is about 96-98% of the incoming photons. If the harmonic components have enough intensity then it is possible to use the second/third order of diffraction to perform single shot spectral measurements. The purple dotted lines correspond to the reflectivity of a single mirror with the same coating and incidence angle as the gratings.*

increased by using a different lens with a smaller FoV at the cost of the loss of some intensity. The simulated resolving powers by considering the grating contribution only**,** and those obtained considering also the finite spatial resolution of detector, are reported in Figure 10. In the same Figure the measured resolving powers as obtained by data acquisitions performed during a beamtime at FERMI in RUN 9 are reported.

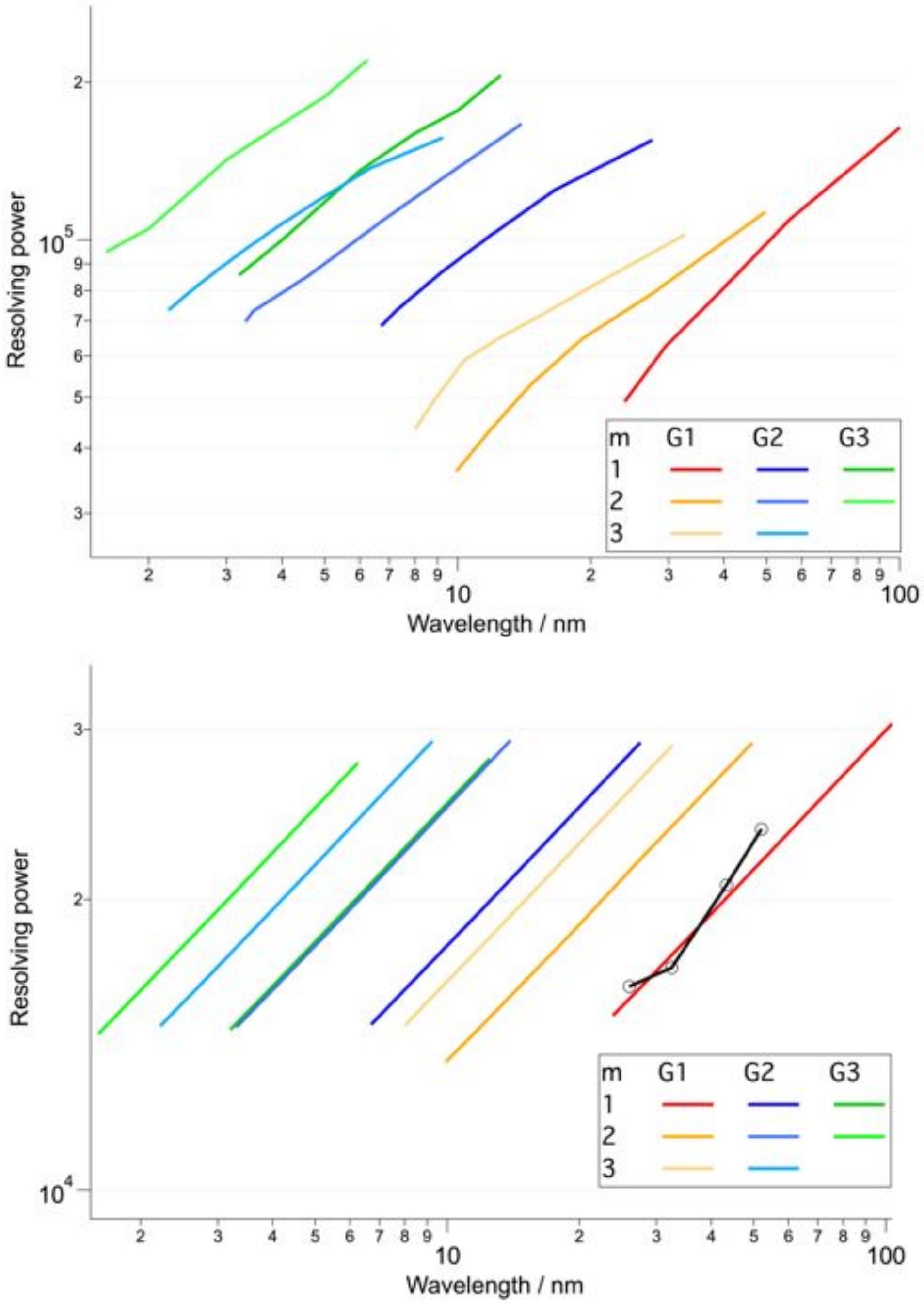

Figure 10 *Simulated gratings (top) and total (bottom) resolving power for the three gratings of PRESTO at the different orders of diffraction. The reason for the drop in resolution is due to the used objective with a large FoV (15.4 mm) in order to collect the entire diffracted photon beam. The black line represents the measurements performed scanning the wavelength of the seed laser using an Optical Parametric Amplifier (OPA).*

By changing the FEL wavelength in steps of 0.1 nm, it has been possible to measure the actual spectrometer resolution in a fraction of the FEL1 wavelength range (26-52 nm, i.e., 24-48 eV) at the first order of diffraction. In fact, as explained in reference [12] once the electron energy and the undulator gaps are fixed, the FEL process is driven by the seed laser wavelength that can be accordingly fine-tuned using the Third Harmonic of the Ti:Sapphire amplifier. This operation provides a variation in the seed laser wavelength up to 0.4% that, combined with the harmonic selection, allow to continuously tune the FEL emitted wavelength. By measuring the transverse relative variation in the positioning of the spectral peak it has been possible to determine the spectrometer resolution, and to derive the actual resolving power (Figure 11, left). The resolving power is resulted slightly lower then expected, probably due to the unavoidable small misalignments and the YAG diffusion. Nevertheless its value is higher than 10^4, high enough to resolve the FERMI spectral distribution with the requested accuracy. These measurements have confirmed that the theoretical resolving power is mainly reduced by the finite size of the CCD pixel. The measured bandwidths have been compared with measurements performed simultaneously tuning the seed laser, and scanning the wavelength across the 1s-4p resonance in He atoms at 52.2 nm, detecting both the UV-visible fluorescence (4p-2s occurring at 400 nm), and EUV fluorescence (4p-1s occurring at 52.2 nm), as explained in more details in [12]. The bandwidths have been found to be in agreement, confirming the proper calibration of the PADReS spectrometer (Figure 11, right).

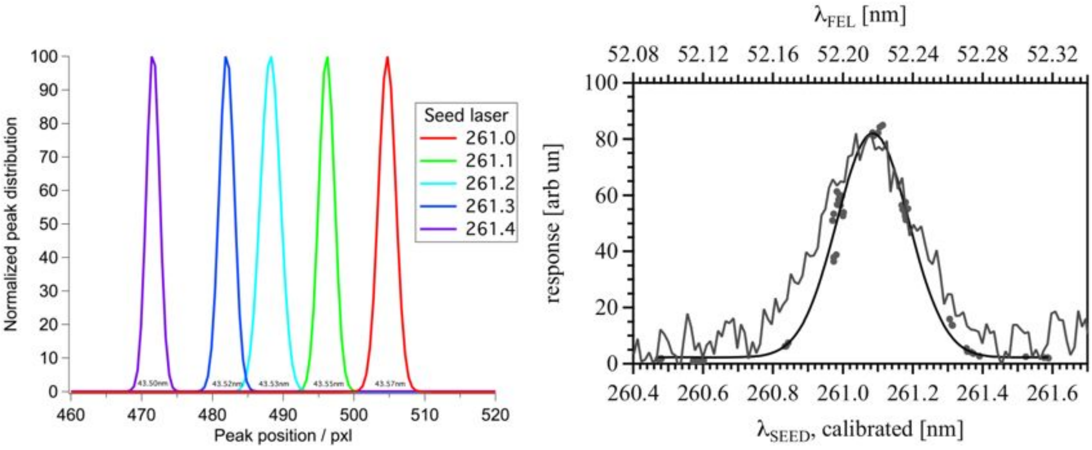

***Figure 11** Left, example of spectral peak shift due to the variation of the seed laser wavelength using an Optical Parametric Amplifier (OPA). These data have been used for the experimental determination of the PRESTO resolving power with good agreement with respect to the simulations. Right (Figure reproduced from [12]), reconstructed He absorption profile scanning the wavelength across the 1s-4p resonance at 52.2 nm ($\lambda_{FEL} = \lambda_{SEED}/5$). Dots: Photomultiplier response versus calibrated wavelength. The comparison between the Gaussian fit of the He signal with a single-shot acquired by PRESTO confirms both the FEL bandwidth as well as the spectrometer calibration*

3.3.5 0^{th}-order delivered to the end-stations

The 0^{th}-order, *i.e.,* the reflected beam, is delivered to the experimental end-stations. For this reason, the photon beam shall not be perturbed in terms of intensity or wave front. The relative variation between the efficiency at the 0-order of diffraction (coming from the ruled part of the optical surface of the gratings) and the reflectivity (coming from the non-ruled mirror-like sides of the same surface) is less than 1% as can be seen comparing the black (efficiency) and purple (reflectivity) curves in Figure 10. This slight difference is negligible for the end users, especially at lower wavelengths where the beam footprint on the surface is small and only the tails are reflected by the non-ruled area.

From the mirror reflection a wave-front deformation is expected in the presence of shape errors and micro-roughness, but it can also be a consequence of a periodic structure; *e.g.,* the grating grooves. The PRESTO grating substrates are flat, except for the presence of minor shape errors and negligible micro-roughness at the surface. Nonetheless, their effect is negligible since their value is well below 0.4 μrad rms in the long wavelength range, and micro-roughness σ less than 1 Å. An estimation of the Peak-to-Valley (P_tV) distortion of the wave front caused by the grooves can be easily computed considering the variation of the optical path for a photon beam reflected by a laminar profile with groove height h and grazing incidence angle α. The distortion of the wave front is therefore mostly negligible since the P_tV is 1.05 nm for G1, 0.35 nm for G2 and 0.70 for G3, which corresponds to a local deformation smaller than $\lambda/50$ at 50 nm for G1, $\lambda/30$ at 10 nm for G2, and $\lambda/10$ at 7 nm for G3. From these results it is clear that the wave front is sensitive to the presence of the high energy grating due to the short wavelengths involved. We have investigated its effect with physical optics simulations performed with the WISE [13] code. The obtained results have confirmed that the Strehl ratio after the reflection over the high energy grating is well above 0.48 at wavelengths longer than 5 nm. This value drops to 0.65 at 3 nm even though an actual degradation of the wave front has not been observed. In any case, from the experience of the first experimental runs at FERMI it is clear that the PRESTO is transparent for the users over most of the FERMI wavelength range.

3.3.6 Additional features

The PRESTO VLS gratings have a non-zero F_{020} term (sagittal focus), thus the beam is focused in the tangential plane only. We can take advantage of this peculiarity by considering not only the horizontal distribution (*i.e.*, the spectral content) but also the vertical one, which is the projection of the photon beam transverse profile. The measurement of the vertical distribution allows the use of PRESTO as a (partial) on-line screen. In fact, as the FERMI FEL radiation has been proven to present circular transverse emission symmetry, the vertical profile measured with the spectrometer is actually the projection of the FEL transverse intensity distribution. In Figure 12 a graphical explanation of this feature is presented for different intensity distributions (TEM_{00}, hollow, and a mix of modes) impinging over the spectrometer optics. The measured diffracted spots at the detector are compared with the footprints on the gratings. Once the vertical dimension/distribution is known, it is then possible to extract the beam divergence, just taking into account the distance between the detector and the last undulator. After having taken a set of images at two different screens and having calculated the angular divergence, a very good agreement with the theoretical values was found, meaning that the PRESTO provides the direct information about the beam divergence without the need to insert any screen blocking the beam.

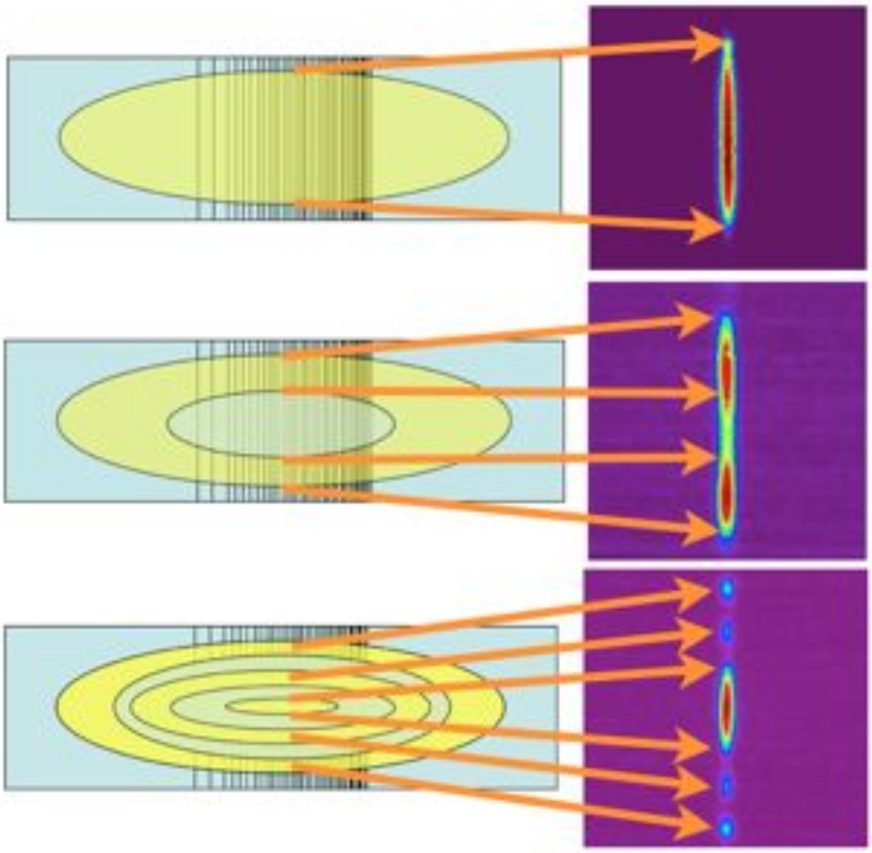

Figure 12 *FEL intensity distribution as seen at the spectrometer detector. Top, a perfect Gaussian beam is emitted by the FEL and its vertical projection is seen as a Gaussian. Centre, a hollow mode caused by an off-resonant condition of the undulators is projected as two vertical peaks. Bottom, a set of mixed modes (Gaussian and hollows) is seen as a central Gaussian and some vertical satellites*

3.3.7 Two colours double-pulse measurements

One of the peculiarities of FERMI is the possibility to generate multiple X-ray pulses, used for pump-probe experiments [14, 15]. This has been accomplished by seeding the electron bunch with two independent ultraviolet seed pulses, with a slightly shifted central wavelength, both tunable in the 260-262 nm range. In this way two independent FEL pulses have been generated at the seventh harmonic of the seed lasers (around 37.1 nm and 37.3 nm) with a variable temporal separation from 300 fs up to 700 fs (the limitations with this method are due to the electron bunch length, the upper limit being around 1 ps, and the seed pulse duration, the lower limit being 150 fs) [16]. Besides the regular determination of the spectral content of the two FEL pulses, PRESTO has been used for two additional tasks: to measure the relative intensity of the pulses, and to help in the determination of the temporal separation between pump and probe. The measurement of the former is non-trivial since the pulses are separated well less than 1 ps, and, in general, an ultra-fast diagnostics system would be required. Unfortunately, the signals generated by the two pulses into the gas-based I0 monitor cannot be distinguished.

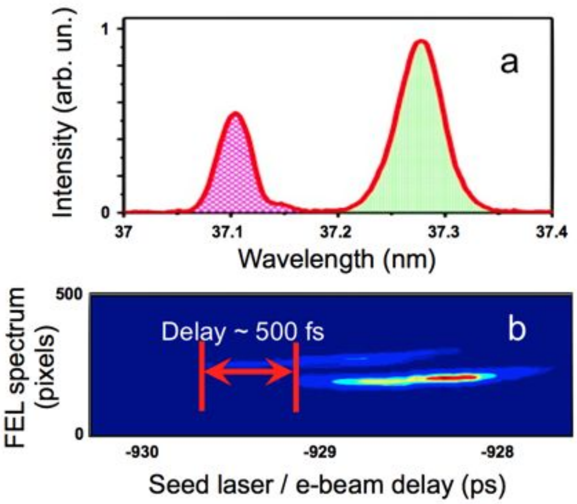

Figure 13 *Top, spectral content and intensities of the pump (right) and probe (left) pulses measured with PRESTO in the 2-color double pulse experiment. Comparing the subtended areas it has been possible to measure on-line and shot-to-shot the relative intensities. Bottom, spectra of both pulses while scanning the relative time delay between the electron beam and the seed laser pulses. The pulse duration was around 50 fs while the separation between the pump-probe has been kept fixed at 500 fs.*

However, comparing the area subtended by both spectra as measured by PRESTO, it was possible to measure the relative intensity between the pulses, with high accuracy and on-line, on a shot-to-shot basis. The temporal separation has been controlled by scanning the delay between the two seed pulses while looking at the resulting FEL spectra of the double emission. In Figure 13 a series of spectral distributions is shown as a function of the relative time delay between the seed lasers and the electron bunch. In the same Figure, besides the independent onset of the two FEL pulses, it can be seen that the central wavelength separation between the two pulses was about 0.2 nm with a relative time delay of 500 fs, a bandwidth RMS about 0.05% of the central wavelength, and a shot-to-shot peak position RMS jitter of about 0.005% of the central wavelength position.

3.4 Auto Correlator–Delay Creator (AC/DC)

The split and delay line AC/DC installed at FERMI is based on the wave-front splitting operated by a knife-edged mirror working at a grazing incidence angle of 2°. The photon radiation is half reflected by the mirror and half transmitted with the consequent splitting of the beam in two half Gaussians. The reflected beam passes through a fixed optical path and is reflected by two plane mirrors. The transmitted beam has a variable optical path and impinges over four plane mirrors before being recombined with the other half at the last mirror, which is similar to the first splitting mirror. Then the recombined beams are sent forward on the same optical travel to the end-stations (Figure 14). By moving concordantly two mirrors along two mechanical guides it is possible to introduce a temporal delay ranging from -2 ps to around 30 ps with a step resolution of 30 fs.

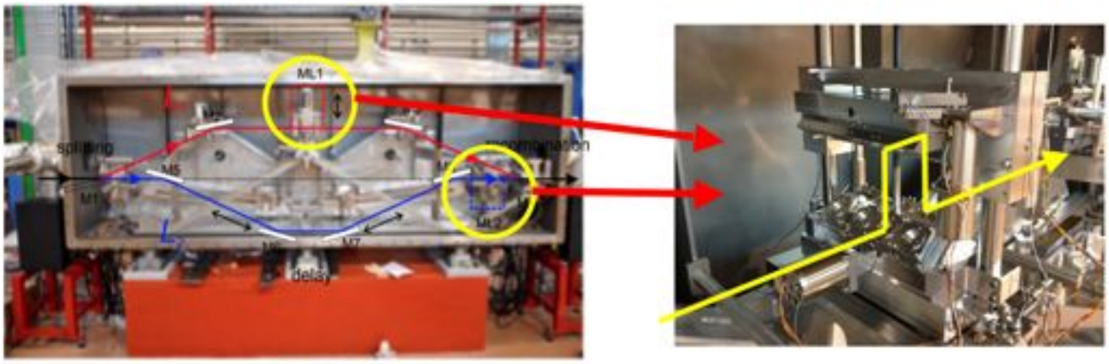

Figure 14 *Left, picture and working principle of the split and delay line seen from a side. After the splitting the half Gaussian beams travel through different optical paths and are eventually recombined. The two additional small delay-lines host the multi-layer mirrors (right) able to extend the time delay up to 1.3 ns.*

The delay range set by the grazing plane mirrors can be further increased introducing additional differences in the two main optical paths. This can be done using, on each path, a dedicated small delay line based on 4 multilayer coated optics working at 45° incidence angle that introduces an additional travel of tens of centimeters. By the proper choice of the dimensions of these delay lines, and even implementing the possibility to control the delay in one of the two, it is possible to extend the delay range up to 1.3 ns. As seen in section 4.1.1, the drawback in using multilayer-based optics is that only some wavelengths are allowed, due to the typical narrow-band reflectivity of the multilayer optics themselves. Nevertheless the additional small delay lines host up to four sets of different multi-layers, that can of course be replaced if needed, in order to provide a selection of photon energies suitable for the experimental needs. At the exit of the AC/DC two sets (one for each branch) of eight solid state filters will be installed in order to be able to select the fundamental or a secondary harmonic of the FEL emission for performing multi-color pump and probe experiments.

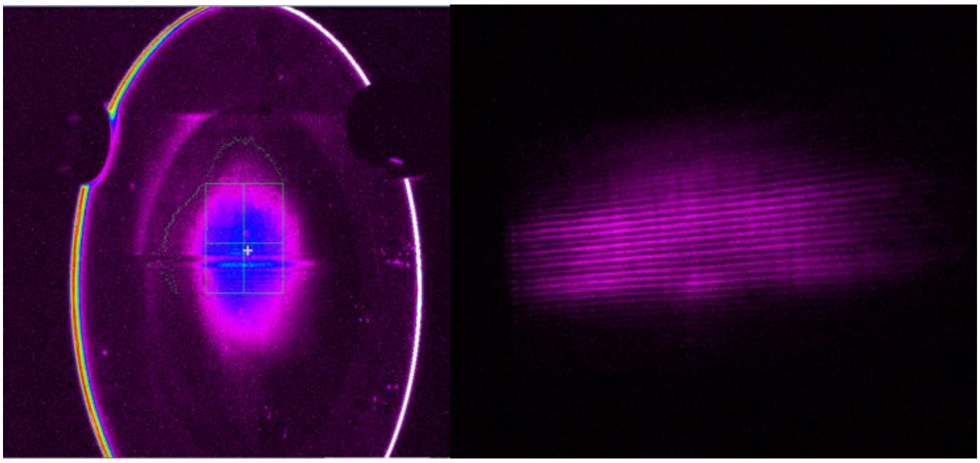

Figure 15 *Left, two half Gaussian beams emerging from the AC/DC as seen at a YAG screen. The structures present are a consequence of the knife-edge wave front splitting technique, and are unavoidable. Right, interference pattern at the end of the beamline, when the two half-beams have been overlapped.*

During the commissioning phase of AC/DC it has been possible to split the FEL radiation into two half Gaussian beams (Figure 15 left) and to overlap the spots at the end of the beamlines. The interference pattern has been observed (Figure 15 right) and, by changing the relative the optical paths of the two branches, the relative time delay has been changed until the fringes have disappeared. By fine scanning the temporal delay it will be possible to perform auto-correlation measurement in order to determine the longitudinal coherence of the FEL radiation: i.e. to measure the pulse duration since the beam is fully coherent.

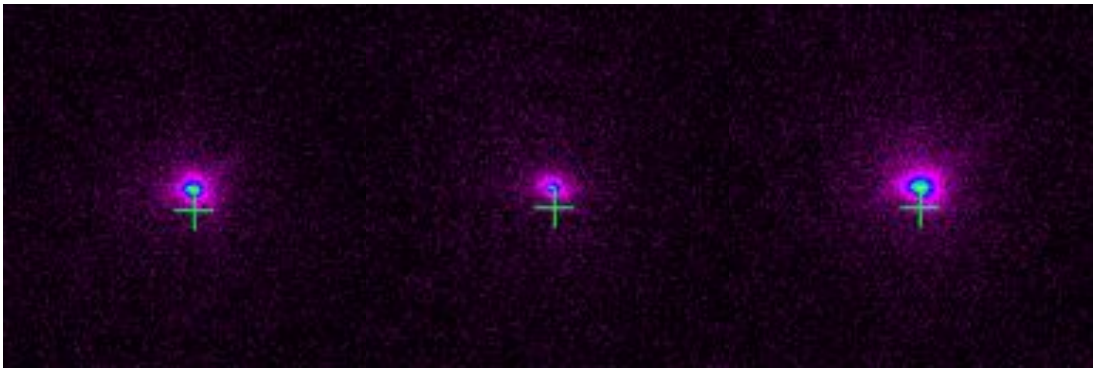

Figure 16 *Left and center, split half Gaussian beams focused inside DiProI end-station. Right, both branches overlapped and focused at the sample position.*

Afterwards, both half beams have been successfully focused by the DiProI's focusing mirrors in order to check the spot position and quality (Figure 16 left and center). Focused at the sample position, they were used for some tests changing the time delay in order to check the overlap stability during a time scan (Figure 16 right). These results confirm the feasibility of AC/DC to perform pump and probe experiments with the FEL radiation. Up to now the AC/DC is still under commissioning, and will be open to the users within the end of 2016.

References

[1] M. Born, E. Wolf, Principles of Optics, 7th ed. (Cambridge University Press, Cambridge, 1999)

[2] B. L. Henke, et al., “Low-Energy X-ray Interaction Coefficients: Photoabsorption, Scattering, and Reflection, Atomic Data and Nuclear Tables”, 27, 1-144 (1982).

[3] Bocchetta, C.J. *et al. FERMI@Elettra FEL conceptual design report* (Sincrotrone Trieste, Trieste, 2007) (https://www.elettra.trieste.it/lightsources/fermi/fermi-machine/fermicdr.html)

[4] S. P. Hau-Riege, et al., "Damage threshold of inorganic solids under free-electron-laser irradiation at 32.5 nm wavelength, APPLIED PHYSICS LETTERS 90, 173128 (2007)

[5] Bieren K. V., "Pencil beam interferometer for aspherical optical surfaces laser diagnostics", in Proceeding of SPIE 343 (1982)

[6] Takacs P. Z. and Qian S. N., "Design of a long trace surface profiler metrology: Figure and finish", in Proceeding of SPIE 749 (1987)

[7] William Burling Peatman, “Gratings, Mirrors and Slits: beamline design for soft X-ray synchrotron radiation sources”, Gordon and Breach Science Publishers (1997)

[8] Schäfers F., “Calculation of grating efficiency” included in: Software codes RAY and REFLEC at BESSY, BESSY Technical Report 202/96, Berlin (1996)

[9] LUMNAB program by M. Nevière, CNRS Marseille

[10] Cerrina F., et al., “Shadow PRIMER”, Center for X-ray Lithography (1994)

[11] Svetina, C., et al., “Characterization of the FERMI@Elettra's on-line photon energy spectrometer”, Proceedings of SPIE - The International Society for Optical Engineering, 8139, art. no. 81390J, (2011)

[12] Allaria, E., et al., “Tunability experiments at the FERMI@Elettra free electron laser”, New Journal of Physics, 14, art. no. 113009, (2012)

[13] Raimondi, L., Spiga, D.,“*Mirrors for X-ray telescopes: Fresnel diffraction-based computation of point spread functions from metrology”*, Astronomy and Astrophysics 573, A17, (2015)

[14] De Ninno, et al.,"Chirped seeded free-electron lasers: Self-standing light sources for two-color pump-probe experiments", Physical Review Letters, 110 (6), art. no. 064801, (2013)
[15] Mahieu, B., et al., "Two-colour generation in a chirped seeded free-electron laser: A close look" Optics Express, 21 (19), pp. 22728-22741, (2013)
[16] Allaria, E., et al., "Two-colour pump-probe experiments with a twin-pulse-seed extreme ultraviolet free-electron laser", Nature Communications, 4, art. no. 2476 (2013)

4 PADReS focusing systems

Non-linear effects, several absorption/emission processes and saturation effects occur only above some fluence thresholds depending on the system under investigation. For these reasons the powerful FEL photon pulses need to be properly focused in order to reach high fluences inside the experimental stations. The FERMI radiation, apart from passing through plane mirrors and diffraction gratings as described before, is not focused until the very last vacuum chambers right before the end-stations. Every beamline has its own dedicated focusing section, designed and realized accordingly to the experimental needs. Moreover, diagnostics of the focused radiation are essential for the optimization of the mirror's performances. Several approaches have been implemented at FERMI to characterize the photon beam spot such as the Wave-Front Sensor (WFS), the ablation of suitable materials, and the direct imaging with scintillators. In this chapter the focusing optical systems will be described in detail with particular attention to the in-house developed active mirrors as well as the employed photon diagnostic for the characterization of the focused beam.

4.1 Working principle of focusing mirrors

After a reflection the photon radiation is deflected and, depending on the shape of the mirror, changes might occur in the beam shape and size. In order to understand how the shape of a mirror affects the photon beam the Fermat's principle, also known as the principle of least time, has to be applied. It states that the optical path from point A to point B must be an extremum. For a system with constant index of refraction (for instance in vacuum) light travels along a straight line. Fermat's principle applied to a system composed of a point source (A), a mirror and an image point (B) states that if the point A is imaged at some point B, then all of the paths from A via the mirror surface to B, described by $P(\xi,\omega,\ell)$, must be equally long [1, 2]. Operatively, the Rayleigh criterion for defining two paths to be "equally long" is that they lie within $\lambda/4$ of each other.

If the mirror has a proper shape then the Fermat's principle is fulfilled and the source will be imaged properly without the presence of aberrations. Referring to Figure 1, the arbitrary path is expressed mathematically as:

$$F = \overline{AP} + \overline{PB}.$$

On the other hand the optical path can be written as the modulus of the vectors whose sum gives the vectors $\overrightarrow{AP}$ (the same applies for $\overrightarrow{BP}$):

$$\overrightarrow{AP} = \overrightarrow{AO_A} + \overrightarrow{O_AO} + \overrightarrow{OP} = \begin{pmatrix} 0 \\ 0 \\ -z \end{pmatrix} + \begin{pmatrix} -r\cos\alpha \\ -r\sin\alpha \\ 0 \end{pmatrix} + \begin{pmatrix} \xi \\ \omega \\ \ell \end{pmatrix},$$

thus

$$\overrightarrow{AP} = \left|\overrightarrow{AP}\right| = \left[(\xi - r\cos\alpha)^2 + (\omega - r\sin\alpha)^2 + (\ell - z)^2\right]^{\frac{1}{2}}$$

$$\overrightarrow{BP} = \left|\overrightarrow{BP}\right| = \left[(\xi - r'\cos\alpha)^2 + (\omega - r'\sin\alpha)^2 + (\ell - z')^2\right]^{\frac{1}{2}}.$$

Following the principle of least time, the focusing condition of the source can be satisfied only if:

$$\frac{\partial F}{\partial \omega} = 0 \quad \text{and} \quad \frac{\partial F}{\partial \ell} = 0.$$

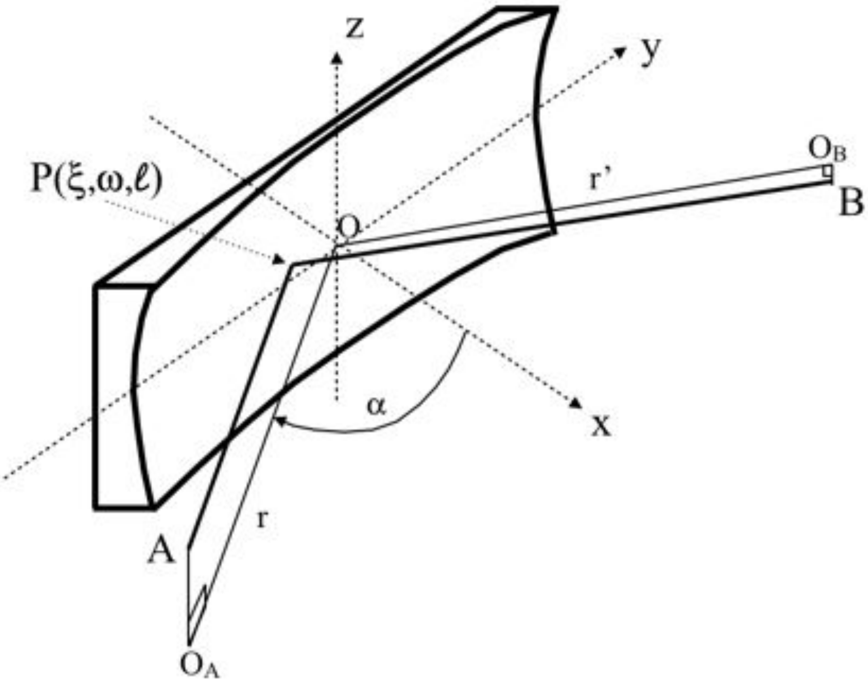

Figure 1 *Schematic representation of the Fermat's principle. Rays from a source point A impinging on a mirror at point P(xwl) will be reflected and imaged to a point B.*

The previous equations can be fulfilled if the mirror's surface shape P(ξ,ω,ℓ) is chosen properly. The general form of the surface, expressed in its local coordinates, is

$$\xi = \sum_{i=0}^{\infty}\sum_{j=0}^{\infty} a_{ij}\omega^i \ell^j,$$

where $a_{00}=a_{10}=0$, and j is an even number. In table 1 the most important a_{ij} terms for the most used mirror shapes (toroidal, paraboloidal, ellipsoidal) are reported.

Applying the Fermat's principle and solving the focusing conditions with the coefficients describing the mirror surface, it is possible to determine the best parameters in order to minimize the aberrations [3]. The opposite is also true: given the mirror parameters it is possible to predict all the properties of the focused spot such as the presence of aberrations, the spot size and displacement.

Table 1 *Most relevant a_{ij} terms for the toroidal, parabolical and ellipsoidal mirror shapes. The terms R and ρ are the tangential and sagittal radii of curvature, α is the angle of incidence with respect to the normal of the mirror, r' is the focal distance of the parabola. The terms a, b and e are respectively the major-minor semi-axes of the ellipse and the eccentricity while the f term is defined as* $f = (1/r + 1/r')^{-1}$, *with r and r' the distances between the pole of the mirror and the source-image respectively. Note that the spherical mirror shape is a degeneration of the toroidal when R=ρ.*

a_{ij}	Toroid	Paraboloid	Ellipsoid
a_{02}	$\frac{1}{2\rho}$	$\frac{1}{4r'\cos\alpha}$	$\frac{1}{4f\cos\alpha}$
a_{20}	$\frac{1}{2R}$	$\frac{\cos\alpha}{4r'}$	$\frac{\cos\alpha}{4f}$
a_{22}	$\frac{1}{4R^2\rho}$	$\frac{3\sin^2\alpha}{32r'^3\cos\alpha}$	$\frac{\sin^2\alpha}{16f^3\cos^3\alpha}\left[\frac{3}{2}\cos^2\alpha-\frac{b^2}{a^2}\left(1-\frac{\cos^2\alpha}{2}\right)\right]$
a_{40}	$\frac{1}{8R^3}$	$\frac{5\sin^2\alpha\cos\alpha}{64r'^3}$	$\frac{b^2}{64f^3\cos\alpha}\left(\frac{5\sin^2\alpha\cos^2\alpha}{b^2}-\frac{5\sin^2\alpha}{a^2}+\frac{1}{a^2}\right)$
a_{04}	$\frac{1}{8\rho^3}$	$\frac{\sin^2\alpha}{64r'^3\cos^3\alpha}$	$\frac{b^2}{64f^3\cos^3\alpha}\left(\frac{\sin^2\alpha}{b^2}+\frac{1}{a^2}\right)$
a_{12}	0	$-\frac{\tan\alpha}{8r'^2}$	$\frac{\tan\alpha}{8f^2\cos\alpha}\left(e^2-\sin^2\alpha\right)^{\frac{1}{2}}$
a_{30}	0	$-\frac{\sin\alpha\cos\alpha}{8r'^2}$	$\frac{\sin\alpha}{8f^2}\left(e^2-\sin^2\alpha\right)^{\frac{1}{2}}$

For completeness in the following the parameters of the mirror shape as a function of the source-image positions (*r*/*r'*) and incident angle (***α***) are reported. For the toroidal mirror the radii of curvature that satisfy the tangential and sagittal focusing condition, with a given the source-image distance (*r*/*r'*) and incident angle ***α***, are:

$$\frac{1}{R}=\left(\frac{1}{r}+\frac{1}{r'_{\mathrm{tang}}}\right)\frac{\cos\alpha}{2},$$

$$\frac{1}{\rho}=\left(\frac{1}{r}+\frac{1}{r'_{\mathrm{sag}}}\right)\frac{1}{2\cos\alpha}.$$

The special case of a spherical mirror has *R*=***ρ***, and it can be seen that the relative displacement of the focal spots in the two direction is $r'_{\mathrm{sag}} = r'_{\mathrm{tang}}\cos^2\alpha$; they are coincident only for α=0 (i.e., in the normal incidence configuration).

Toroidal-spherical mirrors are commonly used at beamlines because they allow to reduce the number of optical elements employed (due to their focusing properties) and because they are commercially available with very high precision in their final shape. On the other hand they suffer from a strong coma-astigmatism and the use of slits before the sample are often required. The EIS-TIMER beamline employs a set of 24 toroidal mirrors as explained in detail in section 4.2.

For the parabolical mirror the equations are:

$$y^2 = 4ax,$$
$$a = r' \cos^2 \alpha,$$

where the location of the pole (axial ray) is at $x_0 = a \tan^2 \alpha$ and $y_0 = 2a \tan \alpha$. Parabolical mirrors have been widely used for collimating the radiation emitted by the source before a monochromator working in the conical diffraction mounting followed by a second parabolical mirror to refocus the beam. These mirrors are difficult to manufacture and present poorer surface quality as compared to the previous case. The fact that typically two parabolical mirrors are needed is another reason not to select them in many cases, also because of the low reflectivity of the composed system and alignment difficulties.

Elliptical mirrors are the best option in terms of focusing quality: their shape allows to image a point to a point by definition. They are virtually aberration-free but are inherently difficult to manufacture with low surface residual errors. Nonetheless, the EIS-TIMEX beamline employs this kind of focusing mirror. The most important equations are:

$$\frac{x^2}{a^2} + \frac{y^2}{b^2} = 1,$$
$$a = \frac{1}{2}(r + r'),$$
$$b = (rr')^{\frac{1}{2}} \cos \alpha,$$

where the location of the pole (axial ray) is at x_0, y_0:

$$x_0 = a\left(1 - \frac{y_0}{b^2}\right)^{\frac{1}{2}},$$
$$y_0 = \frac{rr' \sin(2\alpha)}{2d},$$
$$d = \frac{1}{2}\left(r^2 + r'^2 - 2rr' \cos(2\alpha)\right)^{\frac{1}{2}}.$$

Plane-elliptical surfaces can be generated by extending the plane ellipse along an axis perpendicular to the plane of the ellipse itself, typically the sagittal one. In this case they do not have any focusing property along the sagittal direction while they focus perfectly in the tangential one. These mirrors are the optimal choice for a two-mirror focusing system named Kirkpatrick-Baez [4], the name of their inventors, also referred as KB system. This system has been adopted for two of the FERMI beamlines, and will be described in detail in section 4.3.

More complicated shapes that take into account the transversal extension of the source as well as its intensity/divergence distribution can be mathematically defined such as the elliptical torus, diaboloid, and so on. Up to now the manufacturers are not able to supply such kind of shapes with small residual shape errors. For this reason the previously-mentioned shapes are still used both by synchrotron and FEL beamlines.

Another important quantity that can be predicted regardless of the mirror shape is the magnification factor M. It is defined as the ratio between the source-mirror distance r and the mirror-image distance r': $M=r'/r$. When M equals unity then the system performs a 1:1 imaging of the source. For $M<1$ the optical system de-magnifies the source, and vice versa. This value allows to estimate the best achievable spot size (Σ') in an aberration free system and the expected spot size is basically the product between the demagnification factor and the source size Σ: $\Sigma'=M\Sigma$. At FERMI the source distance is around 100 m and the mirror focal lengths are around 1.5 m, thus the indicative magnification is around 0.015.

The previous analytical discussion is often used as a starting point during the design phase. The best mirror shape and its parameters are approximately determined as well as the expected spot quality. Afterwards, a more complete approach is needed in order to determine the final parameters having considered all the possible tolerances of the system both in term of mirror quality and source/mirror alignment. This can be done via Ray-tracing software simulations where a geometrical approach is used to generate a source with a certain number of photons propagating with the expected parameters (source size, transverse distribution, energy distribution, divergence). These codes allow to generate a set of mirrors/gratings with the desired shape and to propagate the radiation along the beamline considering the actual measured mirror profiles, too. The spot quality can be checked and optimized by systematically varying the free parameters. Once the parameters have been chosen and fixed, the mirror can be purchased, characterized with the metrology instrumentation, and implemented at the beamline.

4.2 EIS focusing mirrors

EIS-TIMER [5-7] is endowed by a set of toroidal mirrors, while an ellipsoidal mirror serves EIS-TIMEX [8, 9]. These mirrors have the advantage of having a fixed shape, are robust, and guarantee good focusing performances. In particular, the EIS-TIMEX focusing mirror has been designed to provide a diffraction-limited spot at the focus in order to reach the highest fluence possible, thus irradiating the matter leading it into an extreme condition. The drawback of these optics is that the focal length is fixed, they are very sensitive to the source position, and there is no control over the spot dimension nor the wave-front.

4.2.1 EIS-TIMER toroidal mirrors

As mentioned in the first chapter, the beamline EIS-TIMER is devoted to the Transient Grating Spectroscopy technique and has a very peculiar design (shown in Figure 2). This is because the photon beam needs to be split twice and then recombined inside the experimental station. The three pulses (two pumps, one probe) have to be overlapped both in space and time with proper angles in order to fulfill the phase matching condition. The beams have also to be (partly) focused in order to generate enough signal to stimulate the sample and to be detected as well.

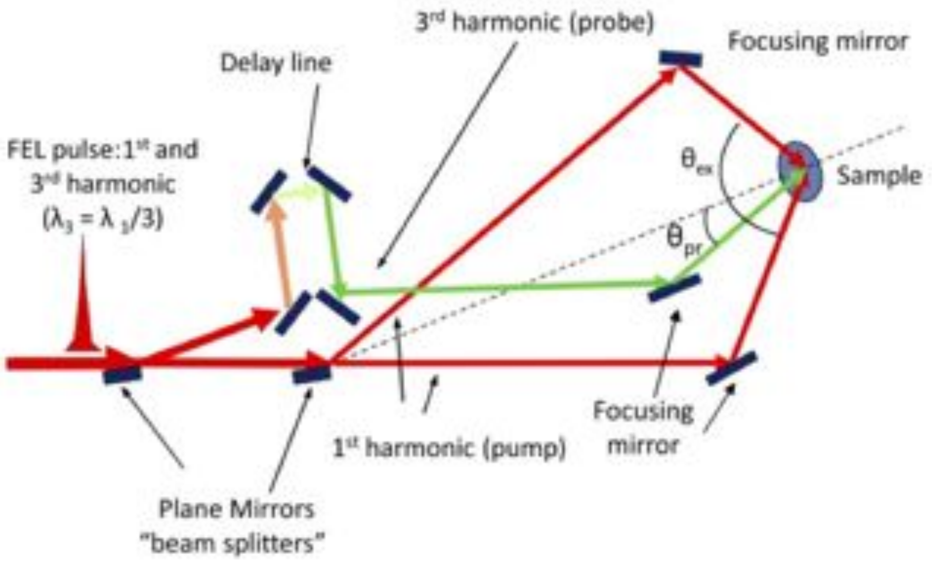

Figure 2 *Sketch of the beamline EIS-TIMER. From left to right: both the fundamental and third FEL harmonics are vertically split into two half-beams. The reflected one passes through a multi-layered delay line that also suppresses the fundamental component leaving the third harmonic only, which is focused at the sample position by a dedicated set of toroidal mirrors accordingly to the phase matching condition. Meanwhile the transmitted half-beam is split in two quarters, focused and then recombined at the sample by means of a set of toroidal mirrors.*

The beamline employs 24 standard VUV/Soft x-ray toroidal focusing mirrors with a bulk substrate. They can be divided into two main sets: the pump branches and the probe branches. The vertical splitting mirror divides the FEL into two half-beams: the "pumps" (horizontal) and "probe" (vertical), respectively. The pump beam propagates until a second splitting mirror is cutting horizontally the beam into two quarters of a Gaussian. Both beams impinge over two toroidal mirrors and are focused inside the EIS-TIMER end-station. There are a total of four vacuum chambers for each pump pulse, in order to obtain four different angles of recombination, in which there are two toroidal mirrors hosted depending on the source (FEL1-2). With this configuration the pump section consists of 16 toroidal mirrors overall. The other half-beam propagates until the multi-layered mirrors composing the delay-line (able to create a delay up to 3 ns), and is then focused by a toroidal mirror. Also in this case there are four different vacuum chambers in order to fulfill the phase matching condition with the pump pulses. Inside every vacuum chamber two toroidal mirrors are present, again one for each source, for a total of eight focusing mirrors.

The requested surface quality meets the standard values for the PADReS mirrors: below 1 μrad rms and 5 μrad rms slope errors, in the tangential and sagittal direction respectively, with a micro-roughness below 3Å rms. All the mirrors, purchased from WinlightX company, have been characterized in the Elettra metrology laboratory by means of the Long Trace Profiler (LTP), white light interferometers, and a Atomic Force Microscope (AFM). The measurements have confirmed that all the mirror parameters met specifications. Various coatings have been chosen in order to maximize the beamline transmission considering the wavelength range covered by each mirror. The mirrors working at a smaller incident angle (closer to the normal direction) have a multi-layer coating in order to increase the reflectivity that would be too low otherwise.

Table 2 *List of the toroidal mirror parameters installed in the EIS-TIMER beamline. The numbers in the name have the following meaning: first number is the source (FEL1 or FEL2), the second is the used harmonic (1st or 3rd) and the last is the increasing number in the order of the working incident angle. The first eight mirrors in the table are devoted to the pump beam (the fundamental harmonic) and there are two for each name listed. The total number of toroidal mirrors employed by EIS-TIMER is 24. The column Δλ indicates the wavelength working range (from–to) of each mirror.*

Name	Δλ nm	R cm	ρ cm	α deg	Coating	Optical area / mm		Bulk dimensions mm		
						L	W	L	W	H
1_1_1	60-20	5851.5	88.5	82.9	C	150	30	160	40	40
1_1_2	60-20	3379	90	80.6	C	150	30	160	40	40
1_1_3	60-20	680	97.6	67.75	Au	100	30	110	40	40
1_1_4	60-20	440	103.4	61.15	Au	70	30	80	40	40
2_1_1	20-10	5900	91	82.9	C	150	30	160	40	40
2_1_2	20-10	3420	92.74	80.6	C	150	30	160	40	40
2_1_3	20-10	675	101	67.75	Au	100	30	110	40	40
2_1_4	20-10	440	107	61.15	ML	70	30	80	40	40
1_3_1	20-6.6	10390	15.45	87.8	C	300	20	310	30	40
1_3_2	20-6.6	5650	15.8	87	C	200	20	210	30	40
1_3_3	20-6.6	1100	16.1	83.2	C	100	20	110	30	40
1_3_4	20-6.6	725	16.2	81.6	TiO2	100	20	110	30	40
2_3_1	6.6-3.3	10500	17.5	87.8	Ni	300	20	310	30	40
2_3_2	6.6-3.3	5670	17.6	87	Ni	200	20	210	30	40
2_3_3	6.6-3.3	1115	18	83.2	Ni	100	20	110	30	40
2_3_4	6.6-3.3	730	18.1	81.6	Ni	100	20	110	30	40

In table 2 all the EIS-TIMER toroidal mirror parameters are reported in terms of incident angle, radii of curvature, coating material and substrate dimension.

The spots generated by these mirrors are quite large compared to the other beamlines (up to 200 μm FWHM), with the presence of a strong coma due to the toroidal mirror shapes. An example of the pump (60 nm) and probe (20 nm) pulses simulated with a ray tracing code are shown in Figure 3. The reasons for the need of a large spot size at the sample is that the interaction region has to be large enough to stimulate a wide portion of the sample and to be easily overlapped with the probe pulse. If the spots are too small the sample might cause unwanted ablation effects and the overlap between the pump-pump and the pump-probe beams might result to be quite hard to achieve. The realization of this unique beamline has required many efforts from both the theoretical and the design side, to the actual manufacturing, and installation as well. Up to now the beamline is under commissioning and the first results will be presented in the next chapter.

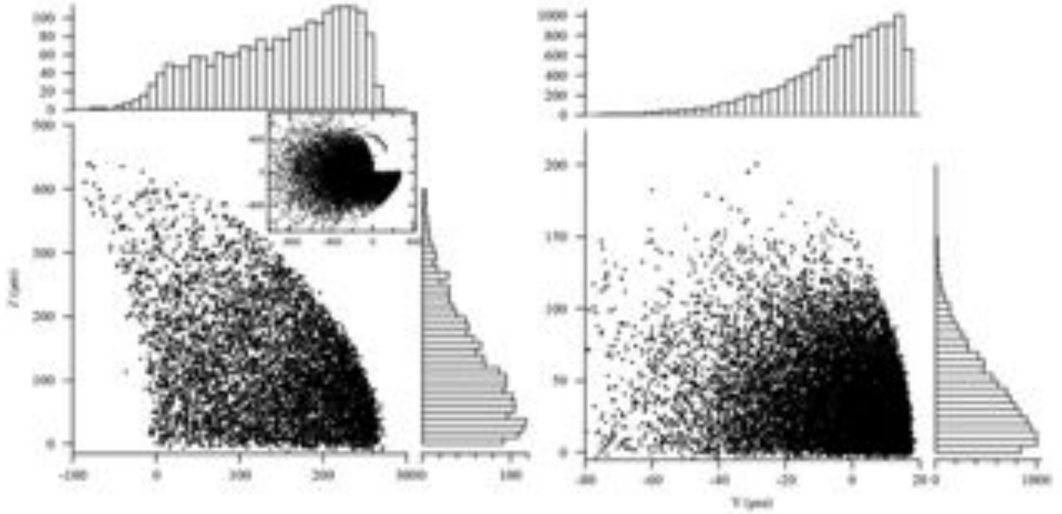

Figure 3 *Focused FEL1 spots simulated via Shadow ray-tracing code (reproduced from [7]). Left: pump quarter beam at 60 nm with a recombination angle of 9.2°. The beam is expected to be around 200×170 µm*^{2} *FWHM. Left insert: spherical aberration effect of the toroidal focusing mirror on the shape of a circular beam that propagates after the cut of the beam splitter mirror. Right: probe half-beam at 20 nm wavelength with a recombination angle of 3.05° and a dimension of 170×120 µm*^{2} *FWHM. In both cases the presence of a strong coma can be seen.*

4.2.2 EIS-TIMEX ellipsoidal mirror

The EIS-TIMEX main mission is to perform time-resolved pump and probe spectroscopy in matter under extreme conditions. This challenging task includes the generation of plasma state and warm dense matter that can be achieved only if the fluence at the sample is extremely high (up to 10^{16} W cm^{-2}). As a consequence the choice of a single ellipsoidal focusing mirror is quite natural: one reflection means a higher overall beamline transmission and the mirror shape is virtually aberration-free. On the other hand ellipsoidal mirrors with high surface quality are very demanding in terms of manufacturing, as it is requested to produce a portion of the ellipsoid very far from the central part located in the middle between the two foci.

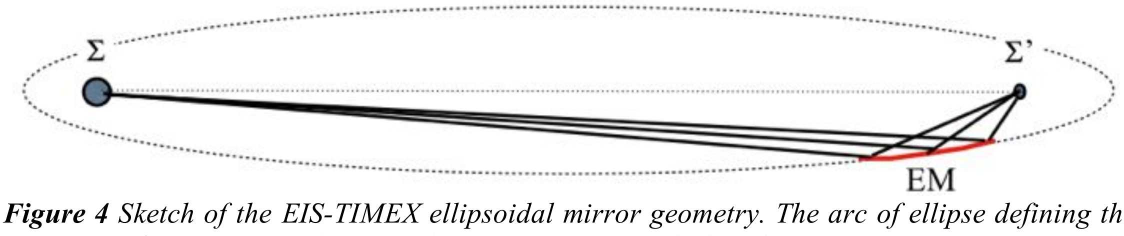

Figure 4 *Sketch of the EIS-TIMEX ellipsoidal mirror geometry. The arc of ellipse defining the mirror surface is very close to the image point and the shape is very asymmetric. The magnification factor is about 0.015 for FEL1 and 0.016 for FEL2.*

In particular the EIS-TIMEX focusing mirror has a strongly asymmetric shape as schematically shown in Figure 4. This is because the mirror is placed far from the source (92494 mm from FEL1, 84846.6 mm from FEL2) and close to the image plane (1400 mm), with a grazing angle of incidence of 2° and an expected demagnification factor of 0.015 and 0.016 for FEL1 and -2, respectively.

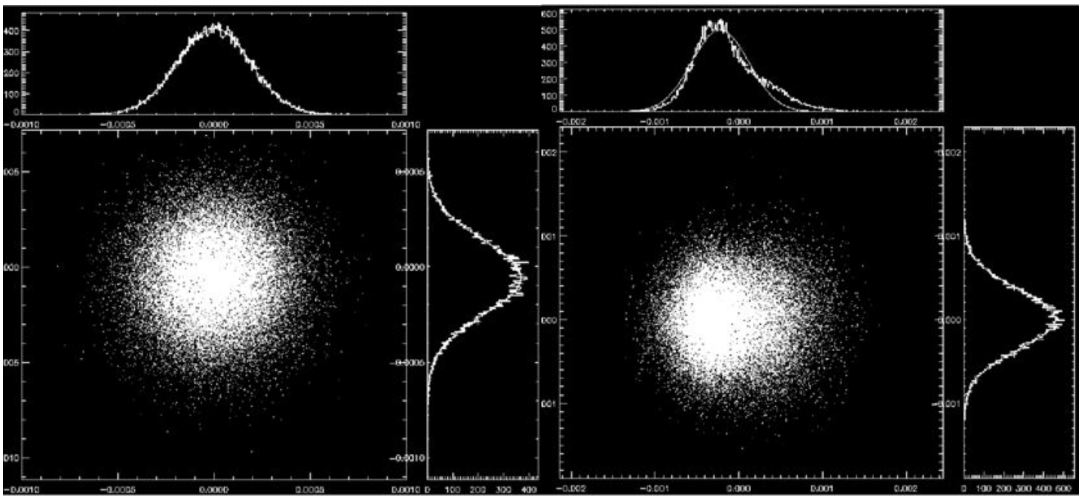

Figure 5 *Comparison of the focused spot (32.5 nm) between ideal (left) and real (right) mirror profiles composing the EIS-TIMEX beamline. The unavoidable slope errors slightly degrade the spot quality.*

The German Zeiss Company has manufactured this mirror with many efforts having obtained a residual shape error of about 1 μrad, which is close to the best achievable result with the current technology available. The presence of slope errors along the whole beamline has been considered and the simulations have shown that the spot becomes slightly astigmatic and presents a negligible coma in the horizontal direction. This effect is more pronounced at longer wavelengths where the divergence is higher and the footprint over the mirror surfaces is bigger (i.e., more irregularities of the surface are seen by the light). A comparison between the ideal and real case at 32.5 nm wavelength is shown in Figure 5. The spot size is expected to increase from 4.5×4.5 μm^2 to 6.5×8.0 μm^2.

4.3 Kirkpatrick-Baez Active Optics System (KAOS)

Single mirror focusing systems are difficult to manufacture and suffer inherently from aberrations, especially in the case of spatially extended sources. For this reason the implementation of corrected optical systems composed of multiple focusing mirrors able to optimize the spot quality is a valuable option. On the other hand these systems have the drawback of having a smaller overall transmission, and the alignment might be challenging. For these reasons the options are usually limited to a two-mirror system. The most common solutions are the Wolter [10], Schwarzschild [11] and Kirkpatrick-Baez (KB) [4] configurations. The former is composed of a parabolic and a hyperbolic mirror, while the Schwarzschild is made of two spherical mirrors (convex and concave) working at normal incidence. These systems have optical elements that are hard to produce (parabolic-hyperbolic shape) with high surface quality, and are very difficult to align. On the other hand in the KB system two plane-elliptical mirrors are employed, which independently focus the photon beam in the two orthogonal planes (Figure 6). The sagittal direction (plane) does not contribute to the focusing, which is relied on the tangential direction only (elliptical). These kind of mirrors have the advantage to be produced with higher figure accuracy compared to a single ellipsoidal focusing mirror, and to decouple the focusing.

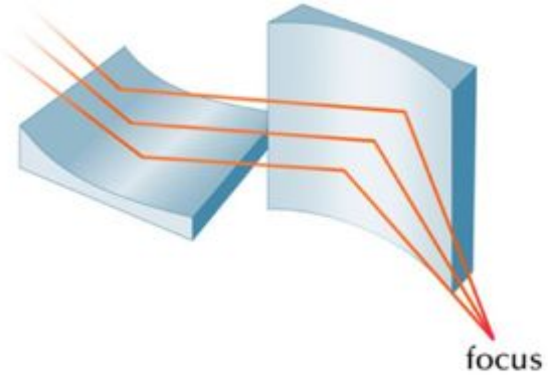

Figure 6 *Schematic representation of the Kirkpatrick-Baez two-mirror focusing system. The plane-elliptical mirrors independently focus the radiation in the two planes.*

The KB system has been adopted at two of the four end-stations: DiProI [12] and LDM [13]. These beamlines have to control the spot size going from few microns (diffraction limit) up to several hundreds of micron, for both FEL sources, accordingly to the experiment. This task has been achieved with the implementation of an active KB system named Kirkpatrick-Baez Active Optics System (KAOS) [14], which is composed of two thin plane mirrors 10 mm-thick that are bent by mechanical pushers. The pushers act on the clamps holding the mirror modifying the surface shape in a controlled way.

As for the other focusing systems, at first the raw theoretical parameters of the best ellipses have been calculated using the equations in section 4.1. From now on the DiProI KAOS only will be described since the LDM systems is identical despite the fact that the source distances are 3.2 m shorter. Due to the PADReS layout the first KB mirror is the vertical focusing (KB_V), which reflects the photon beam parallel to the experimental hall floor after the Vertical deflecting mirror (VDM). It is placed 4.3 m downstream the VDM and 1750 mm upward of the nominal focal position. The horizontal KB (KB_H) is located 550 mm downstream KB_V thus both the source and the focal distances are different compared to the vertical one. As a consequence the two mirrors need to have different elliptical parameters in order to focus the beam at the same position avoiding astigmatism. Moreover, the optimally-focused beam will have a different dimension in the two planes due to the different demagnification factors. Using the theory the main parameters of KAOS have been calculated (the results are summarized in table 3), and the mirrors have been purchased.

Table 3 *DiProI KAOS parameters: distance from the sources (r_{FEL1}- r_{FEL2}), image distance (r'), grazing angle of incidence (α_{Graz}), mirror dimension, semi-major/minor axes (a, b) and demagnification factor (M).*

Parameter	KB_V	KB_H
r_{FEL1}- r_{FEL2} / mm	98754.4-91107	99304.4-91657
r' / mm	1750	1200
α_{Graz} / deg	2	2
Dimension (W×L×H) / mm^3	40×400×10	40×400×10
a / mm	50252.2-46428.5	50252.2-46428.5
b / mm	458.8-440.7	381.0-366.0
M	0.018-0.019	0.012-0.013
Coating – thickness / nm	Au – 30	Au – 30

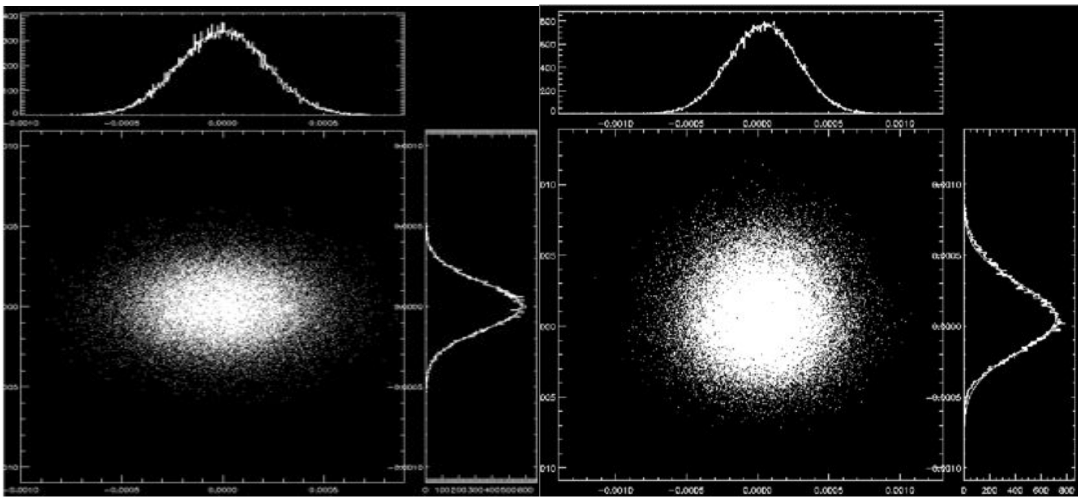

Figure *7 Simulated focused spots inside DiProI end-station for a FEL1 radiation at 32.5 nm with the Shadow Code. Top: ideal mirrors without residual surface errors generate a focal spot of 3.3μm × 5.1μm FWHM. Bottom: actual case having considered the real mirror profiles of the plane mirrors upstream the KAOS. The focused spot presents some minor aberrations and is slightly larger (5.2μm × 5.7μm FWHM) compared to the ideal case.*

After this preliminary estimation of the mirror parameters, ray-tracing simulations have been carried out with Shadow code. The sources have been modeled with a Gaussian TEM_{00} distribution for both intensity and divergence. Considering the actual profiles of the plane mirror composing the transport section for both sources, it has resulted that the actual shape of the KAOS needs to be slightly different compared to the calculated values in order to compensate the movement of the virtual sources (as seen by the mirror) due to the presence of residual figure errors on the plane mirrors.

In the ideal case the expected spot size is around 3.3μm × 5.1μm FWHM for FEL1, and 2.0 μm × 2.9 μm FWHM for FEL2. When the actual profiles of the transport plane mirrors and KAOS are considered, the best achievable focused spot results to be slightly larger and with some minor aberrations. The simulated spot dimensions are then 4.5μm × 6.9μm FWHM for FEL1 and 2.4μm × 3.7μm FWHM for FEL2. Figure 7 compares the expected focused spots with the ideal (top) and real (bottom) mirror profiles at 32.5 nm wavelength radiation for FEL1 source.

After the simulations the metrology investigation over the actual mirrors has followed. As for the plane mirrors, the KAOS has been characterized in all the accessible spatial frequency ranges. The micro-roughness has been measured by means of the AFM and white light interferometer. The mirrors have been proved to be under specifications with 3Å rms of micro-roughness. Then the mirror has been mounted on its holder (a picture is shown in Figure 8) and measured with the LTP.

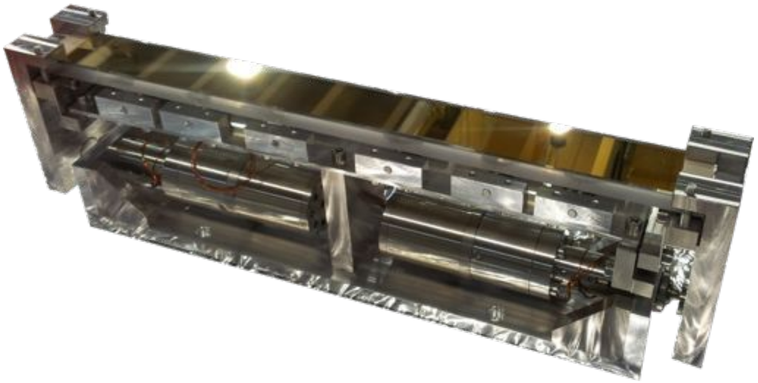

Figure 8 *Picture of one of the two KAOS mirror mounted on its holder and ready to be measured with the LTP. The mirror is clamped at the sides only. Two stepper motors act on the mechanical structure changing the mirror's shape.*

The measurements have been done following the standard protocol used for the characterization of the active optics. The first set of measurements is done without any force applied to the mirror. Then the first actuator is set to a known position-force and the change in the mirror shape is recorded. Afterwards, the second actuator is set to the same position-force as the former and the profile is measured with both forces applied. This procedure allows calculating the response matrix that gives the change in the mirror shape as a function of the force applied (or number of steps for stepper motors) by the actuators.

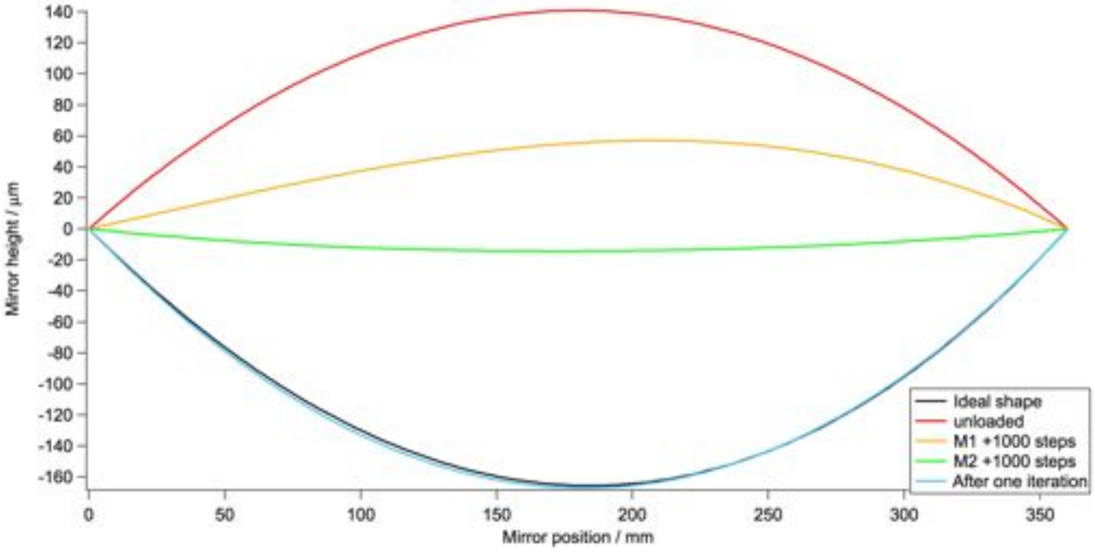

Figure 9 *Mirror profiles measured with the LTP during the characterization of the KAOS. The red curve corresponds to the mirror unloaded where no force was applied to the substrate. The orange and green lines correspond to the mirror profile after having applied 1000 steps to the first (M1) and second (M2) stepper motors, respectively. The black curve represents the ideal ellipse determined with the ray tracing simulations while the azure line is the profile after one iteration, having applied the response matrix of the system.*

The response matrix is a linear approximation and is valid only if the actuators are independent, which is our case. A graph with the profiles measured during this phase with no actuators acting, just the first and then both, is shown in Figure 9. The procedure goes on with the attempt to obtain the desired elliptical shape using the just-calculated response matrix, which provides the number of steps to apply by each actuator. This is an iterative process that generally requires several measurements getting closer to the desired shape until the target of the system is achieved. A comparison between the ideal shape and the best profile obtained after these iterations is shown in Figure 9, while the residual profile, defined as the difference between the best profile and the ideal ellipse, is shown in Figure 10. The residual profile shows some structures that cannot be removed with the current holder-pushers setup with a slope error of 2.4 μrad rms and a P_tV of 235 nm [14]. These values are totally acceptable considering the system tolerances and the fact that an ellipsoidal mirror with the same characteristics would have a residual slope error of 5 μrad rms at least (with consequently worse focusing properties). These results prove that the KAOS is a valuable alternative high-quality system for the FEL focusing

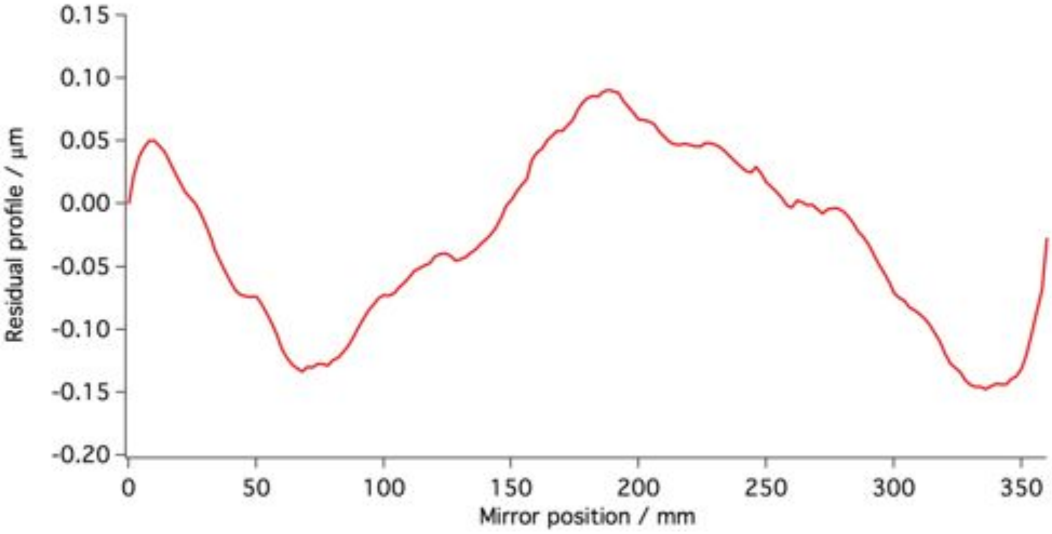

Figure 10 *Best residual profile obtained after several iterations on the KAOS. The slope errors are below 2.4 μrad rms and a P_tV of 235 nm. This result confirms the feasibility of the system being used for focusing the FEL photon beam with high quality.*

Several ray-tracing simulations have been carried out using the best KAOS profiles, confirming that the final shape guarantees a final high focusing performance of the system. The same simulations have been done with a wave-front propagation code (WISE code [15, 16]), which takes into account the wave nature of radiation and predicts accurately the effect of the mirror finite length as well as the actual profile at the focal plane. The results from both approaches have been found to be in agreement except for the presence of some negligible diffraction that could not be predicted by the ray tracing approach by definition. A result of the wave-front propagation simulations at 32.5 nm having considered the actual KAOS profiles is shown in Figure 11.

After the success of the metrology measurements and the simulation results, the KAOS has been installed in the vacuum chamber. Figure 12 shows a picture of the KAOS during the installation phase.
The commissioning of KAOS has been performed during several dedicated beamtimes

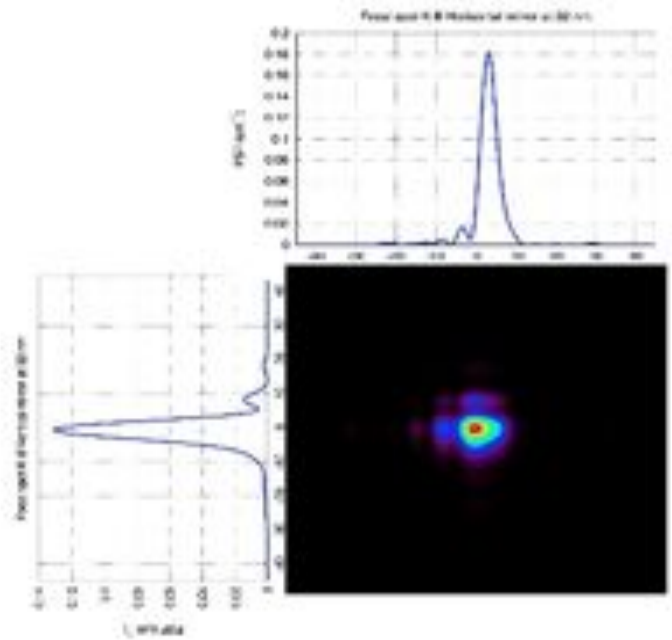

Figure 11 *Results obtained via wave-front propagation simulations (WISE code) using the measured KAOS residual profiles. The small diffraction effect is a combination of the finite size of the mirror and the residual slope errors. The spot size is 5.1 μm × 7.7 μm FWHM.*

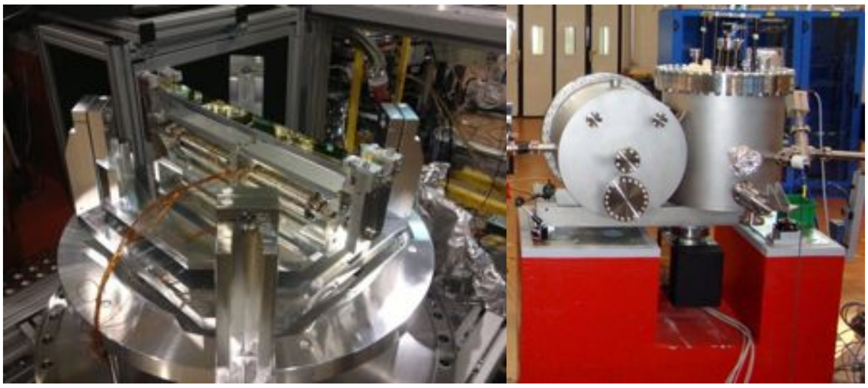

Figure 12 *KAOS mounted on its mechanical holder ready for the installation inside the vacuum chamber before the DiProI end-station.*

distributed over more than one year. The system has shown to be reliable and able to perform as expected, at both DiProI and LDM beamlines.

In the next chapter the most important results in terms of KAOS performances as well as some important experimental applications will be given. Up to now a new design with piezo-actuators instead of stepper motors as pushers is under test. This will permit to increase the resolution in controlling the KAOS shape, avoiding possible backlash effects now present due to the stepper motors as well as reducing heating effects that lead the system to relax after several hours of operation.

4.4 Diagnostics of focused FEL beam

The characterization of the focused spot size and shape is essential in order to know precisely the fluence over the sample and to interpret the experimental results. Various techniques can be used in order to attain this information, with completely different approaches and degree of knowledge of the beam quality. The most common techniques are: direct imaging of the spot via fluorescence screens, single shot ablation of selected material, and Hartmann wave-front sensor. Those techniques, together with their advantages and limitations, will be described in detail in the following sections.

4.4.1 Direct imaging via scintillators

Ce:YAG and phosphorous screens are widely used along the photon transport section. They convert efficiently the VUV/Soft x-ray radiation to visible light allowing to have a visual inspection (by eye or with a visible-light CCD camera) of the beam shape and position along the beamline. The same principle can be applied to the focused spots but with some limitations.

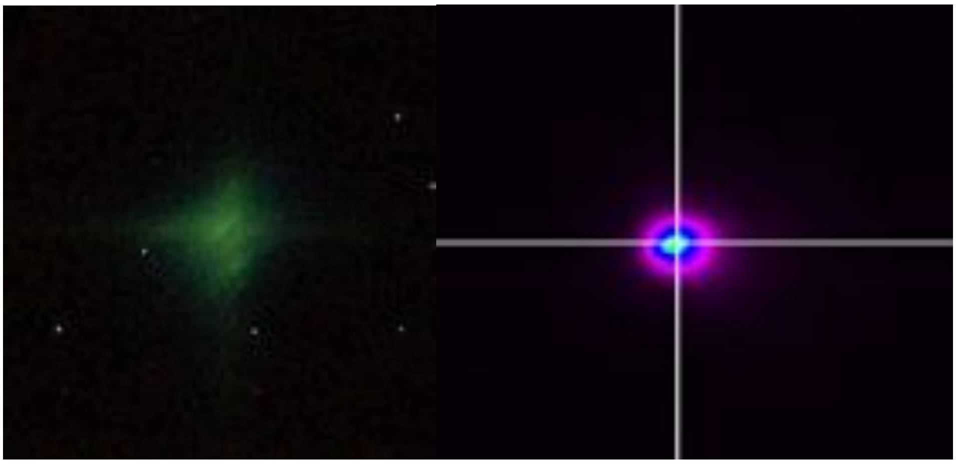

Figure 13 *Focused FEL spots converted in visible light by means of a scintillator (Ce:YAG screen). Left: spot seen with a regular CCD camera at DiProI. The image appears blurred and the details of the intensity distribution inside the spot are missing. Right: spot seen with a telemicroscope at EIS-TIMEX. The resolution allows measuring spots down to 10μm with just some diffusion at the sides of the beam.*

When the screen is placed at the focal plane it suffers from radiation damage from the high power FEL radiation. After a single shot the scintillator shows a hole/crater on the surface, and the focused spot image presents a dark area in its most intense part. For this reason solid-state filters and the gas attenuator must be used, dropping the intensity down to fractions of μJ in order not to damage the screen. On the other hand, the presence of roughness, granular structure, inter-diffusion, non-homogeneity and saturation effects are the cause of a broadening of the converted spot. As a consequence irradiance-dependent nonlinearities lead to artefacts in the measured focused beam profile [17]. With this technique it is possible to determine spot sizes down to 30-50 μm with a simple CCD camera, and down to 10-20 μm with the aid of a telemicroscope (Figure 13). For smaller spot sizes the screens give an upper limit of the spatial dimension but cannot measure accurately the actual size. The main advantage of this technique is that it can provide information shot-to-shot, not requiring a particular setup. Since this technique is based on the intensity distribution measurement in one plane only, no information about the wave-front can be retrieved. If the caustic curve is scanned, by moving the screen longitudinally, then the Wigner function [18] can be obtained and the wave-phase can be reconstructed. Unfortunately, the translation stages inside the FERMI end-stations have a short range and this kind of measurement is not yet possible. In the future it is foreseen to perform the measurement of the caustic curve by means of a Ce:YAG screen mounted into a dedicated slit with inside DiProI end-station.

4.4.2 Ablation

Single shot damaging of a suitable material can be used to measure with high precision the spatial properties of the focused FEL beam. The most commonly used material is Poly(methyl methacrylate) (PMMA) even though bare silicon and diamond are used as well. PMMA ablation has been extensively investigated from IR to hard x-rays [1-9], therefore its radiation physical properties have been explored and understood in a wide range of irradiation conditions. In particular laser-induced ablation of PMMA is governed by non-thermal processes. Extending Liu's method [19] of laser induced ablation it is possible to determine the beam profile and the beam dimension at the focal spot for both Gaussian and non-Gaussian beams.

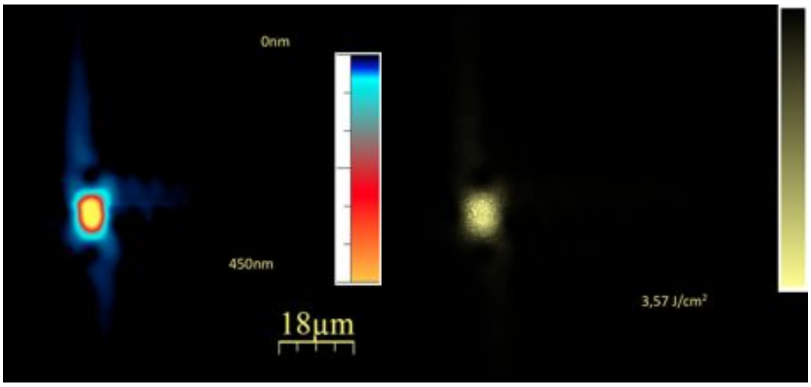

Figure 14 *Left: Crater measured with the AFM for a 32.5 nm wavelength FEL1 radiation with intensity at the sample of 3 μJ. Right: reconstructed fluence distribution within the focused spot.*

The determination of the focused FEL beam quality is obtained following the procedure reported in [20, 21]. Operatively, two steps have to be accomplished in order to fully determine the spatial properties of the focal spot. At first, the imprinting of the PMMA is done at different positions along the focal curve (named z-scan). Afterwards the sample is removed from the vacuum chamber and is analyzed with a Nomarski microscope (differential interference contrast - DIC). In this way the position of the waist position is determined and the sample is then positioned in the focal position with high accuracy. The second step is the fluence scan (f-scan) when several spots are recorded varying the intensity of the FEL by filling up the gas attenuator. Finally, the sample is removed and the crater's depth and area are analyzed via Nomarski microscope and Atomic Force Microscope (AFM). Applying the extended Liu's method the actual focal spot can be reconstructed both in terms of beam size and shape.

It has been mathematically demonstrated that the fluence scan method provides not only a good measure of the beam parameters, but also it characterizes energy distribution within the beam profile. This is true for both Gaussian and non-Gaussian transverse energy distributions, which may significantly influence results of intensity-dependent laser-matter experiments especially on the field of high energy density physics, where nonlinear phenomena play a key role. An example of crater measured with an AFM and the reconstructed fluence distribution is shown in Figure 14. This method is very precise and reliable, providing a direct measurement of the spot characteristics in the actual waist position. The main drawback of this technique is the need to remove the sample from the vacuum chamber (twice) in order to obtain the information. This post-mortem analysis is very time consuming since the experimental vacuum chambers might require several hours in order to be pumped down to the operative pressure. Nevertheless, in recent times it has been tried to perform the crater analysis right within the experimental station by means of a telemicroscope. The resolution of the measured spots is clearly worse compared to the AFM-Nomarski results but this in-situ approach might be useful for the focused beam optimization [22].

4.4.3 Hartmann Wave-Front Sensor

The wave-front $w(x,y;z_0)$ of a beam is defined as the surface perpendicular to its local direction of propagation, i.e., perpendicular to the Poynting vector $\boldsymbol{S}(x,y)$ at a position z_0 on the optical axis. Hartmann wave-front sensor (WFS) measurements are based on the geometrical-optical determination of the local radiation angles $(\beta_x, \beta_y)_{ij}$ by using a pinhole array, which splits the incident wave-front into a variety of individual beams. A camera installed at a distance f behind the array allows recording the spot distribution, yielding the precise position of the partial beams by computing the respective centroids (1st moments). The deviation of these centroid positions $(x_c, y_c)_{ij}$ from given reference positions $(x_r, y_r)_{ij}$ (determined previously with a plane wave-front) describes the local radiation angle $(\beta_x, \beta_y)_{ij}$ and thus the wave-front gradient:

$$\begin{pmatrix} \partial w / \partial x \\ \partial w / \partial y \end{pmatrix}_{ij} = \vec{\beta}_{ij} = \frac{1}{f} \begin{pmatrix} x_c - x_r \\ y_c - y_r \end{pmatrix}_{ij} .$$

A schematic of the Shack-Hartmann WFS working principle is shown in Figure 15 (the Hartmann sensor has an array of pinholes instead of lenses, but the idea is the same). Based on this information, the wave-front is reconstructed using mathematical algorithms. For spherical profiles a modal expansion in Zernike polynomials is the most adequate, since the expansion coefficients correspond to the image aberrations in Seidel's aberration theory [1]. Thus the Hartmann sensor can be used to measure the aberrations present in a focused laser beam.

In addition, the beam profile (i.e., the discrete power/energy density distribution) may be obtained from the acquired spot distribution by integrating the respective pixel counts, with a lateral resolution given by the array pitch (typically about 150 μm).

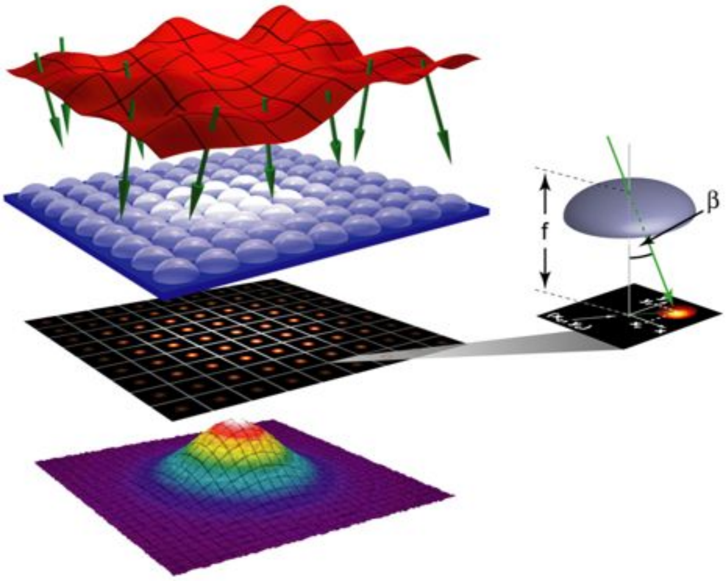

Figure 15 *Measurement principle of the Shack-Hartmann wave-front sensor: The directional distribution (wave-front) of a radiation source may be derived from the exact locations of the spots created by a pinhole array. Integration over this spot distribution yields the beam profile (Credits: MrBeam, Hartmann Wave-front Sensor, Laser-Laboratorium Gottingen e.V., [23])*

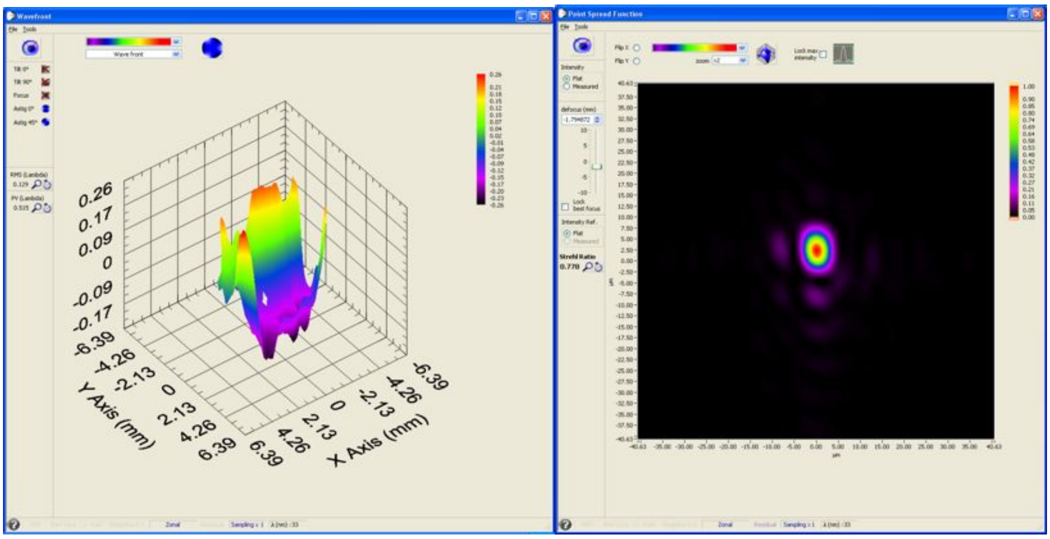

Figure 16 *Left: measured wave-front with the WFS for a 32.6 nm FEL radiation. Right: reconstructed focal spot inside the experimental end-station.*

The WFS employed at FERMI has a 15×15 mm^2 plate of pinholes with 80 μm lateral size each, and 250 μm pitch. The split beams are recorded by a x-ray CCD camera with a pixel size of 24 μm and a field of view of 17×17 mm^2 able to collect the whole photon beam. The instrument can be placed conveniently extra-focus, typically 1.2 m downstream the nominal focal plane, and can be used on-line without interfering with the experiment carried on inside the experimental end-station. The resolution of the reconstructed focused spot is in the sub-μm range, and the system allows to optimize on-line the focusing mirror system by minimizing the Zernike's polynomials. An example of a measured wave-front (left) and its relative reconstructed focused beam (right) is shown in Figure 16. The limitations of this method are related to the low repetition rate of the CCD camera (1 Hz) and the need to work with very low intensity in order to avoid radiation damage of the CCD. Nevertheless, this technique is the most powerful in terms of on-line in-situ characterization and resolution, though it is quite expensive.

References

[1] M. Born, E. Wolf, Principles of Optics, 7th ed. (Cambridge University Press, Cambridge, 1999)
[2] F.A. Jenkins, H.E. White, "Fundamentals of Optics", 4th edition, McGrawHill, New York (1974)
[3] Peatman, W. B. (1997). Gratings, Mirrors and Slits: Beamline Design for Soft X-ray Synchrotron Radiation Sources. New York: Gordon
& Breach
[4] Kirkpatrick, P. & Baez, A. V. (1948). J. Opt. Soc. Am. 38, 766–773
[5] Bencivenga, F., Masciovecchio, C. (2009). Nucl. Instrum. Meth. A, 606(3), 785 – 789; Cucini,
[6] R., Bencivenga, F., Masciovecchio, C. (2011). Opt. Lett. 36(7), 1032–1034.
[7] Cucini, R., Bencivenga, F., Zangrando, M. & Masciovecchio, C. (2011). Nucl. Instrum. Meth. A, 635, 69
[8] Di Cicco, A., Bencivenga, F., Battistoni, A., Cocco, D., Cucini, R., D'Amico, F., Di Fonzo, S., Filipponi, A., Gessini, A., Giangrisostomi, E., Gunnella, R., Masciovecchio, C., Principi, E. & Svetina, C. (2011). vol. 8077, p. 4
[9] Svetina, C., Sostero, G., Sergo, R., Borghes, R., Callegari, C., D'Amico, F., Bencivenga, F., Masciovecchio, C., Di Cicco, A. & Cocco, D. (2011). Nucl. Instrum. Meth. A, 635(1 SUPPL.), S12–S15
[10] H. Wolter, Spiegelsysteme streifenden Einfalls als abbildende Optiken für Röntgenstrahlen, Annalen der Physik, vol. 10, pp. 94-114 (1952)
[11] K. Schwarzschild, Untersuchungen zur geometrischen Optik, II. Astronomische Mitteilungen der Königlichen Sternwarte zu Göttingen, vol. 10, pp. 4-28, (1905)
[12] Pedersoli, E., et al., "Multipurpose modular experimental station for the DiProI beamline of Fermi@Elettra free electron laser" (2011) Review of Scientific Instruments, 82 (4), art. no. 043711
[13] Svetina, C., et al., "The Low Density Matter (LDM) beamline at FERMI: Optical layout and first commissioning"(2015) Journal of Synchrotron Radiation, 22, pp. 538-543
[14] Raimondi, et al., "Status of the K-B bendable optics at FERMI@Elettra FEL", Proceedings of SPIE - The International Society for Optical Engineering, 9208, art. no.920804. (2014)
[15] Spiga, D. & Raimondi, L. (2014). Proc. SPIE, 9209, 92090E
[16] Raimondi, L., Spiga, D.,"Mirrors for X-ray telescopes: Fresnel diffraction-based computation of point spread functions from metrology", Astronomy and Astrophysics 573, A17, (2015)
[17] M. Kirm, et at., "Influence of excitation density on luminescence decay in Y3Al5O12:Ce and BaF2 crystals excited by free electron laser radiation in VUV", phys. stat. sol. C2, 649 (2005)
[18] Bernd Schäfer, et al., "FEL beam characterization from measurements of the Wigner distribution function", Nuclear Instruments and Methods in Physics Research Section A: Accelerators, Spectrometers, Detectors and Associated Equipment, Volume 654, Issue 1, 21 October 2011, Pages 502-507
[19] J. M. Liu, "Simple technique for measurements of pulsed Gaussian-beam spot sizes," Opt. Lett. 7, 196-198 (1982)
[20] J. Chalupský et al., "Characteristics of focused soft X-ray free-electron laser beam determined by ablation of organic molecular solids," Opt. Express 15, 6036 (2007)
[21] J. Chalupský et al., Opt. Express 18, 27836 (2010)
[22] N. Gerasimova, et al., "In situ focus characterization by ablation technique to enable optics alignment at an XUV FEL source" Rev. Sci. Instrum. 84, 065104 (2013)
[23] P. Mercere, et al., "Hartmann wave-front measurement at 13.4 nm with λEUV/120 accuracy", Opt. Lett. 28, 1534-1536 (2003)

5 Experimental results

In this chapter a selection of the most remarkable results obtained from FERMI, PADReS, and the experimental end-stations are presented. The unique properties of the FERMI FEL radiation have been measured by means of the PADReS diagnostics. The outstanding results show not only that the machine is robust and reliable but also that the photon diagnostic section suits perfectly the needs of both users and machine physicists. Moreover, the success of the experimental achievements reported in this chapter could not have been achieved without the essential contribution of the PADReS photon transport and focusing section. During the years it has been proved that the FERMI beamline system fulfills the stability and reproducibility requirements as well as the flexibility to fast switch from different end-stations with different experimental-focusing conditions.
The first section summarizes the most important results obtained with FERMI FEL1 and FEL2 in nominal and exotic configurations. The second section shows the optimization results of the KAOS focusing mirrors followed by two milestone experiments performed at FERMI: the first single shot Coherent Diffraction Imaging, and the Transient Grating spectroscopy experiments.

5.1 FERMI results

The commissioning of the low energy source FEL1 has started in 2011 and lasted for about one year. The results show that the FEL1 source is able to produce high-intensity transform-limited pulses in the EUV/soft x-ray range, with unprecedented stability in intensity, photon energy, and spectral bandwidth, as well as full control of polarization. The first energy spectrum has been recorded on the 23rd December 2011 demonstrating that the spectral content of a seeded FEL based on the HGHG scheme is clean and narrow (Figure 1).

The second phase of the commissioning has continued with the high-energy source FEL2. It has been demonstrated that the double stage cascade FEL based on the fresh bunch technique is able to produce coherent short wavelength radiation (down to 4 nm) with high brilliance, narrow bandwidth, and short pulse duration.

During the following machine runs both FEL sources have been optimized reaching the nominal performance. In addition, some exotic configurations have been exploited allowing to push further the FERMI capabilities. In the following sections the most relevant results will be described.

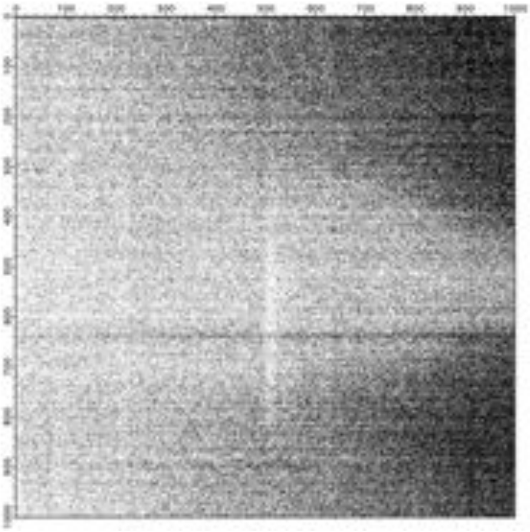

Figure 1 *First energy spectrum recorded during the commissioning of FEL1. The wavelength was set at 43.3 nm (23.6 eV) and the bandwidth was found to be 60 meV.*

5.1.1 FEL1

The standard seed laser wavelength is the third harmonic of a Titanium:Sapphire laser (260 nm) with a pulse duration of 150 fs (FWHM), a peak power of about 100 MW, and a bandwidth of about 0.8 nm, which is about a factor 1.2 larger than the Fourier limit, assuming perfectly Gaussian pulses. During the commissioning, from tens to several hundreds of micro-Joules of FEL emission have been measured with the on-line PADReS I0 monitors and PYDs, tuning the undulators from the 4th harmonic of the seed (65 nm) down to the 13th harmonic (20 nm). Clear evidence of coherent emission has been observed also at the 15th harmonic (17 nm). The measured harmonic conversion has slightly exceeded the theoretical predictions made during the design of the machine [1]. For each harmonic, the FEL has been optimized by tuning the amount of energy modulation produced in the modulator (controlling the seed power) and the strength of the dispersive section (R_{56}). In the following the results obtained at 32.5 nm are shown, while similar results have been obtained in the whole FERMI range [3]. After the optimization of the FEL process to maximize the output power from the six radiators tuned at 32.5 nm in circular polarization, the power as a function of the number of sections contributing to the coherent emission has been measured. Figure 2 shows the measured FEL power evolution along the FEL1 radiators, for both planar and helical undulator configurations. In the inset, the same data are reported in a logarithmic scale, clearly showing the different gain lengths associated with the two polarizations. Fitting the data with an exponential curve has yielded a gain length of about 2.5 meters for planar polarization, and 2.0 meter for circular polarization. This result is in good agreement with both the gain length calculated using the FEL ρ parameter and the formula by Xie [2] evaluated with the electron beam parameters reported in Table 1. As expected, in the case of circular polarization, a shorter gain length and a higher output power has been obtained due to better coupling between the electromagnetic field and the electrons as compared to the case of linear polarization. The measured FEL evolution is also in good agreement with the results of numerical simulation performed using the GINGER numerical code [4]; Figure 2a) reports the predicted FEL output power obtained by simulations.

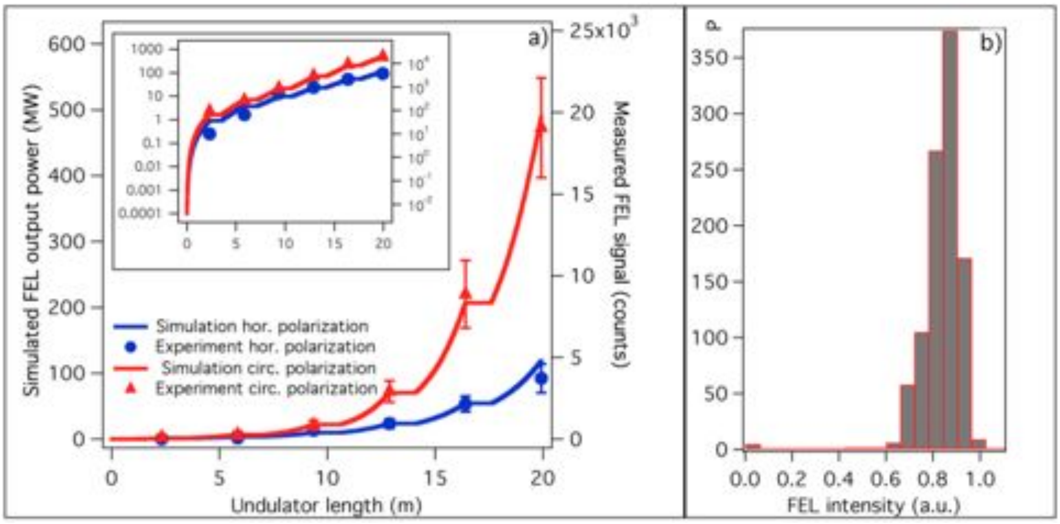

Figure 2 Measured FEL intensity at 32.5 nm [3]. Left: measured FEL energy per pulse (symbols, right axis) as a function of the number of the distance traveled by the electrons inside the radiators, and predicted FEL power from numerical simulations (lines, left axis). Data are shown for both circular (red symbols) and horizontal (blue symbols) polarization of the radiator sections. Error bars reflect the statistical distribution of results obtained from several consecutive pulses. In the inset, the same data are reported in a logarithmic scale. Right: typical shot-to-shot distribution of the pulse energy for 500 consecutive FEL pulses.

***Table 1** Measured electron-beam parameters used to operate FEL1 during the commissioning phase.*

Energy / GeV	1.24
Energy spread rms / keV	<200
Emittance (projected) / mm mrad	~4
Charge / pC	450
Peak current / A	200-300
Beam size rms / μm	~150
Pierce parameter ρ	~0.0013

It is worth noting that FERMI FEL achieved a power close to the level of SASE saturation with a radiator that is about 6-8 gain lengths, while for a SASE FEL generally about 20 gain lengths are needed [5]. Moreover, as shown in Figure 2 right, the measured FEL power fluctuations are of the order of 10%, following an approximately Gaussian distribution. These results show how the use of an external seed allows keeping the power fluctuations under control, without the need to enter deeply into the saturation regime, as it is necessary in the case of SASE [6]. It is important to point out the different origins of power fluctuations in SASE and HGHG FELs. The HGHG process is deterministic, with power fluctuations deriving from shot-to-shot fluctuations in the electron-beam and seed parameters. In principle, in the HGHG process reproducibility can be improved at will, the limit being only technological. The SASE process is, instead, inherently stochastic, so that the statistical distribution of the FEL pulse parameters can only be modified by acting on the exponential or saturated operating regime.

Due to the fact that the seed laser imprints its coherence properties onto the electron beam, the FEL produced by the HGHG is expected to have a very good transverse coherence at the very beginning of the process. Figure 3 left shows the transverse FEL profiles of the FERMI FEL operating at 32.5 nm in horizontal polarization characterized with the PADReS transverse coherence measurement system. Data analysis shows that the FEL pulses are very close to a diffraction- limited Gaussian beam. The FEL spot size measured on the two screens is in good agreement with expectations for a Gaussian beam with a beam waist at the exit of the last undulator of about 200 μm, consistent with the electron beam size at that point. Moreover, very good transverse coherence is also confirmed by the results of a double-slit Young's experiment [7], shown in Figure 3 right. A preliminary analysis indicates that more than 90% of the diffraction pattern intensity is maintained at a slit separation of 0.8 mm.

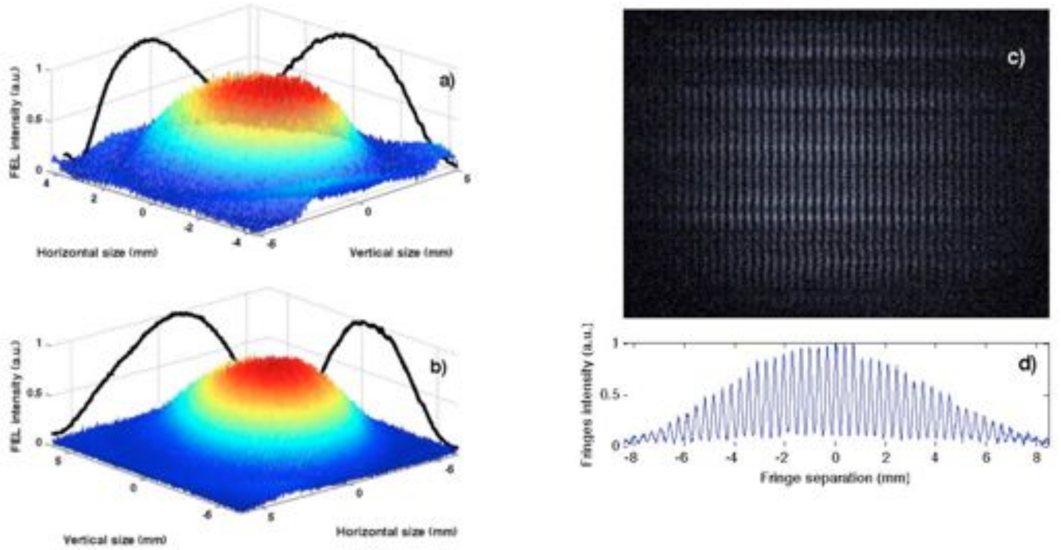

***Figure 3** Left: FEL spot sizes measured on the PADReS YAG screens positioned 52.4 m a) and 72.5 m b) downstream from the radiator exit. The main signal is well reproduced by a Gaussian profile and is characterized by a variance of about 2 mm at the first YAG, and 2.6 mm and 2.4 mm at the second YAG in both the vertical and horizontal directions. Right: c,d) Image and projection of the interference pattern recorded on the second YAG screen when the FEL beam propagates through two 20 μm slits, separated by 0.8 mm, placed about 8.5 meters upstream the screen.*

The FEL1 pulse length has been characterized during dedicated machine and users beamtimes both confirming that the delivered pulses are well below 100 fs rms. The experimental description as well as the obtained results have not been published yet, therefore no experimental data can be shown in here.

One of the most attractive features of seeded FELs, including those employing HGHG, is the possibility of obtaining highly-stable output spectra [8-10]. As already demonstrated in previous experiments [11], the spectral properties of the pulses produced by an HGHG FEL are strongly related to the spectral properties of the seed laser. The results obtained with FEL1 are shown in Figure 4, where both a single-shot spectrum (Figure 4 left) and a sequence of 500 consecutive single shot spectra (Figure 4 right) acquired with the photon energy spectrometer PRESTO (low energy grating). The Figure also shows the measured spectrum of the seed laser pulse. For both pulses the spectra are displayed in meV around the central photon energy, i.e., 4.8 eV (260 nm) for the seed and 38.5 eV (32.5 nm) for the FEL. The measured FEL bandwidth was 20 meV (rms), yielding a relative bandwidth of about $5\cdot10^{-4}$. Experimentally, the relative spectral bandwidth measured at FERMI is about an order of magnitude smaller than that observed at SASE FELs operating in the EUV and soft X-ray spectral regions [12]. Another very important property of light sources to be used for energy-resolved experiments is the wavelength (or photon-energy) stability. The measurements shown in Figure 4 right indicate that the normalized photon-energy stability is of the order of $7\cdot10^{-5}$ (rms), a noticeable improvement when compared to previous SASE FEL results obtained in the same photon energy range [13]. The deterministic nature of the HGHG process allows to achieve substantial improvements relative to SASE FELs.

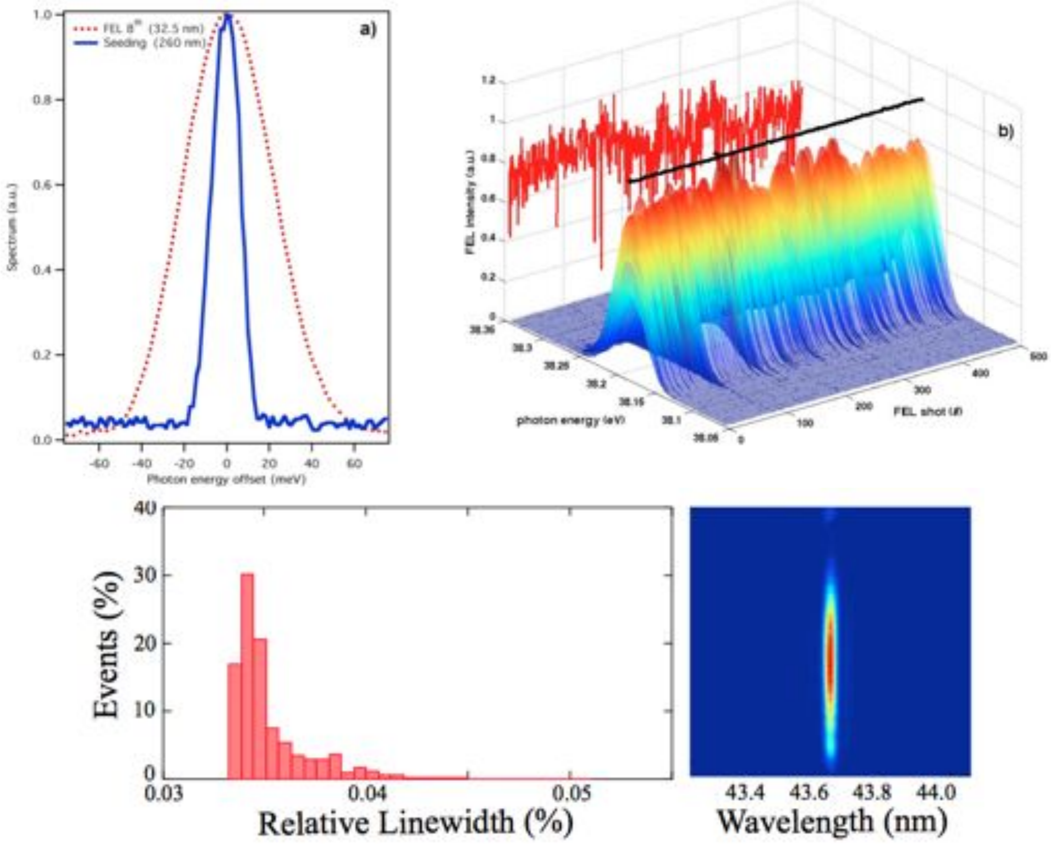

Figure 4 *Top, single shot and multi-shot spectra at 32.5 nm [3]. Top-Left: measured FEL and seed laser spectrum (dashed red and continuous blue lines respectively). Top-Right: Acquisition of five hundreds consecutive FEL spectra. Bottom-Right: single shot spectrum at 43.7 nm (*$n = 6$*) measured with PRESTO and relative line-width statistical distribution (Bottom-Left).*

Another important difference that distinguishes FERMI from other short-wavelength FEL user facilities is its capability to control the polarization of the emitted light. While other FELs use planar undulators, which only emit linearly polarized radiation, FERMI operates with APPLE-II type undulators that allow a continuous change in polarization from purely linear to purely circular, thus in principle guaranteeing strong control to users of the polarization state of FEL radiation. Such polarization control is an important and attractive feature, as it gives access to new areas of science not explorable with those FELs that are restricted to linearly polarized emission. During 2014 a campaign fully dedicated to characterize the FEL1 polarization has been carried out [14]. Three different experimental setups have been employed, having used both DiProI

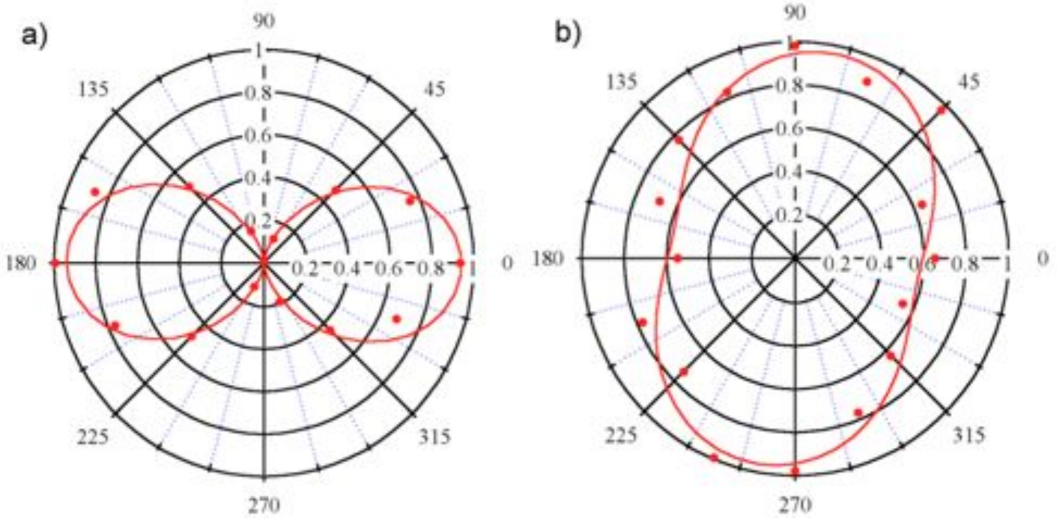

__Figure 5__ Example of the processed signal of the e-TOF showing single shot data for the electron beam distribution on He for the FEL at 32.5 nm horizontally polarized a) and circularly right polarized b).

and LDM beamlines in turn. At DiProI an electron-Time-Of-Flight (e-TOF) and a VUV-optical polarimeter have been mounted in series, while a fluorescence polarimeter has been used at LDM. Scanning through most of the FEL1 wavelength range (26 nm – 55 nm) for both linear and circular polarizations, it has been demonstrated that FERMI has full control of the emitted polarization indeed. The KAOS system has been essential for this kind of measurements since the FEL focused spot has been moved and optimized from one setup to the other several times. Moreover the fast change from DiProI to LDM has demonstrated the reliability of the PADReS switching mirror system.

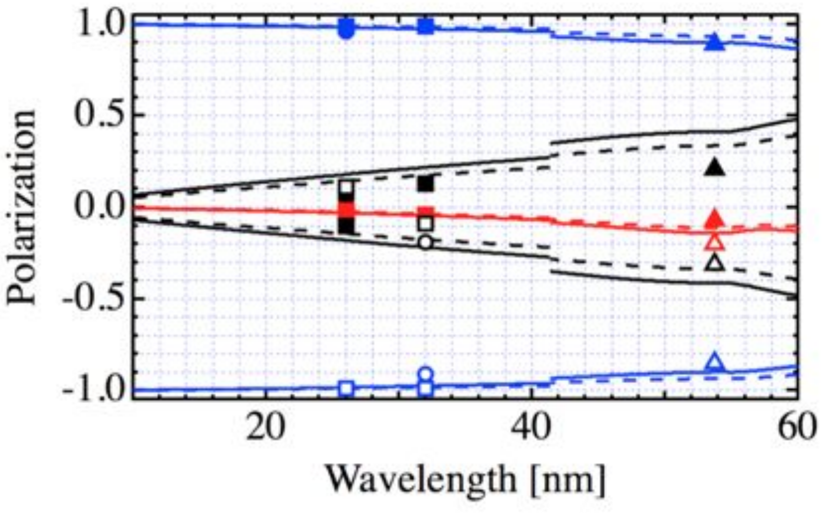

__Figure 6__ Predicted impact of the LDM (dashed lines) and DiProI (continuous line) beamline optics on the Stokes parameters (Red = S1/S0, Black = S2/S0, Blue = S3) for a circular polarized light produced at the undulator. Predictions are shown together with measured Stokes parameters at the experimental stations (circular right filled symbols, circular left empty symbols) with LDM setup (triangles), VUV optical polarimeter (circles) and e-TOF polarimeter (squares).

As an example a set of measurements done with the e-TOF at 32.5 nm for both linear horizontal and circular polarized light are shown in Figure 5. It has been shown that the small ellipticity measured at the end-stations in the case of circular polarized light is due to the presence of the grazing mirrors composing the PADReS, which induce a polarizing effect. In fact, the *s* and *p* component of the electric field are not transmitted in the same way due to the grazing incidence geometry with consequent change in the final polarization of the FEL radiation. Nevertheless, the possibility to tune the APPLE-II undulators allows to generate an elliptically polarized light to compensate the beamline dichroism, providing purely circular polarized radiation to the users. In Figure 6 the measured Stokes parameters in case of circularly polarized FEL light are reported together with the predicted beamline induced polarizing effect (including roughness and contamination) for both the LDM and DiProI beamline mirrors. The Figure shows that the measured behavior is in very good agreement with the optical calculations accounting for the mirror different response to *s* and *p* polarization components.

5.1.2 FEL1 exotic configurations

Recently the possibility to generate and use two-color double-pulses to perform pump-probe experiments has been demonstrated. Several methods have been studied and adopted successfully. The most straightforward one is the regular HGHG operation with the undulators set at different harmonics of the seed laser wavelength. For instance, considering the standard operation of the seed laser (260 nm), the first four radiators can be set at the 4th harmonic (65 nm) while the last two at the 8th (32.5 nm). In this way it is possible to generate two collinear pulses with different energies; however, the control of the relative intensity is poor, and there is virtually no control over the time separation between the two FEL pulses.

A second approach consists in exploiting the so-called over-bunching effect inside the undulators occurring when the power of the seed laser is increased beyond the standard regime. As described in [15], when there is no energy chirp in the seed pulse (i.e., a spatial wavelength distribution along the laser pulse) and the intensity is moderate, then the standard HGHG process occurs. When the power of the seed is increased, the FEL pulse temporally splits in two because the seed power is too high in the middle of the pulse itself: a beating between the two sub-pulses involves a frequency modulation but the spectrum remains centered on a single peak at the harmonic n of the constant seed frequency ω_0. Finally, when the seed laser power is high and the seed pulse frequency distribution is linearly chirped, the combination with the temporal pulse splitting leads to the creation of two separated FEL spectral peaks corresponding to the harmonics of the frequencies ω' and ω'' at the respective position of each sub-pulse (see a sketch in Figure 7).

By changing either the seed laser power or the strength of the dispersive section (R_{56}), it is possible to control both the temporal distance and the spectral separation between the generated pulses. The temporal separation between pulses can be directly retrieved from the measurement of the FEL spectrum and from the knowledge of the seed chirp properties. This approach allows to generate two-color jitter-free double pulses that can be used for pump-probe experiment, with the only limitation on the overall pulses separation, which is of course within the electron bunch length (less than 1 ps at FERMI) and the maximum power of the seed laser.

The experimental demonstration of this intriguing non-trivial process is shown in Figure 8, where a series of FEL spectra acquired with the PRESTO low energy grating are displayed as a function of the seed laser intensity with a fixed time separation of about 200 fs.

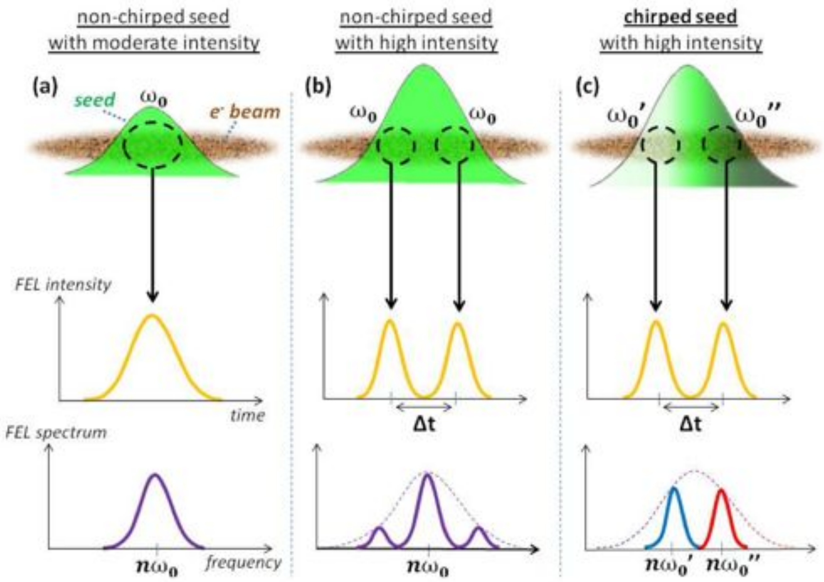

Figure 7 *Sketch of the seed-electrons interaction and resulting FEL (temporal and spectral) outputs for different seed configurations: no chirp and moderate seed intensity a), no chirp and high seed intensity b), chirped seed with high intensity c). In c), the chirp of the seed combined with the temporal pulse splitting leads to the creation of two separated spectral peaks corresponding to the harmonics of the frequencies ω' and ω'' at the respective position of each sub-pulse.*

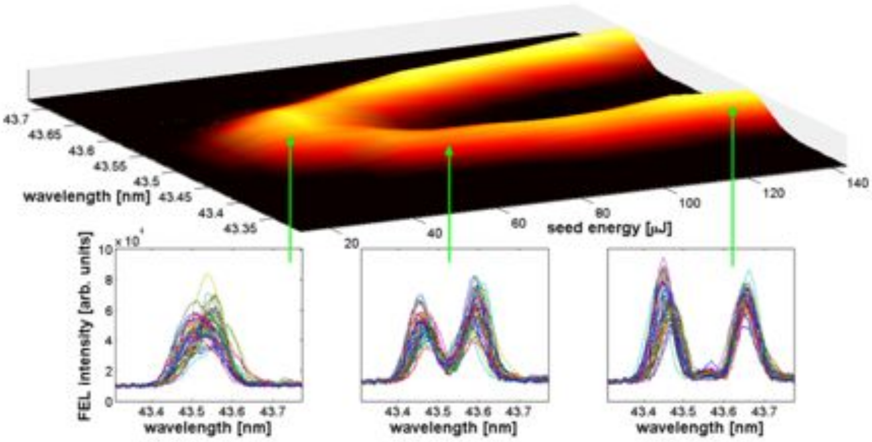

Figure 8 *Experimental characterization of the spectral separation between FEL peaks, as a function of seed energy per pulse. The inserts show the spectrum of fifty consecutive shots, integrated at the positions indicated by the arrows.*

The third approach, originally proposed by Freund and O'Shea [16], consists of seeding the electron bunch with multiple laser pulses. During an internal beamtime (described in [17]) two ultraviolet laser pulses (180 fs pulse duration each) with tunable wavelength, variable time separation, and variable intensity ratio have been used. The seed lasers have been focused over two separated parts of the electron bunch inside the modulator (the first undulator) in order to create two regions with different energy modulations. After the passage through the chicane the two energy modulations have been converted into two different density modulations. The following undulators have been set at the 7th harmonic of resonance of the average seed wavelength, and the FEL process has occurred with the emission of two time separated FEL pulses with different wavelength (pump and probe).

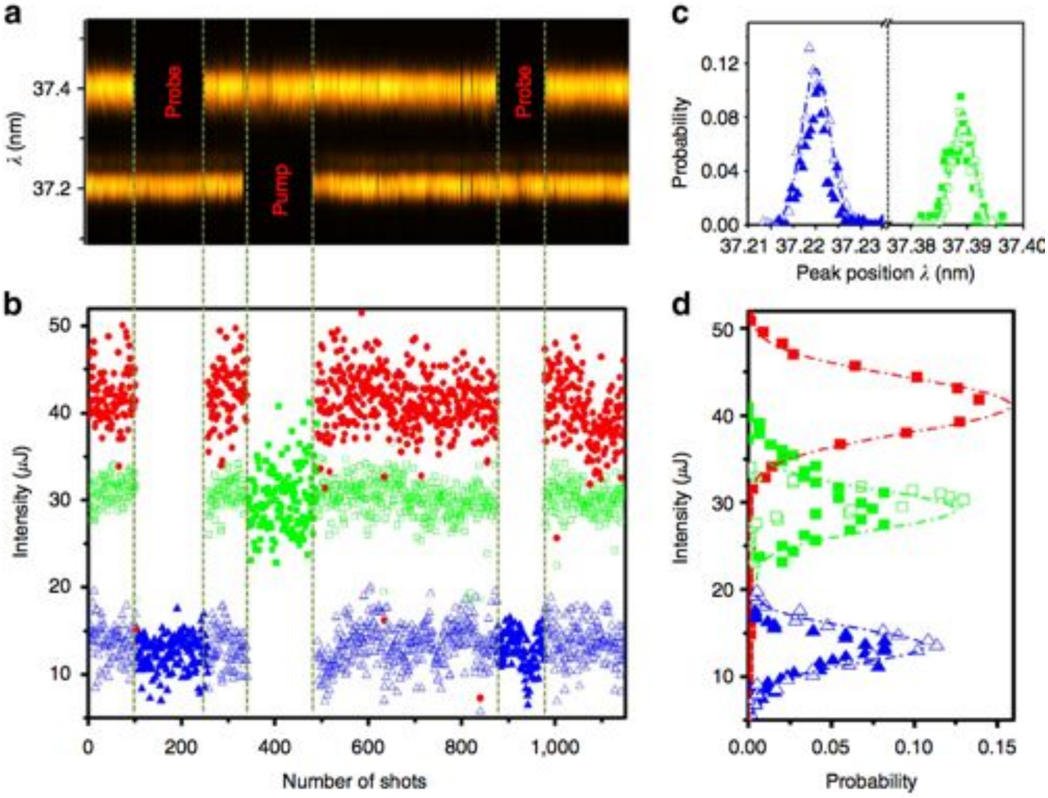

Figure 9 *Spectral and intensity stability of twin-seeded FEL radiation measured with PRESTO. a) single-shot FEL emission spectra and b) corresponding intensities. Green dash lines highlight the intentional blocking of one of the seed laser arms (pump or probe) in order to suppress one of the FEL pulses. The filled markers identify the FEL emission configuration: double FEL emission using twin laser seed pulses (red circles, total signal), single FEL emission probe signal only (blue triangles), and single FEL emission pump signal only (green squares). The open markers are the absolute intensities of a single pulse (green for pump and blue for probe) for two-color emission, obtained from the corresponding peak area in the spectra. Probability distribution for the peak wavelength jitter c) and emission intensity d). The colors correspond to the configurations reported in panel (b)****.***

The advantage of this method is that the time-energy separation as well as the ratio between the generated FEL pulses can be controlled by the original seed lasers. In addition, if the two lasers start from the same source (for instance if a Ti:Sapphire radiation is split, the third harmonics are generated, and an Optical Parametric Amplifier is used) then the two emitted FEL pulses are virtually jitter-free. The drawback of this technique is the upper/lower limits in the achievable delay between the two pulses. The minimum separation between the pulses is given by the seed pulse duration, while the upper limit is limited by the electron bunch length: in our case it ranged between 300 fs and 700 fs. In Figure 9 a sequence of 1150 consecutive single-shot FEL emission spectra acquired with PRESTO and the corresponding intensities for just the pump, the probe, or both pump-probe pulses are shown. The time delay between the pulses was set at 500 fs, and it can be seen that by blocking one of the two seed pulses just one FEL pulse was emitted without changing the electron bunch properties. The so-generated two-color twin FEL pulses have been used to perform a proof-of-principle diffraction experiment with a Ti grating at DiProI. Using the double FEL pulses, tuned across the Ti M-edge, and varying the fluences of the FEL pump pulse, we have shown the occurrence of FEL-induced transparency above a certain fluence threshold. The results are qualitatively described by changes of the optical constants at the wavelength of the probe, and the fluence dependence and both the changes of absorption and refraction coefficients were evaluated and the results are reported in [18].

It is worth to notice that the first experimental proof of the double-colour double-pulse emission in all the previously-mentioned configurations has been provided by the PADReS photon diagnostics system, and in particular by PRESTO. In fact, only exploiting its unique characteristics of being operative online and shot-to-shot, it has been possible to characterize and monitor the spectral content of the FEL pulse(s). Moreover, only the achievable energy resolution of the instrument made the precise spectral determination of the double-pulse possible. Finally, and most important, the determination of the relative intensity of the two FEL pulses was possible only through PRESTO, which can acquire and display both the pulses even if they are temporally displaced by less than a ps. The gas-based intensity monitors, on the other way, cannot resolve such narrow time displacements, and only shows an average signal that generates from the sum of the two individual pulses.

5.1.3 FEL2

The commissioning of the high-energy source FEL2 has taken a longer time compared to the FEL1. That is due to the more complex machine scheme, which is composed of two different stages employing a larger number of undulators. As described in chapter 1 the FEL2 first stage is a compact replica of FEL1: the seed laser impinges on the electron bunch inside the modulator transferring its properties. After the passage through a magnetic chicane two radiators are set at a harmonic n_1 of the seed frequency λ_{seed} with consequent coherent FEL emission at $\lambda_{1^{st}} = \lambda_{seed}/n_1$ (in the 32 nm – 65 nm wavelength range). The commissioning of this first part has been concluded in May 2012 with average photon intensities between 1-5 μJ obtained with the electron parameters reported in table 2. In October 2012 the commissioning have continued with the second stage emission where the electrons are decoupled from the just emitted FEL light and then overlapped again inside a second modulator in a fresh part of the bunch. This second seeding at shorter wavelength allows to start the FEL process inside the next six radiators (set at an harmonic n_2 of the first stage frequency) generating radiation at a wavelength $\lambda_{2^{nd}} = \lambda_{1^{st}}/n_2 = \lambda_{Seed}/(n_1 \times n_2)$. In this way wavelengths between 20 nm and 4 nm (June 2013) have been emitted. The details of the results described hereafter are reported in [19].

Table 2 *Measured electron-beam parameters used to operate FEL2 during the commissioning phase.*

Energy / GeV	1.0 – 1.5
Energy spread rms / keV	~100
Emittance (projected) / mm mrad	~1.5
Charge / pC	500
Peak current / A	300-500
Beam size rms / µm	~150

In Figure 10 a sketch of the FEL2 machine layout with the typical gain curve of the second stage inside the radiators, measured with the I0 monitors, is shown. It has been proved that the second stage output increases by more than one order of magnitude as the number of radiator sections increases from 3 to 6. The measured increase in the output power is a clear evidence of the exponential gain process typical of FELs operating in the high gain regime. The transverse intensity distribution from the second stage has been measured with the PADReS Ce:YAG screens proving that it follows a Gaussian profile in the far field (Figure 10 right) in the whole spectral range of operation. During the commissioning phase average energy per pulse higher than 100 µJ at 10.8 nm and 10 µJ at 4 nm have been measured in circular polarization. However the energy stability is poorer compared to the FEL1 source: fluctuations around 50% FWHM have been measured. This is because the first stage fluctuations are around 20% FWHM (mainly due to timing jitter between the electrons and the seed, as well as to variations of the electron beam properties along the pulse such as energy and current) and they propagate and amplify during the FEL amplification process in the second stage.

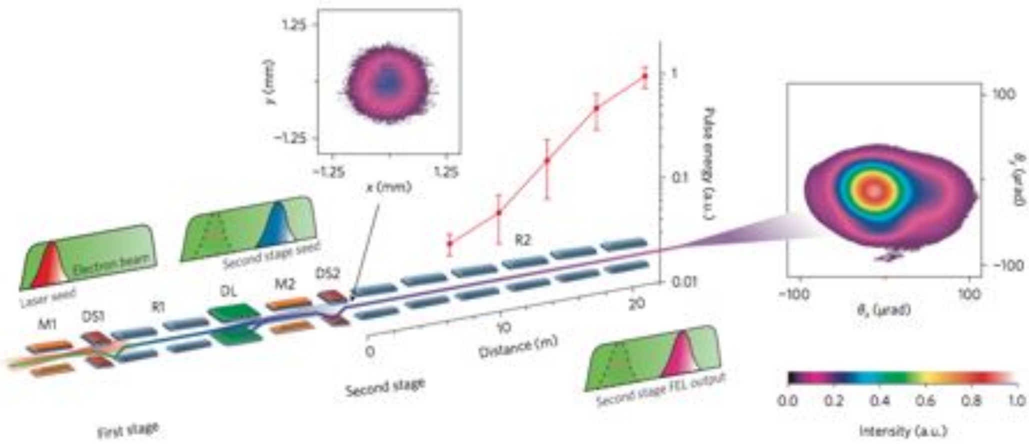

Figure 10 *Layout of FEL2 HGHG double-stage scheme. The first stage is a compact replica of FEL1 source. In the fresh bunch scheme the first stage is followed by the chicane delay line (DL), which ensures that the first-stage-emitted radiation is superimposed temporally over a fresh part of the electron bunch in the second-stage modulator (M2) to begin the upshift process again. The second-stage radiators (R2) are resonantly tuned to a harmonic n_2 of the first-stage radiation. The exponential growth of the second-stage FEL output as a function of the number of resonant radiators is shown, together with the downstream transverse mode shapes of the radiation emitted by each stage (32 nm in the first stage and 10.8 nm in the second stage).*

The spectral content has been measured with the PRESTO medium and high energy gratings. It has been proved that the spectrum is clean with relative bandwidths in the order of $7 \cdot 10^{-4}$ at 10.8 nm. In Figure 11 the spectral content of a single shot at 5.4 nm ($n_1 \times n_2$=48) is shown together with its statistic relative bandwidths over 1400 shots. Recently the fourth harmonic component at 1.3 nm has been observed. Figure 11 right shows the measured spectral line demonstrating the capability of FEL2 to reach the soft x-ray region. The first FEL2 user dedicated beamtimes will begin during 2016.

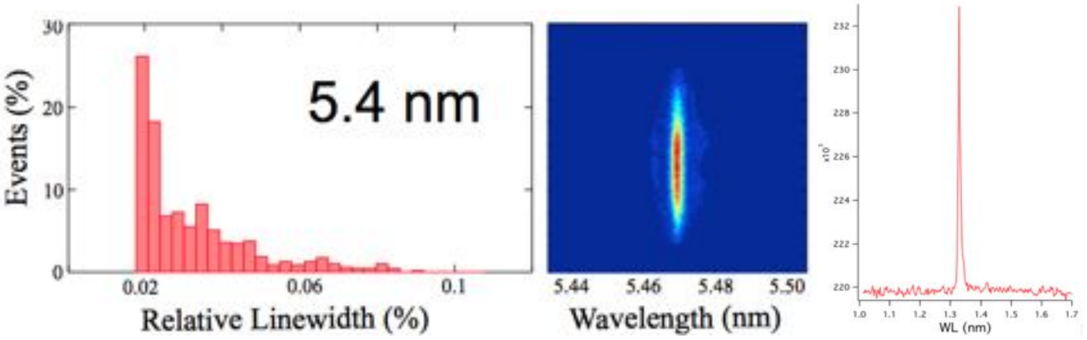

Figure 11 *Single-shot FEL spectra from the second stage and 5.4 nm (center) and histogram distribution of the spectral relative bandwidth (left). Right: first evidence of coherent emission at 1.3 nm. The spectral content is narrow and clean.*

The results obtained during the commissioning of both FEL1 and FEL2 represent an overall success on many fronts. First of all it has been demonstrated that the FEL radiation can be generated via the HGHG scheme in single and double stage configurations. The unique properties of the FERMI light, such as high power, transverse and longitudinal coherence, Gaussian transverse mode, polarization, wavelength tunability and transform-limit ultra-short pulses make FERMI a unique tool for probing matter with unprecedented control. Moreover it has been proved that the PADReS diagnostics and transport/focusing sections have been properly designed, installed, and commissioned, in order to fulfill both the machine and experimental requirements.

5.2 KAOS focusing performances

The optimization of the KAOS with the FEL radiation has lasted about one year. The reasons are the limited availability of radiation at the beamline, and the progressive and constant increase in the performance of the focused beam diagnostics during the time. Several measurement campaigns, devoted to the optimization of the focal spot at LDM and DiProI, have been carried out having employed the techniques described in chapter 4.

Ce:YAG and phosphorous screens have been widely employed because they allow to obtain an on-line visual inspection of the focused FEL beam. But the limitation in their spatial resolution and their very low damage threshold make impossible to reach the diffraction limit of the system. Nevertheless, these scintillators have been extremely useful in the first optimization phase for alignment purposes, and when the spot sizes were above 50 μm. The actual optimization of the KAOS mirror shape has been obtained with the implementation of a Hartmann Wave-Front Sensor (WFS) (from Laser-Laboratorium Gottingen e.V.) that has allowed to reduce the central part of the beam down to 10 μm × 15 μm FWHM. This result has been confirmed after the ablation of a PMMA sample as shown in Figure 12.

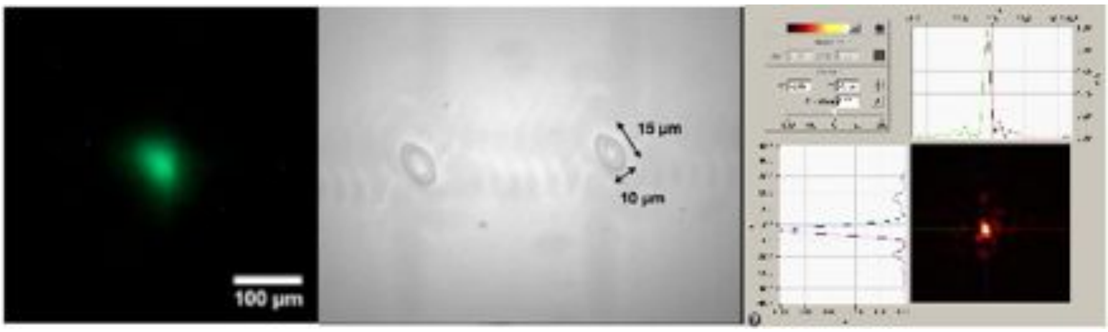

Figure 12 *Left: focused spot as seen at a phosphorous screen inside the DiProI end-station. Center: PMMA ablation after the KAOS optimization confirming the spot size measured with the Hartmann wave-front sensor (right).*

Considering that the diffraction limit of the KAOS is around 5 μm FWHM, there was still room for improvement. Unexpectedly, when a further reduction of the spot size has been tried, a cross-like shape started to appear from the spot. Indentation over PMMA and measurements with the WFS have confirmed the peculiar shape of the focused spot as shown in Figure 13.

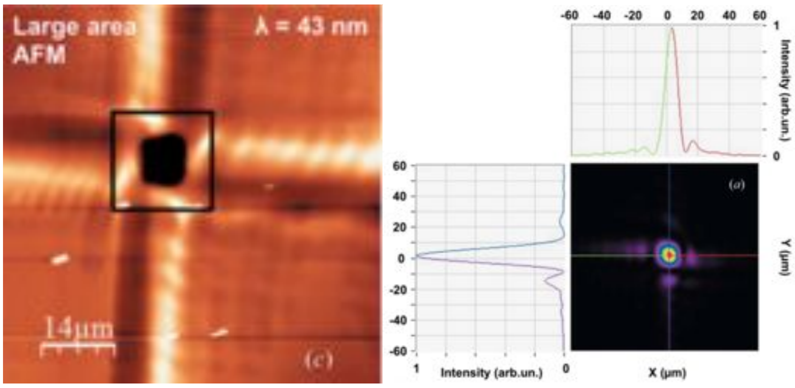

Figure 13 *Left: PMMA indentation of the FEL focused spot. The cross-like shaped beam is confirmed with the WFS measurements (right).*

By changing the radiation energy it has been seen that the effect was negligible at short wavelengths and became strong at the longer wavelengths. Since the mirrors are achromatic optics, this effect had to be geometrical. In fact, as explained in the previous chapters, the divergence of the FERMI photon beam is directly proportional to the wavelength. As a consequence, the longer wavelength reached the sides of the mirrors and, when the beam footprint size was comparable to the tangential mirror dimension, the focused spot resulted to be strongly aberrated. For this reason a set of baffles (metallic blades) to spatially define the photon beam, have been installed right before the KAOS, and the mirrors have been checked again in the metrology laboratory. The metrological inspection has shown that the sides of the mirrors were not bending as expected and that a residual sinusoidal shape was superimposed to the nominal ellipse [20].

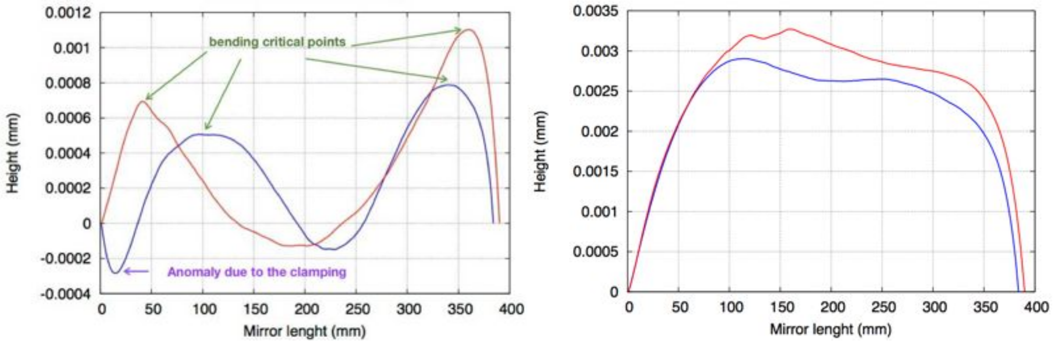

Figure 14 *Left: KAOS measured residual profiles before the recovery (blue horizontal KB, red vertical KB). The sinusoidal shapes have been the cause of the degradation of the focused spot quality. Right: KAOS residual profiles after the recovery. Most of the surface shows the expected shape except for the extreme part of the sides.*

The measured KAOS profiles (Figure 14 left) have been used for simulating the system performances at focus with the WISE code [21-23]. The results have been found to be in agreement with the PMMA ablation and the hypothesis that the shape of the mirrors was out of specification has been confirmed (Figure 15). The cause had been attributed to the clamping, and the mirrors have been unmounted and mounted again in their holders. Afterwards, the new response matrix (see chapter 4) has been calculated and the best profiles obtained. The residual errors have been remarkably reduced except for the extreme part of the sides, where the effect of the clamping was unavoidable (Figure 14 right).

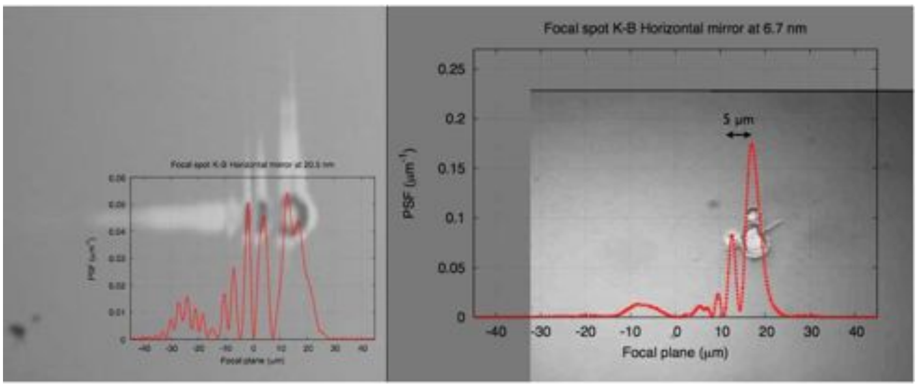

Figure 15 *Comparison between the ablation craters over PMMA and the simulated spots with the WISE code (red curves). The results have confirmed that the geometrical effect was due to the degraded mirror shape.*

After the mirror recovery the KAOS have been reinstalled before the end-stations. With the aid of the baffles the nominal focal spot sizes have been reached in both DiProI and LDM end-station employing the WFS and the ablation technique. Figure 16 shows the good agreement between the PMMA indentation and the WFS reconstruction at 32.5 nm wavelength.

Up to now the mirrors are performing as expected, and with the aid of the WFS the mirror shape can be controlled following the users requirements. Several experiments have been successfully accomplished thanks to the KAOS focusing capabilities, both in the DiProI and LDM end-stations. The possibility to reach the diffraction limited spot size combined with the unique properties of FERMI have recently allowed to perform the first short wavelength coherent control experiment at LDM. In the experiment phase control of two FEL pulses (4th and 8th harmonics) at the attosecond level has been demonstrated, thus opening the way for unique ultra-fast experiments where the electron wave-packet can be shaped [24]. In the near future this will allow to understand important processes in gasses and condensed matter like chemical reactions, catalysis, photosynthesis and solar energy production.

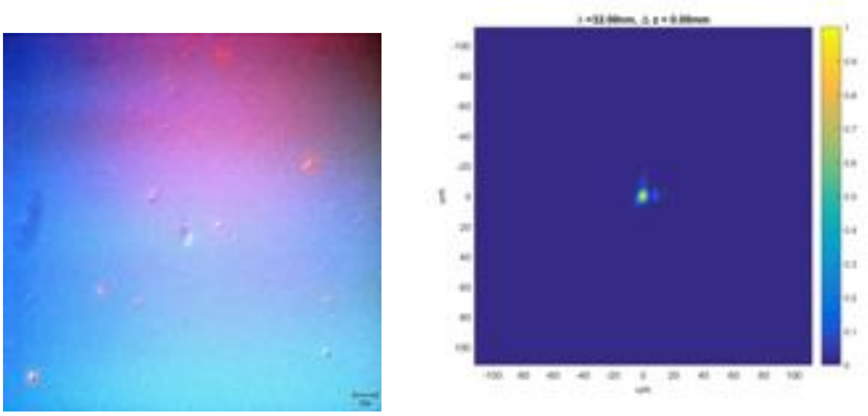

Figure 16 *Left: PMMA ablation imprint (the black bar corresponds to 20 μm) and WFS reconstruction (right) of the focused FEL (32.5 nm) after the KAOS recovery and optimization. The measured spot size is around 5.5 μm FWHM for both techniques.*

Many experiments requiring lower fluences but full control of the photon beam inside the experimental chamber has been done thanks to the active shape of KAOS. By using the actuators and with the aid of the WFS, the focused beam size has been changed from tens up to hundreds of microns accordingly to the user needs. Spots of the order of 10-30 μm FWHM have allowed to measure for the first time the conformation sequence recovery of a non-periodic object from the diffraction pattern before destruction [25] opening the possibility to characterize the different conformational states of protein molecules. Larger spots (30-100 μm FWHM) have been used to perform the first Coherent Diffraction Imaging experiment (see section 5.3 for details) or to probe the ultra-fast demagnetization dynamics after a spatially localized optical excitation with a nanometer scale spatial resolution [26]. It has also been possible to probe the ionization dynamics of resonantly excited helium nano-droplets [27] as well as to observe a novel collective autoionization process in these multiply-excited systems [28].

The possibility of enlarging the spots even more (100-500 μm FWHM) have permitted to study the ultra-fast spin-switching of a ferromagnetic alloy by means of the resonant magneto-optical Kerr effect [29].

Finally the possibility to control the focal length of the KAOS (i.e., the longitudinal position of the focal spot) has allowed to host non-standard experimental setups like the mini-TIMER (see section 5.4 for details) or to use an external experimental chamber installed downstream of the already existing end-station. For instance, it has been possible to optimize the focal spot around 3 meter downstream DiProI determining the Magnetization and Microstructure Dynamics in Fe/MnAs/GaAs(001) [30] or performing two-colour resonant-pump resonant-probe magnetic scattering opening the way for studying the dynamics of complex relaxation processes, such as Auger cascades or sequential multiple ionization, and of charge transfer processes in large molecules and clusters [31].

It is worth to stress that the fore mentioned outstanding results could have not been obtained without the possibility to fully control the focal spot size and position. The

KAOS has been proved to be essential and reliable for all the experimental needs, and will be adopted by the future beamline MagneDyn as well (see chapter 6 section 6.2 for details). In the near future an upgrade of the pushers will be done in order to achieve higher stability in the long period of operation of the system. The stepper motors will be replaced by piezo-actuators able to curve the mirrors with higher resolution and stability.

5.3 First single shot Coherent Diffraction Imaging at DiProI

The first proof-of-principle CDI experiments with fixed targets [32] have been carried out with 32.5 nm pulses at DiProI end-station using the indirect detection system described in chapter 1. The target objects have been fabricated by Focused Ion Beam (FIB) depositing a 100 nm thick platinum film on 50×50 μm^2 wide, 20 nm thick Si_3N_4 windows. As shown in Figures 17 (a, b), around the main objects three reference dots of 250 nm diameter, at the vertex of an equilateral triangle, have been deposited to perform holographic imaging. To guarantee sufficient contrast for reconstruction of the image from the measured speckle pattern, the distance between the reference dots and the sample center has been chosen to secure that the hologram did not overlap with the autocorrelation function of the object. Figures 17 (c, d) show the diffraction pattern, measured hitting the sample with a single focused FEL pulse. For a FEL pulse energy of ~20 μJ the photon flux density in the focal spot on the sample was $2.6 \cdot 10^9$ ph/μm^2. The recorded diffraction patterns contained about 10^8 photons and recorded information at the edges of the CCD plane up to a spatial frequency of 9.8 μm^{-1}, which is equivalent to diffraction limited resolution of about 50 nm. For the simple object in Figure 17 a) (FERMI logo) some structural information could be directly inferred from analysis of the diffraction pattern. The oval diffraction modulation with a periodicity of about 0.5 μm^{-1} in Figure 17 c) corresponded to the circular ring of the object with real space dimension of about 2 μm, while the bright stripe at about 20° with respect to the vertical axis was due to the stretched triangle below the ring forming the object. For the more complex object, shown in Figure 17 b) (Christmas tree), a real space reconstruction has been necessary to obtain structural information. Inside both diffraction patterns in Figures 17 (c, d) a fine modulation of 0.1 μm^{-1} and 0.067 μm^{-1}, respectively, could be seen corresponding to the spatial distance between main object and reference dots. Such fine amplitude modulation encoded the relative phase between the scattering wave from the object and the reference dots, allowing fast reconstruction of the image with a single Fourier transform process of the diffraction pattern. In the obtained holograms the reference signal has been sufficiently strong to reconstruct the objects: in the first case, Figure 17 e), six holograms of different intensities could be seen, while in the second case, Figure 17 f), only four holograms were visible. This difference could be ascribed to non-homogenous illumination of the structures in a single-shot mode.

The diffraction patterns in Figures 17 (c, d) can also be used to reconstruct the scattering object applying phase retrieval techniques. Figures 17 (g, h) show the obtained reconstruction using 2000 iterations of the Relaxed Averaged Alternating Reflections (RAAR) algorithm [33] combined with a “Shrinkwrap” dynamic support constraint [34] without any *a priori* knowledge about the object. The reconstructed image showed both the main object and the reference dots. It should be noted that, while in Figure 17 g) three dots are present, only two are visible in the reconstruction of

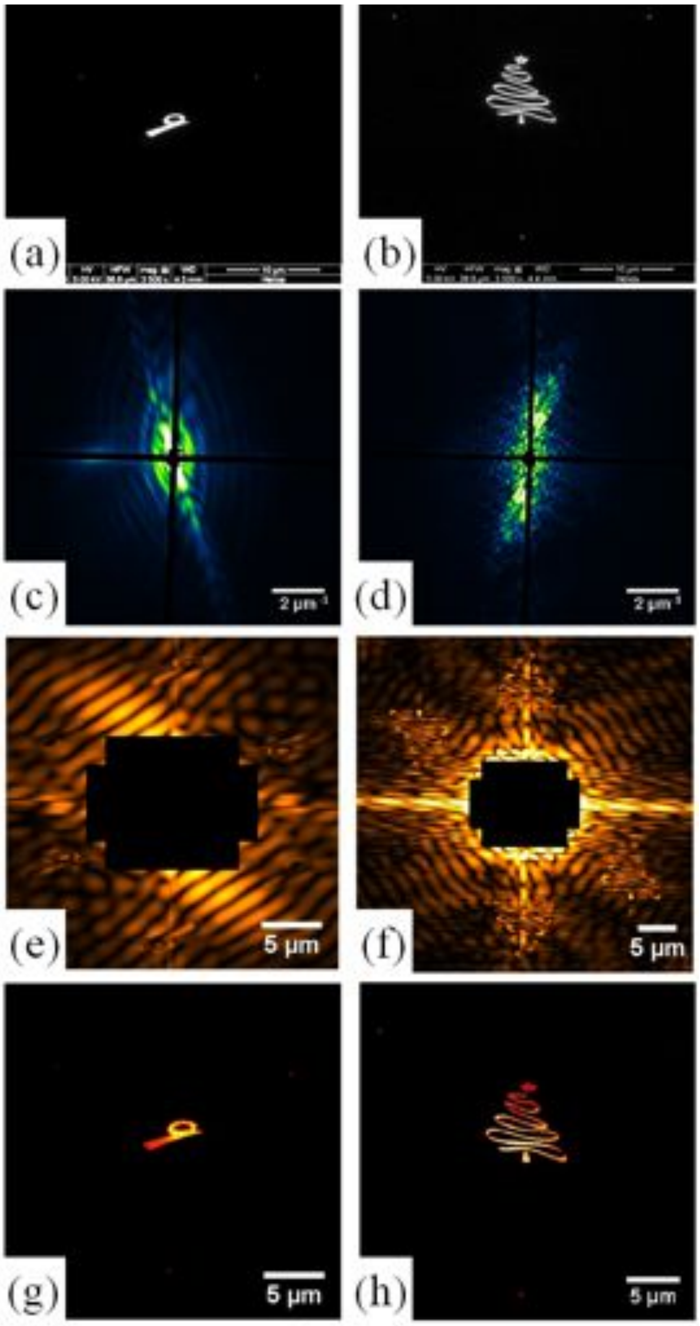

Figure 17 *First CDI result obtained at DiProI end-station [32]. a), b): SEM images of the samples. c), d): single- shot diffraction pattern with 32.5 nm FEL pulse. e), f): Holographic reconstruction of the objects. g), h): Phase retrieval reconstruction.*

the object in Figure 17 h), consistently with the supposed partial illumination of the sample in the last case. These results confirm that the intensity and temporal structure of the FEL1 pulses are sufficient to get a snapshot image of the micro object before its Coulomb-explosion.

5.4 Mini-TIMER experiment

Four-wave mixing (FWM) processes, based on third-order non-linear light-matter interactions, can combine ultrafast time resolution with energy and wavevector selectivity, and enables to explore dynamics inaccessible by linear methods [18, 35-40]. The coherent and multi-wave nature of FWM approach has been crucial in the development of cutting edge technologies, such as silicon photonics [41], sub-wavelength imaging [42] and quantum communications [43]. All these technologies operate with optical wavelengths, which limit the spatial resolution and do not allow probing excitations with energy in the eV range.
The extension to shorter wavelengths, that is the extreme ultraviolet (EUV) and soft-x-ray range, allows to improve the spatial resolution and to expand the excitation energy range, as well as to achieve elemental selectivity by exploiting core resonances [44-47]. So far, FWM applications at these wavelengths have been prevented by the absence of coherent sources with enough brightness and suitable experimental setups. FWM can be generally described as an inter-modulation phenomenon in non-linear optics where two or three coherent laser pulses are overlapped in space and time on a sample generating one or two new pulses. It is a phase-sensitive process and, in order to be efficient, the involved pulses have to fulfill the phase matching conditions (Figure 18b). The simpler case of non-degenerate FWM is the Transient Grating (TG) in which two pulses (pumps), having the same polarization and wavelength, are overlapped into a sample and the elastically scattered third pulse (probe) is observed. In a generic TG experiment, the interference of the two time-coincident pulses results in a standing electromagnetic wave with spatial periodicity $\Lambda = \lambda/2\sin\theta$, where λ and 2θ are the wavelength and crossing angle of the two interfering pulses, respectively. Such an excitation couples with the internal degrees of freedom of the sample, leading to a modification of the optical properties of the material. The time evolution of the induced grating encodes the time evolution of the sample's excitations with wave-vector (Q) equal to that of the grating ($2\pi/\Lambda$). These effectively couple with the induced transient grating and their time evolution can be probed by looking at the diffraction of a third (time delayed) pulse, provided that the latter fulfills the phase matching conditions, which, in such TG experiments, reduces to the Bragg scattering condition. In the first few fs the interactions only involve the electronic degrees of freedom, while at ps time scales rearrangements of atomic-density fluctuations, such as inter- and intra-molecular vibrations, occur. Slower processes like heat and particle diffusions take place at much longer times (>ns). More in general TG allows to exploit the impulsive Rayleigh, Brillouin, and Raman scattering processes [48].

The first step towards the direction of EUV/soft x-ray FWM has been done at FERMI with the Mini-TIMER experiment [49]. Mini-TIMER is a compact setup specifically developed for demonstrating the feasibility of TG experiments with a FEL. Figure 18a shows a sketch of the Mini-TIMER experiment: two FEL pulses (wavelength λ_{EUV}=27.6 nm, with estimated time duration around 60-80 fs, pulse energy $I_{EUV1} \approx I_{EUV2} \approx 5$ μJ, spot size ≈0.04 mm^2, with a crossing angle 2θ=6.16^o) have been overlapped on a vitreous SiO$_2$ sample with the surface oriented orthogonally to the bisector of the FEL beams. The interference of the two pulses have generated EUV TG with a spatial periodicity $\Lambda=\lambda_{EUV}/2\sin(\theta) \approx 256.8$ nm. An optical pulse (λ_{OPT}=392.8 nm, time duration ≈100 fs, pulse energy $I_{OPT} \approx 2$ μJ, spot size ≈0.002 mm^2), coplanar to the FEL beams, has been sent into the sample at an angle of incidence θ_B=49.8°. The polarization of the fields was orthogonal to the scattering plane.

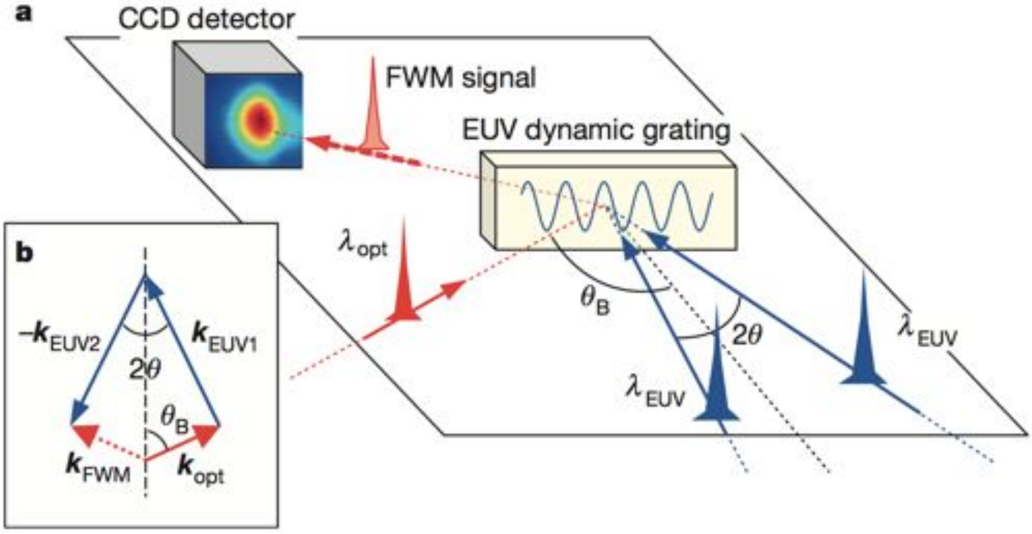

Figure 18 *FWM experiments with EUV/soft x-ray transient gratings [49]. a) Sketch of the FEL-based FWM experiment: 2θ, θ_B, λ_{EUV} and λ_{OPT} are the crossing angle between the two FEL beams that generate the EUV dynamic grating, the angle between their bisector (dotted black line) and the optical beam, the FEL wavelength and the laser wavelength, respectively. A CCD sensor is placed in the expected propagation direction of the FWM signal beam ($\mathbf{k}_{FWM}$), which is determined by the phase matching condition (shown in b; here $\mathbf{k}_{OPT}$, $\mathbf{k}_{EUV1}$ and $\mathbf{k}_{EUV2}$ are the wave-vectors of the optical and of the two FEL pulses, respectively).*

The chosen (λ_{EUV}, λ_{OPT}, 2θ, θ_B)-values have fulfilled the phase matching condition (Figure 18b), which in the present TG experiment have reduced to: $\lambda_{EUV}\sin(\theta_B)=\lambda_{OPT}\sin(\theta)$. This determines the propagation direction of the FWM signal: $\mathbf{k}_{FWM}=\mathbf{k}_{EUV1}-\mathbf{k}_{EUV2}+\mathbf{k}_{OPT}$, where $\mathbf{k}_{EUV1,2}$ and $\mathbf{k}_{OPT}$ are the wave-vectors of the EUV fields and of the optical one, respectively. Along $\mathbf{k}_{FWM}$ the non-linear signal, radiated by different portions of the sample, yields to a FWM signal propagating downstream the sample as a well-defined beam. The experiment has been carried out at the DiProI end-station using a purposely designed experimental setup based on the wave-front splitting of the FEL beam by means of a grazing incidence plane mirror with a sharp edge. The FEL focusing has been provided by the above-mentioned KAOS focusing system that has been slightly detuned to relax the spot size at the sample in order to avoid sample damage. Let just underline that without the KAOS capabilities it would have not been possible to control the spot shape and dimension needed for the experiment. The FEL properties have been acquired on a shot-to-shot basis by the PADReS on-line diagnostics and an Al filter has been used to remove the spurious seed laser radiation. The layout of the experimental set-up used to generate and probe the TG is shown in Figure 19a. The system to split and recombine the FEL beams was based on three 70 mm-long carbon-coated plane mirrors (M1, M2 and M3) working at grazing incidence (≈3°). M1 could be inserted into the path of the incoming FEL beam by a y-translation, and has been used as a wave-front beamsplitter. The two split beams propagating downstream M1 have been recombined on the sample by mirrors M2 and M3. The design position of the mirrors corresponds to a parallelogram geometry, where the splitting angle after M1 (2α=6 °) equals the crossing angle at the sample (2θ) and the M1-M2 distance ($d1$=125 mm) equals the M3-sample one ($d2$). In this case the optical path difference (ΔL) between the FEL path 1 (FP1) and FEL path 2 (FP2) vanishes, ensuring the time coincidence of the crossed FEL beams. The system had several motorized degrees of freedom to adjust the mirror positions and angles during the experiment and have been used to change the value of 2θ (in the 3^o-9^o range) keeping fixed the arrival time difference of the two FEL pulses ($\Delta t_{EUV\text{-}EUV}$) or vice-versa. The possibility to vary $\Delta t_{EUV\text{-}EUV}$ (in the ±0.2 ps range for $2\theta \approx 6^o$) at fixed 2θ makes the setup a compact split and delay device, with the advantage of the angular discrimination of the two FEL pulses.

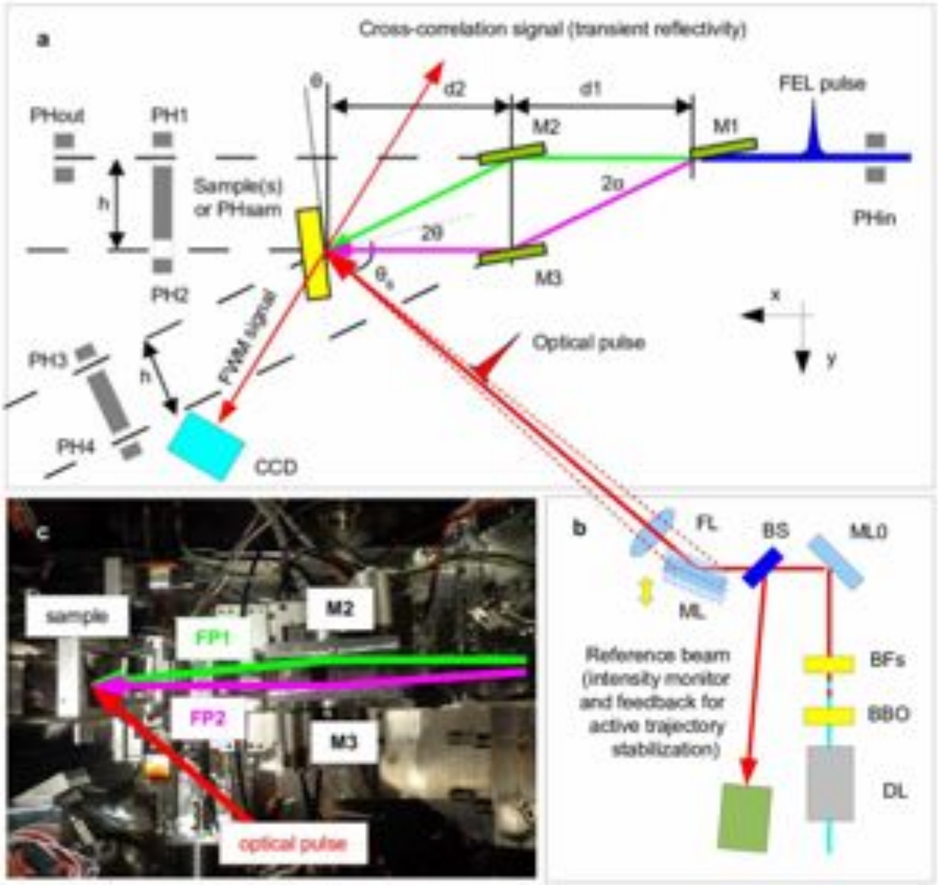

Figure 19 *Experimental set-up for FEL-based FWM measurements [49]. a) Top-view layout of the experimental set-up used to split and recombine the FEL beams. b) Top-view layout of the experimental set-up used to control the optical beam. c) Top-view picture of the set-up: the two FEL paths (FP1 and FP2) downstream of M1 and the trajectory of the optical pulse are indicated.*

Indeed, from atomic force microscopy measurements on permanent gratings (carried out after the experiment) we were able to determine the actual value of 2θ (i.e., $6.16^o \pm 0.02^o$) used in the FWM measurements. Such deviations with respect to the design value (6^o) have been compensated by a slight change of the FEL wavelength (λ_{EUV}) and the incidence angle of the optical pulse at the sample (θ_B).

A sketch of the system used to control the optical pulse (probe), external to the end-station, is shown in Figure 19b. This pulse was a fraction of the seed laser, thus ensuring "jitter-free" conditions, i.e., the FEL-optical timing jitter (<10 fs rms) [50] is much shorter than the pulse duration. An optical delay line (DL) has been used to set the time delay (Δt) between the FEL pulses and the optical one in the -10 to +300 ps range. The optical beam has been frequency-doubled at 392.8 nm wavelength by a BBO

(Barium Boron Oxide) crystal, and routed into the sample by a reflective mirror (ML; grazing angle ≈22.5°) and a focusing lens (FL; focal length 600 mm), whose focal plane contained the crossing point of the two FEL beams. The ML could be translated along the y-direction, in order to change θ_B (in the 47°-51° range) without varying the position of the laser spot at the sample.

An accurate determination of the temporal and spatial coincidence of the three input beams has been obtained by cross-correlation measurements [51] based on FEL-induced transient optical reflectivity changes ($\Delta R/R$) from a Si_3N_4 reference sample. In such measurements M3 has been removed from FP2 to collect the cross-correlation trace between the optical pulse and the FEL pulse coming from FP1. The half-drop of the $\Delta R/R$ profile has been assumed as Δt=0. Afterwards, M2 has been removed and M3 has been inserted in order to collect the cross-correlation trace associated to the FEL pulse coming from FP2. Iterative measurements, carried out by varying the pitch of M1 and roto-translating M3, keeping fixed the FEL trajectory downstream M3, have allowed to set the condition $\Delta t_{EUV\text{-}EUV}$=0. Furthermore, since the amplitude of the $\Delta R/R$ drop is proportional to the FEL fluence at the sample [52], such measurements also have allowed to equalize the fluence level of the two FEL beams in the interaction region.

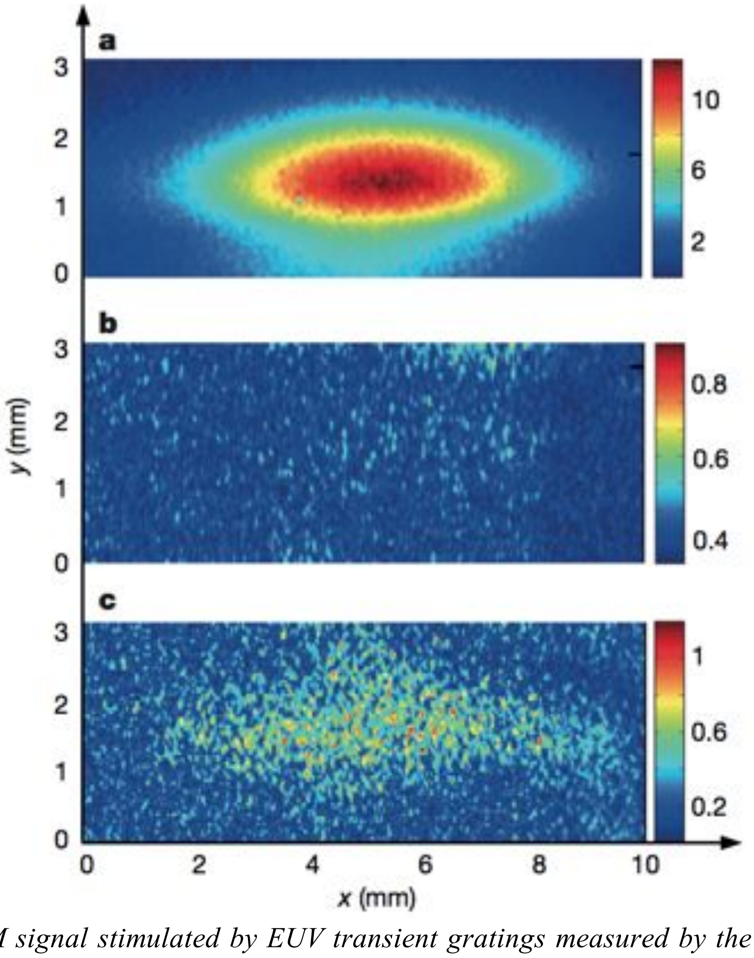

Figure 20 *FWM signal stimulated by EUV transient gratings measured by the CCD placed in the direction of* $\mathbf{k}_{FMW}$ *(x and y are the directions parallel and orthogonal to the scattering plane, respectively, while the color scale reports the average number of photons per FEL shot). The images have been acquired at* $\Delta t=0$ *(a),* $\Delta t=-0.5ps$ *(b) and* $\Delta t=70ps$ *(c) [49].*

Once the time-space coincidence of the three beams has been set, the phase matching condition, necessary to observe the FWM signal, have been optimized by acting on θ_B. The signal has been recorded by a Princeton Instrument PI-MTE back-illuminated Charged Coupled Device (CCD) camera with frame format 2048x2048 pixels and 13.5x13.5 μm^2 pixels size. The detector has been positioned ≈250 mm downstream the sample, and oriented at an angle of ≈49°. A 15x5 mm^2 slit has been placed in front of the CCD in order to reduce spurious light, mainly coming from diffuse scattering of the optical pulse (transmitted through the sample) reflected by the walls of the experimental chamber. Figure 20a shows a CCD image of the FWM signal beam acquired at Δt=0, whereas Figures 20b and 20c report the measurement at Δt=-0.5 ps (before the generation of the TG) and Δt=70 ps (the time evolution), respectively. The observation of a signal that had propagated along $\mathbf{k}_{\mathrm{FWM}}$ for Δt>0 in the concurrent presence of the three input beams undoubtedly has demonstrated the occurrence of FWM processes stimulated by EUV transient gratings. The total intensity of the FWM signal (I_{FWM}) at Δt=0 was about $\approx 6 \cdot 10^5$ photons/pulse, corresponding to an efficiency $\eta_{FWM}=I_{FWM}/I_{opt}\approx 1.5 \cdot 10^{-7}$. For each probed Δt-value five CCD images (exposure time: 1 minute) have been acquired with the FEL on, and two with the FEL off (to remove the background due to diffuse scattering of the optical laser). Such frequent and accurate determination of the background has allowed to account for small drifts in the CCD response during the Δt-scan, which has lasted several hours. After background subtraction a low-pass Fourier filter has been applied in order to reduce the noise and improve the contrast. The intensity stability of the FEL has been typically better than 7 % during the acquisition of the FEL on images, and about 20 % throughout the whole Δt-scan.

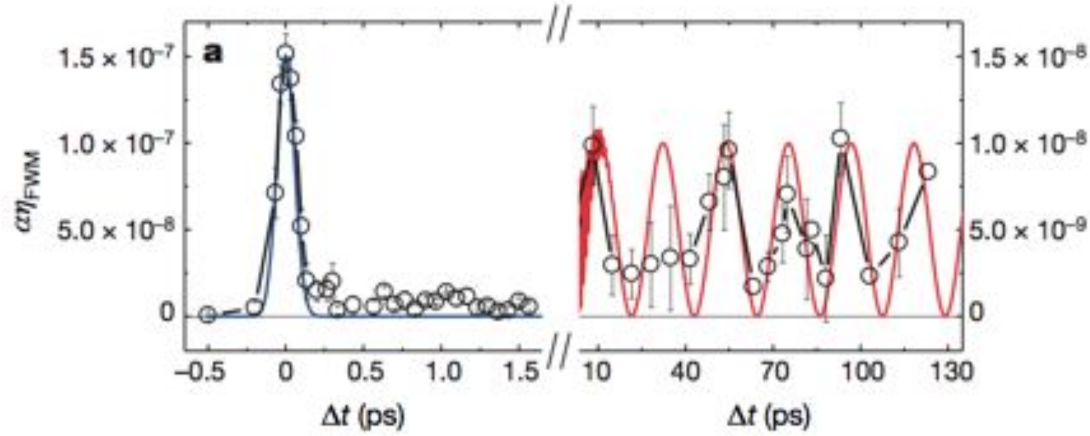

Figure 21 *Time evolution of the FWM signal. Black circles (connected by lines where there is a clear peak) show the time dependence of the FWM signal, scaled to the intensity of the input beams (error bars are estimated as one standard deviation of the set of CCD images corresponding to the same Δt value); the blue and red lines are the expected signal modulation due to Raman and acoustic modes, respectively (right-hand y axis plots same quantity as left-hand axis, but on an expanded scale [49].*

In a proof-of-principle spirit it has been assumed that the time dependence of the FWM signal was due to impulsively stimulated vibrational modes, which can be observed in the time-dependent coherent FWM signal [53]. The time evolution of the measured signal η_{FWM} is shown in Figure 21 (the data are scaled by the factor $\alpha=I_{EUV1}(\Delta t=0)\cdot I_{EUV2}(\Delta t=0)/[I_{EUV1}(\Delta t)\cdot I_{EUV2}(\Delta t)]$. Approaching Δt=0 from negative delays a fast rise of the FWM signal has been detected. For Δt>0 an appreciable FWM signal has been observed over the whole probed Δt-range (i.e., up to 130 ps). The signal observed at large Δt (>10 ps) has been ascribed to thermal relaxations and longitudinal acoustic modes. The latter is expected to induce a signal modulation at frequency $\nu_{LA}=c_s/L\approx 23.2$ GHz (where c_s=5970 m/s is the sound velocity of vitreous SiO_2), which is compatible with the obtained data. During the FWM measurements the FEL fluence has been kept below 50 mJ/cm^2 in order to avoid the creation of permanent gratings. In fact, the creation of permanent gratings has been observed after an exposure of about 100's FEL shots at FEL fluences larger than ≈50 mJ/cm^2 per pulse. The illumination of these permanent gratings by the optical laser has led to a diffracted signal along $\mathbf{k}_{\mathrm{FWM}}$ even in the absence of the FEL pulses.

After the experiment a set of Atomic Force Microscope (AFM) topographies have been acquired over the sample. The scans have been performed with a XE-100 (Park Instruments) instrument in contact mode, using commercial cantilevers (Mikromasch, CSC38, spring constant k=0.03-0.09 N/m), with samplings of 1024 pixels in both directions. Figure 22 shows the AFM images (8x8 μm^2) in a non-irradiated area (a), a strongly irradiated area with fluence above 50 mJ/cm^2 (b), and the low fluence irradiated area where the experiments have been performed (c). Figures 22 d,e,f) report the corresponding depth profiles of the sample surface while the corresponding Power Spectral Densities (PSDs) of the line profiles are shown in Figure 22 g, h, i).

The non-irradiated area presented a roughness of about 0.6 nm rms and 5 nm peak-to-valley. A grating with peak-to-valley amplitude of about 18 nm and a period of 256.7±0.9 nm (corresponding to $2\theta=6.16^{\circ}\pm0.02^{\circ}$) was clearly visible in the sample surface irradiated at high FEL fluence. No specific frequencies have been found in the non-irradiated sample (the peak at ≈35 μm^{-1} is an artifact due to the electronic noise of the employed AFM device), while the first peak at ≈0.5 μm^{-1} in the PSD, shown in Figure 22h), reveals a modulation with a period of ≈2 μm, most likely due to diffraction effects from the mirrors. The sample surface irradiated at low fluence has shown a roughness similar to that of the non-irradiated sample, and frequencies ascribable to the formation of permanent gratings were absent.

The high grating visibility after multi-shot illumination indicates that the shot-by-shot fluctuations in the optical path difference (i.e., in the relative phase) between the crossed FEL pulses have been lower than λ_{EUV}. Such a low phase jitter might in principle allow for lithographic applications. Indeed, the interference between coherent FEL pulses would permit to imprint permanent gratings with a pitch as short as a few nm's by exploiting larger crossing angles and shorter FEL wavelengths.

The results obtained with Mini-TIMER have demonstrated the generation of dynamic EUV gratings using fully coherent FEL pulses for the first time. The non-linear interactions between the induced grating and an optical pulse have allowed to observe the first FEL-stimulated FWM signal, that encodes the dynamics of impulsively stimulated collective vibrational modes. This suggests how EUV transient gratings can drive coherent excitations into the sample and pave the way for the practical exploitation of non-linear optics in the EUV/SXR range. In a future experiment the optical pulse will be replaced by a EUV/SXR one to probe vibrational modes in the range k_{ex}=0.1-1 nm^{-1}. This range, inaccessible by optical FWM, can be probed by using photon wavelengths down to 10 nm (i.e., well within the range of FERMI), and is of special relevance for the investigations of disordered systems. Indeed, the origin of their thermodynamic peculiarities (e.g., the highly debated excess specific heat) seems to be related to mesoscopic heterogeneities extended over a few nm length-scales, which can be revealed by the anomalous behavior of vibrational modes in the so far unexplored k_{ex}-range [54].

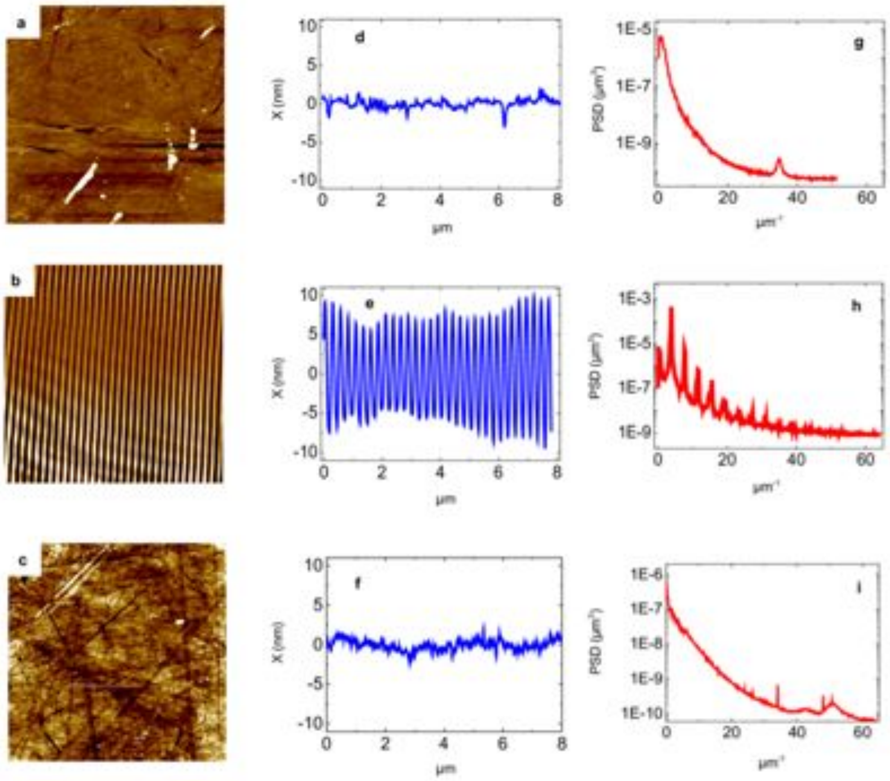

Figure 22 *AFM topographies [49]. AFM topographies of 8x8* μm^2 *areas of the sample surface as follows: in a region that was not irradiated a), in an area irradiated by 300 FEL shots at a fluence larger than 50 mJ* cm^{-2} *b), and in an area continuously irradiated by FEL pulses at low fluence c). d–f, Representative depth profiles of the sample surface along the green lines shown in a–c, respectively. The power spectral densities (PSD) corresponding to data reported in d–f are shown in g–i, respectively.*

References

[1] Bocchetta, C.J. et al. FERMI@Elettra FEL conceptual design report (Sincrotrone Trieste, Trieste, 2007)
[2] Xie, M. Exact and variational solutions of 3D eigenmodes in high gain FELs. Nucl. Instrum. Methods A 445, 59–66 (2000)
[3] E. Allaria et al. "Highly coherent and stable pulses from the FERMI seeded free- electron laser in the extreme ultraviolet". In: Nature Photonics 6.10 (2012), pp. 699– 704
[4] Fawley, W.M. A user manual for GINGER and its post-processor XPLOTGIN, LBNL Technical Report, LBNL-49625 (2002)
[5] Saldin, E.L., Schneidmiller, E.A. & Yurkov, M.V. The physics of free electron lasers (Springer, Berlin, 2000)
[6] Ackermann, W. et al. Operation of a free-electron laser from the extreme ultraviolet to the water window. Nature Photon. 1, 336–342 (2007)
[7] Singer, A. et al. Transverse-coherence properties of the free-electron-laser FLASH at DESY, Phys. Rev. Lett. 101, 254801 (2008)
[8] Yu, L.H. et al. High-gain harmonic-generation free-electron laser. Science 289, 932–934 (2000)
[9] De Ninno G. et al. Generation of ultrashort coherent vacuum ultraviolet pulses using electron storage rings: A new bright light source for experiments. Phys. Rev. Lett. 101, 053902 (2008)

[10] Lambert, G. et al. Injection of harmonics generated in gas in a free-electron laser providing intense and coherent extreme-ultraviolet light. Nature physics 4, 296–300 (2008)
[11] Allaria, E., et al., Tunability of a seeded free-electron laser through frequency pulling. Eur. Phys. Lett. 89, 64005 (2010)
[12] Ackermann, W. et al. Operation of a free-electron laser from the extreme ultraviolet to the water window. Nature Photon. 1, 336–342 (2007)
[13] Welch, J. et al. FEL Spectral Measurements at LCLS, Proc. FEL2011, 461–464, (2011)
[14] Allaria, E., et al., "Control of the polarization of a vacuum-ultraviolet, high-gain, free-electron laser" (2014) Physical Review X, 4 (4), art. no. 041040
[15] Mahieu, B., et al., Two-colour generation in a chirped seeded free-electron laser: A close look (2013) Optics Express, 21 (19), pp. 22728-22741
[16] Freund, H. P. & O'Shea, P. G. Two-color operation in high-gain free-electron lasers. Phys. Rev. Lett. 84, 2861–2864 (2000)
[17] Allaria, E., et al., Two-colour pump-probe experiments with a twin-pulse-seed extreme ultraviolet free-electron laser (2013) Nature Communications, 4, art. no. 2476
[18] Bencivenga, F., et al., Multi-colour pulses from seeded free-electron-lasers: towards the development of non-linear core-level coherent spectroscopies (2014). Faraday Discuss. 171, 487–503
[19] E. Allaria et al. "Two-stage seeded soft-X-ray free-electron laser". In: Nature Photonics 7.11 (2013), pp. 913–918
[20] L. Raimondi, et al., "K-B bendable system optimization at FERMI@Elettra FEL: Impact of different spatial wavelengths on the spot size" (2013) Proceedings of SPIE - The International Society for Optical Engineering, 8848, art. no. 88480B
[21] Raimondi, L. & Spiga, D. (2010). Proc. SPIE, 7732, 7732..
[22] Spiga, D. & Raimondi, L. (2014). Proc. SPIE, 9209, 92090E
[23] Raimondi, L. & Spiga, D. (2015). Astron. Astrophys. 573, A17.
[24] K. C. Prince et al., "Coherent control with a short-wavelength free-electron laser", Nature Photonics (2016) in press
[25] C. Yoon, et al., "Conformation sequence recovery of a non-periodic object from a diffraction-before-destruction experiment," Opt. Express 22, 8085-8093 (2014)
[26] Von Korff Schmising, et al., "Imaging ultrafast demagnetization dynamics after a spatially localized optical excitation" , Physical Review Letters, Vol. 112 - 21, pp. 217203 (2014)
[27] Katzy R, et al., "Migration of surface excitations in highly-excited nanosystems probed by intense resonant XUV ", Journal of Physics B: Atomic, Molecular and Optical Physics, Vol. 48 - 24, pp. 244011 (2015)
[28] Laforge AC, et al., "Collective autoionization in multiply-excited systems: A novel ionization process observed in Helium Nanodroplets", Scientific Reports, Vol. 4 (2014)
[29] Yamamoto S, et al., "Ultrafast spin-switching of a ferrimagnetic alloy at room temperature traced by resonant magneto-optical Kerr effect using a seeded free electron laser", Review of Scientific Instruments, Vol. 86 - 8, pp. 083901 (2015)
[30] Spezzani C, et al., "Magnetization and Microstructure Dynamics in Fe/MnAs/GaAs(001): Fe Magnetization Reversal by a Femtosecond Laser Pulse", Physical Review Letters, Vol. 113 - 24, pp. 247202 (2014)
[31] E. Ferrari et al., "Widely tunable two-colour seeded free-electron laser source for resonant-pump resonant-probe magnetic scattering", Nature Communications 7, Article number: 10343 (2016)
[32] Capotondi, F., et al., "Coherent imaging using seeded free-electron laser pulses with variable polarization: First results and research opportunities" (2013) Review of Scientific Instruments, 84 (5), art. no. 051301
[33] Marchesini S (2007), "A unified evaluation of iterative projection algorithms for phase retrieval", Review of Scientific Instruments 78 011301
[34] Marchesini S, He H, Chapman H N, Hau-Riege S P, Noy A, Howells M R, Weierstall U and Spence J C H, (2003) "X-ray image reconstruction from a diffraction pattern alone", Physical Review B 68 140101
[35] Bloembergen N. Nonlinear optics and spectroscopy, Rev. Mod. Phys. **54**, 685-695 (1982).
[36] Boyd, W. R. Nonlinear Optics (Academic Press, 2008)
[37] Dhar, L., Rogers, J. A. & Nelson, K. A. "Time-resolved vibrational spectroscopy in the impulsive limit", Chem. Rev. **94**, 157-193 (1994)
[38] Cundiff, S. T. & Mukamel, S. Optical multidimensional coherent spectroscopy. Physics Today **66**, 44-49 (2013)
[39] Bencivenga, F. et al. "Nanoscale dynamics by short-wavelength four wave mixing experiments", New J. Phys. **15**, 123023 (2013)

[40] Tanaka, S. & Mukamel, S., "Coherent X-ray Raman spectroscopy: a nonlinear local probe for electronic excitations", Phys. Rev. Lett. **89**, 043001 (2002)
[41] Foster, M. A. et al., "Broad-band optical parametric gain on a silicon photonic chip", Nature 441, 960-963 (2006)
[42] Chen P.-Y. & Al A., "Subwavelength imaging using phase-conjugating nonlinear nanoantenna arrays", Nano Lett. 11, 5514-5518 (2011)
[43] Boyer, V., Marino, A. M., Pooser, R. C. & Lett, P. D., "Entangled images from four-wave mixing", Science 321, 544-547 (2008)
[44] Tanaka, S., Chernyak, V. & Mukamel, S., "Time-resolved X-ray spectroscopies: Nonlinear response functions and Liouville-space pathways", Phys. Rev. A **63**, 063405 (2001).
[45] Adams, B, "Nonlinear X-ray optics: The next phase for X-rays", Nat. Phys. **7**, 675-676 (2011)
[46] Glover, T. E. et al., "X-ray and optical wave mixing" Nature **488**, 603-608 (2012)
[47] Tamasaku, K., Sawada, K., Nishiboro, E. & Ishikawa, T., "Visualizing the local optical response to extreme ultraviolet radiation with a resolution of λ/380", Nat. Phys. **7**, 705-708 (2011)
[48] Dhar, L., Rogers, J. A. & Nelson, K. A. "Time-resolved vibrational spectroscopy in the impulsive limit", Chem. Rev. **94**, 157-193 (1994)
[49] Bencivenga, F. et al. (2015). Nature (London). 520, 205–208
[50] Danailov, M. B. et al. "Towards jitter-free pump-probe measurements at seeded free electron laser facilities" Opt. Express 22, 12870-12879 (2014)
[51] Gahl, C. et al. "A femtosecond X-ray/optical cross-correlator", Nat. Phot. 2, 165-169 (2008)
[52] Casolari, F. et al. Role of multilayer-like interference effects on the transient optical response of Si_3N_4 films pumped with free-electron laser pulses. Appl. Phys. Lett. 104, 191104 (2014)
[53] Ruhman, S., Joly, A. G. & Nelson, K. A. Time resolved observations of coherent molecular vibrational motion and the general occurrence of impulsive stimulated scattering. J. Chem. Phys. 86, 6563-6565 (1987)
[54] Schirmacher, W. et al. Vibrational excitations in systems with correlated disorder. Phys. Status Solidi C 5, 862–866 (2008)., Ferrante, C. et al. Acoustic dynamics of network-forming glasses at mesoscopic wavelengths. Nat. Commun. 4, 1793 (2013)

6 Forthcoming beamlines at FERMI

The current number of beamline operating at FERMI is four: EIS-TIMER, EIS-TIMEX, DiProI, and LDM. The scientific case covered by these end-stations is wide: absorption-emission spectroscopy (gasses, clusters, solid, and metastable matter), transient grating spectroscopy, (resonant) diffraction and microscopy of organic and inorganic samples, dynamic evolution of complex systems represent some of the scientific topics studied at FERMI. In the near future this scientific case will be expanded including the study of magnetic properties (MagneDyn) and coherent control of matter through non-linear phononics (TeraFERMI). In this chapter the design of the FERMI's future beamlines will be described in detail together with the scientific case.

6.1 TeraFERMI

As explained in chapter 1 Free Electron Lasers are based on the extraction and acceleration of electron bunches, and the use of chains of undulators. The linear acceleration sections (LINACs) produce naturally terahertz (THz) radiation permitting to extend the working range of operation of these facilities by using dedicated undulators, bending magnets (Coherent Synchrotron Radiation, CSR) or a dedicated target (Coherent Transition Radiation, CTR) [1-6]. In particular, these mechanisms overcome the restrictions of other standard THz sources, where the maximum power and/or bandwidth are limited. After the FEL process, the electron bunch is deflected from the FEL trajectory by means of a set of bending magnets that send the electrons to the main beam dump (MBD). At FERMI a vacuum chamber hosting a set of thin metallic target screens right before the MBD in order to exploit the Coherent Transition Radiation (CTR) process has been installed. CTR allows to obtain high intensity polarized light in a wide TeraHertz range (0.3-15 THz) that will be transported inside the Experimental Hall (EH) and used for a wide set of experiments by the beamline TeraFERMI.

6.1.1 TeraFERMI scientific case

Thanks to the great advancements that have been achieved during the last two decades, THz spectroscopy is now widely employed in many fields of science and technology, ranging from solid-state-physics to biology, medicine, industrial production and homeland security. A new frontier in THz science is now represented by the possibility to produce ultra-short, coherent, intense radiation pulses suitable to manipulate and control material properties. To this aim, one needs THz pulse energies from the μJ to the mJ range and electric field peak values beyond 100 kV cm^{-1}. The key advantage in using THz photons, with respect to the more conventional visible and near-infrared photo-excitations, is that they allow to directly populate low-energy, single-particle and collective excited states, without ”heating” the overall electron bath. This allows focusing only on the dynamics of interest, instead of dealing with dissipation phenomena. THz light couples to electronic, magnetic and vibrational degrees of freedom, thus offering the possibility to address an extremely wide range of excitations. Moreover, THz photons resonant with an infrared active phonon mode can be employed to tune the bond-length. If the excitation is strong enough, lattice vibrations with even symmetry can be activated through the ionic Raman scattering [7,8]. On the other hand, THz photons can directly couple to the electrons. It has been shown that THz electric fields can be used as an ultra-fast gate of interlayer charge transport in copper oxide superconductors [9,10]. The THz electric field can also be used to reduce the Coulomb activation barrier in a Mott insulator. This phenomenon, modeled by the Poole-Frenkel effect, has been exploited to drive an insulator-to-metal transition in VO_2 [11]. In this experiment, a metamaterial-based resonator has been employed in order to enhance the THz electric field by one order of magnitude, up to 3.3 MV cm^{-1}. Indeed, at such high field values the bias voltage acting at the atomic scale is on the order of 100 mV, close to typical Coulomb repulsion energy values ($U \sim$ eV). Finally, THz pulses can also couple to magnetic excitations. Indeed an electric field value of 3.3 MV cm^{-1} corresponds to a magnetic field as high as 1 T. This provides the possibility to switch on and off magnetic states with unprecedented fs-scale resolution. While some pioneering work has been performed by directly employing the magnetic field associated with a relativistic electron bunch [12] this opportunity is still largely unexploited.

Besides solid-state physics, non-linear THz spectroscopy is expected to provide new insights into chemistry and biology. Reaction coordinates and conformational landscapes are highly susceptible to be modified upon intense THz excitation. This should allow the possibility of using THz light to tune chemical reactions and control the tertiary and quaternary structure of macromolecules [13].

In the last few years, progresses in the development of laser-based THz pulsed sources have made accessible some of the experiments outlined above. On the high frequency side, close to mid-infrared frequencies, optical parametric amplifiers can provide photon fluence in the mJ cm^{-2} range through different-frequency mixing. This technique has been successfully employed to excite the highest energy infrared phonon of manganites, but does not presently allow to produce intense light pulses with spectral components below 15 THz.

At lower frequencies, optical rectification in $LiNbO_3$ thanks to the so-called tilted wave-front technique has provided the opportunity to enter the realm of non-linear spectroscopy in the 0.1-1 THz range. The main challenge with these set-ups is the optimization of the poor efficiency ($\eta \sim 10^{-4}$) in the optical rectification processes. Recently, conversion efficiency up to $\eta \sim 10^{-4}$ has been reported [14], thus providing 125 μJ per pulse. However, this was achieved at the expenses of the pulse duration (> 1 ps) and spectral content. Other means to improve the overall THz pulse intensity by making use of ever increasing laser power need employing larger $LiNbO_3$ crystals and larger spot sizes, at the expense of brightness.

Between these two techniques, THz generation in organic crystals (DAST, OH1, DSTM) allows to fill the 1-10 THz gap. THz pulses up to 20 μJ have been demonstrated in DAST [15]. Still, the usage of organic crystals is intrinsically limited by the rather low radiation damage threshold. An accelerator-based THz source does not suffer from any of the limitations described above, both in terms of maximum power and broadband coverage.

6.1.2 TeraFERMI source

As mentioned in the introduction, the TeraFERMI source is located in the MBD section, where electrons from both FEL1 and FEL2 merge into a single line, before being dumped. A couple of meters before the MBD a dedicated vacuum chamber hosts a set of metallic screens that will be inserted within the electron trajectory. When the ultra relativistic electrons pass through the target, an intense current raises on the metallic screen radiating back both in the forward and backwards directions. A sketch of the source is shown in Figure 1. The TeraFERMI source chamber is equipped with two different type of screens for CTR: either a Si substrate (5 cm diameter) covered with an Al coating 1 μm-thick, or a free standing 1 μm-thick Al membrane. A variable slit between two Si-based emitters can also be used as a source for Coherent Diffraction Radiation.

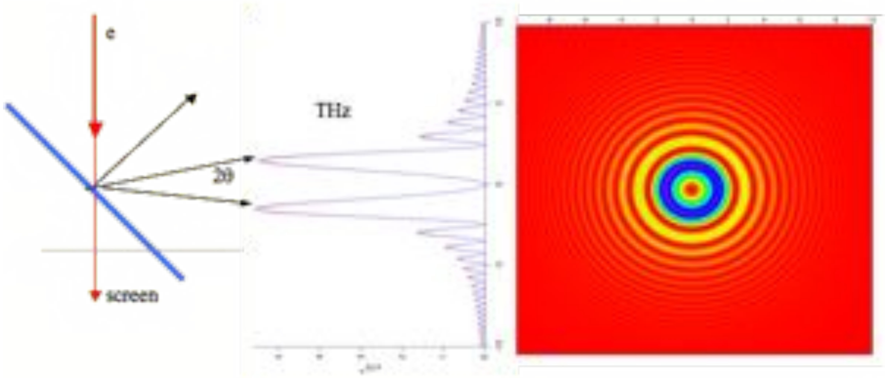

Figure 1 *Coherent Transition Radiation (CTR) mechanism: the relativistic electron bunch interacts with a metallic target and generates a broadband Terahertz radiation with a cylindrical transverse distribution and high divergence. The slight asymmetry is due to the 45 deg of incidence angle of the electron bunch over the metallic screen.*

As described in detail in [16,17], a good prediction of the emission properties in both near and far field can be obtained by applying the generalized Ginzburg-Frank formula [18]. The emitted radiation is expected to be radially polarized with cylindrical symmetry along the propagation axis, with an effective source size of $r_{\text{eff}} = \gamma\lambda$, with γ Lorentz factor and λ the wavelength of the radiation. The angular divergence is a function of the frequency as well, being larger at low frequencies up to 14 degree. The spectral range covered by TeraFERMI is expected to be exceptionally wide: from 0.3 THz up to 15 THz, limited only by the divergence of the photon beam and the transmission of the optical elements (viewports, mirrors, filters, polarimeters) with intensities ranging between 10^2-10^4 μJ and a pulse length of 50 fs for an electron bunch of 500 pC [19]. In Figure 2 the calculated emission for CTR emission at FERMI is shown. At 75 mm from the source a 600 μm thick CVD diamond window separates the main chamber (ultra high vacuum) from the rest of the beamline (low vacuum). The diamond has a high transmission along the whole TeraFERMI frequency range, around

70 %, and an almost constant index of refraction, thus any dispersion will be negligible. With its clear aperture of 20 mm, the window will be a natural filter: it will be able to transmit only radiation above 0.3 THz due to the high divergence at lower frequencies. The surfaces are wedged of about 0.5 degree in order to maximize the transmission at all the frequencies and avoid propagating multiple back-forward reflections. The residual tilt due to the wedge will be compensated by the first plane mirror as described in the next section.

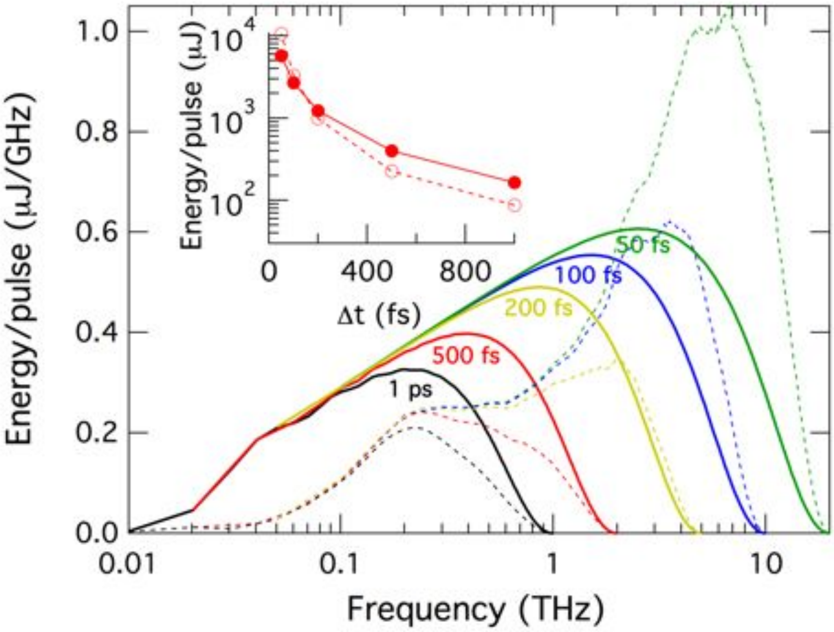

Figure 2 *Calculated emission for CTR emission. The calculation considers 1 nC relativistic (1.2 GeV) electron bunches, with a rectangular profile of variable length. The radiation is emitted by a CTR screen of radius 3 mm, and over a 200 mrad acceptance angle. Full lines indicate the far-field calculation, while dashed lines correspond to the near-field, with the light being collected at a distance of 5 cm from the emitting screen. In the inset are reported the energy per pulse values, as a function of the bunch length, for far- (full line and symbols) and near- (dashed line and empty symbols) field approximations (Credits [19]).*

6.1.3 Photon transport

After the window the first chamber hosts a plane mirror and the first diagnostic section. The diagnostic system is composed of a translation stage with a screen coupled to a visible CCD camera (in air) dedicated to the alignment of the source. In addition, an off-axis parabolic mirror will collect and focus the radiation inside a pyroelectric detector for measuring the emitted intensity in the whole frequency spectrum. The first plane mirror is able to rotate and translate in order to correct residual vertical misalignments of the source due, for instance, to the wedged window. After the first chamber a set of 9 chambers follows, which host plane and focusing mirrors. All the mirrors work at 45 degree of incidence angle and are 220 mm wide and 282.8 mm long (with an elliptical lateral shape) in order to collect as much light as possible avoiding the aperture diffraction. A particular attention has been devoted to the finishing of the surfaces. In fact, the effect of figure errors and roughness might lead to aberrations of the wave-front and scattered light, with a general loss of intensity and performance at the sample. For this reason we have opted for Gold-coated Aluminum substrates presenting a surface accuracy Peak-to-Valley below 3 μm (in clamped conditions), and a micro-roughness below 9 nm rms.

Table 1 *Mirror names, distance from the source, profile shape and focal length for the TeraFERMI beamline. All mirrors have a substrate with an elliptical shape with semi-major axis of about 141 mm and semi-minor axis of 100 mm.*

Mirror	Source distance / mm	Shape	f / mm
PM1	480	Plane	∞
TM1	1254	Toroidal	680
TM2	3900	Toroidal	510
TM3	5678	Toroidal	800
TM4	14070	Toroidal	3250
PM2	15570	Plane	∞
TM5	22822	Toroidal	3000
PM3	24222	Plane	∞
PM4	30180	Plane	∞
TM6	31180	Toroidal	1400

A sketch of the layout of the beamline is shown in Figure 3 and the mirror parameters are reported in table 1. The optical path has a ”zig-zag” pattern so to fulfill the radiation safety regulations and to transport the light from the undulator hall to the experimental hall passing through the safety hutch. The adopted scheme employs four plane mirrors and six focusing mirrors: the idea is to create intermediate focuses along the beamline in order to limit the beam size within the dimension of the optics. Spherical mirrors have not been considered an option because the placement of the focal spot is different in the two directions (the focused beam is astigmatic). For this reason we have opted for focusing mirrors with a toroidal shape (manufactured by Kugler), i.e., two different radii of curvature along the tangential and sagittal axis. In this way the beam results stigmatic and limited in its transverse dimension. Two long corrugated beampipes, one in the undulator hall and the other in the safety hutch, will diffract on purpose the undesired off-axis radiation (the low frequencies).

One of the sub-products of the CTR is the emission of visible light on-axis that will be used for alignment purposes. In fact, before every mirror, a movable screen can be inserted and imaged by a CCD camera, while the pointing can be changed by moving the mirror upstream. The overall optical path from the source to the entrance of the TeraFERMI hutch (located in the experimental hall) is about 33 m. Before the hutch the beam is focused six times and the last focus lies at the beginning of the experimental hutch with a maximum size around 30 mm at 0.3 THz, getting smaller at higher frequencies (for instance it goes down to 12 mm at 1 THz).

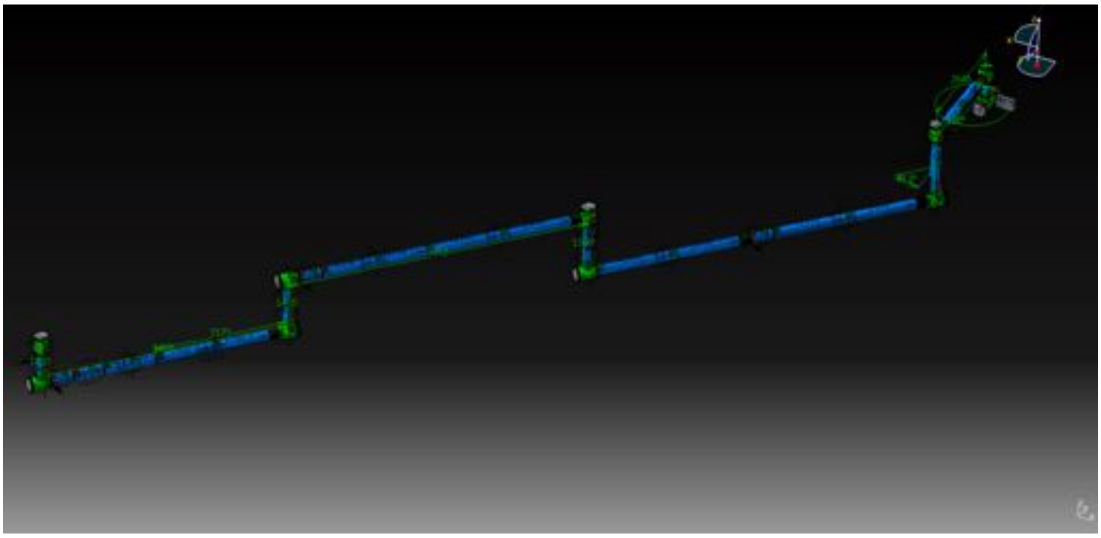

***Figure 3** Layout of the TeraFERMI beamline. From right to left: source chamber and plane/toroidal mirrors. The ”zig-zag” pattern has been chosen respecting the radiation safety regulations. A set of six toroidal mirrors creates intermediate focuses in order to limit the transverse beam dimension, while four plane mirrors simply deflect the photon beam.*

The design and performance predictions of the whole beamline have been calculated with the THz-Transport Code, based on numeric 2D Fourier transform. It is worth to notice that the whole TeraFERMI beamline is in the near field condition since the far field approximation is fulfilled when $D>\gamma^2\lambda$ thus, considering a representative $\gamma=2300$ and $\lambda=1$ mm, for very long distances. Starting from the CTR emission the monochromatic beam has been propagated through the Diamond window, plane and toroidal mirrors, and apertures until the TeraFERMI hutch. In this way it has been possible to evaluate the focused spot size and transmission of the beamline at the various frequencies. An example of the simulation results in the whole working range is shown in Figure 4. These calculations have been performed in the whole spectrum and then combined in order to evaluate the overall spot at the entrance of the end-station.

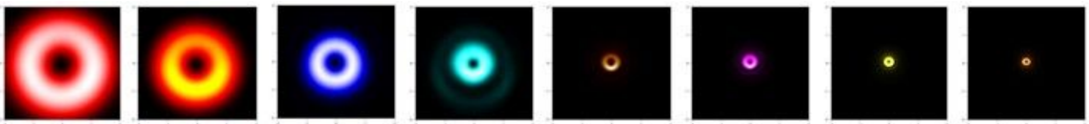

***Figure 4** (from left to right) Simulated spots at 0.3-0.4-0.6-1-3-5-10-15 THz at the entrance of the TeraFERMI hutch in the FERMI experimental hall. The field of view is the same for all the simulations (4 mm) and the spot size dependence over the radiation frequency is evident.*

In Figure 5 the transmission of the beamline is shown after taking into account the transmission of the Diamond window and the presence of the mirrors. It can be seen that the first toroidal mirror (blue line) is the major cause of the drop in the total transmission that is, nevertheless, high enough in the whole frequency range ranging from 83.5 % (at 0.3 THz) to 95.3 % (at 15 THz).

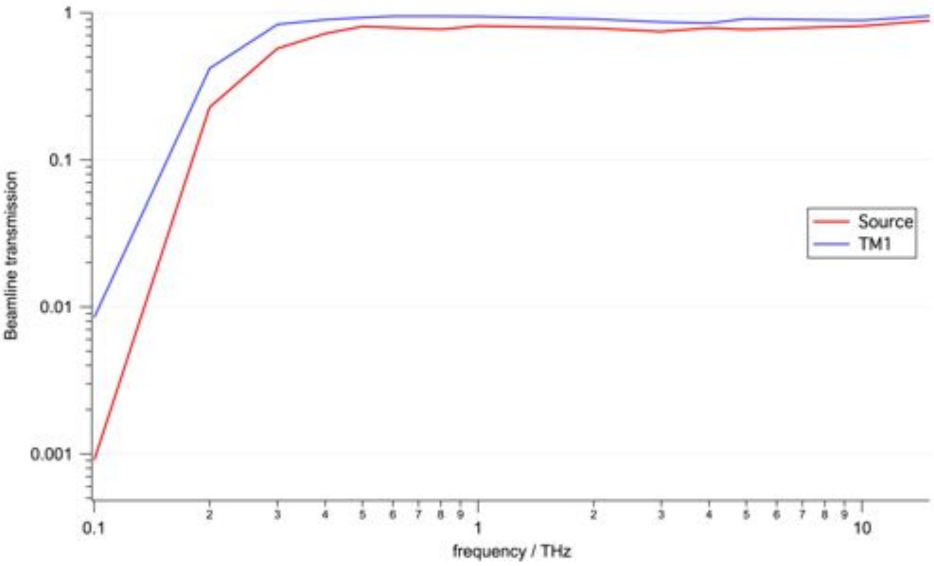

Figure 5 *Transmission due to the presence of the Diamond window and the optical elements. The red line refers to the total intensity emitted by the source without considering the geometrical losses due to the viewport. The blue line is the realistic case considering the radiation passing through the viewport only. It can be seen that the low frequency radiation is filtered by geometrical effects at the viewport.*

The installation of the source chamber, transport pipes, diagnostic screens, mirrors and vacuum chambers has been finished. In Figure 6 some pictures of the installation phase are shown. The first tests followed by the pilot experiment are planned for the first half of 2016.

Figure 6 *Transport pipes and vacuum chambers of the TeraFERMI beamline inside the safety hutch (left) and undulator hall (center). Right: plane mirror mounted in its holder and ready to be installed.*

6.1.4 Refocusing section and experimental set-up

As previously mentioned, at the entrance of the TeraFERMI hutch the beam is focused with a maximum dimension of about 30 mm at 0.3 THz. This beam has to be filtered, polarized, split, eventually recombined, and most important focused as much as possible in order to increase the electric field amplitude at the sample. The wide range of experiments planned at TeraFERMI has been considered, and a versatile set-up has been adopted. In the following we present the set-up that will be used to perform commissioning and pilot experiments. Our aim is to characterize the power and spectral content of the THz beam as well as its time structure. Such goal can be achieved through electro-optic sampling, in the 0.3-10 THz range [20].

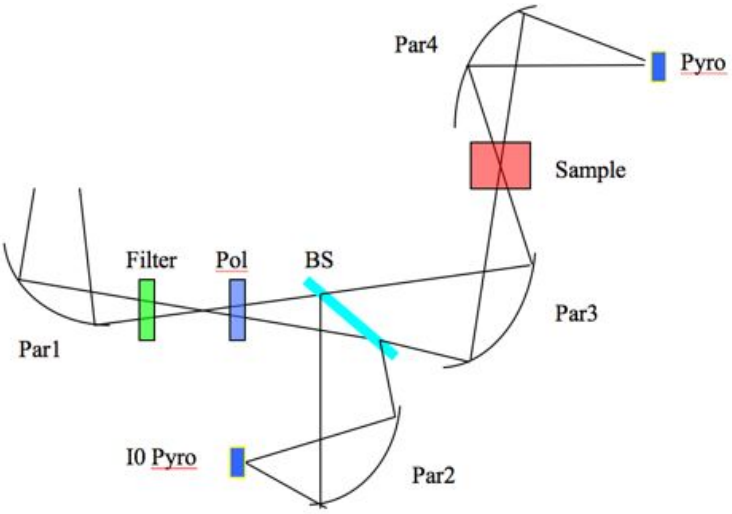

***Figure** 7 Schematic layout of the TeraFERMI refocusing section for the pump-probe pilot experiment. The THz beam is focused while being filtered and polarized. Then it is split into two beams: one for the on-line measurement of the I0 (with a dedicated mirror, Par2) and one that will be used as a pump pulse. This pulse is focused close to the diffraction limit by another focusing mirror (Par3). The beam is then refocused (Par4) over a pyro-detector that measures the radiation transmitted by the sample.*

On the other hand we also wish to perform first nonlinear experiments on prototype materials. The scheme presented here allows to easily switch between electro-optic sampling to THz-pump/Vis-probe experiments with the help of a synchronized laser (either 780 or 1560 nm) source. Moreover, THz nonlinear transmission, i.e., the study of the variations in the transmitted light as a function of the beam intensity, will also be possible. A reference channel allowing to self-normalize the results by taking into account possible fluctuations of the source has been envisaged. The optical layout has been designed as follows (see a sketch of the layout in Figure 7): the incoming beam is focused by an off-axis parabolic mirror (Par1) that focuses the beam at a distance of 215 mm while passing through a set of filters-polarimeter. Afterwards, it propagates through a beam splitter where part of the radiation is reflected to a second off-axis parabolic mirror (Par2) focusing the radiation into a pyro-detector placed 61.6 mm downstream, used as an on-line I0 monitor. The fraction of radiation transmitted by the splitter is collected by another off-axis parabolic mirror (Par3) that focuses the terahertz radiation to the sample (hosted inside a dedicated chamber) at a distance of 61.6 mm where the interaction between radiation and matter will occur. Both Par2 and Par3 will be placed 500 mm downstream Par1. The light transmitted by the sample will then be collected by a fourth off-axis parabolic mirror (Par4, 150 mm downstream Par3) and focused into a second pyro-detector placed 116 mm downstream. All the parabolic mirrors are supposed to work at an incidence angle of 45 degrees. In Figure 8 are shown the results of the wave-front propagation simulations over the parabolic mirrors and the relative focal spots simulated with Terahertz-Transport code [21] at 1 THz.

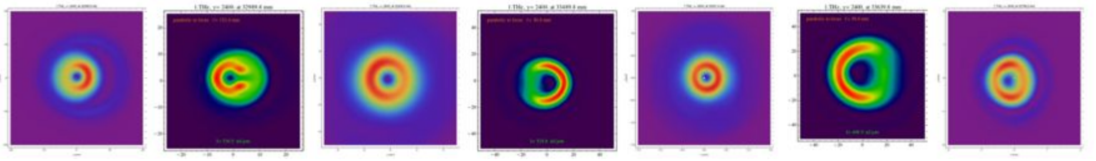

Figure 8 *Refocusing section spots inside the TeraFERMI hutch simulated with TeraHertz-Transport Code [21] at 1 THz. From left to right: incoming focused spot from the last toroidal mirror (TM6, FOV=40 mm), footprint over the first parabolic mirror (Par1, FOV=46 mm), intermediate focus due to Par1 (FOV=10 mm), footprint over the second/third parabolic mirrors (Par2/3, FOV=100 mm), spot at the I0 pyro-detector and at sample (FOV=3 mm), footprint over the last parabolic mirror (Par4, FOV=100 mm) and spot at the pyro-detector in transmission after the sample (FOV=4 mm). The spot at focus is expected to be diffraction limit: i.e. around 1 mm at 1 THz.*

6.2 MagneDyn

The future Magneto Dynamics (MagneDyn) beamline will be devoted to study the electronic states and the local magnetic properties of excited and transient states of complex systems by means of the time-resolved X-ray absorption spectroscopy (TR-XAS) technique. The beamline will use the FERMI high-energy source, covering the wavelength range from 60 nm down to 1.3 nm. An on-line photon energy spectrometer will allow to measure the spectrum with high resolution while delivering most of the beam to the end-stations. Downstream, the beam will be possibly split and delayed, by means of a delay line, and then focused with a set of active KB mirrors. These mirrors will be able to focus the radiation in one of the two MagneDyn experimental chambers: the electromagnet end-station and the Resonant Inelastic X-ray Scattering (RIXS) end-station. After an introduction of MagneDyn scientific case, the optical components and the performances of the beamline will be discussed extensively.

6.2.1 MagneDyn Scientific case

Magnetism is an essential feature of the macroscopic world. Nowadays, advanced applications of magnetic phenomena are at the bases of the widespread technology underlying magnetic storage, quantum computing, spintronics and energy recovery, which have fuelled a renaissance in magnetism research [22]. At the moment, one of the most fascinating aspects in magnetism is the ultrafast disappearance, creation and control of magnetic states and the novel dynamical quantum magnetic effects, which emerge in two-, one- and zero dimensional systems [23,24]. Correspondingly, a central problem in modern magnetism research is the understanding of the magnetization in out-of equilibrium excited states [25]. Such states, typically initiated by changes in temperature, optical excitations, fields (charge currents) or spin currents, define the operational processes and timescales in magnetic devices. Their understanding is therefore of paramount importance from both a scientific and a technological perspective. However, due to this strong non-equilibrium state, the conventional description of magnetic phenomena in terms of thermodynamics, namely the magnetic precession described by an adiabatic approach through the Landau-Lifshitz equations, is no longer valid. As a result, the ultrafast channels for transferring energy and angular momentum between photons, electrons, spins, and phonons remain elusive and a subject of intense debate. For example, theoretical explanations of the ultrafast demagnetization have been suggested, but the underlying mechanism is not fully understood. Models such as phonon-assisted Elliot-Yafet spin flip [26-31], electron-magnon scattering processes [26], superdiffusive transport [32], and, more recently, dynamic exchange splitting [33] have been proposed. All these approaches capture only partially the faceted aspects of non-adiabatic spin dynamics, revealing the complexity and the difficulty in describing a ferromagnetic system under strong optical excitation. Consequently, the multidimensional and simultaneous observations of different degrees of freedom, which compete to be responsible for the out-of-equilibrium magnetic phenomena, is now mandatory and will unlock the gate to the non-equilibrium exotic physics of the ultra-fast magnetism. The fact that many fundamental aspects of the nature of magnetism occurs in the sub-picosecond time regime [34] combined with the intrinsic sensitivity of circular polarized photons as a tool to investigate basic components of magnetism in matter [31,35,36] makes FERMI a versatile state-of-art light source for topical research on magnetism.

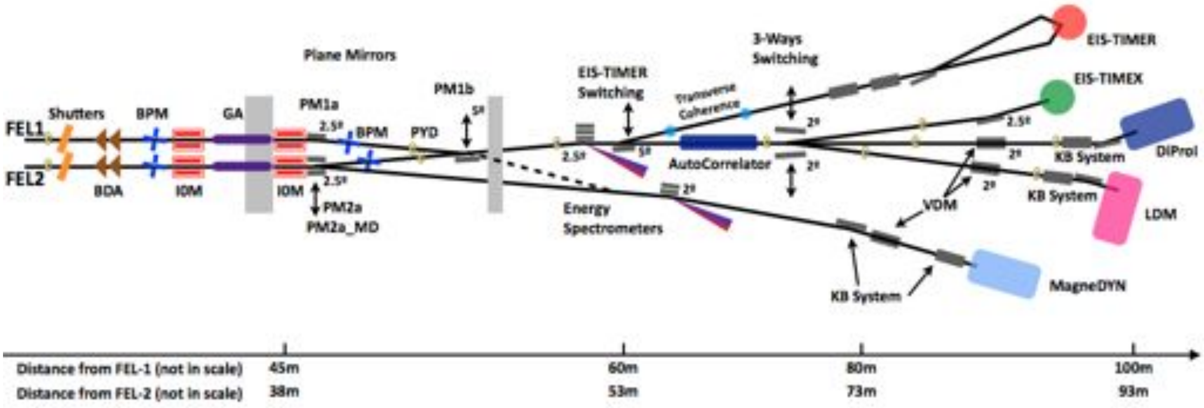

Figure 9 *Layout of the PADReS system and end-station at FERMI. Left to right: shutters, beam defining apertures (BDA), beam position monitors (BPM), intensity monitors (I0), gas absorber (GA), four plane mirrors inside the safety hutch ($PM1_a$, $PM1_b$, $PM2_a$, $PM2_{aMD}$), Ce:YAG screens, Photodiode-YAG-Diagnostics (PYD). At the beginning of the experimental hall sit the photon energy spectrometers and the Auto-correlator Delay-Creator (AC/DC), followed by the five beamlines with their refocusing systems.*

More in general, the FERMI FEL, with coherent, high-brightness, circularly polarized X-rays at energies resonant with the 3d-4d-transition metal ions, will permit the investigation in real time of fundamental magnetic interactions such as the exchange interaction, responsible for the existence of magnetic order, and spin-orbit interaction. The MagneDyn initiative aims at combining the unprecedented and unique properties of the FERMI FEL light with complementary X-ray and optical spectroscopies, which have been demonstrated to be effective tools to access different aspects of magnetic phenomena, such as spin and orbital angular momenta (XMCD), low lying magnetic, orbital and charge excitations (RIXS), magneto-optical and non-thermal photomagnetic effects (MOKE). The MagneDyn beamline will deliver the FEL light to two experimental end-stations: the first station, equipped with a 2T electromagnet and a 10K cryomanipulator, will be dedicated to combine XMCD and MOKE experiments; the second end-station, which is provided with a commercial XES spectrometer, will be devoted to RIXS experiments.

6.2.2 Photon transport

Unlike the other FERMI beamlines, MagneDyn is planned to be fed by the high-energy source FEL2 from both the first stage (covering the low energies) and second stage (for the high energies). For this reason a brand new branch of PADReS will be implemented in order to measure and manipulate the photon beam down to the two planned end-stations. The layout is hereafter described (shown in Figure 9) while the main optical components will be discussed in the next sections in detail. The beamline is planned to start inside the safety hutch, a restricted access area at the beginning of the experimental hall, by means of a Gold-coated plane mirror, named $PM2a_{MD}$ located 41.4 m downstream the last undulator. The beam will then be reflected to the on-line photon energy spectrometer, about 17 m downstream, where a small fraction of the radiation will be diffracted by one of the two diffraction gratings employed to measure on-line the spectral content, as for the PRESTO (see chapter 3 section 3.3). After the spectrometer the beam propagates freely for 14 m until the first element of the KAOS (Kirkpatrick-Baez Active Optics System) designed to focus the FEL light in the horizontal direction. After 1.2 m the beam will be reflected by another plane mirror devoted to raise the beam vertically, named Vertical Deflecting Mirror (VDM_{MD}). About 4.3 m after the VDM_{MD} the beam will be finally reflected by the second element of KAOS, and focused in the vertical direction inside one of the experimental end-stations.

Table 2 *MagneDyn mirrors characteristics and quality*

Mirror	$PM2a_{MD}$	KBM_H_{MD}	VDM_{MD}	KBM_V_{MD}
Bulk material	Silicon	Glass-based	Silicon	Glass-based
Dimension / mm^3	350×60×70	400×40×10	410×40×50	400×40×10
Roughness rms / nm	<0.3	<0.3	<0.3	<0.3
Optical area / mm^2	300×30	360×20	390×20	360×20
Tan radius / km	>30	>1	>30	>1
Sag radius / km	>30	>3	>30	>3
Tan slope error / µrad	<0.5	<0.5	<0.5	<0.5
Sag slope error / µrad	<5	<5	<5	<5
Coating-thickness / nm	Au - 30	Au - 30	Au - 30	Au - 30

The number of mirrors/gratings employed by the beamline will be five (six considering the two gratings) and all of them will work at 2 degree of grazing incidence, in order to maximize the beamline transmission keeping the dimension of the substrates reasonable. The total length of the beamline, from the last undulator of FEL2 to the focal spot inside the first experimental vacuum chamber, will be around 80 m. In the following sections each optical element as well as its features will be described in detail. The first plane mirrors $PM2a_{MD}$ and VDM_{MD} (placed 32.2 m downstream

$PM2a_{MD}$) will collect the whole incoming beam in both direction and for both mirrors the tangential and sagittal radii of curvature will be more than 30 km in order to prevent unwanted focusing effects. The surface quality is within the standards of the other mirrors employed at the other FERMI beamlines so to guarantee wave-front preservation and limit possible aberrations of the photon beam. The substrates have a Gold coating with a negligible surface roughness so to avoid scattering effects of the reflected light that cannot be focused properly. In table 2 all the mirror parameters are summarized.

6.2.3 On-line Photon Energy Spectrometer

After $PM2a_{MD}$ the photon beam will impinge on the on-line photon energy spectrometer. The working scheme is similar to the already installed PRESTO [37,38] and is composed of two diffraction gratings, one for the low and the other for the high energy ranges. The zeroth order of diffraction will be delivered almost unperturbed to the users (i.e., the full FEL photon beam from the source) while the first-second order of diffraction will be used for the characterization of the spectral content. In order not to perturb the photon beam, the substrates will be flat while the gratings will be Variable Line Spacing (VLS), meaning that the groove density is not constant along the substrate. In this way the diffraction angles are different along the tangential direction of the grating with consequent focusing into the detector. Neither entrance nor exit slits will be used.

Table 3 *Main parameters of the gratings composing the photon energy spectrometer. The coefficients D_i have been chosen in order to focus the diffracted radiation over the detector while the profile parameters and the coatings have been fixed considering the absolute efficiency of the gratings.*

Parameter	LE	HE
Wavelength range / nm	6.75 - 60.5	1.05 - 6.75
Energy range / eV	20.5 - 185	130 - 1180
Groove density D_0 / gr mm^{-1}	600	3750
D_1 / gr mm^{-2}	4.20×10^{-1}	2.6
D_2 / gr mm^{-3}	2.10×10^{-4}	1.30×10^{-3}
D_3 / gr mm^{-4}	9.50×10^{-11}	5.90×10^{-10}
Groove profile	Laminar	Laminar
Groove height / nm	10	4
Groove ratio (w/d)	0.7	0.7
Coating-thickness / nm	a-C / 30	Au / 30

Since the incidence angle is constant (2 degree) the focal displacement is a function of the radiation wavelength, forming the so-called focal curve. For this reason the detector will be mounted over a X-Y translation stage allowing to follow the diffracted spot. The two gratings will both have a 200×25×40 mm^3 (L×W×H) Fused Silica flat substrate with a clear aperture of 180×20 mm^2 while just the central part will be ruled with a dimension of 60×17 mm^2. This is because just a small fraction of the incoming photon beam is enough to measure the spectral properties of the FEL while maximizing the beamline transmission. For the same reason the groove profiles have been chosen to be laminar so to have a relatively low efficiency (between 0.4% - 4%) at the first order of diffraction but high enough at the second (between 0.5% - 2%).

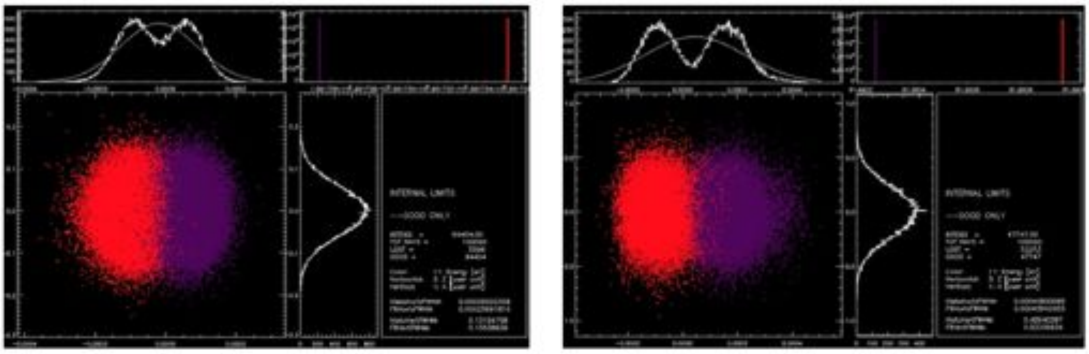

Figure 10 *Simulated spots at the detector with SHADOW code at 6.25 nm (left) and 20 nm (right) wavelengths radiation.*

The low energy grating (LE) will cover the wavelength range from 6.75 nm up to 60.5 nm (20.5 eV - 185 eV), and will have a 30 nm single layer of coating made of amorphous Carbon (a-C). The high energy grating (HE) will cover the wavelength range from 2.1 nm up to 9.6 nm (130 eV - 590 eV) by using the first order of diffraction, and will measure down to 1.05 nm (1180 eV) using the second one. As for the mirrors, the spectrometer substrates will have a small tangential (below 0.5 µrad rms) and sagittal (below 5 µrad rms) slope errors with a residual radius of curvature greater than 30 km, and a micro-roughness below 0.4 nm rms. These specifications will guarantee the preservation of the wave-front, the transverse spot quality as well as the minimization of the scattered light.

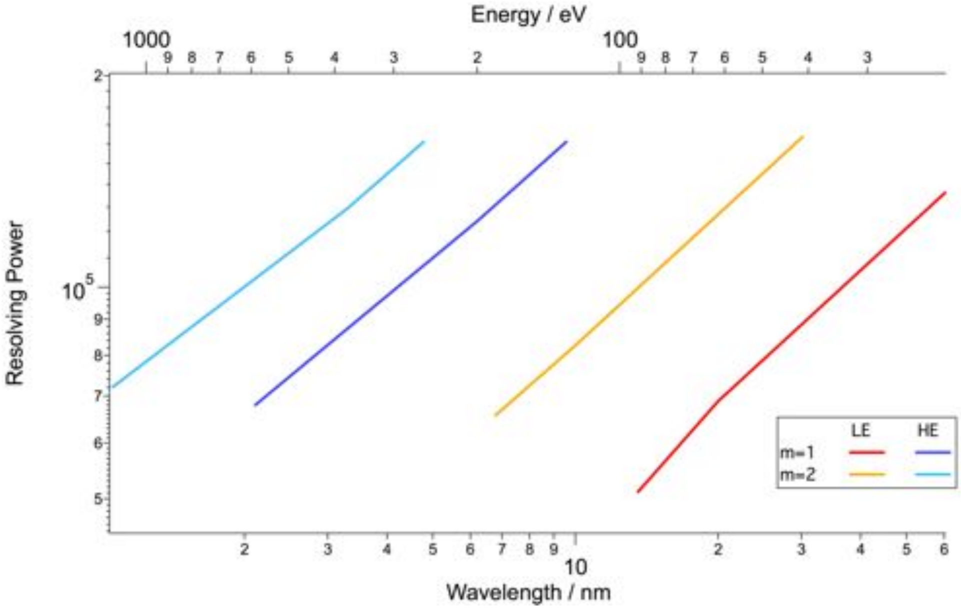

Figure 11 *Calculated resolving power of both gratings having used the Rayleigh criterion. The various colors correspond to different orders of diffraction: red (first, LE), orange (second, LE), blue (first, HE) and magenta (second, HE).*

The gratings VLS coefficients have been calculated using the theoretical formulas at first, and have been optimized with ray-tracing simulation afterwards. In table 3 all the main parameters of the gratings are summarized. The spectrometer performance in terms of spot size and resolving power has been simulated by means of ray tracing simulations adopting the Rayleigh criterion for the latter. Thanks to the high number of illuminated grooves the theoretical resolving power of the system is expected to be high: around 10^5 over the whole wavelength range (Figure 10, spots: left HE at 6.25 nm, right LE at 20 nm. Figure 11: calculated resolving powers).

The grating efficiency has been calculated with the REFLEC [39] and LUMNAB [40] codes for both the diffracted and transmitted beams considering the groove profile and coating of both gratings.

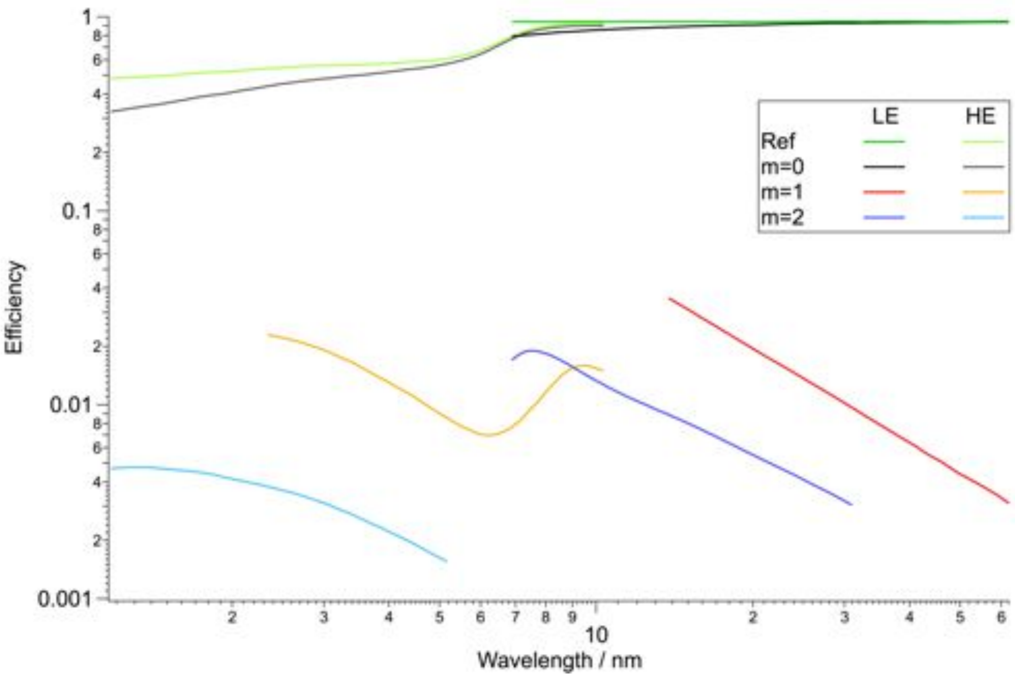

Figure 12 *Grating efficiency at the zeroth (m=0 black/grey), first (m=1 red/orange) and second (m=2 blue/azure) orders of diffraction for the low (LE) and high (HE) energy gratings in the whole FERMI FEL2 wavelength range. The intensity used by the spectrometer is much lower than the total radiation delivered to the users (zeroth order m=0), and is slightly lower then the lines corresponding to the reflectivity of a single mirror with the same coating and incidence angle as the gratings.*

For the LE grating the relative efficiency is expected to be between 0.5% and 3% for both the first and second orders of diffraction. The HE grating will have an efficiency between 0.8% and 2% at the first order while the second order will be around 0.5%. The transmitted beam by the grating (zeroth order of diffraction) is expected to have a slightly lower intensity than in case of a regular mirror used instead (reflectivity), as shown in Figure 12. In order to measure the spectral content, the diffracted FEL radiation will be focused on to a dedicated movable detector able to track the focal curve displacement. The detector is foreseen to be a YAG screen (in vacuum) coupled with a visible CCD camera (in air), as for PRESTO. This solution allows to keep a high resolving power working in air as well as the possibility of a fast replacement of the YAG screen in the case of damage due to the radiation.

6.2.4 KAOS at MagneDyn

The focusing section will be composed of a set of two active plane-elliptical mirrors mounted in the Kirkpatrick-Baez (KB) configuration similar to the already adopted KAOS solution at DiProI and LDM [41,42] (see chapter 4 section 4.3). As previously described, the KB geometry allows to decouple the vertical and horizontal focusing, and the available substrates have a much higher surface quality compared to the ellipsoidal mirrors. The reasons why the beamline needs active mirrors are the following:

- Sources: end-stations and wave-front correction. As described previously, FEL2 provides two photon beams: the low energy from the first stage (down to 20 nm) and the high energy from the second stage. These stages are separated by about 28.8 m, meaning that for a fixed focal length the beams cannot be both focused properly.

- Two experimental end-stations: a magnet and a RIXS separated by about 1 m. In order to move the focal spot inside the working chamber the mirrors have to be of variable focal length.

- Wave-front control: the possibility to change the mirror shape will allow controlling the wave-front of the photon beam.

The active mirrors will have a flat substrate of fused silica with an overall dimension of 400×40×10 mm^3 (L×W×H), i.e., much thinner than the regular mirrors employed along the beamlines. The clear aperture will be 360×20 mm^2 with a residual radius of curvature above 3 km within any 70 mm-long area along the mirror itself; the slope errors will be below 0.5 µrad rms and 5 µrad rms for the tangential and sagittal directions, respectively; the micro-roughness will be below 0.3 nm rms. The relaxed constrains of the residual radius of curvature is due to the fact that the mirrors are thin since they have to be deformable. Both mirrors will be coated with a single layer made of 30 nm of Gold. The mirrors will be mounted on a dedicated holder custom-designed in such a way that only the sides are clamped while the central part is free to be bent. By applying two unequal forces with a set of pushers over the sides it will be possible to change the mirror tangential shape accordingly to the user needs. Every pusher will be composed of a stepper motor coupled to a piezo-electric actuator: the former for the coarse mirror shape, the latter for fine optimization.

The only difference between the already operative KAOS system at DIPROI or LDM and the MagneDyn KAOS will be the fact that the two mirrors will not be installed in cascade (in series) but will be 5.5 m apart, with the $\mathrm{VDM}_{\mathrm{MD}}$ in between. As a consequence, the demagnification factor of the two mirrors will be different with a small focus in the vertical direction and a wider one in the horizontal. In particular, the horizontal KB will demagnify the source by a factor of 10, while this number rises up to 39 for the vertical one. This means that the focused beam will not be circular but ellipsoidal with an average ratio between the two axes of about 4. This will not be a problem since inside both experimental chambers a horizontal entrance slit will be used, limiting the beam dimension in the vertical direction and allowing the horizontal component to pass unperturbed.

The spots at the focus have been simulated considering the whole beamline system (mirrors/gratings) by ray tracing (Shadow code [43]) as well as wave-front propagation simulations (WISE code [44-46]). The source has been modeled as a Gaussian distribution with a transverse dimension of 125 μm sigma and a divergence following the relation $\sigma'_{\mu rad} = k\lambda_{nm}$, with k=1.25 for FEL2 first stage and 1.5 for FEL2 second stage. The results are in agreement with both approaches (apart from some diffraction effect due to the finite size of the mirrors), and the spots are expected to be 14 μm × 3.5 μm (H×V) FWHM at the electro-magnet chamber, and 16 μm × 5.3 μm FWHM at RIXS. In Figure 13 some selected simulated spots at 20 nm (62 eV) inside the electromagnet end-station are shown, having used ray tracing (left) and wave-front propagation (right) methods. In the case of very long wavelengths generated in the first stage, where the divergence is higher, the diffraction effects cause the spot to be wider in the horizontal direction, leading to a spot up to 30 μm FWHM at 60 nm (21 eV).

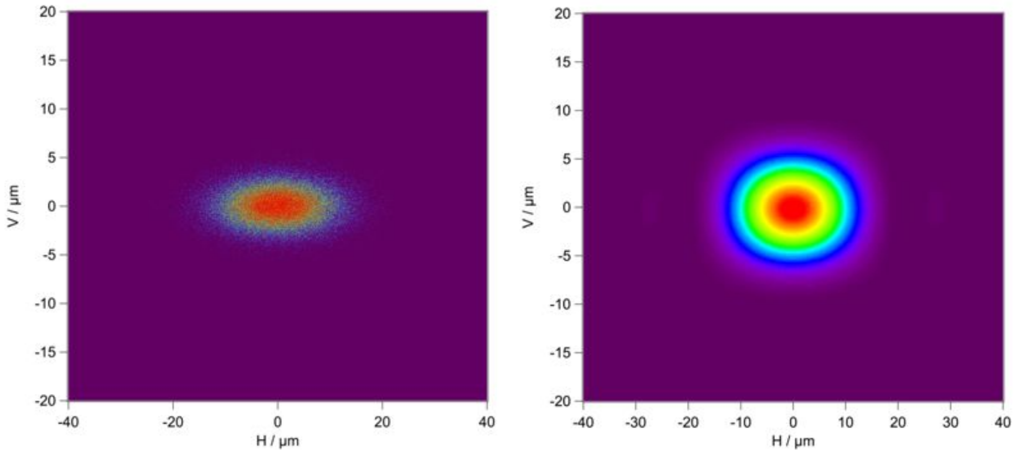

Figure 13 *Comparison between simulated spots at the focus inside the electromagnet end-station at 20 nm (62 eV). The ray-tracing (left) results are in good agreement with the wave-front propagation simulations (right) but for some negligible diffraction effects. The spot size is expected to be around 14 μm × 3.5 μm (H×V) FWHM.*

6.2.5 Beamline transmission and polarization

Considering the presence of the various coatings employed and the incidence angles, the beamline transmission has been calculated with particular attention to the effect on the polarization. In fact, one of the key elements for studying the magnetic properties of the materials is the presence of pure circular polarized light. Since the beamline will employ grazing-incidence single-layered mirrors, three working in the horizontal direction and two in the vertical, the degree of polarization of the radiation is expected to be mostly conserved. However, for the longer wavelengths (above 30 nm) a small effect will be present leading to a slightly elliptical polarized light when circular polarized radiation will be provided by the machine. Moreover, the presence of APPLE-II undulators allows to control the polarization of the emitted radiation. In particular, it can be generated with ellipsoidal polarization in such a way that the beamline itself acts as a compensation making it circular at the experimental end-stations.

The beamline transmission has been maximized using a grazing incident geometry for all the mirrors (2 degree of grazing incidence) employing a proper Gold-coating over the substrates (apart from for the LE grating which has Amorphous-Carbon coating). It ranges from 70 % for the long wavelengths (7–60 nm, 21-177 eV), between 10% and

20% for the range 3 nm - 6 nm (207-413 eV), and drops down to 7 % for the very short wavelengths (around 1 nm, 1240 eV).

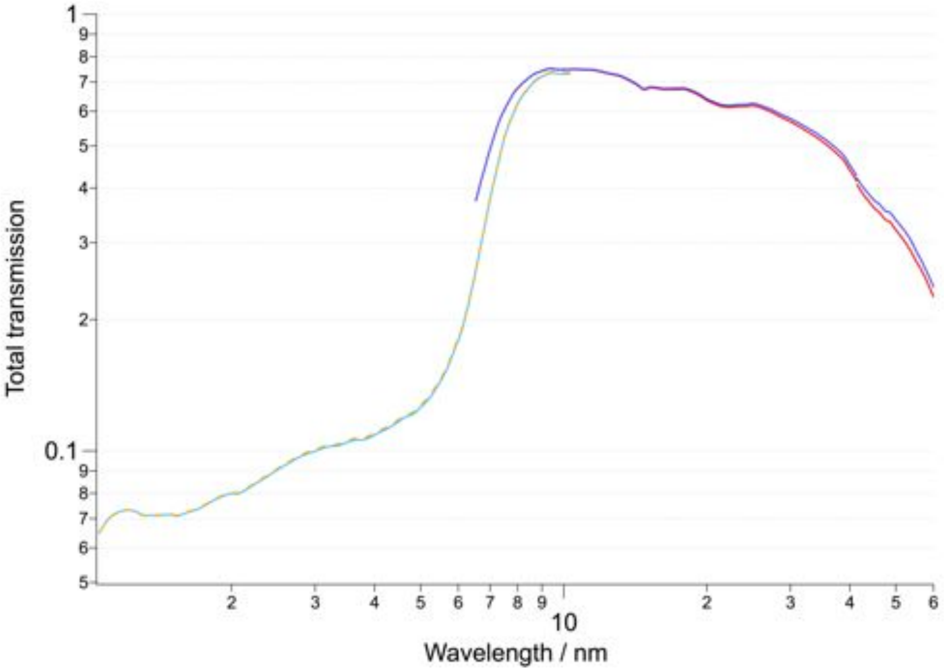

Figure 14 *Total beamline transmission for horizontal (blue/azure) and vertical (red/orange) linear polarized light. The simulations have taken into account the mirrors/gratings reflectivity/efficiency as well as the geometrical losses due to the finite size of the mirrors.*

In addition to the mirror reflectivity, another important cause of loss of beamline transmission derives from the geometrical losses. They are due to the finite size of the mirrors as well as to the presence of apertures. In fact, the photon beam divergence is linearly correlated to the wavelength meaning that the longer the radiation wavelength, the larger the transverse spot along the beamline. Their effect is negligible at wavelength below 20 nm (62 eV), where the beam is confined within the length of the mirrors. At longer wavelength, for radiation emitted in the first stage, the geometrical cuts become relevant with a transmission going from 87% at 30 nm (41 eV) down to 45% at 60 nm (21 eV). The overall beamline transmission is shown in Figure 14, having taken into account both reflectivity and geometrical losses in the whole FEL2 range.
Considering a photon pulse energy at the source of about 100 μJ, it is expected to obtain a pulse energy at the sample of the order of 58 μJ at 30 nm, and 20 μJ at 6 nm. These intensities will correspond to a fluence at the sample of the order of 2.5×10^{12} W cm^{-2} and 8.2×10^{11} W cm^{-2}, respectively. Of course the photon beam can be attenuated by means of a set of dedicated solid-state filters (such as Aluminum, Zirconium, Palladium, etc.) and/or by using the PADReS gas attenuator already operative. Moreover, the beam size can be easily enlarged by acting on the KAOS mirrors shape in order to reduce even more the fluence, if needed.

MagneDyn is expected to be assembled at the beginning of 2016 in a basic configuration consisting of all the mirrors (plane and KBs) without the photon energy spectrometer. Within the 2016 the beamline will be commissioned and the gratings, as well as the whole spectrometer mechanical system, will be purchased. In the future the 14 meter-free space between the spectrometer and the first focusing mirror (KB$_H$) will be filled with a wave-front split and delay line similar to the already installed Auto-

Correlator/Delay-Creator (AD/CD). Another possible upgrade will be merging the low energy source FEL1 with the beamline. This will extend the working energy range up to 100 nm with higher intensities.

References

[1] Gensch, M., et al. "New infrared undulator beamline at FLASH." Infrared Physics & Technology 51.5 (2008): 423-425

[2] Tavella, F., et al. "Few-femtosecond timing at fourth-generation X-ray light sources." Nature Photonics 5.3 (2011): 162-165

[3] Stojanovic, N., & Drescher, M. (2013). Accelerator-and laser-based sources of high-field terahertz pulses. Journal of Physics B: Atomic, Molecular and Optical Physics, 46(19), 192001

[4] Carr, G. Lawrence, et al. "High-power terahertz radiation from relativistic electrons." Nature 420.6912 (2002): 153-156

[5] Daranciang, Dan, et al. "Single-cycle terahertz pulses with> 0.2 V/Å field amplitudes via coherent transition radiation." Applied Physics Letters 99.14 (2011): 141117

[6] M.C. Hoffmann, S. Schulz, S. Wesch, S. Wunderlich, A. Cavalleri, and B. Schmidt, Optics Letters 36, 4473 (2011)

[7] M. Forst et al., Phys. Rev. B 84, 241104 (2011)

[8] M. Forst et al., Nature Photonics 7, 854 (2011)

[9] A. Dienst, et al., Nature Photonics 5, 485 (2011)

[10] D. Fausti, et al., Science 331, 189 (2011)

[11] M. Liu et al., Nature 487, 345 (2012)

[12] I. Tudosa, et al., Nature 428, 831 (2004)

[13] M.S. Sherwin, et al., “Opportunities in THz Science”, Report of a DOE-NSF-NIH Workshop, (2004)

[14] J.A. Fulop, et al., Optics Express 37, 557 (2012)

[15] C.P. Hauri, et al., Appl. Phys. Lett. 99, 161116 (2011)

[16] S. Casalbuoni, B. Schmidt, and P. Schmuser, TESLA Report 2005-15

[17] S. Casalbuoni, et al., ”Ultrabroadband terahertz source and beamline based on coherent transition radiation”, Phys. Rev. ST Accel. Beams 12, 030705 (2009)

[18] I.M. Frank, V.I. Ginzburg, J. Phys. (USSR), 9 (1945), 353

[19] A. Perucchi, et al., ”The TeraFERMI terahertz source at the seeded FERMI free-electron-laser facility”, Rev. Sci. Instrum. 84, 022702 (2013)

[20] S. Casalbuoni et al., “Numerical studies on the electro-optic detection of femtosecond electron bunches”, Phys. Rev. Spec. Top. - Accel. Beams 11, 1–18 (2008)

[21] http://www.desy.de/~schmidtb/THz-Transport

[22] Stohr, J., & Siegmann, H. C., “Magnetism: From Fundamentals to Nanoscale Dynamics”, by J. Stöhr and H.C. Siegmann. Springer Series in Solid-State Physics, Vol. 152. Berlin: Springer, (2006)

[23] Bigot, J.-Y., et al., “Coherent ultrafast magnetism induced by femtosecond laser pulse”, Nature Physics, 5(7), 515.

[24] Tudosa, I., et al., “The ultimate speed of magnetic switching in granular recording media”, Nature, 428(6985), 831–833, (2004)

[25] Kirilyuk, A., et al., Reviews of Modern Physics, (2010)

[26] Carpene, E., et al., “Dynamics of electron-magnon interaction and ultrafast demagnetization in thin iron films”, Physical Review B, 78(17), 174422, (2008)

[27] Cinchetti, M., et al., “Spin-Flip Processes and Ultrafast Magnetization Dynamics in Co: Unifying the Microscopic and Macroscopic View of Femtosecond Magnetism”, Physical Review Letters, 97(17), 177201, (2006)

[28] Koopmans, et al., “Explaining the paradoxical diversity of ultrafast laser-induced demagnetization”, Nature Materials, 9(3), 259–265, (2009)

[29] Koopmans, et al., “Unifying ultrafast magnetization dynamics”, Physical Review Letters, 95(26), (2005)

[30] La-O-Vorakiat, et al., Physical Review Letters, 103(25), 257402 EP, (2009)

[31] Stamm, C., et al., “Femtosecond modification of electron localization and transfer of angular momentum in nickel”, Nature Materials, 6(10), 740–743, (2007)

[32] Battiato, M., Carva, K., & Oppeneer, P. M., “Superdiffusive Spin Transport as a Mechanism of Ultrafast Demagnetization”, Physical Review Letters, 105(2), 027203, (2010)

[33] Mueller, B. Y., et al., “Feedback Effect during Ultrafast Demagnetization Dynamics in Ferromagnets.”, Physical Review Letters, 111(16), 167204, (2013)
[34] Beaurepaire, E., et al., “Ultrafast spin dynamics in ferromagnetic nickel”, Physical Review Letters, 76(22), 4250–4253, (1996)
[35] Boeglin, C., et al., “Distinguishing the ultrafast dynamics of spin and orbital moments in solids”, Nature, 465(7297), 458–461, (2010)
[36] Wietstruk, M., et al., “Hot-Electron-Driven Enhancement of Spin-Lattice Coupling in Gd and Tb 4f Ferromagnets Observed by Femtosecond X-Ray Magnetic Circular Dichroism”, Physical Review Letters, 106(12), 127401, (2011)
[37] Svetina, C., et al., “Characterization of the FERMI@Elettras on-line photon energy spectrometer”, in Advances in X-Ray/EUV Optics and Components VI, Morawe, C., Khounsary, A. M., and Goto, S., eds., Proceedings of SPIE - The International Society for Optical Engineering 8139, 81390J, (2011).
[38] Svetina, C., et al., “PRESTO, the on-line photon energy spectrometer at FERMI: design, features and commissioning results”, Journal of Synchrotron Radiation, In press, (2015)
[39] Schäfers F., “Calculation of grating efficiency” included in: Software codes RAY and REFLEC at BESSY, BESSY Technical Report 202/96, Berlin, (1996)
[40] LUMNAB program by M. Nevière, CNRS Marseille
[41] Raimondi, L., et al., “K-B bendable system optimization at FERMI@Elettra FEL: Impact of different spatial wavelengths on the spot size”, Proceedings of SPIE - The International Society for Optical Engineering, 8848, art. no. 88480B, (2013)[42] Raimondi, L., et al., “Status of the K-B bendable optics at FERMI@Elettra FEL”
(2014) Proceedings of SPIE - The International Society for Optical Engineering, 9208, art. no. 920804
[43] Cerrina F., et al., “Shadow PRIMER”, Center for X-ray Lithography, (1994)
[44] Raimondi, L., Spiga, D., “Self-consistent computation of x-ray mirror point spread functions from surface profile and roughness,” in Proceedings of SPIE - The International Society for Optical Engineering 7732, (2010)
[45] Spiga, D., Raimondi, L., “X-ray optical systems: From metrology to Point Spread Function”, Proceedings of SPIE - The International Society for Optical Engineering, 9209, art. no. 92090E, (2014)
[46] Raimondi, L., Spiga, D., “Mirrors for X-ray telescopes: Fresnel diffraction-based computation of point spread functions from metrology”, Astronomy & Astrophysics, Volume 573, id.A22, 19 pp. (2015)

Conclusions and outlooks

The Italian FERMI Free Electron Laser (FEL) project is objectively an overall success, recognized by the scientific community and demonstrated by the high number of proposals submitted in the different calls for external experiments as well as the high impact publications. From the machine side it has been proven that the seed laser-based High Gain Harmonic Generation scheme (both single and double cascade configurations) is able to generate electromagnetic radiation with unprecedented properties. In particular, it has been shown that the seed laser characteristics are fully inherited by the amplified VUV/soft x-ray FEL light, and that the latter can be controlled and finely tuned by means of the machine parameters. In addition, it has been demonstrated that the machine can operate in exotic configurations such as the one providing tunable two-colour double pulses for pump-probe experiments.

This big success should be necessarily linked to the whole Photon Analysis Delivery and REduction System (PADReS). The results obtained during the commissioning phase of the machine, in fact, have been possible only thanks to the PADReS photon diagnostics, which have been proven to be a reliable and robust system able to acquire the FEL parameters on-line and shot-to-shot. It should be noted that all the diagnostic and optical systems implemented along PADReS are custom-made, and based on in-house design. Their implementation and commissioning have represented a challenge that was eventually won, making PADReS a reliable and solid system capable of characterizing the FEL radiation.
In particular, with PADRES it is possible to determine: i) the transverse intensity and divergence distributions measured with the screens placed all along the beamlines, ii) the intensity measured with the aid of the I0 monitors and attenuated by means of the gas attenuator and solid state filters installed along PADReS, iii) the spectral content measured by means of the PRESTO spectrometer (probably the most important diagnostic) with extremely high resolution in a non-invasive way, and finally iv) the photon beam defined with the beam defining apertures and checked in position with the on-line beam position monitors. All the PADReS instrumentation is implemented in the acquisition system, and its most important parameters are routinely recorded in real time providing feedback to the machine physicists, and the scientists too.

Besides the diagnostic section, also the photon transport along the beamlines has played a crucial role in the commission and operation of the facility, and it was demonstrated to fully meet specifications: the employed mirrors do not perturb the beam wave-front, the overall transmission is very high, and the focused photon beam is thoroughly usable by the experimentalists. In particular, the unavoidable slight change in the polarization properties, due to the different reflectivity of the *s* and *p* component caused by the orientation of the different optics, can be compensated by changing the polarization at the source. The Auto-Correlator/Delay-Creator (AC/DC) has been successfully commissioned and is now used by the scientists for pump and probe experiments: it can split and recombine the beam inside the experimental chambers creating a controllable time delay between the two pulses up to 30 picoseconds with a step resolution of 30 fs. In addition, the PADReS focusing section has been able to focus the FEL radiation within few microns spot sizes, reaching the diffraction limit of the system. Finally, and likely most important, the Kirkpatrick-Baez Active Optics System (KAOS) has been designed, realized, and commissioned so to fulfill the experimental requirements: it allows to fully control the focal spot in both size and longitudinal position. Its opto-mechanical design, completely new and developed from the prototype-level, has resulted to be simultaneously simple and effective, guaranteeing at the same time the reliability requested by an operative user facility. Thanks to this unique system, the FEL radiation has been focused in different conditions, for different beamtimes, allowing to perform successfully several important experiments in the fields of microscopy, spectroscopy, and magnetism.

Meanwhile, the commissioning of EIS-TIMER beamline is in progress and will be concluded within 2016, and the transient grating spectroscopy technique with VUV/soft x-rays photons will be soon available to the users.

The obtained outstanding experimental results are the signature that the FERMI FEL is a worldwide centre of excellence for top-level research, and that the PADReS systems (diagnostics and beamlines) are able to perform at their best in the most disparate experimental configurations. These achievements are of course the result of the efforts of the FERMI team, which is composed by many groups such as the machine physicists, the machine operators, accelerator, laser, control and software, and PADReS groups, as well as the beamline scientists and users.

In the future the machine will be upgraded from 10 to 50 Hz repetition rate and the high-energy source will be optimized for emitting high intensity radiation down to 1 nanometer. More exotic configurations will be investigated, opening new possibilities for the accelerator physics and the experimentalists. The PADReS system is now undergoing several upgrades, in order to maximize the efficiency and reliability of the whole system. In particular, new mirror coatings will be progressively introduced to increase the overall transport transmission especially at short wavelengths, sets of filters will be implemented along the beamlines, new gases will be used for the attenuation of the beam, the multi-layer delay line will be installed inside the AC-DC (allowing to increase the temporal delay between the pulses up to 1.3 nanoseconds), and the KAOS actuators will be renewed providing more stability and reproducibility to the system. In addition, two more beamlines are under construction: the MagneDyn and TeraFERMI. These beamlines will extend the FERMI scientific case considerably and the results will span from ultra-fast dynamics of magnetic systems to the vibrational modes of organic and inorganic samples.

Many FEL user facilities are now implementing photon diagnostics and optical components based on the PADReS design. Several fruitful collaborations, both scientific and technological, have been established with a mutual benefit for the various laboratories involved.

The future of FELs, and in particular of FERMI, is bright. The challenges will be many and with more and most important scientific discoveries still to come.

Author research

The content of this PhD Thesis is the result of the joint efforts of the whole FERMI team and collaborators from all around the world. My contribution in the development of the PADReS photon transport, focusing and diagnostics sections has been significant. From the diagnostics side I have performed the optical design, the metrology characterization, the installation and the commissioning/optimization of the PRESTO spectrometer (probably the most important photon diagnostic at FERMI). Together with the PADReS team I have contributed to the Photodiode-YAG-Detector (PYD) and I0 monitors absolute calibrations, and to the commissioning of the Beam Defining Apertures (BDA), the Gas Attenuator (GA), the Beam Position Monitors (BPM), the Transverse Coherence system as well as the Auto-Correlator Delay Creator (AC/DC) instrument. From the photon transport side I have calculated the overall transmission for all the beamlines evaluating the polarization effect due to the presence of the grazing incident mirrors.

I have designed the EIS-TIMEX beamline having considered the scientific case and the technological state-of-the-art for the x-ray focusing mirrors. During the beamline commissioning I have demonstrated that my optical design and simulations of the focusing ellipsoidal mirror meet the beamline requirements providing diffraction limited spot sizes with fluences at the sample up to 10^{17} W cm^{-2}.

During these three years I have been deeply involved into the design and realization of a custom solution for the DiProI and LDM focusing sections: the Kirkpatrick-Baez Active Optics System (KAOS). I have contributed to the optical design and metrology characterization/optimization of the system. Together with the PADReS team I have optimized the focusing performances by means of the photon diagnostics, reaching the diffraction limit of the system.

During the FERMI commissioning I have actively participated to the characterization of the FEL properties of both FEL1 and FEL2 in standard and exotic configurations, providing support to the machine physicists and performing the measurements with the PADReS photon diagnostics. I have also been involved into the commissioning of the EIS-TIMEX, DiProI and LDM end-stations providing the focused radiation and the support with the PADReS team. Later on, I have taken part into the commissioning of the EIS-TIMER beamline been able to create and detect the transient grating signal. The commissioning will be concluded within the end of 2016 and the beamline will open to the users.

Meanwhile I have performed the optical design of the two future beamlines MagneDyn and TeraFERMI extending the FERMI scientific case and providing new tools for the investigation of magnetic and vibrational properties of organic and inorganic materials at a nano-scopic level.

In addition, together with the PADReS team, I have routinely aligned the beamlines for both the machine studies and the user experiments providing the focal spots requested by the users. During the beamtimes I have actively participated to the experiments providing support from the diagnostics and focusing side. In particular for the Mini-TIMER experiment I have aligned the beamline and provided the focusing with KAOS. I have also performed the Atomic Force Microscope (AFM) measurements of the sample under investigation proving the creation of a permanent grating when the FEL intensity was above 50 mJ cm^{-2}.

During the PhD I have also published on many relevant scientific journals (see the list in the Author Publication) as principal author and co-author, and have participated to many international conferences and workshops as a contributed and invited speaker. In addition, I have been a referee for Nuclear Instruments and Methods in Physics Research Section A (NIMA) and Journal of Synchrotron Radiation (JSR).

In the future I will be involved in designing two more photon energy spectrometers for the EIS-TIMEX end-station, in the commissioning of EIS-TIMER, and the construction/commissioning of the MagneDyn and TeraFERMI beamlines. Meanwhile I will continue supporting the FEL users during the beamtimes together with the PADReS group.

Author publications (during the PhD)

[1] K. C. Prince, E. Allaria, C. Callegari, R. Cucini, G. De Ninno, S. Di Mitri, B. Diviacco, E. Ferrari, P. Finetti, D. Gauthier, L. Giannessi, N. Mahne, G. Penco, O. Plekan, L. Raimondi, P. Rebernik, E. Roussel, C. Svetina, M. Trovò, M. Zangrando, M. Negro, P. Carpeggiani, M. Reduzzi, G. Sansone, A. N. Grum-Grzhimailo, E. V. Gryzlova, S. I. Strakhova, K. Bartschat, N. Douguet, J. Venzke, D. Iablonskyi, Y. Kumagai, T. Takanashi, K. Ueda, A. Fischer, M. Coreno, F. Stienkemeier, Y. Ovcharenko, T. Mazza and M. Meyer
Coherent control with a short-wavelength free-electron laser
(2016) Nature Photonics, doi:10.1038/nphoton.2016.13 (In press)

[2] Ferrari, E., Spezzani, C., Fortuna, F., Delaunay, R., Vidal, F., Nikolov, I., Cinquegrana, P., Diviacco, B., Gauthier, D., Penco, G., Ribic, P.R., Roussel, E., Trovo, M., Moussy, J.-B., Pincelli, T., Lounis, L., Manfredda, M., Pedersoli, E., Capotondi, F., Svetina, C., Mahne, N., Zangrando, M., Raimondi, L., Demidovich, A., Giannessi, L., De Ninno, G., Danailov, M.B., Allaria, E., Sacchi, M.
Widely tunable two-colour seeded free-electron laser source for resonant-pump resonant-probe magnetic scattering
(2016) Nature Communications, 7, art. no. 10343.

[3] Svetina, C., Cocco, D., Mahne, N., Raimondi, L., Ferrari, E., Zangrando, M.
PRESTO, the on-line photon energy spectrometer at FERMI: Design, features and commissioning results
(2016) Journal of Synchrotron Radiation, 23, pp. 35-42.

[4] Bencivenga, F., Zangrando, M., Svetina, C., Abrami, A., Battistoni, A., Borghes, R., Capotondi, F., Cucini, R., Dallari, F., Danailov, M., Demidovich, A., Fava, C., Gaio, G., Gerusina, S., Gessini, A., Giacuzzo, F., Gobessi, R., Godnig, R., Grisonich, R., Kiskinova, M., Kurdi, G., Loda, G., Lonza, M., Mahne, N., Manfredda, M., Mincigrucci, R., Pangon, G., Parisse, P., Passuello, R., Pedersoli, E., Pivetta, L., Prica, M., Principi, E., Rago, I., Raimondi, L., Sauro, R., Scarcia, M., Sigalotti, P., Zaccaria, M., Masciovecchio, C.
Experimental setups for FEL-based four-wave mixing experiments at FERMI
(2016) Journal of Synchrotron Radiation, 23, pp. 132-140.

[5] Svetina, C., Mahne, N., Raimondi, L., Caretta, A., Casarin, B., Dell'Angela, M., Malvestuto, M., Parmigiani, F., Zangrando, M.
MagneDyn: The beamline for magneto dynamics studies at FERMI
(2016) Journal of Synchrotron Radiation, 23, pp. 98-105.

[6] Matruglio, A., Dal Zilio, S., Sergo, R., Mincigrucci, R., Svetina, C., Principi, E., Mahne, N., Raimondi, L., Turchet, A., Masciovecchio, C., Lazzarino, M., Cautero, G., Zangrando, M.
A novel approach in the free-electron laser diagnosis based on a pixelated phosphor detector
(2016) Journal of Synchrotron Radiation, 23, pp. 29-34.

[7] Svetina, C., Mahne, N., Raimondi, L., Perucchi, A., Di Pietro, P., Lupi, S., Schmidt, B., Zangrando, M.
Photon transport of the superradiant TeraFERMI THz beamline at the FERMI free-electron laser
(2016) Journal of Synchrotron Radiation, 23, pp. 106-110.

[8] Bencivenga, F., Cucini, R., Capotondi, F., Battistoni, A., Mincigrucci, R., Giangrisostomi, E., Gessini, A., Manfredda, M., Nikolov, I.P., Pedersoli, E., Principi, E., Svetina, C., Parisse, P., Casolari, F., Danailov, M.B., Kiskinova, M., Masciovecchio, C.
Four-wave mixing experiments with extreme ultraviolet transient gratings
(2015) Nature, 520 (7546), pp. 205-208.

[9] Raimondi, L., Svetina, C., Mahne, N., Cocco, D., Capotondi, F., Pedersoli, E., Manfredda, M., Kiskinova, M., Zangrando, M.
Active optics systems at FERMI free electron laser
(2015) Adaptive Optics: Analysis, Methods and Systems, AO 2015, p. 289.

[10] Svetina, C., Grazioli, C., Mahne, N., Raimondi, L., Fava, C., Zangrando, M., Gerusina, S., Alagia, M., Avaldi, L., Cautero, G., De Simone, M., Devetta, M., Di Fraia, M., Drabbels, M., Feyer, V., Finetti, P., Katzy, R., Kivimäki, A., Lyamayev, V., Mazza, T., Moise, A., Möller, T., O'Keeffe, P., Ovcharenko, Y., Piseri, P., Plekan, O., Prince, K.C., Sergo, R., Stienkemeier, F., Stranges, S., Coreno, M., Callegari, C.
The Low Density Matter (LDM) beamline at FERMI: Optical layout and first commissioning
(2015) Journal of Synchrotron Radiation, 22, pp. 538-543.

[11] Allaria, E., Badano, L., Bassanese, S., Capotondi, F., Castronovo, D., Cinquegrana, P., Danailov, M.B., D'Auria, G., Demidovich, A., De Monte, R., De Ninno, G., Di Mitri, S., Diviacco, B., Fawley, W.M., Ferianis, M., Ferrari, E., Gaio, G., Gauthier, D., Giannessi, L., Iazzourene, F., Kurdi, G., Mahne, N., Nikolov, I., Parmigiani, F., Penco, G., Raimondi, L., Rebernik, P., Rossi, F., Roussel, E., Scafuri, C., Serpico, C., Sigalotti, P., Spezzani, C., Svandrlik, M., Svetina, C., Trovó, M., Veronese, M., Zangrando, D., Zangrando, M.
The FERMI free-electron lasers
(2015) Journal of Synchrotron Radiation, 22, pp. 485-491.

[12] Capotondi, F., Pedersoli, E., Bencivenga, F., Manfredda, M., Mahne, N., Raimondi, L., Svetina, C., Zangrando, M., Demidovich, A., Nikolov, I., Danailov, M., Masciovecchio, C., Kiskinova, M.
Multipurpose end-station for coherent diffraction imaging and scattering at FERMI@Elettra free-electron laser facility
(2015) Journal of Synchrotron Radiation, 22, pp. 544-552.

[13] Spezzani, C., Ferrari, E., Allaria, E., Vidal, F., Lounis, L., Ciavardini, A., Delaunay, R., Capotondi, F., Pedersoli, E., Coreno, M., Svetina, C., Raimondi, L., Zangrando, M., Ivanov, R., Nikolov, I., Demidovich, A., Danailov, M., De Ninno, G., Popescu, H., Eddrief, M., Kiskinova, M., Sacchi, M.
Optically induced Fe magnetization reversal in Fe/MnAs/GaAs(001)
(2015) Proceedings of SPIE - The International Society for Optical Engineering, 9512, art. no. 95120I.

[14] Zangrando, M., Cocco, D., Fava, C., Gerusina, S., Gobessi, R., Mahne, N., Mazzucco, E., Raimondi, L., Rumiz, L., Svetina, C.
Recent results of PADReS, the Photon Analysis Delivery and REduction System, from the FERMI FEL commissioning and user operations
(2015) Journal of Synchrotron Radiation, 22, pp. 565-570.

[15] Poletto, L., Frassetto, F., Miotti, P., Gauthier, D., Fajardo, M., Mahieu, B., Svetina, C., Zangrando, M., Zeitoun, P., De Ninno, G.
Grating-based pulse compressor for applications to FEL sources
(2015) Proceedings of SPIE - The International Society for Optical Engineering, 9512, art. no. 951210.

[16] Masciovecchio, C., Battistoni, A., Giangrisostomi, E., Bencivenga, F., Principi, E., Mincigrucci, R., Cucini, R., Gessini, A., D'Amico, F., Borghes, R., Prica, M., Chenda, V., Scarcia, M., Gaio, G., Kurdi, G., Demidovich, A., Danailov, M.B., Di Cicco, A., Filipponi, A., Gunnella, R., Hatada, K., Mahne, N., Raimondi, L., Svetina, C., Godnig, R., Abrami, A., Zangrando, M.
EIS: The scattering beamline at FERMI
(2015) Journal of Synchrotron Radiation, 22, pp. 553-564.

[17] Zangrando, M., Mahne, N., Raimondi, L., Svetina, C.
The soft x-ray free-electron laser fermi@elettra
(2015) Springer Series in Optical Sciences, 197, pp. 23-40.

[18] Bencivenga, F., Cucini, R., Capotondi, F., Battistoni, A., Mincigrucci, R., Giangrisostomi, E., Gessini, A., Manfredda, M., Nikolov, I.P., Pedersoli, E., Principi, E., Svetina, C., Parisse, P., Casolari, F., Danailov, M.B., Kiskinova, M., Masciovecchio, C.
FEL-based transient grating spectroscopy
(2015) Proceedings of SPIE - The International Society for Optical Engineering, 9512, art. no. 951212.

[19] Spezzani, C., Ferrari, E., Allaria, E., Vidal, F., Ciavardini, A., Delaunay, R., Capotondi, F., Pedersoli, E., Coreno, M., Svetina, C., Raimondi, L., Zangrando, M., Ivanov, R., Nikolov, I., Demidovich, A., Danailov, M.B., Popescu, H., Eddrief, M., De Ninno, G., Kiskinova, M., Sacchi, M.
Magnetization and Microstructure Dynamics in Fe/MnAs/GaAs (001): Fe Magnetization Reversal by a Femtosecond Laser Pulse
(2014) Physical Review Letters, 113 (24).

[20] Mazza, T., Ilchen, M., Rafipoor, A.J., Callegari, C., Finetti, P., Plekan, O., Prince, K.C., Richter, R., Danailov, M.B., Demidovich, A., De Ninno, G., Grazioli, C., Ivanov, R., Mahne, N., Raimondi, L., Svetina, C., Avaldi, L., Bolognesi, P., Coreno, M., O'Keeffe, P., Di Fraia, M., Devetta, M., Ovcharenko, Y., Möller, T., Lyamayev, V., Stienkemeier, F., Düsterer, S., Ueda, K., Costello, J.T., Kazansky, A.K., Kabachnik, N.M., Meyer, M.
Determining the polarization state of an extreme ultraviolet free-electron laser beam using atomic circular dichroism
(2014) Nature Communications, 5, art. no. 3648.

[21] Svandrlik, M., Allaria, E., Bencivenga, F., Callegari, C., Capotondi, F., Castronovo, D., Cinquegrana, P., Coreno, M., Cucini, R., Cudin, I., Danailov, M.B., D'Auria, G., De Monte, R., De Ninno, G., Delgiusto, P., Demidovich, A., Di Mitri, S., Diviacco, B., Fabris, A., Fabris, R., Fawley, W.M., Ferianis, M., Ferrari, E., Finetti, P., Fröhlich, L., Furlan Radivo, P., Gaio, G., Gauthier, D., Gelmetti, F., Giannessi, L., Kiskinova, M., Krecic, S., Lonza, M., Mahne, N., Masciovecchio, C., Milloch, M., Parmigiani, F., Penco, G., Pivetta, L., Plekan, O., Predonzani, M., Principi, E., Raimondi, L., Rebernik Ribic, P., Rossi, F., Rumiz, L., Scafuri, C., Serpico, C., Sigalotti, P., Spezzani, C., Svetina, C., Trovò, M., Vascotto, A., Veronese, M., Visintini, R., Zangrando, D., Zangrando, M.
Fermi status report
(2014) IPAC 2014: Proceedings of the 5th International Particle Accelerator Conference, pp. 2885-2887.

[22] Raimondi, L., Svetina, C., Mahne, N., Cocco, D., Capotondi, F., Pedersoli, E., Manfredda, M., Kiskinova, M., Keitel, B., Brenner, G., Plönjes, E., Mey, T., Mann, K., Zangrando, M.
Status of the K-B bendable optics at FERMI@Elettra FEL
(2014) Proceedings of SPIE - The International Society for Optical Engineering, 9208, art. no. 920804.

[23] Svetina, C., Dell'Angela, M., Mahne, N., Malvestuto, M., Parmigiani, F., Raimondi, L., Zangrando, M.
MagneDyn: The future beamline for ultrafast magnetodynamical studies at FERMI
(2014) Proceedings of SPIE - The International Society for Optical Engineering, 9207, art. no. 92070E.

[24] Zangrando, M., Fava, C., Gerusina, S., Gobessi, R., Mahne, N., Mazzucco, E., Raimondi, L., Rumiz, L., Svetina, C.
The experience of the FERMI@Elettra photon beam transport and diagnostics system (PADReS) during three years of continuous support of machine and user experiments: Achievements, lessons learned, and future upgrades
(2014) Proceedings of SPIE - The International Society for Optical Engineering, 9210, art. no. 921003.

[25] Mahieu, B., Allaria, E., Danailov, M.B., Demidovich, A., De Ninno, G., Di Mitri, S., Ferrari, E., Fröhlich, L., Gauthier, D., Giannessi, L., Mahne, N., Penco, G., Raimondi, L., Ribic, P.R., Spampinati, S., Spezzani, C., Svetina, C., Trovò, M., Zangrando, M.
Chirp control in a seeded free-electron laser
(2014) Optics InfoBase Conference Papers.

[26] Allaria, E., Diviacco, B., Callegari, C., Finetti, P., Mahieu, B., Viefhaus, J., Zangrando, M., De Ninno, G., Lambert, G., Ferrari, E., Buck, J., Ilchen, M., Vodungbo, B., Mahne, N., Svetina, C., Spezzani, C., Di Mitri, S., Penco, G., Trovó, M., Fawley, W.M., Rebernik, P.R., Gauthier, D., Grazioli, C., Coreno, M., Ressel, B., Kivimäki, A., Mazza, T., Glaser, L., Scholz, F., Seltmann, J., Gessler, P., Grünert, J., De Fanis, A., Meyer, M., Knie, A., Moeller, S.P., Raimondi, L., Capotondi, F., Pedersoli, E., Plekan, O., Danailov, M.B., Demidovich, A., Nikolov, I., Abrami, A., Gautier, J., Lüning, J., Zeitoun, P., Giannessi, L.
Control of the polarization of a vacuum-ultraviolet, high-gain, free-electron laser
(2014) Physical Review X, 4 (4), art. no. 041040.

[27] Finetti, P., Allaria, E., Diviacco, B., Callegari, C., Mahieu, B., Viefhaus, J., Zangrando, M., De Ninno, G., Lambert, G., Ferrari, E., Buck, J., Ilchen, M., Vodungbo, B., Mahne, N., Svetina, C., Spezzani, C., Di Mitri, S., Penco, G., Trovò, M., Fawley, W.M., Rebernik, P., Gauthier, D., Grazioli, C., Coreno, M., Ressel, B., Kivimäki, A., Mazza, T., Glaser, L., Scholz, F., Seltmann, J., Gessler, P., Grünert, J., De Fanis, A., Meyer, M., Knie, A., Moeller, S.P., Raimondi, L., Capotondi, F., Pedersoli, E., Plekan, O., Danailov, M., Demidovich, A., Nikolov, I., Abrami, A., Gautier, J., Lüning, J., Zeitoun, P., Giannessia, L.
Polarization measurement of free electron laser pulses in the VUV generated by the variable polarization source FERMI
(2014) Proceedings of SPIE - The International Society for Optical Engineering, 9210, art. no. 92100K.

[28] Svandrlik, M., Allaria, E., Bencivenga, F., Callegari, C., Capotondi, F., Castronovo, D., Cinquegrana, P., Cudin, I., Dal Forno, M., Danailov, M.B., D'auria, G., De Monte, R., De Ninno, G., Demidovich, A., Di Mitri, S., Diviacco, B., Fabris, A., Fabris, R., Fawley, W.M., Ferianis, M., Ferrari, E., Finetti, P., Froehlich, L., Radivo, P.F., Gaio, G., Giannessi, L., Kiskinova, M., Loda, G., Lonza, M., Mahne, N., Masciovecchio, C., Parmigiani, F., Penco, G., Plekan, O., Predonzani, M., Principi, E., Raimondi, L., Rossi, F., Rumiz, L., Scafuri, C., Serpico, C., Sigalotti, P., Spampinati, S., Spezzani, C., Sturari, L., Svetina, C., Trovo', M., Vascotto, A., Veronese, M., Visintini, R., Zangrando, D., Zangrando, M., Mahieu, B., Craievich, P.
Fermi seeded FEL progress report
(2013) IPAC 2013: Proceedings of the 4th International Particle Accelerator Conference, pp. 1182-1184.

[29] Di Mitri, S., Allaria, E., Castronovo, D., Cinquegrana, P., Craievich, P., Danailov, M.B., D'auria, G., De Ninno, G., Demidovich, A., Diviacco, B., Fawley, W.M., Ferianis, M., Ferrari, E., Froehlich, L., Gauthier, D., Gaio, G., Giannessi, L., Ivanov, R., Mahieu, B., Mahne, N., Nikolov, I., Parmigiani, F., Penco, G., Raimondi, L., Serpico, C., Sigalotti, P., Spampinati, S., Spezzani, C., Svandrlik, M., Svetina, C., Trovo, M., Vascotto, A., Veronese, M., Zangrando, D., Zangrando, M.
Double stage seeded fel with fresh bunch injection technique at fermi@elettra
(2013) IPAC 2013: Proceedings of the 4th International Particle Accelerator Conference, pp. 1185-1186.

[30] Raimondi, L., Svetina, C., Mahne, N., Cocco, D., Capotondi, F., Pedersoli, E., Kiskinova, M., Keitel, B., Brenner, G., Plönjes, E., Mey, T., Mann, K., Zangrando, M.
K-B bendable system optimization at FERMI@Elettra FEL: Impact of different spatial wavelengths on the spot size
(2013) Proceedings of SPIE - The International Society for Optical Engineering, 8848, art. no. 88480B.

[31] Allaria, E., Bencivenga, F., Borghes, R., Capotondi, F., Castronovo, D., Charalambous, P., Cinquegrana, P., Danailov, M.B., De Ninno, G., Demidovich, A., Di Mitri, S., Diviacco, B., Fausti, D., Fawley, W.M., Ferrari, E., Froehlich, L., Gauthier, D., Gessini, A., Giannessi, L., Ivanov, R., Kiskinova, M., Kurdi, G., Mahieu, B., Mahne, N., Nikolov, I., Masciovecchio, C., Pedersoli, E., Penco, G., Raimondi, L., Serpico, C., Sigalotti, P., Spampinati, S., Spezzani, C., Svetina, C., Trovò, M., Zangrando, M.
Two-colour pump-probe experiments with a twin-pulse-seed extreme ultraviolet free-electron laser
(2013) Nature Communications, 4, art. no. 2476.

[32] Allaria, E., Castronovo, D., Cinquegrana, P., Danailov, M.B., D'Auria, G., Demidovich, A., Di Mitri, S., Diviacco, B., Fawley, W.M., Ferianis, M., Froehlich, L., Gaio, G., Ivanov, R., Mahne, N., Nikolov, I., Penco, G., Raimondi, L., Serpico, C., Sigalotti, P., Spezzani, C., Svandrlik, M., Svetina, C., Trovo, M., Veronese, M., Zangrando, D., Mahieu, B., Dal Forno, M., Giannessi, L., Zangrando, M., De Ninno, G., Ferrari, E., Parmigiani, F., Gauthier, D.
Double stage seeded fel with fresh bunch injection technique at fermi
(2013) FEL 2013: Proceedings of the 35th International Free-Electron Laser Conference, pp. 723-727.

[33] Allaria, E., Bencivenga, F., Callegari, C., Capotondi, F., Castronovo, D., Cinquegrana, P., Cudin, I., Dal Forno, M., Danailov, M.B., D'Auria, G., De Monte, R., De Ninno, G., Demidovich, A., Di Mitri, S., Diviacco, B., Fabris, A., Fabris, R., Fawley, W.M., Ferianis, M., Ferrari, E., Froehlich, L., Furlan Radivo, P., Gaio, G., Giannessi, L., Kiskinova, M., Lonza, M., Mahieu, B., Mahne, N., Masciovecchio, C., Parmigiani, F., Penco, G., Predonzani, M., Principi, E., Raimondi, L., Rossi, F., Rumiz, L., Scafuri, C., Serpico, C., Sigalotti, P., Spampinati, S., Spezzani, C., Svandrlik, M., Svetina, C., Trovo, M., Vascotto, A., Veronese, M., Visintini, R., Zangrando, D., Zangrando, M., Craievich, P.

Fermi@elettra status report
(2013) FEL 2013: Proceedings of the 35th International Free-Electron Laser Conference, pp. 546-549.

[34] Zangrando, M., Giannessi, L., Allaria, E., Bencivenga, F., Capotondi, F., Castronovo, D., Cinquegrana, P., Danailov, M.B., Demidovich, A., Di Mitri, S., Diviacco, B., Fawley, W.M., Ferrari, E., Froehlich, L., Ivanov, R., Kiskinova, M., Mahieu, B., Mahne, N., Masciovecchio, C., Nikolov, I., Pedersoli, E., Penco, G., Raimondi, L., Serpico, C., Sigalotti, P., Spampinati, S., Spezzani, C., Svetina, C., Trovo, M., Gauthier, D., De Ninno, G., Fausti, D.
Jitter-free time resolved resonant cdi experiments using two-color fel pulses generated by the same electron bunch
(2013) FEL 2013: Proceedings of the 35th International Free-Electron Laser Conference, pp. 753-756.

[35] Bencivenga, F., Baroni, S., Carbone, C., Chergui, M., Danailov, M.B., De Ninno, G., Kiskinova, M., Raimondi, L., Svetina, C., Masciovecchio, C.
Nanoscale dynamics by short-wavelength four wave mixing experiments
(2013) New Journal of Physics, 15, art. no. 123023.

[36] Allaria, E., Castronovo, D., Cinquegrana, P., Craievich, P., Dal Forno, M., Danailov, M.B., D'Auria, G., Demidovich, A., De Ninno, G., Di Mitri, S., Diviacco, B., Fawley, W.M., Ferianis, M., Ferrari, E., Froehlich, L., Gaio, G., Gauthier, D., Giannessi, L., Ivanov, R., Mahieu, B., Mahne, N., Nikolov, I., Parmigiani, F., Penco, G., Raimondi, L., Scafuri, C., Serpico, C., Sigalotti, P., Spampinati, S., Spezzani, C., Svandrlik, M., Svetina, C., Trovo, M., Veronese, M., Zangrando, D., Zangrando, M.
Two-stage seeded soft-X-ray free-electron laser
(2013) Nature Photonics, 7 (11), pp. 913-918.

[37] Mahieu, B., Allaria, E., Castronovo, D., Danailov, M.B., Demidovich, A., De Ninno, G., Di Mitri, S., Fawley, W.M., Ferrari, E., Fröhlich, L., Gauthier, D., Giannessi, L., Mahne, N., Penco, G., Raimondi, L., Spampinati, S., Spezzani, C., Svetina, C., Trovò, M., Zangrando, M.
Two-colour generation in a chirped seeded free-electron laser: A close look
(2013) Optics Express, 21 (19), pp. 22728-22741.
[36] Bencivenga, F., Raimondi, L., Svetina, C., Masciovecchio, C.
Four wave mixing using coherent FEL radiation
(2013) Proceedings of SPIE - The International Society for Optical Engineering, 8778, art. no. 877807.

[38] Raimondi, L., Svetina, C., Mahne, N., Cocco, D., Abrami, A., De Marco, M., Fava, C., Gerusina, S., Gobessi, R., Capotondi, F., Pedersoli, E., Kiskinova, M., De Ninno, G., Zeitoun, P., Dovillaire, G., Lambert, G., Boutu, W., Merdji, H., Gonzalez, A.I., Gauthier, D., Zangrando, M.
Microfocusing of the FERMI@Elettra FEL beam with a K-B active optics system: Spot size predictions by application of the WISE code
(2013) Nuclear Instruments and Methods in Physics Research, Section A: Accelerators, Spectrometers, Detectors and Associated Equipment, 710, pp. 131-138.

[39] Spiga, D., Raimondi, L., Svetina, C., Zangrando, M.
X-ray beam-shaping via deformable mirrors: Analytical computation of the required mirror profile
(2013) Nuclear Instruments and Methods in Physics Research, Section A: Accelerators, Spectrometers, Detectors and Associated Equipment, 710, pp. 125-130.

[40] Capotondi, F., Pedersoli, E., Mahne, N., Menk, R.H., Passos, G., Raimondi, L., Svetina, C., Sandrin, G., Zangrando, M., Kiskinova, M., Bajt, S., Barthelmess, M., Fleckenstein, H., Chapman, H.N., Schulz, J., Bach, J., Frömter, R., Schleitzer, S., Müller, L., Gutt, C., Grübel, G.
Invited Article: Coherent imaging using seeded free-electron laser pulses with variable polarization: First results and research opportunities
(2013) Review of Scientific Instruments, 84 (5), art. no. 051301.

[41] Svetina, C., Mahne, N., Raimondi, L., Rumiz, L., Zangrando, M., Allaria, E., Bencivenga, F., Callegari, C., Capotondi, F., Castronovo, D., Cinquegrana, P., Craievich, P., Cudin, I., Dal Forno, M., Danailov, M.B., D'Auria, G., De Monte, R., De Ninno, G., Demidovich, A., Di Mitri, S., Diviacco, B., Fabris, A., Fabris, R., Fawley, W.M., Ferianis, M., Ferrari, E., Froehlich, L., Radivo, P.F., Gaio, G., Giannessi, L., Kiskinova, M., Lonza, M., Mahieu, B., Masciovecchio, C., Nikolov, I.P., Parmigiani, F., Pedersoli, E., Penco, G., Predonzani, M., Principi, E., Rossi, F., Scafuri, C., Serpico, C., Sigalotti, P.,

Spampinati, S., Spezzani, C., Svandrlik, M., Trovo, M., Vascotto, A., Veronese, M., Visintini, R., Zangrando, D.
Status and achievements at FERMI@Elettra: the first double cascade seeded EUV-SXR FEL facility open to users
(2013) Proceedings of SPIE - The International Society for Optical Engineering, 8849, art. no. 88490O.